UNIVERSITÀ DEGLI STUDI DI TRIESTE

XXVIII CICLO DEL DOTTORATO DI RICERCA IN

NANOTECNOLOGIE

NANOCOMPOSITE SYSTEMS BASED ON POLYSACCHARIDES AND ORGANIC/INORGANIC NANOSTRUCTURES FOR BIOMEDICAL APPLICATIONS

(SSD BIO/10 – Biochimica)

DOTTORANDO

DAVIDE PORRELLI

COORDINATORE

PROF. LUCIA PASQUATO

SUPERVISORE DI TESI

DOTT. ING. ANDREA TRAVAN

TUTORE

DOTT. IVAN DONATI

TUTORE

DOTT. MASSIMILIANO BORGOGNA

ANNO ACCADEMICO 2014/2015

UNIVERSITÀ DEGLI STUDI DI TRIESTE

XXVIII CICLO DEL DOTTORATO DI RICERCA IN

NANOTECNOLOGIE

NANOCOMPOSITE SYSTEMS BASED ON POLYSACCHARIDES AND ORGANIC/INORGANIC NANOSTRUCTURES FOR BIOMEDICAL APPLICATIONS

(SSD BIO/10 – Biochimica)

DOTTORANDO

DAVIDE PORRELLI

COORDINATORE

PROF. LUCIA PASQUATO

SUPERVISORE DI TESI

DOTT. ING. ANDREA TRAVAN

TUTORE

DOTT. IVAN DONATI

TUTORE

DOTT. MASSIMILIANO BORGOGNA

ANNO ACCADEMICO 2014/2015

When a blind beetle crawls over the surface of a curved branch,
it does not notice that the tracks it has covered is indeed curved.
I was lucky enough to notice what the beetle did not notice.
(Albert Einstein)

TABLE OF CONTENT

LIST OF ABBREVIATIONS

^{1}H-NMR: Nuclear Magnetic Resonance proton spectra

A_{490}: absorbance at 490 nm

A_{690}: absorbance at 690 nm

A9: BDNF expressing D16

AB: Acid-Base component of solid surface energy

AFM: Atomic Force Microscopy

ALP: ALkalyne Phosphatase

BCA: BiCinhoninic Acid assay

BDNF: Brain-Derived Neurotrophic Factor

BHI: Brain Heart Infusion

BMSC: Bone Marrow Stromal Cell

BMP: Bone Morphogenetic Protein

β-TCP: beta tricalcium phosphate

β-tub III: β-tubulin III

BV/TV: Bone Volume / Total Volume

CA: Contact Angle

ChAT: Choline acetyltransferase

Chitlac-nAg: nAg synthesized in CTL

CFU: Colony-Forming Unit

CLSM: Confocal Laser Scanning Microscopy

C_m: Membrane capacitance

CNS: Central Nervous System

CNT: Carbon Nanotube

CPC: Calcium Phosphate Cement

CPMG: Carr-Purcell-Meiboom-Gill

CRIO: CRyo-Prepared IsOtropic

CRIOsc: alginate scaffolds prepared with CRIO process

D7: MN progenitors

D16: GFP-expressing MABs

DA: Degree of Anisotropy

DAPI: 4',6-diamidino-2-phenylindole

DBM: Demineralized Bone Matrix

DI: Diiodomethane

DMEM: Dulbecco's Modified Eagle Medium

DWCNT: Double-Walled CNT

E: Young compression modulus

η: viscosity

EDC: 1-Ethyl-3-(3-dimethyla minopropyl) carbodiimide

EDTA: EthyleneDiamineTetraacetic acid

EG: Ethylen Glicole

ELISA: Enzime Linked ImmunoSorbant Assay

f-CNT: functionalized CNT

f_0-CNT: pristine/un-derivatized CNT

f_1-CNT: CNT functionalized through the diazonium salt-based arylation reaction

f_2-CNT: oxidized CNT

f_3-CNT: CNT functionalized the through 1,3-dipolar cycloaddition of azomethines ylides reaction

F10: NGF expressing D16

FBS: Fetal Bovine Serum

F_G: mole fraction of alginate monomers as α-l-guluronic acid

F_{GG}: fraction of α-l-guluronic acid dimers

F_{GM+MG}: fraction of any mixed sequence of α-l-guluronic acid and β-d-mannuronic acid

F_M: mole fraction of alginate monomers as β-d-mannuronic acid

F_{MM}: fraction of β-d-mannuronic acid dimers

FITC: Fluorescein IsoThioCyanate

G: shear modulus

G': storage/elastic modulus

G'': loss/viscosity modulus

GDL: δ-glucono lactone

GF: Growth Factor

GFAP: Glial Fibrillary Acid Protein

γ^+: acid term of γ^{tot}

γ^-: base term of γ^{tot}

γ^{AB}: polar term of γ^{tot}

γ^{LW}: apolar term of γ^{tot}

γ^{tot}: total surface free energy

HAp: HydroxyApatite

HEPES:4-(2-hydroxyethyl)-1-iperazineethanesulfonic acid

hMSC: human Mesenchimal Stem Cell

ICP-OES: Inductively Coupled Plasma - Optical Emission Spectroscopy

IGF-1: Insuline-like Growht Factor-1

ISISA: Ice Segregation Induced Self Assembly

ISISAsc: alginate scaffolds prepared by the ISISA process

LB: Luria-Bertani

LDH: Lactate DeHydrogenale

λ_{em}: emission wavelength

λ_{exc}: excitation wavelength

LF-NMR: Low Field Nuclear Magnetic Resonance

LOD: Limit Of Detection

LW: Dispersive component of solid surface energy

MAB: MesoAngioBlast

MB: microbeads

***μ*-CT**: micro-Computed Tomography

MES: 2-(N-morpholino)ethanesulfonic acid

MG63: human osteosarcoma cell line

MN: Moto Neurons

MSC: Mesenchimal Stem Cell

MTS:(3-(4,5-dimethylthiazol-2-yl)-5-(3-carboxymethoxyphenyl)-2-(4-sulfophenyl)-2H-tetrazolium)

MW: Molecular Weight

MWCNT: Multi-Walled CNT

Mxy: x-y component of the magnetization vector

nAg: silver nanoparticles

nAg-MB: microbeads with nAg

NF: Neurotrophine

$N_{G>1}$: average α-l-guluronic acid -block length larger than 1

NGF: Nerve Growth Factor

NHS: N-HydroxySuccinimide

NMR: Nuclear Magnetic Resonance

Np: Number of parameters

NT: Neurotrophine

NT-3: Neurotrophin-3

OD: Optical Density

PBS: Phosphate-Buffered Saline

PDMS: PolyDiMethylSiloxane

PEG: PolyEthylene Glycol

PFA: Paraformaldehyde

PMMA: Poly(Methyl MethAcrylate)

PNIPAAm: Poly(*N*-isopropylacrylamide)

PS: PolyStyrene

PSCs: Post Synaptic Currents

PU/Zn: PolyUrethane embedded with Zinc

r_2: proton transversal relaxation rate

RGD: Arginylglycylaspartic acid

R_{in}: Input Resistance

ROS: Reactive Oxygen Species

rpm: revolutions per minute

RSD: Relative Standard Deviation

SBF: Simulated Body Fluid

SC: Stem Cell

SD: Standard Deviation

SEM: Scanning Electron Microscopy

SPI: Spinal Cord Injury

σ_{UCS}: Ultimate Compression Strenght

SWCNT: Single-Walled CNT

T_2: proton transversal relaxation time

Tb.N: Trabecular Number

Tb.Sp: Trabecular Spacing

Tb.Th: Trabecular Thickness

TEM: Transmission Electron Microscopy

TGA: Thermogravimetric Analysis

UV-Vis: UV visible spectroscopy

VEGF: Vascular Endothelial Growth Factor

W^{AB}: Work of adhesion of AB component

W^{LW}: Work of adhesion of LW component

ABSTRACT

This PhD thesis deals with the development of bioactive polysaccharide-based biomaterials for bone tissue and neural tissue engineering. Alginate was chosen for its gel forming properties; hyaluronic acid and chitlac (a lactose-modified chitosan) were chosen for their bioactive properties. The properties of these polysaccharides have been implemented by introducing gelatin, functionalized Carbon Nanotubes (f-CNTs) and silver nanoparticles (nAg).

In the first part of the work, the dispersibility and aggregation tendency of f-CNTs have been characterized by means of Low Field Nuclear Magnetic Resonance (LF-NMR). It was also possible to correlate the f-CNTs concentration to the proton transversal relaxation rate of water. Alginate/f-CNTs solutions and hydrogels have been analyzed by LF-NMR, rheology and uniaxial compression tests; these investigations showed that the f-CNTs are able to affect nanocomposite properties depending on their concentration and functionalization.

In the second part of the work, the preparation of a bioactive (bridging) implant for the treatment of Spinal Cord Injury is described. Neuronal cells and mesoangioblasts (MABs) engineered for the production of neurotrophines have been cultured and co-cultured on polysaccharide-coated glass substrates in order to evaluate the biological effects of chitlac. Chitlac-coated surfaces where shown to possess higher surface energies if compared to chitosan-coated ones and enable the formation of wider neural networks with improved electrical activity. The co-cultures confirmed the higher bioactivity of chitlac/alginate substrates and the biological role of neurotrophines. Porous scaffolds of alginate/chitlac have been prepared; these scaffolds where shown to be stable in simulated body fluid for over a month. The mechanical properties of rehydrated scaffolds where proved to be similar to those of neural tissue. Biological properties of chitlac substrates enriched with f-CNTs are currently under investigation.

In the third part of the work, tridimensional scaffolds and injectable fillers were developed for the treatment of non-critical bone defects. Porous scaffolds with different pore morphologies have been prepared by freeze casting of alginate/HAp hydrogels. Isotropic porosity was obtained by freezing the constructs in a cryostat, while anisotropic porosity was obtained by the Ice Segregation Induced Self Assembly process. Physical, mechanical and biological analyses revealed that the differences

in pore morphology determine differences in the mechanical properties of the scaffolds. Biocompatible f-CNTs have been used to implement the isotropic scaffolds; the biological analyses showed that the presence of f-CNTs does not affect scaffold properties.

Osteoconductive/antimicrobial injectable bone fillers, based on alginate/HAp microbeads dispersed in polysaccharide mixtures, have been developed. Microbeads were enriched with nAg synthesized in chitlac. Antimicrobial assays proved the antibacterial properties of the microbeads towards bacteria in suspension and on pre-formed biofilms. Biological assays showed the biocompatibility of the microbeads and their ability to sustain osteoblast proliferation. The fillers prepared by dispersing microbeads in polysaccharide mixtures were shown to be easily injectable through surgical syringes. *In vivo* studies on a rabbit model of non-critical bone defect pointed out the biocompatibility and the osteoconductivity of the composite materials. Further studies are ongoing in order to evaluate the possibility to further implement the bioactive properties of the microbeads by addiction of gelatin.

RIASSUNTO

Questa tesi di dottorato descrive lo sviluppo di biomateriali a base di polisaccaridi per applicazioni di ingegneria tissutale ossea e neuronale. L'alginato è stato scelto per la sua abilità di formare idrogeli, l'acido ialuronico e il chitlac (un chitosano modificato con gruppi lattosidici) sono stati scelti per la loro bioattività. Le proprietà di tali polisaccaridi sono state implementate introducendo gelatina, nanotubi di carbonio funzionalizzati (f-CNT) e nanoparticelle di argento (nAg).

Nella prima parte del lavoro, la dispersibilità e la tendenza all'aggregazione dei f-CNT è stata caratterizzata grazie alla risonanza magnetica nucleare a basso campo (LF-NMR). Inoltre è stato possibile correlare la concentrazione dei f-CNT alla velocità di rilassamento trasversale dei protoni dell'acqua. Soluzioni e idrogeli di alginato e f-CNT sono stati analizzati tramite LF-NMR, studi reologici e test di compressione uniassiale; queste indagini hanno mostrato che i f-CNT sono in grado di influenzare le proprietà dei nanocompositi in base alla loro concentrazione e funzionalizzazione.

Nella seconda parte del lavoro è descritta la preparazione di un impianto bioattivo per il trattamento delle lesioni spinali. Neuroni e mesangioblasti (MAB) ingegnerizzati per la produzione di neurotrofine sono stati coltivati e co-coltivati su substrati vetrosi ricoperti di polisaccaridi, in modo da valutarne gli effetti su tali cellule. Le superfici contenenti chitlac hanno mostrato di possedere energie di superficie più alte di quelli contenenti chitosano e di consentire la formazione di reti neuronali estese con un'attività sinaptica aumentata. Le co-culture hanno evidenziato la bioattività dei substrati contenenti chitlac e alginato e il ruolo biologico delle neurotrofine. Sono stati preparati scaffold porosi di alginato e chitlac; tali scaffold sono risultati stabili per più di un mese in un fluido mimante il plasma sanguigno. Le proprietà meccaniche degli scaffold reidratati si sono mostrate simili a quelle del tessuto neuronale. Sono in corso studi sulle proprietà biologiche di substrati di chitlac implementati con f-CNT.

Nella terza parte del lavoro sono stati sviluppati scaffold tridimensionali e riempitivi iniettabili per il trattamenti di difetti ossei non critici. Scaffold con diversi tipi di porosità sono stati preparati grazie alla liofilizzazione di idrogeli di alginato/idrossiapatite (HAp). La porosità isotropica è stata ottenuta grazie al congelamento in criostato, mentre quella anisotropa grazie al metodo definito *Ice*

Segregation Induced Self Assembly. Le analisi fisiche, meccaniche e biologiche hanno rivelato che le differenze nella morfologia dei pori determinano differenze nelle proprietà meccaniche dei costrutti. f-CNT biocompatibili sono stati usati per implementare gli scaffold isotropici. Le analisi biologiche hanno mostrato che la presenza dei f-CNT non condiziona l'effetto degli scaffold sugli osteoblasti.

Sono inoltre stati sviluppati riempitivi iniettabili osteoconduttivi e antimicrobici basati su microparticelle di alginato/HAp disperse in soluzioni polisaccaridiche. Le microparticelle sono state implementate con nAg sintetizzate in chitlac. Test antimicrobici hanno mostrato l'attività antibatterica delle microparticelle sia su batteri in sospensione che su biofilm preformato. Test biologici *in vitro* hanno mostrato la biocompatibilità delle microparticelle e la loro abilità di supportare la proliferazione di osteoblasti. I riempitivi preparati disperdendo le microparticelle in soluzioni polisaccaridiche sono risultati essere facilmente iniettabili attraverso siringhe per uso chirurgico. Studi *in vivo* su un modello di difetti ossei non critici hanno mostrato la biocompatibilità e l'osteoconduttività dei riempitivi. Studi preliminari sono stati effettuati al fine di implementare ulteriormente le proprietà bioattive delle microparticelle grazie all'introduzione di gelatina.

LIST OF PUBLICATIONS AND PROCEEDINGS

PUBLICATIONS

1. “Alginate–hydroxyapatite bone scaffolds with isotropic or anisotropic pore structure: material properties and biological behavior”. **D. Porrelli**, A. Travan, G. Turco, E. Marsich, M. Borgogna, S. Paoletti, I. Donati, *Macromol. Mater. Eng*. **2015**, *300*(10), 989-1000

2. “Antibacterial-Nanocomposite Injectable Bone Filler Based on Silver Nanoparticles and Polysaccharides” (submitted to Acta Biomaterialia)

3. “Evaluation of concentration and dispersion of functionalized carbon nanotubes in aqueous media by means of Low Field Nuclear Magnetic Resonance” (in preparation, planned journal: ACS Nano)

4. “Mechanical, spectroscopical and biological behavior of functionalized carbon nanotubes (f-CNTs) in alginate matrices” (in preparation, planned journal: Biomacromolecules)

5. “Relaxometry and rheological behavior of purified alginate” (in preparation, planned journal: Biomacromolecules)

6. “Nanocomposite biomaterials based on natural polysaccharides for the development of new cell-instructive 3D scaffold driving central nervous system (CNS) reconstruction” (in preparation, planned journal: Biomaterials)

7. “Injectable antimicrobial nanocomposite bone filler for non-critical bone defects: *in vivo* evaluation of biocompatibility and osteoconductivity” (in preparation, planned journal: Acta Biomaterialia)

PROCEEDINGS

“In-vivo study of injectable nanocomposite bone filler based on metal nanoparticles and biopolymers” **D. Porrelli**, A. Travan, E. Marsich, M. Borgogna, S. Paoletti, I. Donati. COST MP1301 NEWGEN Meeting, March 17-18, 2016, Aveiro, Portugal (oral communication)

"Antimicrobial Nanocomposite Bone-Filler Based on Metal Nanoparticles and Biopolymers". **D. Porrelli**, A. Travan, E. Marsich, M. Borgogna, S. Paoletti, I. Donati, European Congress and Exhibition on Advanced Materials and Processes, September 20-24, 2015, Warsaw, Poland. (oral communication)

"Nanocomposite biomaterials based on natural polysaccharides for the development of new cell-instructive 3D scaffold driving central nervous system (CNS) reconstruction". M. Medelin, M. Pulin, **D. Porrelli**, A. Travan, M. Borgogna, M. Cok, I. Donati, E. Marsich, R. Scardigli, S. Paoletti, L. Ballerini, Society for Neuroscience Annual Meeting 2015 "Advancing the Understanding of the Brain and Nervous System", October 17-21, 2015, Chicago, U.S.A. (poster)

"A resorbable biomaterial for the prevention of anastomotic leakage following colorectal cancer surgical treatment: the AnastomoSEAL project"; I. Donati, E. Marsich, M. Borgogna, A. Travan, L. Tarusha, F. Scognamiglio, P. Sacco, **D. Porrelli**, S. Palmisano, P. Tarchi, N. de Manzini, S. Paoletti, EuroNanoforum, June 18-20, 2013, Dublin, Ireland. (poster)

"Nanocomposite scaffolds based on carbon nanostructures and polysaccharides" **D. Porrelli**, M. Cok, A. Travan, E. Marsich, I. Donati, M. Borgogna, S. Bosi, M. Prato, S. Paoletti, NanoMedicine School, September 10-11, 2013, Trieste, Italy. (poster)

"Nanocomposite scaffolds based on carbon nanostructures and polysaccharides" **D. Porrelli**, M. Cok, A. Travan, E. Marsich, I. Donati, M. Borgogna, S. Bosi, M. Prato, S. Paoletti, 1st PhD Symposium, October 7-9, 2013, Grado, Italy. (poster)

"Marine sponge skeleton as a potentially attractive scaffold for attachment, growth and proliferation of human osteoblast cells" T. Szatkowski, J. Brzezińska, **D. Porrelli**, A. Travan, I. Donati, G. Turco, H. Ehrlich, T. Jesionowskia, Nano Konferencja, June, 25-27, 2015, Poznan, Poland. (poster)

"Synthesis and physicochemical characterization of marine sponge skeleton-hydroxyapatite composite" T. Szatkowski, J. Brzezińska, **D. Porrelli**, A. Travan, I. Donati, G. Turco, H. Ehrlich, T. Jesionowskia, X Summer School for PhD Students "Interfacial phenomena in theory and practice", June 21-27, 2015, Sudomie, Poland. (oral communication)

1 INTRODUCTION

1.1 TISSUE REGENERATION AND TISSUE ENGINEERING

1.1.1 BIOMATERIALS DESIGN

Tissue regeneration and tissue engineering are highly multidisciplinary fields that combine different approaches for the restoring, the maintenance or the improvement of tissue functions or whole organs.[1] These fields arise from the synergistic combination of materials engineering, biology and medicine, and exploit the use of biomaterials, cells, growth factors (GFs), nanomedicine, immunomodulation, gene therapy and other techniques. The design of biomaterials is aimed at the preparation of hydrogels, scaffolds, membranes, and injectable materials that have to allow, sustain and promote cell adhesion, migration, proliferation, differentiation and function. The most investigated approach for tissue engineering is the preparation of scaffolds, which can be implemented with bioactive compounds and loaded with cells harvested from the patients.[2,3]

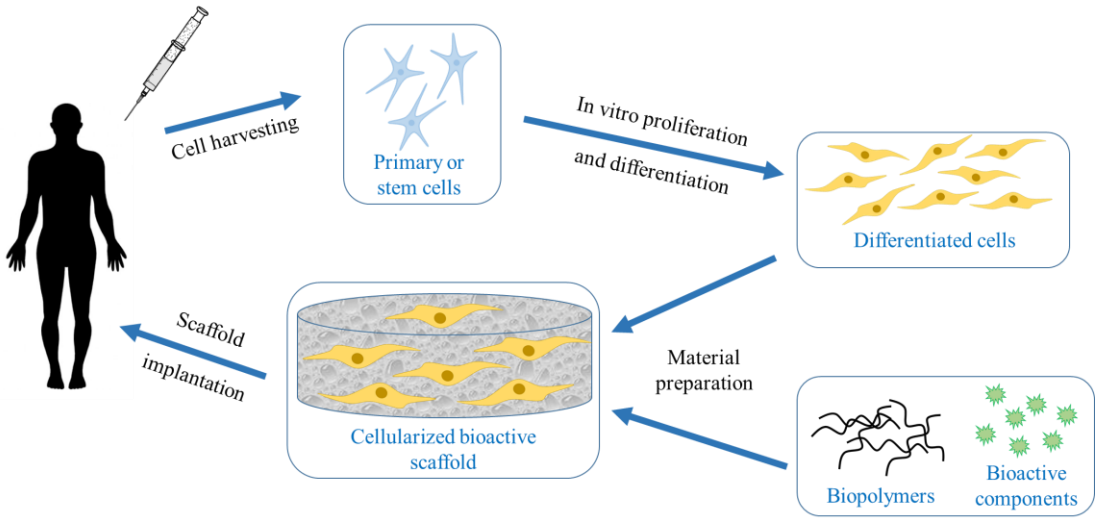

Figure 1. Schematic representation of the preparation of ideal cellularized/bioactive scaffolds for tissue engineering, by using cells harvested from the patients.

Figure 1 shows a schematic representation of a typical tissue engineering approach: first of all, primary or stem cells (SCs) are harvested from the patients; the possibility to use autologous cells enables to avoid any immune reaction to a cellularized scaffolds. Scaffolds can be prepared by

using natural-derived or synthetic materials, and can be implemented with bioactive components, such as GFs. The harvested cells are expanded and differentiated *in vitro* for the specific application and loaded into the scaffolds; the processes can be performed in bioreactors, in order to mimic the *in vivo* environment. At the end of the process, the cellularized bioactive scaffolds are implanted into the patient.[4-6]

1.1.1.1 Biomaterials implementation with growth factors

The stimulation of cell differentiation and growth, and of tissue regeneration, can be achieved by the introduction of GFs in the scaffolds. The classical approaches are based on the covalent conjugation of GFs to the components of the biomaterials, or on the physical entrapment of GFs inside the polymer matrices. The GFs embedded in the biomaterials are, in this way, able to interact with cells, or to be released during the degradation of the biomaterials.[7,8] These approaches have some drawbacks, principally related to the difficulty of obtaining a long-term controlled delivery; this issue is partially overcame by the preparation of biomaterials containing stimuli-responsive components that can be triggered to release the GFs upon pH or temperature variations, enzymatic cleavage, ionic interactions or external stimuli.[7,9]

1.1.1.2 Cell loading in biomaterials

Several research groups have implemented biomaterials by loading cells for a wide range of applications. The preparation of these materials follows specific protocols for the harvesting and the cultivation of cells and for their loading and encapsulation into materials, such as scaffolds and hydrogel microspheres.

Scaffolds for tissue engineering can be loaded with primary cells or SCs that will differentiate, upon appropriate conditions, in the cells of the target tissue. This approach has been used for the preparation of tridimensional hydrogels and porous scaffolds loaded with MSCs (Mesenchymal Stem Cells), BMSCs (Bone Marrow Stromal Cells) or SCs derived from adipose tissue, for applications of tissue regeneration in bone,[10] cartilage,[11] heart valves,[12] skin,[13] nerve,[14] alveolar cleft,[15] tendon and muscles[16] and wound healing.[17]

The biomaterials can be also loaded with GFs-producing cells. This strategy helps to overcome the problems related to the loading and the release of GFs, guaranteeing a sustained and controlled

release of these bioactive molecules. Moreover, cells seeded into the scaffolds can synthesize extracellular matrix (ECM) and create a permissive environment for cell growth.[18] The main applications of this approach are in the fields of neural and bone tissue regeneration. For example, scaffolds containing Bone Morphogenetic Protein (BMP-2)-producing cells were proved to improve the heterotopic bone formation,[19] and scaffolds containing Vascular Endothelial Growth Factor (VEGF)-producing BMSCs enhanced vascularization, osteogenesis and resorption of the scaffold itself.[20]

1.2 BIOPOLYMERS FOR BIOMATERIALS

As discussed before, the main approach in the tissue engineering consists in the preparation of biocompatible biomaterials that can contain cells and bioactive molecules. The choice of the components that are used for the preparation of the biomaterials depends on their final properties and applications: for example, metallic implants or thermosets can be used for the restoring of large bone defects, biopolymers can be used for the preparation of membranes and tridimensional scaffolds, for the electrospinning and wet spinning of fibers or for injectable materials.

The present thesis is focused on the combination of biopolymers, nanostructures and cells for the preparation of tridimensional, biopolymer-based scaffolds and injectable composites, to be employed in bone and neural tissue regeneration. After the description of biopolymers and tissue regeneration strategies, the introduction will focus on two main issues: the healing of non-critical bone defects and the neural tissue regeneration in Spinal Cord Injury (SCI). The strategies for the implementation of biomaterials for these applications will be presented.

Biopolymers used for the preparation of biomaterials can be classified in two main categories: polysaccharides and proteins; the most commonly used are alginate, hyaluronic acid and chitosan, among polysaccharides, and collagen and gelatin among proteins.[21] Other polysaccharides include cellulose, agarose and dextran and other proteins include elastin, fibrin, fibronectin laminin and silk.

1.2.1 PROPERTIES AND APPLICATIONS OF POLYSACCHARIDES

Alginate

Alginate is a polyuronate, a polysaccharide that contains carboxylic groups in the C6, and is derived from algae and bacteria.[22] Its structure consists of 1→4 linked α-L-guluronic acid and β-D-mannuronic acid in different blocks and portions within the polysaccharide chain (Figure 2). The monomer blocks can be composed by a sequence of guluronic monomers (G blocks), mannuronic monomers (M blocks) or a mixing of the two monomers (MG blocks).

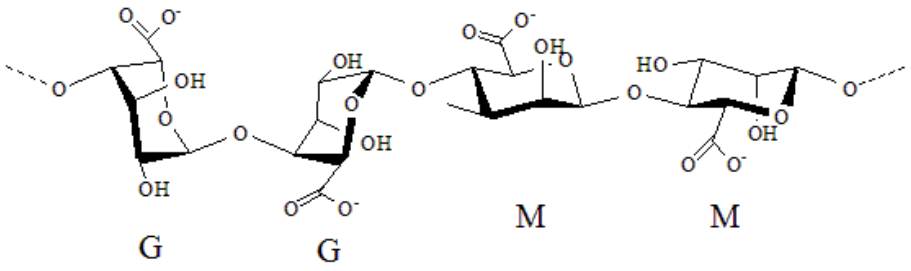

Figure 2. Chemical structure of alginate.

An important feature of alginate is the ability to form hydrogels upon interaction with divalent cations, such as Ca^{2+}. These hydrogels are typically composed by the 95-99% of water and their properties depend on alginate concentration and composition, and on the concentration and typology of the cations. Several studies showed the different affinity of alginate for cations such as Pb^{2+}, Cu^{2+}, Cd^{2+}, Zn^{2+}, Ca^{2+}, Mg^{2+}, Ba^{2+}, Sr^{2+}. The affinity for the divalent cations is explained by considering the alginate chain structure that can bind the cations and form the so-called “egg-box” structure (Figure 3).[23,24]

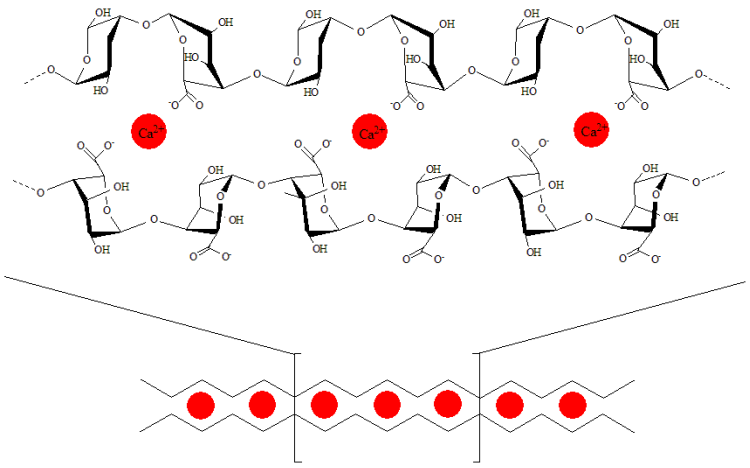

Figure 3. Schematic representation of the egg-box model: the structure of the G blocks allows to the carboxylic groups of the guluronic monomers to interact and coordinate the calcium ions in a well-ordered structure.

The affinity of alginate for the different divalent cations is highly selective, and for the alkaline earth metals is $Mg^{2+} << Ca^{2+} < Sr^{2+} < Ba^{2+}$. Moreover, it has been shown that the cations affinity is not related to the composition of MM and MG blocks and that it increases with the increasing of the G blocks number and length.[24,25] Lastly, the strength of the alginate hydrogels depends on the concentration of the divalent cations, as shown in the model reported in Figure 4.

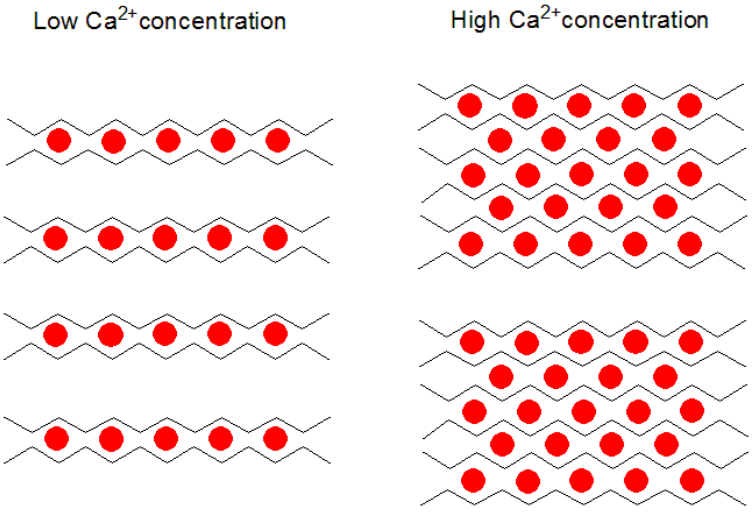

Figure 4. Schematic representation of the calcium concentration increasing effect: on the left, low calcium concentration results in low dense egg-boxes, on the right dense and compact egg-boxes are formed upon the addition of high calcium concentration.

Alginate is biocompatible and does not trigger immune or adverse tissue reactions; it possesses hemostatic properties[26,27] and it has been used to enrich medications for skin grafts in order to accelerate the wound healing.[28] It is a very versatile polysaccharide for the preparation of biomaterials in form of membranes, films, hydrogels, porous scaffolds, fibers and foams, for several applications in wound healing, bone, cartilage and neural tissue regeneration.[29-31]

Chitosan

Chitosan is a polysaccharide obtained from crab-shell chitin deacetylation in alkaline environment; it is characterized by having different degrees of deacetylation (40-98%). It is widely used in the pharmaceutical industry and in biomedical application and as adjuvant in diets for its lipids binding properties.[32-34] Its structure consists of β(1→4) linked D-glucosamine e N-acetyl-D-glucosamine, arranged in helix stabilized by hydrogen bonds (Figure 5).

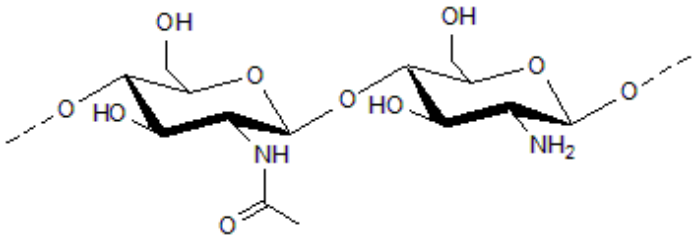

Figure 5. Chemical structure of chitosan.

Due to the presence of amino groups, a consequence of the deacetylation process, chitosan is soluble in acid environment, in which it behaves as a polycation. The chemical reactivity of the amino groups can be exploited for the functionalization and modification of chitosan; moreover, cross-linking agents can react with amino groups allow obtaining biomaterials in form of fibers and hydrogels. The biomedical applications of chitosan are limited by its scarce solubility in water and physiological environment; however, these characteristics can be tailored by chemical modifications of chitosan.[35]

Likewise to alginate, chitosan is a good candidate for the preparation of biomaterials. It is biocompatible and biodegradable and it possesses antibacterial and wound-healing properties. Moreover, chitosan possesses gel-forming properties (in the presence of polyanions and glicerophosphates) and can it be used to obtain porous structures. Chitosan and its derivatives have been widely used in several tissue engineering applications for the stimulation of the regeneration

and healing of skin, bone, cartilage, liver, nerve and blood vessels.[35]

Hyaluronic acid

Hyaluronic acid is a high molecular weight glycosaminoglycan; it is not covalently bound to proteins and is the simplest among glycosaminoglycan; it is present in most of all tissues and biological fluids.[36] Its structure consists in 1→4 and 1→3 linked D-glucuronic acid e N-acetyl-D-glucosamin (Figure 6).

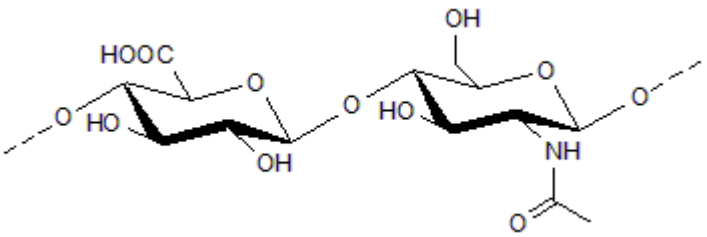

Figure 6. Chemical structure of hyaluronic acid.

Hyaluronic acid is highly hydrophilic and its aqueous solutions display peculiar viscoelastic properties. Owing to these properties, this polysaccharide plays a key role in the modulation of mechanical properties and water content of the ECM, and is responsible for the viscoelastic properties of the synovial fluid.[36,37] Moreover, hyaluronic acid modulates and triggers several biological functions thanks to the presence of specific membrane receptors: the interactions with CD44 can modulate cell migration, proliferation, differentiation, and adhesion, and can also regulate tissue regeneration, angiogenesis and immune response.[36-39]

Hyaluronic acid for biomedical application can be extracted from rooster comb or rabbit skin, or obtained through recombinant synthesis from Streptococci. Hyaluronic acid is widely used in biomedical applications (such as the treatment of articular pathologies, aesthetic surgery, wound healing) and cosmetics.[39] It can be used as a bioactive component within the biomaterials or, thanks to chemical modifications and crosslinking agents, it can be used in the form of hydrogels or scaffolds for cell delivery.[40]

Cellulose

Cellulose is a non-biodegradable, biocompatible, linear polysaccharide composed by β(1→4) linked D-glucose. In nature, it is one of the most widespread polymeric material. Cellulose

possesses hemostatic properties[41] and can be employed in form of fibers for the preparation of reinforcement mashes for membranes. It can be also used for the preparation of hydrogels and scaffolds for vascular devices, bone tissue regeneration and other applications, and for the preparations of drug delivery systems.[42]

Agarose

Agarose is a linear polysaccharide that consists of repeating agarobiose units. Agarobiose is a disaccharide made up of D-galactose and 3,6-anhydro-L-galactopyranose. It can be used for the preparation of hydrogels and scaffolds and it is commonly used in combination with proteins, such as gelatin or laminin, because of its poor biological properties. Agarose-based biomaterials have been used for neural growth, corneal organotypic substitutes and for cartilage repair.[43-45]

Dextran

Dextran is a biocompatible, branched polysaccharide that consists of α1→6 and α 1→3 linked glucose, and possesses anti-thrombotic properties. Dextran can be used for the preparation of porous scaffolds and implant coatings, and can be modified in order to enhance its bioadhesive properties.[46,47]

1.2.2 PROPERTIES AND APPLICATIONS OF PROTEINS

Collagen

Collagen is the most abundant protein of the mammalian connective tissue, the main component of the ECM and it is present in all connective tissues of the body.[48,49] Collagen is present in 29 isoforms and it is structured in a right-handed triple helix, which is stabilized by hydrogen bonds and N-π* interactions formed by three left-handed α-helixes (Figure 7).[50,51]

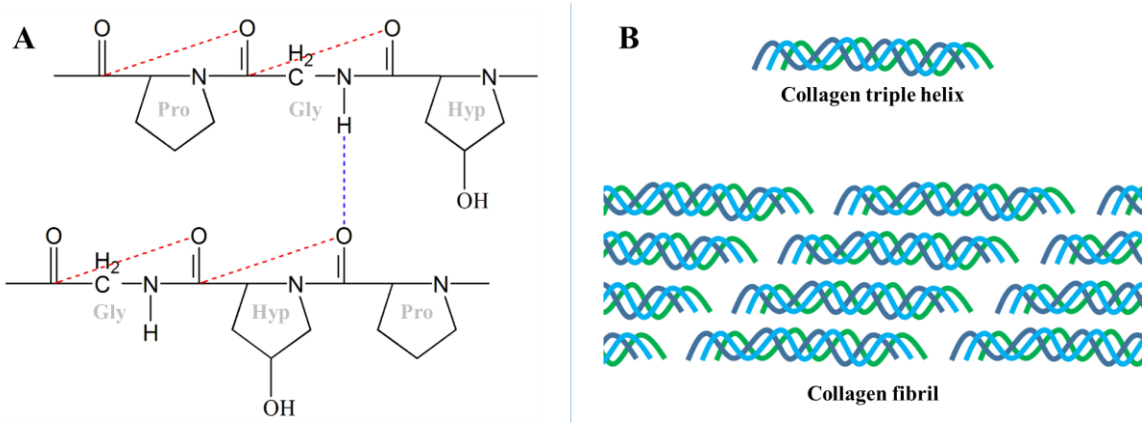

Figure 7. **A**) Collagen triple helix stabilized by hydrogen bonds (blue dashed line) and n→π* interactions (red dashed line). **B**) Collagen fibers assembly (adapted from Chattopadhyay *et al.*[52]).

Among the isoforms, collagen I is the most used for biomedical applications because of its highest abundance in the ECM.[52] It can be extracted from animal tissues (horse and bovin tendon and skin, rat tail, porcine skin)[53] or obtained through recombinant synthesis from *E. coli*.[54]

Collagen possesses a rigid structure and a good mechanical resistance; these properties, together with its biocompatibility and biodegradability, make the collagen a good coice for the preparation of different types of biomaterials, such as hydrogels, foams, membranes, beads and scaffolds. It can be used for the preparation of scaffolds for cell loading, injectable materials for surgical applications, drug delivery systems and membranes for wound healing.[52] Collagen drawbacks derive from its water insolubility: collagen has to be solubilized in acidic conditions and it is difficult to process, moreover it is difficult to control its degradation rate.[48,55]

Gelatin

Gelatin is obtained through thermal denaturation of animal derived collagen; the process leads to the triple helix denaturation and the formation of uncoiled structures (Figure 8).

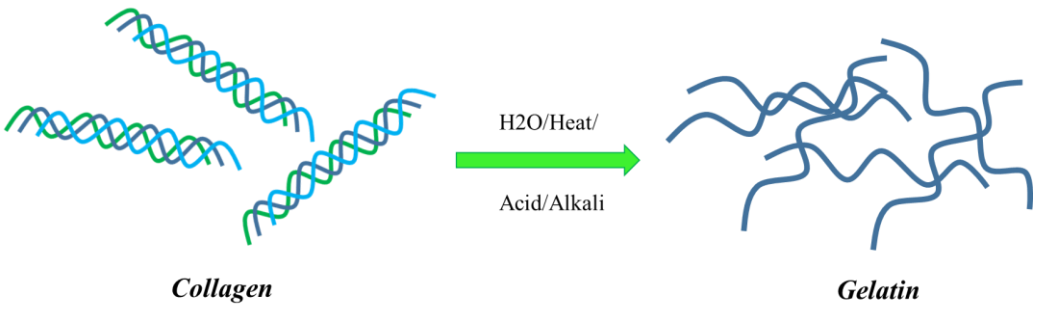

Figure 8. Schematic representation of collagen denaturation process for the obtaining of gelatin.

Gelatin possesses biological properties similar to collagen (biocompatibility, biodegradability and cell adhesiveness) and in addition, thanks to the denaturation process, gelatin is water soluble and less immunogenic; moreover, the denaturation helps to expose the RGD (arginylglycylaspartic acid) peptides of collagen, which are recognized by cells and trigger biological responses such as adhesion and proliferation. For these reasons gelatin is a good material for biomedical applications.[55,56]

Due to its lower mechanical properties, gelatin is often cross-linked or used in association with other polysaccharides, such as alginate and chitosan.[57-59] For example, in situ forming hydrogels for wound-dressing or bone tissue engineering applications have been prepared combining gelatin with alginate.[60,61]

Elastin

Elastin is a hydrophobic insoluble protein that constitutes the ECM. The content of elastin depends on the mechanical properties required from the tissues and it is abundant in skin, lungs, elastic ligaments and blood vessels.[62-65] Soluble elastin protein, derived from elastin hydrolysis, can be used for the fabrication of biomaterials with different mechanical properties and in different forms like hydrogels, films, nanoparticles, sponges and nanoporous materials. Elastin can be used for the preparation of skin substitutes, vascular constructs and drug delivery systems.[66]

Fibrin

Fibrin is a protein derived from fibrinogen and plays a key role in the coagulation cascade and thus in wound healing process. Fibrin contains peptides and domains that are recognized by cells and

can be used for the preparation of scaffolds with good cell adhesiveness. Fibrin scaffolds have been widely used as a support for the growth of stem or primary cells to be employed for the regeneration of several tissues.[48,67,68]

Fibronectin

Fibronectin is a protein component of the ECM, where it can bind different proteins such as collagen and fibrin. It possesses self-assembly characteristics; the mats that are formed upon its aggregation can be used as scaffolds for neural tissue engineering applications.[48,69] The main domain of its structure (the central cell binding domain) contains RGD peptides, which are essential for cell adhesion; moreover, fibronectin promotes cell proliferation, migration and differentiation.[70,71]

Laminin

Laminin is a group of heterotrimeric glycoprotein; is one of the major component of basement membranes and plays an essential role in cell adhesion, migration, proliferation and angiogenesis, with a specific role in the neurite outgrowth.[72] In the field of tissue regeneration it is mostly used for the functionalization (by adsorption or chemical crosslinking) of scaffolds in order to improve their regeneration capacity, with specific applications in neural tissue regeneration.[73,74]

Silk

Silks are biocompatible proteins that are mostly obtained from the domesticated silkworm (*Bombyx mori*) and from some spiders (*Nephila clavipes* and *Araneus diadematus*).[75] Due to its peculiar mechanical properties, flexibility and high tensile strength, silk is a good material for the preparation of suture and load-bearing scaffolds with higher mechanical properties than other biopolymer-based scaffolds. The main fields of applications are cartilage and bone tissue engineering.[75,76]

1.3 SPINAL CORD TISSUE REGENERATION

The spinal cord is an organ of the central nervous system (CNS) placed in the spinal column and possesses several functions; the main functions are the transmission of the neural signals between the periphery and the cortex, and the coordination of sensory, motor and autonomic functions.[77]

The organization of the spinal cord (reported in Figure 9) consists of segments composed by the dorsal root ganglia that contain the sensory neuron bodies, whose axons travel into the spinal cord. The grey matter of the spinal cord consists in interneurons that receive the information from neurons descending from the brain, and in primary afferent neurons; moreover, it contains neuroglia cells.[77]

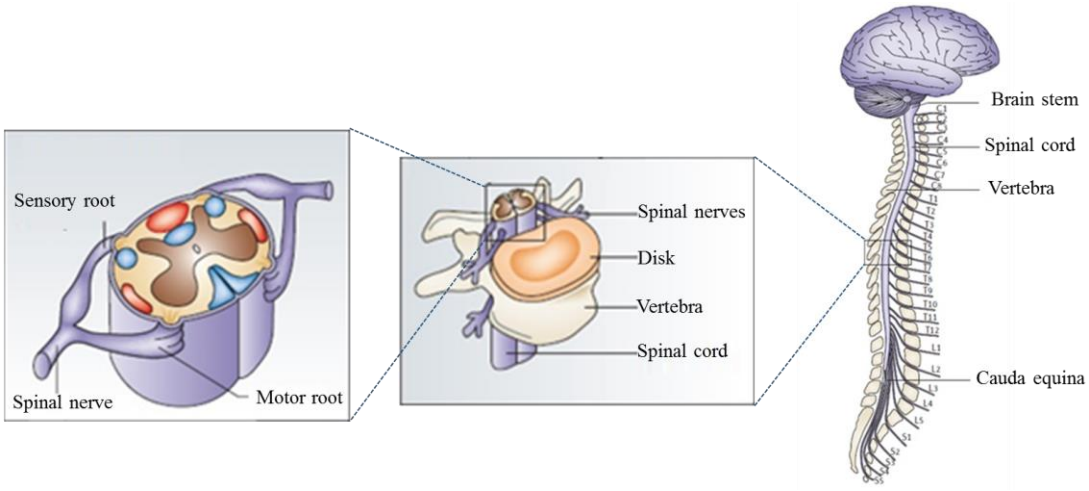

Figure 9. Schematic representation of the anatomic organization of the spinal cord (adapted from Bradbury *et al.*[78]).

Within the human body, CNS is the organ with the most limited capability of repair or regeneration, posing a challenge that is difficult for clinicians to overcome.[79] Apart from the low intrinsic regenerative ability of neurons, the CNS is also characterized by a specific glial reaction following injury and an inhibitory environment that prevent axon regrowth leading to severe and permanent deficits.[78]

1.3.1 SPINAL CORD INJURY AND CURRENT THERAPIES

Spinal cord injury (SCI) is a devastating clinical condition that significantly impacts the ability of affected individuals to produce functional movements and often results in paraplegia or quadriplegia.[78] SCI can be caused by traumas or by other pathologies; the non-traumatic SCI can be induced, for example, by vertebral spondylosis, tumor compression, vascular ischemia, neuronal motor diseases, infectious abscess and transverse myelitis. Every year 12000 new cases of SCI in the USA are reported, with a total number of ~259000 patients living with SCI;[80] the incidence in

Europe is slightly lower.[81,82] Given the complications caused by the SCI, the costs related to the hospitalization and the assistance to the patients are very high.[83]

Likewise to other CNS injuries, it can be divided in two phases: primary and secondary. The primary injury involves the immediate damage to neural tissue and surrounding soft tissues, generically caused by mechanical impact, ischemia or haemorrhage; the tissue damages worsen the injury over time and lead to the secondary injury.[84] The second phase consists of several processes that comprise focal vascular changes, congestion, petechial haemorrhages, massive secondary cell death and degradation of distal axon ends; it is accompanied by edema and impairs the microcirculation, leading after several days to the formation of a cystic region and glial scar tissue.[84,85] These events are also accompanied by oligodendrocyte apoptosis and inhibition of myelin regeneration, and by Wallerian degeneration (the degeneration of the distal part of a damaged axon).[78] In the Figure 10 is reported a schematic representation of the events that take place in the SCI site.

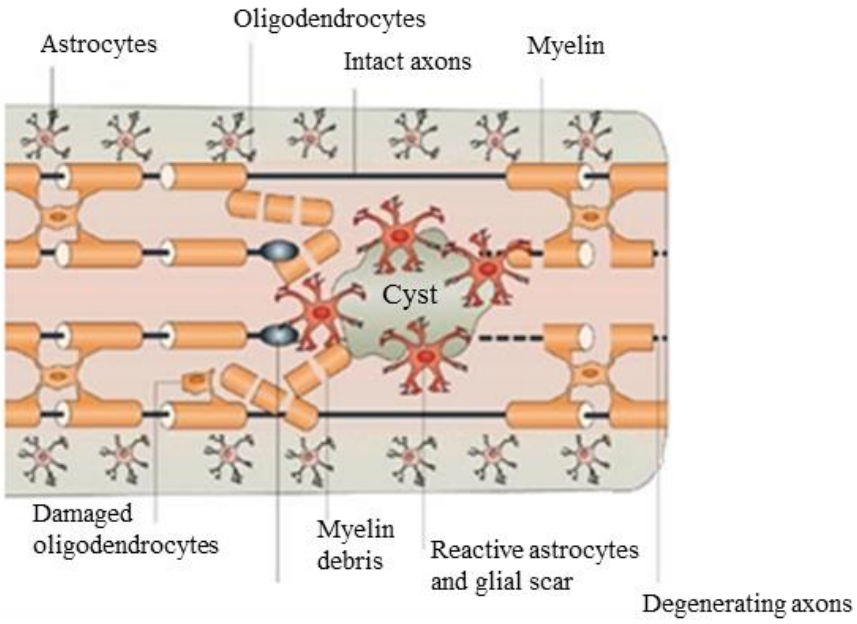

Figure 10. Schematic representation of the nerve injury site (adapted from Yiu *et al.* [86]).

The injury environment is highly complex; it changes and evolves with the formation of the glial scar, which plays an initial protective role, but leads to the producton of molecules that inhibit the axonal regrowth. Moreover, the migration of oligodendrocytes, astrocytes and fibroblasts leads to

the formation of tissue that isolates the site of primary injury and to the production of other molecules that inhibit the axonal regrowth and trigger apoptotic pathways.[86-88]

Given the complexity of the injury, which involves cell growth inhibition and apoptosis and the formation of a cystic cavity, it is necessary to design a multidisciplinary approach for the neural tissue regeneration and the recovery of the tissue functions. Currently there are no therapies able to repair the damage of the spinal cord; the common strategies involve a plethora of curative interventions towards prevention of cell death or towards stimulation of axonal regrowth, inhibition of immune and inflammatory reactions, enhancement of axonal transmission or amelioration of secondary damage, thanks to pharmacological approaches and multi-system neurorehabilitative interventions.[78,89-92]

1.3.2 RESTORING THE NEURAL NETWORK: THE BRIDGING IMPLANT STRATEGY

In this contest, the advantages offered by the use of tridimensional biomaterials (scaffolds and hydrogels) appear to be very promising for the development of a new strategy that could stimulate neural tissue and axonal regrowth, thus inducing the formation of new synapses for the restoring of the lost neural circuits.[89,93] In order to act as a bridging implant, an ideal scaffold should possess specific characteristics: the ability to fit the cystic cavity, proper morphology, mechanical properties and degradation rate, the ability to deliver cells and growth factors and, preferably, electrical conductivity.[6,94-97] In particular, regarding the morphology, an ideal scaffold should possess oriented/channel-like pores in order to guide the neuronal and axonal growth[6,94,98] with pore dimension around 50-100 μm for scaffold colonization.[94,99,100] The electrical conductivity can be achieved by the introduction of conductive polymers, such as polypirrole[100] or carbon nanotubes (CNTs), as described in the following paragraphs.

1.3.2.1 Scaffolds design for neural tissue engineering

Among the wide range of possible materials that can be employed for the preparation of scaffolds for neural tissue engineering, biopolymer-based biomaterials are very promising candidates for their biocompatibility, gel forming properties, biodegradability and bioactivity.[94] Several methods and processes can be used for the preparation of scaffolds and hydrogels with oriented pores, containing alginate or chitosan as structural components. In alginate hydrogels these structures can

be obtained thanks to an oriented gelation[101] or through mechanical stretching of the materials.[102] Anisotropic porous structures can also be obtained by means of directional supercritical CO_2 foaming,[103] after the freeze-casting of hydrogels that have been frozen in an oriented way on a cooled plate[98,104,105] or by the Ice Segregation Induced Self Assembly (ISISA) process in a liquid nitrogen bath[106-110] or in dry ice.[111]

For example Francis *et al.* reported the preparation of a scaffold with aligned pores prepared with chitosan and alginate: the scaffold possesses mechanical properties similar to the neural tissue and was able to guide the neurite growth of the dorsal root ganglia.[94] Alginate, chitosan and gelatin-based scaffolds have been successfully used, in combination with GFs or RGD peptides, to promote neural differentiation and nerve regeneration.[112-114]

Specific biologically relevant proteins and polysaccharides can be used as bioactive components within the scaffolds. For example, hyaluronic acid has proved to reduce astrocyte proliferation thus helping to attenuate the inflammatory response and gliosis in the surrounding tissue;[115] moreover, it was demonstrated that the presence of hyaluronic acid supports angiogenesis and inhibits glial scar formation.[116] Fibrin has been used for the preparation of scaffolds for the delivery of neurotrophin-3 (NT-3), resulting into enhanced neural fiber sprouting in rats;[117] on the other hand, the aligned fibers of fibronectin mats can orient the axonal growth in rat damaged spinal cord.[118]

1.3.2.2 Sustained neurotrophine synthesis: co-cultures with engineered mesoangioblasts

An interesting approach for the implementation of neural scaffolds and the improvement of their bioactivity is represented by the incorporation of cells that are able to synthesize and locally release neurotrophines (NTs) such as NT-3, Nerve Growth Factor (NGF) and Brain Derived Neurotrophic Factor (BDNF). This approach guarantees a sustained, selective and controlled release for long periods. Sasaki *et al.* showed an improved locomotor recovery for rat after the transplantation of gene-modified human mesenchymal stem cell (hMSCs) that overexpressed BDNF.[119] These cells were also used in combination with agarose scaffolds and showed an improved tissue regeneration.[98] Genetically engineered neural stem cells that overexpressed NT-3, seeded in poly(ε-caprolactone) (PCL) scaffolds, proved to increase behavioural and electrophysiological recovery in rats with hemisection surgery in the spinal cord.[120]

A promising cell lineage that can be used in this approach is represented by the mesoangioblasts (MABs): these cells are self-renewal multipotent progenitors of mesodermal tissue that have already been utilized for tissue engineering[121] and can be isolated from small biopsies of postnatal human skeletal muscle.[122] Su *et al.* showed that it is possible to genetically engineer these cells to induce the production and release of NGF and BDNF.[123] The positive effects of these cells were proved in terms of viability and electrophysiological activity of primary neuronal cells and adult organotypic hippocampal slices when cultured in the presence of MABs conditioned media. Moreover, the effect of BDNF produced by the engineered MABs is higher than that obtained with the administration of recombinant BDNF.[123]

Altogether, these results show the great potential of the development of scaffolds enriched with bioactive components and genetically modified cells, to be employed in the design of bridging implant strategy, since the supplementation of NTs and of other bioactive compounds can sustain the survival and functional recovery of neurons by modulating the post-injury microenvironment.

1.4 BONE TISSUE REGENERATION

Bone tissue is a specialized form of connective tissue that plays key roles in several physiologic functions: to name a few, protection and support for organs, movement, blood production, storage and homeostasis of calcium and other minerals, blood pH regulation, mesenchymal and hemopoietic cell progenitors housing.[5] It is mainly composed of inorganic mineral crystals, that accounts for the 60-70% of the dry mass; the principal mineral component is hydroxyapatite (HAp, $Ca_{10}(PO_4)_6(OH)_2$), but there are also small amounts of other inorganic salts.[124] The remaining part of the dry mass is composed for the 10–20% by collagen fibers, with a prevalence of collagen type I, proteoglycans and non-collagenous proteins such as osteocalcin, osteopontin, osteonectin, fibronectin and thrombospondin.[125-127] According to the structure, bone can be categorized in two types: the cortical (compact) and the trabecular (cancellous or spongy) bone. The 80% of the skeletal bone is composed of cortical bone; it possesses a high elastic modulus (~20 GPa) and a low porosity (5-10%) and its average ultimate compression strength is 105-131 MPa.[128,129] In contrast, the porosity of trabecular bone is higher (approximately 50–95%), but it presents lower mechanical properties: the elastic modulus ranges from 25 to 240 MPa, while the ultimate compressive strength ranges from 0.2 to 10.4 MPa.[75,130]

1.4.1 BONE TISSUE DAMAGES AND COMMON THERAPEUTIC APPROACHES

Bone tissue damages can derive from diseases such as osteogenesis imperfecta, osteoarthritis, osteomyelitis, and osteoporosis, or from traumatic injury, orthopedic surgeries (*e.g.* total joint arthroplasty, spine arthrodesis, implant fixation, etc.) and primary tumor resection.[5] The treatment of bone defects has a huge clinical and economic impact: osteoporotic fractures are at great risk of bone defects, especially in women over 60 years old, and according to recent reports there are more than one million patients who need bone grafts in Europe and United States each year.[75] Moreover, the number of patients and the related costs are increasing; for example the number of total joint arthroplasties and revision surgeries in the US has increased from 700000 in 1998 to over 1.1 million in 2005, while medical expenses relating to fracture, reattachment, and replacement of hip and knee joint was estimated to be over $20 billion in 2003 and was predicted to increase to over $74 billion by the year 2015.[5]

Several factors can impair the self-repair of bone upon mechanical fixation, such as large bone defect size, infections and poor vascularization, thus resulting in non-unions. These issues are frequent in bone fractures related to injuries or in joint arthroplasties. Other cases can be tumor resection or massive traumatic bone loss.[5] In all these cases, it is necessary to fill the bone defect with a substitutionary material. The gold standard for the treatments of bone defect is the use of autogenous bone grafts: bone is harvested from the pelvis or the iliac crest and is placed within the bone defect. Although the reliability and the efficacy of this treatment, there can be several complications: 30% of the cases are related to donor site morbidity, pain, paresthesia, prolonged hospitalization and rehabilitation, increased risk of deep infection, hematoma, inflammation, which can impair the outcomes of the healing process. Moreover, the restricted availability of autologous bone is a critical issue for this approach.[5,131]

Other alternatives are the use of allografts from human donors or xenografts from non-human organisms, but these treatments are associated with a high risk of infection, disease transmission and host immune responses.[132-137] Common medical procedures include also the use of metallic pins, screws, plates, and rods to stabilize and align the fractured bone, although the use of these devices is associated with extended surgery and healing time, stress shielding induction, and risks for infection and chronic pain.[138]

In many cases, bone defects can be small and non-critical defects: these defects can heal on their own in a certain time. Non-critical bone defects can derive from the removal of fracture fixation devices (pins, screws, screw-plate devices, and rod entry holes), from the excision of small tumors, areas of infection, voids (after revision joint replacement), traumatic injuries, cysts and pathologies characterized by an altered balance between bone tissue deposition and resorption.[139-142] These defects and voids represent a hot spot for mechanical stresses that can cause fractures; thus it is necessary to accelerate their healing.[140]

1.4.2 BIOMATERIALS FOR BONE TISSUE REGENERATION

The drawbacks and the limitations associated with the use of auto-, allo- and xenografts have addressed and motivated the research toward the development of tissue engineering strategies and the optimization of bone substitutes. The use of synthetic bone substitutes enables to reduce the surgical procedures and the risk of infection or immunogenicity, and to eliminate the risk of disease transmission.[5,75] Moreover, synthetic scaffolds can be loaded with bioactive molecules or cells before implantation.

An ideal bone substitute should possess specific morphological, mechanical and biological characteristics in order to mimic properly the bone tissue, and to support and enhance bone healing. The materials employed should favor bone cell migration and adhesion into the scaffold (osteoconduction) and promote osteogenic differentiation (osteoinduction); moreover, the porosity of the scaffolds should be enough for the migration of cells, for the diffusion of nutrients and gases and for neoangiogenesis. The materials should be able to integrate and interact with the surrounding tissue without the growth of fibrous capsules on the bone-implant interface (osteointegration) and in some cases they have to be able to provide a mechanical support to the affected area. Lastly, the materials should be sterilizable without loss of properties and their degradation has to proceed in a controlled manner during the new bone tissue development.[143,144]

Biopolymer based bone substitutes can be prepared in two main formulations: tridimensional structures and injectable composites. In both cases these biomaterials are implemented with an osteoconductive component, such as HAp or other calcium phosphate ceramics.[145] HAp, whose crystalline structure is reported in Figure 11, is the major mineral component of bone and can be syntherized to obtain a bioceramic for bone scaffolds and fillers.[146]

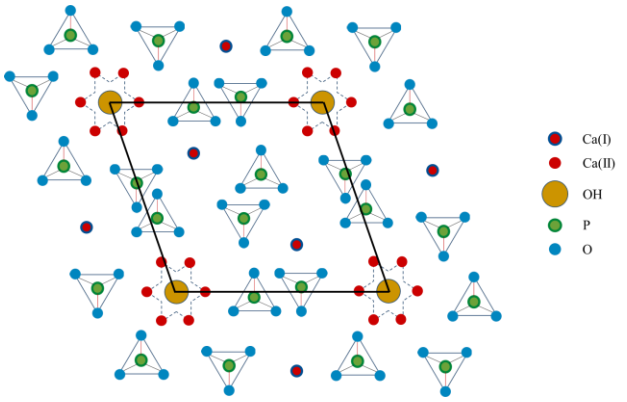

Figure 11. Crystalline structure of HAp.

HAp is characterized by excellent osteoconductivity, osteoinductivity, good biocompatibility and bioactivity *in vivo*; it can be used for the preparation of prosthesis coatings for the improvement of osteointegration, or for the implementation and reinforcement of polymeric scaffolds.[147,148] In the following paragraphs the two main categories of bone fillers and their clinical use are described.

1.4.2.1 Tridimensional scaffolds

Biopolymer-based tridimensional scaffolds can be prepared by different techniques: thermally induced phase separation, solvent casting and particulate leaching, solid free form fabrication techniques, supercritical-fluid technology, chemical cross-linking and electrospinning.[149,150] Biopolymers, and in particular polysaccharides, offer the advantage to be water soluble and very easily exploitable for the preparation of biomaterials in physiological conditions, without using toxic reagents.[149] In all cases, the porous structure has to satisfy certain requirements: the pores have to be highly interconnected, their size distribution has to favor cell colonization and proliferation and the formation of new blood vessels. In literature, the desired scaffold properties include a porosity in the range of 70 – 90% and a pore size in the range of 50 – 600 μm.[147,151-153] These characteristics can be easily tailorable by changing polymer concentration, polymerization conditions and by grafting of chemicals and functional groups;[154] furthermore, the scaffolds bioactivity can be tuned by addition of functional groups, peptides, proteins and cells.[154] The main disadvantages of biopolymers in the preparation of tridimensional structures are represented by their low mechanical properties;[147,149] therefore, the implementation of these structures with calcium phosphate materials, such as HAp, is very useful to overcome this issue, besides giving more bioactive features to the biomaterials.[147]

Alginate is a good candidate for the preparation of tridimensional scaffolds thanks to its gel forming properties. It has been used for the preparation of porous scaffold enriched with antimicrobial properties[155] and for mineral-coated scaffolds using biomimetic approaches.[156] It has been also used in combination with peptides and growth factor such as RGD, VEGF and BMP-2[157,158] leading to an increased bone formation and for the co-culturing of bone cells in order to increase the bioactivity.[159] Chitosan scaffolds have been prepared in combination with collagen[160] and with different methods of cross-linking[161,162] in order to obtain scaffolds with good bioactivity and mechanical properties. Chitosan has been also added to silk/HAp scaffolds to increase their mechanical properties[163] and used in combination with bioactive molecules such as insulin-like growth factor-1 (IGF-1), BMP-2 and RGD peptides to increase their bioactivity.[164] In addition to polysaccharides, collagen has been widely used for the preparation of tridimensional bone scaffolds; in combination with PCL or bioactive glass it showed to has the ability to support osteoblasts growth and differentiation, with an increased alkaline phosphatase (ALP) activity and osteocalcin/osteopontin expression.[165-167]

1.4.2.2 Injectable bone fillers

Injectable bone fillers represent an attractive strategy for the treatment of bone defects caused by traumatic injuries, cysts and pathologies characterized by an altered balance between bone tissue deposition and resorption;[139,141,142] they can also be employed to relieve the pain and to strengthen osteoporotic bones.[142] These materials hold great promise in clinical applications thanks to their advantages that include minimal tissue injury, nearly no influence on blood supply, easy operation and negligible postoperative pain.[4] The two main categories of injectable fillers are calcium phosphate cements (CPCs) and polymeric fillers. CPCs have the great advantage to be chemically and structurally similar to the mineral component of the bone tissue, but they are not easily injectable through syringes and cannulas[168,169] and they lack of adequate porosity and degradation rate.[170] The polymeric fillers offer the possibility to prepare materials whose injectability and degradation rate can be tailored.[171]

Several works reported in literature are based on a synergistic combination of polysaccharides and mineral component such as β-tricalcium phosphate (β-TCP), HAp, CPCs and bioactive glass, for the preparation of injectable fillers. Such materials, at the same time, possess good osteoconductive

and osteoinductive properties, and present degradation rate and injectability that can be tailored. Suzuki *et al.* reported the enhanced osteoconductive properties, degradation rate and injectability of octacalcium phosphate dispersed with hyaluronic acid.[172] Nejadnik *et al.* developed an injectable nanocomposite hydrogel based on calcium phosphate nanoparticles and bisphosphonate-functionalized hyaluronic acid; these hydrogels possess good bioactive properties, together with a proper degradation rate and robustness.[173] Sohrabi *et al.* developed and characterized bioactive glass dispersed in an alginate/hyaluronic acid mixture in order to prepare a filler with a good injectability.[174]

1.4.2.3 Orthopedic clinical practice

Commercially available materials are commonly based on HAp, β-TCP, bioactive glass, collagen and demineralized bone matrix (DBM); they can be formulated as granules, sponges and matrices, cements, putties, pastes, block and cylinders.[175]

To report some examples, BIOMET EUROPE developed HAp based cylinders and blocks for the treatment of tibial and radial fractures and for bone tumor surgery (Endobone®) and several calcium phosphate-based and DBM-based pastes for the treatment of orthopedic trauma and as bone void fillers (Alpha-BSM®, EquivaBone™, CarriGen®); DEPUY developed a collagen/HAp-based matrix that can be mixed with bone marrow and is used in spinal surgery (Healos®); ORTHOVITA prepared a collagen/β-TCP foam for spinal and trauma surgery (Vitoss®) and a bioactive glass cement for vertebroplasty and as bone void filler (Cortoss®); STRYKER has developed a HAp/polyvinilpyrrolidone injectable cement for small defects and not load-bearing applications (HydroSet™); SYNTHES prepared β-TCP blocks and granules as cancellous bone void filler in trauma, spinal and reconstruction surgery (ChronOS™); BONALIVE LTD, using bioactive glass, developed granules, putty and plates for bone cavity filling and orbital floor reconstruction.

Despite the huge availability of bone graft substitutes, scaffolds and injectable fillers, in the clinical practice the gold standard remains the use of autografts for their ability to provide the three essential features required for the bone regeneration: osteoconductivity, osteoinductivity, osteogenicity. Bone graft substitute used in the clinical practice are always osteoconductive, but only in some cases are also osteoinductive; moreover, limited data have been reported on their properties and their effect, with respect to the autografts, thus making difficult their informed selection and use.

The cost of these materials is another important issue, but, despite it is usually higher than autografts and allograft procedures, it is an affordable expense if it is considered that these materials are fully characterized, easily stored, sterile and available for an immediate use.[175]

The main concern in the clinical practice is related to the possibility of microbial infection development, which, despite the surgical procedures and care, accounts for the 5% of biomaterial implantation interventions;[139,176] this percentage increases up to 14% for dental implants due to particular exposure to bacteria.[177] In general, peri-implants infections are more serious than infections of temporary implants, since the latter cause pain and discomfort and only in some cases the use of systemic antibiotics and re-application of the implant is needed; on the other hand, peri-implants infections can result in bone damage, secondary surgical interventions, implant failure and in some cases, mortality.[139,178] In order to overcome this issue, the research is investigating the incorporation of antibiotics in the biomaterials and their local delivery inside to target tissue; for example, poly(methyl methacrylate) (PMMA) cements for joint arthroplasty procedures can be loaded with small amounts of gentamicin and tobramycin.[176] Even if the delivery of antibiotics incorporated in biomaterials can be a good strategy for the prevention of peri-implant infections, there is a great concern regarding the development of multi-resistant bacteria strains and the need of novel strategies based on novel antimicrobial compounds.[139,176,179,179]

1.5 IMPLEMENTATION OF BIOPOLYMER-BASED BIOMATERIALS

Despite all the advantages offered by the use of polysaccharide and protein-based biomaterials, they can be further implemented with respect to the specific requirement of the final application. Several strategies can be adopted in order to tailor and improve the mechanical, physical and biological properties of biopolymers-based biomaterials; one possibility is the chemical modification/grafting of polysaccharides with bioactive chemical groups, and molecules, in order to modify the physical-chemical and biological properties of the polysaccharides; another possibility is the implementation of the biomaterials with structures and compounds that can provide the required characteristics.[29,150,180,181] The nanotechnologies can be used for the nanofabrication of materials, the micro- and nanopatterning of surfaces and the preparation of smart nanomaterials for the drug delivery;[3,182] moreover, biomaterials can be implemented with nanostructures in order to tailor specific properties of the materials, such as electrical conductivity

or antimicrobial properties.[183-186] In bone and neural tissue engineering the low mechanical properties of the polysaccharides, their lack of electrical conductivity and, in some cases, the low bioactivity emphasize the need of strategies for the tailoring and amelioration of these features.[150]

1.5.1 ENGINEERED POLYSACCHARIDES

Polysaccharides can be chemically modified in order to tailor their properties and to make them useful materials for the preparation of different types of biomaterials. For example, alginate can be conjugated with poly(*N*-isopropylacrylamide) (PNIPAAm) for the preparation of thermoresponsive and thermoreversible hydrogels, or it can be modified with RGD peptides to introduce cell ligands for bioadhesion. Alginate can be also functionalized with methacrylic groups to be used for free radical polymerizations, and it can be also functionalized with peptides and gelatin to enhance its bioactivity.[29,56]

Regarding hyaluronic acid, one of the most used derivatives is its benzyl ester (HYAFF®). Thanks to its physical-chemical properties, HYAFF® can be easily processed to obtain several types of biocompatible devices such as tubes, membranes, non-woven fabrics, gauzes and sponges for application in vascular, skin, cartilage and neural tissue regeneration.[187,188]

Functionalization of chitosan is aimed at the improvement of its water solubility and at the introduction of chemical groups and active functions.[189,190] Chitosan can be modified by addiction of sugars group, dendrimers, cyclodextrins and crown ethers principally for drug delivery applications[191] as well as for the improvement of its bioactivity.[35] Moreover, chitosan can be grafted to synthetic or natural polymers in order to improve its mechanical or biological properties.[35]

1.5.1.1 Chitlac: a lactose-modified chitosan

Chitosan can be covalently modified by an N-alkylation between lactose molecules and the amino groups of chitosan: the reaction leads to the formation of a branched polysaccharide named “chitlac” (Figure 12).[181,192]

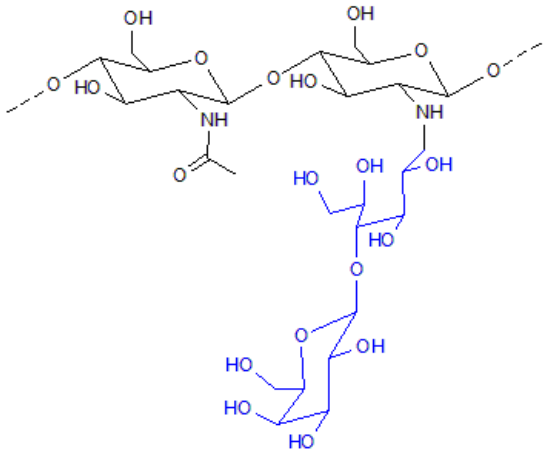

Figure 12. Chemical structure of chitlac.

This modification makes chitosan soluble in water and at physiological pH, leading to an improvement in its processability; in this form chitosan is miscible with anionic polysaccharides such as alginate and hyaluronic acid,[193] and it can be used for the preparation of tridimensional hydrogels and microspheres.[184,194] Chitlac has also been used for the preparation of bioactive coatings for methacrylic thermosets[195] and alginate scaffolds,[155] showing bioactive properties such as increased osteoblasts proliferation and ALP activity, and increased bone-implant contact in the case of chitlac-coated thermosets.[196] Chitlac has also proved to induce chondrocytes aggregation and synthesis of type II collagen and glycosaminoglycan by chondrocytes.[181] A similar effect has been showed by encapsulating chondrocytes in alginate and alginate/chitlac microbeads: the presence of chitlac led to a notable increase of proliferation if compared with alginate microbeads.[194]

It has been shown that the biological effects of chitlac are mediated by galectins.[181,197,198] Galectins are a family of β-galactoside-binding lectins that have in common a structurally conserved domain, the carbohydrate recognition domain, which recognizes the β-galactoside-containing carbohydrate moieties of glycoconjugates.[199] Galectins are able, in the ECM, to bind laminin, fibronectin, and elastin; they are also able to mediate biological activities such as adhesion, growth and functions of cells, thus regulating tissue homeostasis, composition, reorganization, and mechanical performance.[200] Marcon *et al.* found that galectin-1 was highly expressed in the chondrocyte aggregates formed in the presence of chitlac, suggesting a possible biological role.[198] Moreover

galectins expression has been associated to wound healing,[201] regulation of epithelial cells[202] and neural tissue regeneration.[203]

1.5.2 NANOTECHNOLOGIES AND BIOMATERIALS

Nanotechnologies offer several opportunities for the tailoring and the implementation of physical-chemical, mechanical and biological properties of biomaterials. The strategies for biomaterials preparation, which involve the use of nanotechnologies, can be divided into two main categories: the production of nanostructured biomaterials and the implementation of biomaterials with organic or inorganic nanostructures.

1.5.2.1 Nanostructured biomaterials

Nanostructured biomaterials can be prepared by nanoscaled modification of the material surface and morphology by means of lithography, chemical etching, micro-contact printing, self-assembly or electrospinning of nanofibers.

The nanopatterning of surfaces and the nanostructuration of the materials can have several positive effects on the biological interactions between cells and materials, by creating and mimicking the natural architecture of extracellular matrix.[3,204]

The nanofibrous scaffolds combine in a synergistic way the high "surface area to volume" ratio of the nanofibers and the microporosity of the scaffolds, creating an environment that favors cell adhesion, proliferation, migration and differentiation, thus presenting all the desired properties for tissue engineering concepts.[205,206] These structures represent a promising approach for muscle, bone and vascular tissue engineering.[204]

1.5.2.2 Organic and inorganic nanostructures

Organic and inorganic nanostructures can be added to polymer matrices for several purposes. For instance, drug-loaded polymer nanoparticles can be embedded in matrices for a controlled delivery; nanostructured ceramics, CNTs and polymer nanofibers can be mixed to the polymers in order to reinforce the structures, while metal nanoparticles can be used to provide antimicrobial properties. The advantages of these approaches are strictly related to the dimension of the nanostructures: their high surface area to volume ratio and the peculiar physical-chemical properties that arise from their

nano-dimensions enable unique interactions between these nanostructures, the polymer matrices and cells. These interactions lead for example to mechanical reinforcement of the structures and enhanced cell adhesion and functions.[150,176,184,207,208]

1.5.2.3 Carbon nanotubes

CNTs are, together with graphene and fullerenes, an allotropic form of carbon. They are used in several applications such as material engineering, industrial and energetic applications and tissue engineering.[95,209,210] CNTs are organized in one or more cylindrical graphene-like sheets of sp^2 carbon atoms, which form tubes with fullerene-like extremities. Depending on the number of graphene-like sheets that compose their structure, CNTs they can be distinguished in single-walled (SW-), double-walled (DW-) or multi-walled carbon nanotubes (MWCNTs).[211,212] Their diameter is comprised between 0.5 – 1.5 nm for the SWCNTs and over 100 nm for the MWCNTs, and they can be long up to some centimeters.[185] Due to their peculiar dimension, CNTs are characterized by a high aspect ratio (length to diameter ratio) and high surface area; these characteristics together with the presence of dangling bonds on the side walls, allow modifying the CNTs for several biomedical applications, and make them able interact with polymer matrices, proteins and cells.[185,213]

The structure of the CNTs is responsible for their unique physical properties: CNTs are the strongest material with a tensile strength up to 60 GPa[214,215] and a Young modulus higher than 1 TPa.[216,217] CNTs are also electrically conductive and behave like semiconductor or metallic depending on their chiral vector (the vector perpendicular to the graphene sheet rolling direction) and can carry currents greater up to 10^4 times than those carried by normal metals.[218-220]

Over the last two decades, CNTs have been receiving great attention for biomedical applications. Their unique morphological and chemical properties are very attractive to develop systems to be employed in drug delivery, phototermal and photodynamic therapy, gene therapy, cancer theranostic, diagnostic, biosensing and tissue engineering.[221-223] In particular, in the field of tissue engineering, CNTs can play an essential role in the creation of a biomimic environment thanks to their dimensions, nanoroughness, surface reactivity, interactions with water molecules, cells and polymers.[95,150,213,224-227] CNTs have been widely used and investigated for the culturing and the differentiation of several cell types for applications in bone, muscle, cardiac and neural tissue

regeneration.[228] Several research groups have focused their efforts on the development of nanostructured hydrogels and scaffolds based on the combination of natural or synthetic polymers and CNTs, where the latter play different roles such as the reinforcement of the polymer matrix,[176,222,229] the improvement of the electrical conductivity of the scaffolds,[183] and the improvement of material surface roughness and wettability.[230]

In particular, in the field of bone tissue engineering, CNTs proved to allow and sustain adhesion, proliferation and function of osteoblasts;[209,231,232] moreover, they are able to trigger and enhance the deposition of ECM and the nucleation of HAp.[233-235] Interestingly, it has also been reported that MWCNTs are able to regulate the bone cells, inhibiting the differentiation and the function of osteoclasts.[236]

CNTs are widely investigated also for neural tissue engineering applications. The immobilization of CNTs on two dimensional substrates allowed culturing neural cells and spinal cord organotypic slices on CNTs layers; electrophysiology measurements showed that CNTs are biocompatible and able to sustain neural cells functions and nervous impulse transmission.[95,237,238] CNTs have been also entrapped in polydimethylsiloxane (PDMS) in order to create tridimensional sponge-like scaffold in which neuron can be grown and analyzed: CNTs remarkably boosted synaptic activity also in this condition, and such scaffold can be also potentially used as an implant for the neural tissue engineering.[99]

The use of CNTs in biomedical applications can be limited also by their low water solubility, and the possible presence of toxic metals and other impurities due to the production process.[211,239] The *in vivo* toxicity of CNTs is strongly debated;[240] this depend on the fact that the studies are not standardized and take into consideration several typologies of cells and CNTs; moreover, CNTs toxicity is related to their dimension, purity grade, number of layers, dispersibility and aggregation tendency.[241,242] The toxicity of CNTs can be diminished by their functionalization with chemical groups and macromolecules that increase their water solubility,[186] for example the 1,3-dipolar cycloaddition make the CNTs biocompatible and for B and T cells, whose viability and function wass not affected after CNTs endocytosis.[243] CNTs dispersed in biopolymers or functionalized with polyethylene glycol (PEG) can be gradually eliminated by the organism.[244,245] CNTs functionalized with amino groups or peptides do not negatively affect the viability and the electrical

function of neurons.[246,247] Moreover, it has been observed that in certain conditions, functionalized carbon nanotubes (f-CNTs) can be degraded by oxidative enzymes.[248] Another important positive aspect of the functionalization is that during the chemical processes of purification and washing, catalytic metal and other impurities are removed, reaching very low, irrelevant and biocompatible percentages.[249]

CNTs can be functionalized by chemical processes and covalent modifications, or by non-covalent interactions with several types of molecules. Among chemical processes, the most important is the oxidation, performed at high temperatures in the presence of sulfuric or nitric acid, which introduce hydroxyl and carboxylic groups on CNTs surface.[250,251] Regarding the non-covalent modifications, CNTs can be wrapped with polymer chains (polysaccharides, proteins, nucleic acids) or can interact, through hydrophobic and π-π *stacking* interactions, with drugs and molecules with non-polar and aromatic groups.[213] Lastly, CNTs can be covalently conjugated with macromolecules and chemical groups that can be electrically charged; the most important are the arylation reactions based on diazonium salts, developed by Tour and colleagues,[252,253] and the 1,3-dipolar cycloaddiction developed by Prato and colleagues;[186,254] both reactions allow an easy surface modification of CNTs with polar or electrically charged chemical groups.

1.5.2.4 Silver nanoparticles

The development of multi-resistant bacteria strains is a serious concern for the use of antibiotics in the design of biomaterials. Therefore, there is a strongly need of novel and highly effective strategies and compounds not susceptible to bacterial resistance development. There is a wide variety of new agents based on inorganic and organic/polymeric materials that have been proved to act as wide spectrum agents; some examples are represented by silver, antimicrobial peptides, materials able to generate reactive oxygen species and carbon-based materials.[208]

Among those compounds, silver has been known for centuries for its bactericidal activity and has been already used in several topical applications for the prevention and the control of bacterial infections.[255] In particular silver nanoparticles (nAg) are one of the most widely used antibacterial compounds in the clinical practice.[208] nAg, through the release of silver ions, the generation of reactive-oxygen-species and the interaction with cell membranes, DNA and sulfur containing proteins have shown antibacterial activity both against Gram-positive and Gram-negative bacteria

strains, but also against fungi and viruses.[208,256-261] nAg have also proved to be toxic for methicillin-resistant strains of *S. aureus* and *S. epidermidis*,[262] and to enhance the antimicrobial activity of antibiotics.[263-265]

nAg toxicity for eukaryotic cells is also strongly debated; the same mechanisms that are active against bacterial cells can result in toxic effects also on eukaryotic cells, in particular membrane damage and reactive-oxygen-species (ROS) production. The latter can be worsened by the damages that nAg can induce on the proteins involved in anti-oxidant defense mechanisms.[266-268]

Another issue related with the use of nAg is their stability, as the agglomeration in microparticles and aggregates significantly affects and decreases their antimicrobial properties.[269]

Novel nanotechnological strategies for the development of biocompatible wide spectrum agents involve the preparation of systems, for example silver decorated polymeric nanostructures, which are able to guarantee a long-term stability of nAg, controlling and normalizing their size and shape and reducing their toxicity.[208]

In this contest the preparation of a stable form of nAg, synthesized, dispersed and stabilized in polysaccharides, is an interesting strategy for the implementation of bioactive and antimicrobial properties in biomaterials. In particular, the process reported by Travan *et al.* in 2009 enables to synthesize, disperse and stabilize the nAg by the reduction of silver ions in the presence of chitlac (Figure 13).[184]

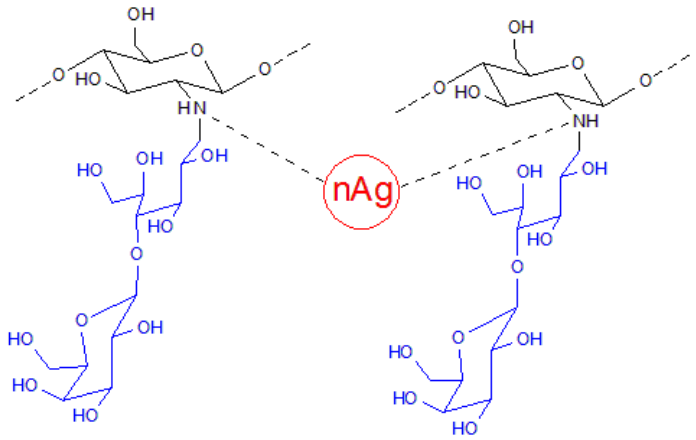

Figure 13. Schematic representation of silver nanoparticle stabilization by chitlac.

In this form, the nAg are confined inside a polymer matrix and can be stabilized over time. At the same time, the system guarantees a slow release of silver ions that can exert the antimicrobial activity, without being toxic for eukaryotic cells. The chitlac containing silver nanoparticles system (chitlac-nAg) has been thoroughly investigated for the preparation of antimicrobial coatings,[195,196,270] and tridimensional hydrogels and microbeads in combination with alginate.[184]

2 AIMS OF THE WORK

Nanotechnology represents a fertile ground for the development of novel bioactive biomaterials. In tissue engineering, such biomaterials can be designed and prepared by taking advantage of engineered polysaccharides. The present work, by using the combination of different polysaccharides and organic/inorganic nanostructures, aims at the development and characterization of novel biomaterials to be employed in bone and neural tissue engineering. This thesis has three main objectives:

2.1 CHARACTERIZATION OF FUNCTIONALIZED CARBON NANOTUBES (f-CNTs) DISPERSIONS AND NANOSYSTEMS

Specific aims:

- Evaluation of f-CNTs concentration, dispersibility and aggregation tendency in aqueous and polymeric dispersions by means of Low Field Nuclear Magnetic Resonance (LF-NMR).
- Spectroscopical, mechanical and rheological characterization of alginate/f-CNTs solutions and hydrogels by means of LF-NMR, uniaxial compression tests and rheological measurements.

2.2 DEVELOPMENT OF A BRIDGING IMPLANT FOR THE SPINAL CORD INJURY TREATMENT

The second objective is part of PRIN-MIUR project “Spinal injury: towards the development of cell-instructive scaffolds for nerve tissue repair” (2014-2017).

Specific aims:

- Preparation morphological and physical characterization of polysaccharide coated glass substrates

- Evaluation of biocompatibility and biological effects of the polysaccharide-coated glass substrates on two dimensional neuronal network model and on co-cultures of motoneuron progenitors and engineered mesoangioblasts.
- Preparation and characterization of porous alginate scaffolds, functionalized with chitlac, with isotropic or anisotropic pore morphologies.

2.3 DEVELOPMENT OF FILLERS FOR NON-CRITICAL BONE DEFECTS HEALING

Specific aims:

- Determination of the morphological differences and of the influence of pore morphology on stability, mechanical performances and biological properties of alginate/hydroxyapatite (HAp) scaffolds.
- Implementation of alginate/HAp scaffolds with f-CNTs and biological characterization.
- Development of an antimicrobial injectable bone filler based on alginate/HAp microbeads implemented with silver nanoparticles (nAg)
- Characterization of stability, morphology, biocompatibility, biological properties and injectability of the microbeads
- *In vivo* evaluation of biocompatibility and osteoconductive properties of the injectable filler on a rabbit model of non-critical bone defects.
- Preparation and characterization of alginate/HAp materials implemented with collagen and gelatin.

Acknowledgments and collaborations

f-CNTs have been provided by prof. Maurizio Prato research group (Department of Chemical and Pharmaceutical Science, University of Trieste).

Rheological and LF-NMR measurements have been performed in collaboration with prof. Mario Grassi and Michela Abrami (Department of Engineering and Architecture, University of Trieste).

The PRIN-MIUR project involves the laboratories of Prof. Laura Ballerini (SISSA, Trieste) and Dr. Raffaella Scardigli (CNR, Laboratory of Neurotrophic factors and Neurodegenerative Diseases of Prof. Antonino Cattaneo).

The *in vivo* studies have been performed in collaboration with Prof. Niko Moritz and Dr. Julia Kulkova (Turku Clinical Biomaterials Centre, TCBC, University of Turku).

COST Action MP1301 and Consorzio Interuniversitario per le Biotecnologie, are acknowledged for the financial support during the visiting research period at TCBC.

3 RESULTS AND DISCUSSION

The work described in this thesis deals with the preparation and characterization of polysaccharide-based biomaterials, implemented with silver nanoparticles (nAg) and functionalized carbon nanotubes (f-CNTs), for applications in bone and neural tissue engineering. This work can be divided in three major sections: i) the first one is focused on the determination of the effects of the f-CNTs presence on the spectroscopical, rheological and mechanical properties of dispersions and polysaccharide-based nanosystems; ii) the second one describes the preparation of polysaccharide-coated two-dimensional substrates for the evaluation of the biological effects of different polysaccharides on the behavior and function of neural cells, and the preparation of a tridimensional scaffold for neural tissue engineering; iii) the third one describes the preparation and the characterization of polysaccharide-based tridimensional scaffolds and antimicrobial injectable fillers for the bone tissue engineering.

3.1 CHARACTERIZATION OF FUNCTIONALIZED CARBON NANOTUBES DISPERSIONS AND NANOSYSTEMS

As discussed in the introduction, several research groups have proposed the use of CNTs for biomedical and tissue engineering applications, in particular for the preparation of biocompatible nanocomposite biomaterials in the form of solutions, hydrogels or scaffolds.[150,180,185]

In order to optimize the contribution of CNTs to the nanocomposite materials, it is very important to investigate how CNTs are dispersed within the biomaterial matrix and how they interact with the surrounding environment, namely with water molecules, polymeric chains and cells.[150] In particular, the interaction between water molecules and CNTs modifies several properties of the material, like wettability, consequently affecting protein adsorption and cell adhesion.[224,225] However, the final aggregation state within the matrix is affected by the dispersion and stability of the initial aqueous CNTs systems.

Several techniques have been employed to evaluate the dispersion of CNTs inside polymeric matrices such as transmission and scanning electron microscopy,[224] and scattering techniques, like dynamic light scattering or small angle x-ray scattering.[271] Moreover, it has been recently demonstrated that the presence of CNTs in solution alters its echographic response and therefore they have been proposed as potential contrast agents.[272]

In this work, Low Field-Nuclear Magnetic Resonance (LF-NMR) was used for the characterization of aqueous dispersions of MWCNTs, pristine or covalently functionalized with different chemical groups (Figure 14).[252,273,274]

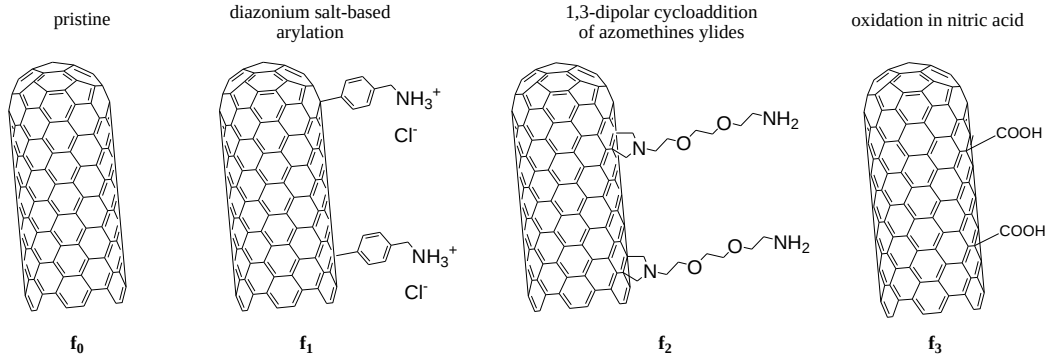

Figure 14. Schematic representation of the f-CNTs used in this work

3.1.1 EVALUATION OF THE AGGREGATION TENDENCY OF FUNCTIONALIZED CARBON NANOTUBES DISPERSED IN AQUEOUS MEDIA

It has been demonstrated that CNTs are able to interact with surrounding water molecules[275,276] and to influence the relaxation time of the latter, depending on the functional groups exposed on their surface.[277,278] Therefore the T_2 spin-spin NMR relaxometry of protons in water, being sensitive to the constraints of the molecule,[279] can be a useful technique to quantitatively evaluate concentration, dispersion and aggregation of f-CNTs in water solutions. In fact, the stability of f-CNTs in water strongly depends on the nature and extent of their chemical substitution, in particular with polar and even ionic groups to reduce the unfavorable solute-solvent interactions. Visual inspection of suspensions of the f-CNTs in water at the concentration of 0.1 % (w/V) reveals such tendency, in particular for the pristine, un-derivatized f_0-CNTs. Moreover, aggregation manifests as a significant time-dependent effect; sonication helps producing a visible dispersion of f-CNTs.

The effect of CNTs on the relaxation time of water and the aggregation tendency in aqueous systems has been evaluated measuring $\overline{T}_2$ of the dispersions at different time intervals. f-CNTs have been dispersed in pure water and in culture medium (complete DMEM in water), in view of future studies on CNTs in cell-containing systems. Moreover, the chosen f-CNTs have been dispersed in an aqueous alginate solution (2% w/V) in order to evaluate the ability of LF-NMR to detect the aggregation tendency of CNTs in this condition. The reasons for choosing alginate are manifold: *i*) alginate is a very hydrophilic polymer, and as such it may severely affect the structuring of water and the ensuing effect on the solubility of co-solutes; *ii*) alginate is an anionic polyelectrolyte, and its negative charges may trigger different interactions with differently charged CNTs; *iii*) alginate is one of the most important biopolymers used in the preparation of scaffolds and, in general, in tissue engineering, which may be interesting areas of application of CNTs.

In general, $\overline{T}_2$ was found to be notably lowered upon addition of CNTs although such effect strongly depended on their dispersion state (the $\overline{T}_2$ values recorded for water and for f-CNTs-free aqueous solutions are quite long: water, ~ 2400 ms; DMEM, ~ 2200 ms; alginate, ~ 1400 ms).

Preliminary experiments were carried out for the various f-CNTs, in the absence or in the presence of co-solutes (DMEM or alginate), adjusting the sonication time for each case to the goal of reaching a visual disappearance of massive aggregation (*i.e.* good dispersion). The results are reported in Figure 15, A to C.

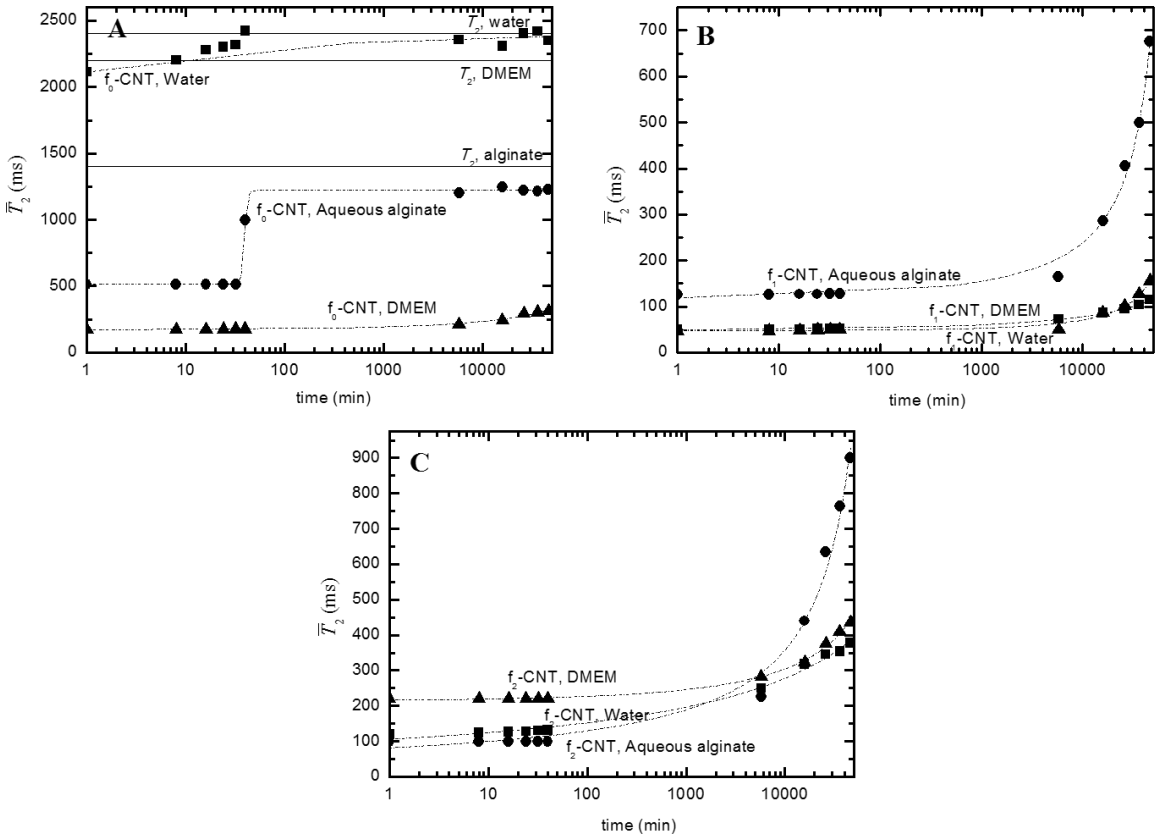

Figure 15. Time dependence of the average relaxation time ($\overline{T}_2$) of dispersions of f_0-CNTs (**A**), f_1-CNTs (**B**) and f_2-CNTs (**C**), in pure water (■), in DMEM (▲) and in alginate (●). f-CNTs concentration: 0.1 % (w/v).

As general statements, *i*) the $\overline{T}_2$ values of all f-CNTs show a more or less marked time-dependence; *ii*) the range of $\overline{T}_2$ values span over two orders of magnitude, from about 45 ms (for f_1-CNTs in DMEM) to that of pure water (for f_0-CNTs at long times). Correspondingly, it is possible to identify three extreme types of behavior. In pure water, f_0-CNTs display $\overline{T}_2$ values, which started from values close to that of pure water, for further increase during the time interval of the experiment, practically reaching the value of the relaxation time of free water molecules after 40 minutes. The latter effect seemed to be clearly correlated with the ongoing massive macroscopic aggregation of CNTs.

f_0-CNTs in DMEM, and both f_1-CNTs and f_2-CNTs in all conditions: *i*) show much lower $\overline{T}_2$ values than f_0-CNTs in water, indicating an initial condition of much better dispersion. As demonstrated by Cheng *et al.*,[280] serum proteins are able to adsorb on the CNTs surface, a phenomenon that leads to a better dispersion of the CNTs;[281] *ii*) seem to conform to an exponential increase of $\overline{T}_2$ values with time (this is evident by plotting the data as a linear function of time: data not shown). This behavior can be clearly associated with an increasing association, however starting from values much lower than those of un-derivatized f_0-CNTs in pure water. A discussion of the specific effect of the co-solute (DMEM or alginate) on the $\overline{T}_2$ values is postponed to the following paragraph.

Finally, the time dependence of the $\overline{T}_2$ values of f_0-CNTs in aqueous alginate show a peculiar behavior, inasmuch as after some sort of induction time of about 40 min, they show an abrupt increase which sigmoidally reaches a plateau at $\overline{T}_2$ values not very far from those of water in aqueous alginate at 2% concentration. This behavior is at variance with both above described case: it is tempting to suggest an all-or-none equilibrium between two states of solvation/interaction with alginate. In an initial step, f_0-CNTs might be rather well dispersed, until the rapid onset of a reorganization of the CNTs around the polyanion (which very rapidly achieves its final "equilibrium" condition), characterized by an overall effect on the relaxation time of water very similar to alginate itself. It should be recalled that the mass ratio of alginate-to-CNTs is 20:1, thus making the dominant role of the ionic polysaccharide very plausible. Given the limited time window of the experiments, it is not possible to make any speculation if also in the cases of f_1-CNTs and f_2-CNTs with alginate, the observed strong increase of $\overline{T}_2$ values at long times would also lead to some sort of plateau close to the $\overline{T}_2$ value of CNT-free alginate solution, with generality of the process.

Overall, comparing the relaxation results with the visualization of the f-CNTs dispersions over time, it can be concluded that T_2-NMR is a reliable technique to detect aggregate formation.

3.1.2 CORRELATION BETWEEN $\overline{r_2}$ AND CONCENTRATION OF FUNCTIONALIZED CARBON NANOTUBES DISPERSED IN AQUEOUS MEDIA

f-CNTs have been dispersed at various concentrations in deionized water, in complete DMEM and in alginate solution (2% w/V in water), to verify if the hypothesis that a single type of associated (and solvated) CNT species in the initial step of solution dispersion was confirmed by an observed linearity of the dependence of $\overline{T}_2$ values on concentration. Moreover, to exclude possible non homogeneous effects of sample preparation on the observed data, it was decided to subject the various samples to the same time of sonication, namely 30 minutes.

The analysis performed by LF-NMR, right after the sample preparation and sonication, showed a good linear correlation between $\overline{r_2}$ (with $\overline{r_2} \equiv \overline{T}_2^{-1}$) and the CNTs concentration in water and in DMEM for all f-CNTs, except for the case of f_0-CNTs when they are dispersed in water (Figure 16, A and B).

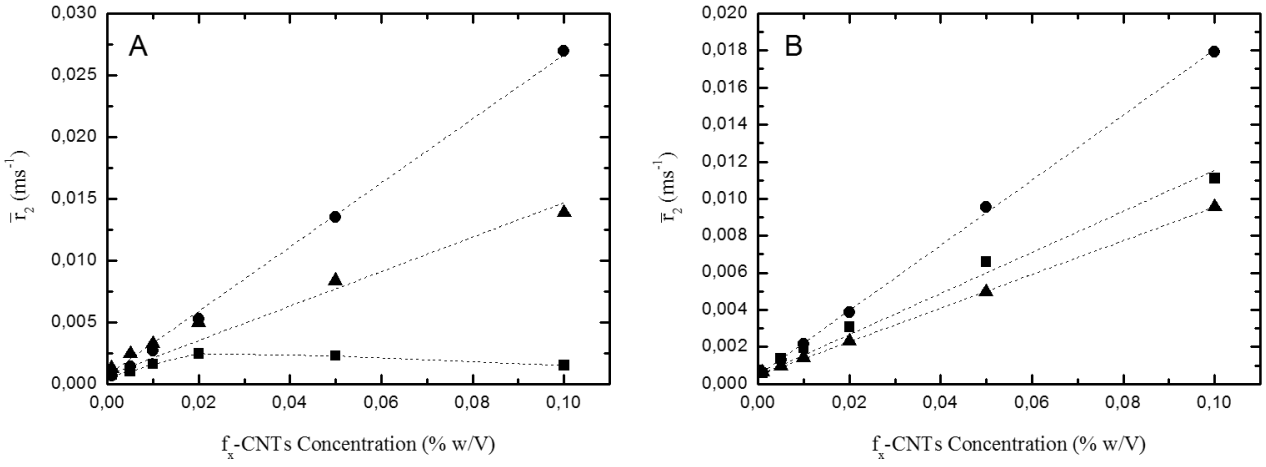

Figure 16. Concentration dependence of the average relaxation rate ($\overline{r_2}$) of dispersions of f_0-CNTs (■), f_1-CNTs (●) and f_2-CNTs (▲) in water (**A**) and in DMEM (**B**). Data points taken at 30 min sonication.

Given the calculated value of $\overline{r_2}$ of water and DMEM from $\overline{T_2}$ ($\overline{r_2}$ water = $4.1_7 \cdot 10^{-4}$ s^{-1}; $\overline{r_2}$ DMEM = $4.5_5 \cdot 10^{-4}$ s^{-1}), it was decided to fit the observed data points with those constrained intercept values. The parameters resulted from the linear fitting (R^2 and slope) are reported in Table 1.

Table 1. Parameters of the linear fitting for the f-CNTs dispersed in water and in DMEM.

dispersant	*f_0-CNTs*		*f_1-CNTs*		*f_2-CNTs*	
	R^2	slope	R^2	slope	R^2	slope
water	n.d.	n.d.	0.9982	0.26	0.977	0.14
DMEM	0.9936	0.11	0.9997	0.18	0.9998	0.09

In other words, such procedure corresponds to assuming a constant contribution from "free" water (overwhelming in mass but practically negligible as to effects on $\overline{r_2}$) and attributing all the observed increase of $\overline{r_2}$, with C_p, to f-CNT. The good statistical quality of the fit (as shown by R^2) seems to support the validity of the procedure.

The experiments described in the previous paragraph showed the high tendency of f_0-CNTs to aggregation and precipitation in water, thus not allowing them to be stably dispersed in water. At variance, DMEM was proved to increase the solubility and stability of f_0-CNTs dispersions, given the linear correlation between concentration and $\overline{r_2}$.

In the case of f_1- and f_2-CNTs in DMEM, a decrease of $\overline{r_2}$ is observed with respect to the corresponding values in pure water (slightly above 30%), pointing to trend which has been so far interpreted as deriving from some sort of association/phase separation. One should recall that DMEM contains salts (*i.e.* it has a significant value of ionic strength and hence may contribute to electrostatic shielding), as well as various components (first, but not only, glucose) deeply modifying (in particular, increasing) the solution viscosity. However, and more important, amphiphilic compounds (like proteins or other serum components) might effectively act as suspending agents for the hydrophobic CNTs,[280] at the same time affecting the intrinsic relaxation properties of water. In fact, CNTs are known to be stabilized by surfactant micelles.[282] The observed proportional decrease of $\overline{r_2}$ in DMEM with respect to pure water could derive from an effect of the medium components on the intrinsic relaxation of water around CNTs. Alternatively (or, more probably, additionally) the effect could stem from an aggregation mechanism of CNTs,

usually referred to as a "closed association",[283] in which solute association does not proceed indefinitely upon increase of concentration (like in a usual association/precipitation equilibrium), but, rather, through the formation of soluble clusters of quasi-stoichiometric composition (like in micelle formation). In this view, using the linear fitting equation for the f_1-CNTs and f_2-CNTs dispersed in water, and the corresponding $\overline{r_2}$ values (in DMEM) it is possible to estimate the soluble and the aggregate fractions of the f-CNTs in DMEM (Figure 17), respectively, assuming that the $\overline{r_2}$ values in pure water correspond to a condition of optimal dispersion (no aggregation).

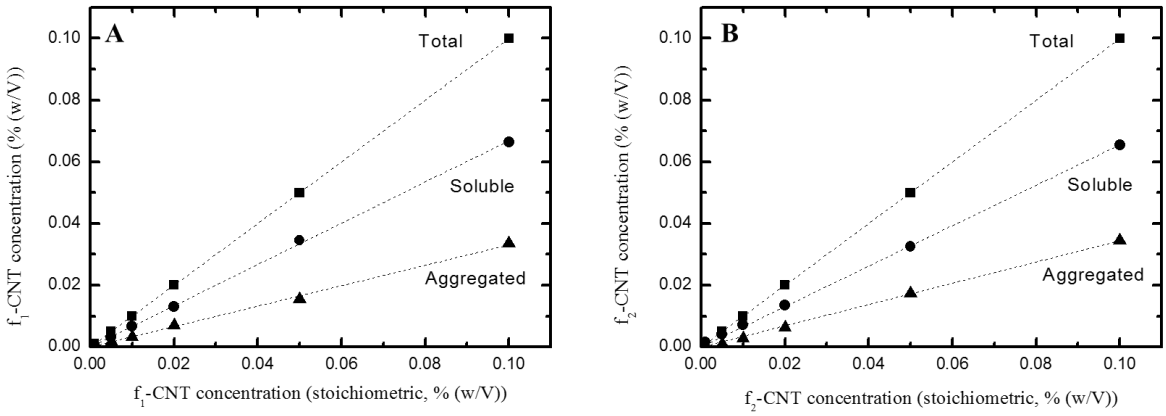

Figure 17. Concentration of active (soluble, ●) and non-active (aggregated, ▲) components and total f-CNTs (■) as a function of the total f-CNTs concentration for f_1-CNTs (**A**) and f_2-CNTs (**B**) dispersed in DMEM.

The percentage of the aggregated f-CNTs, as a function of the f-CNTs concentration, is reported in Figure 18. In this graph, the previous mentioned "closed association" phenomenon is clearly showed as the asymptotic relation between the f-CNTs aggregated fraction and the f-CNTs concentration.

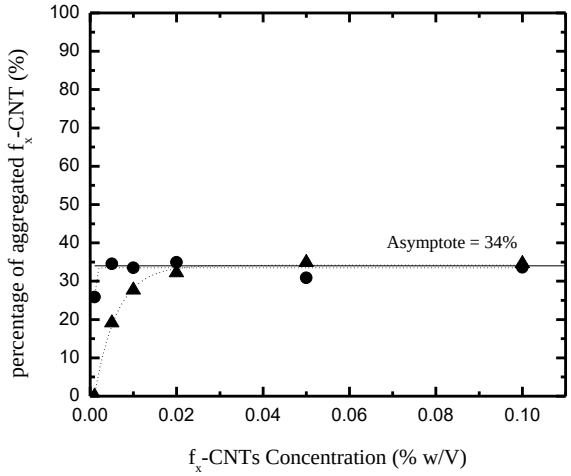

Figure 18. Percentage of aggregated f-CNTs function of f-CNTs concentration for f_1-CNTs (●) and f_2-CNTs (▲) dispersed in DMEM.

A useful pictorial representation of the two hypotheses is given by Figure 1, A and B, respectively, of Reference 282, in which the cross-section model of an individual fullerene nanotube in a cylindrical SDS micelle (A) and of a seven-tube bundle of fullerene nanotubes coated by a layer of sodium dodecyl sulphate (B) are modelled. On the basis of the $\overline{r_2}$ data alone, it is impossible to ascertain the validity of either interpretation, or of both simultaneously. Further work is then required, in particular including the study of the separate effects of, *e.g.*, ionic strength, nature and valence of the ionic species, viscosity of the aqueous system, specific effects of amphiphilic co-solutes, possibly by using other types of techniques (*e.g.* scattering methods[284]).

At any event, analysis of Figure 2 allows to state that $\overline{r_2}$ of water molecules measured by means of low-field NMR can be a useful, quick and cost-effective technique for the quantification of dispersed f-CNTs in water.

When the f-CNTs are dispersed in an alginate solution (2% w/V) the situation is more complicated. The concentration dependence of $\overline{r_2}$ for the three types of f-CNTs is reported in Figure 19.

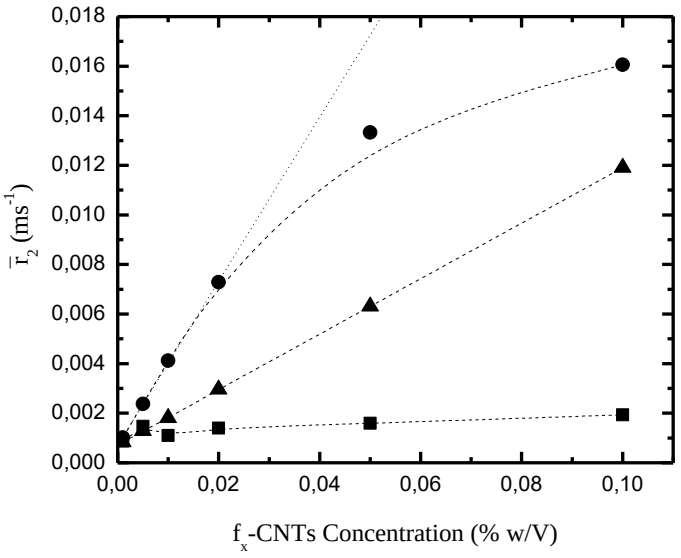

Figure 19. Concentration dependence of the average relaxation rate ($\bar{r}_2$) of dispersions of f_0-CNTs (■), f_1-CNTs (●) and f_2-CNTs (▲) in alginate aqueous solution (2% w/V), after 30 minutes of sonication.

From the graph reported in Figure 19 it can be seen that the three types of f-CNTs show three different types of behavior: *i*) f_0-CNTs, similarly to what already seen in water, are not well dispersed and their $\bar{r}_2$ values cannot be directly related to their concentration; *ii*) f_1-CNTs manifest an initial very good dispersion, followed, for concentrations equal or larger than 0.04%, by a tendency to a negative deviation from linearity, which is a clear symptom of association; *iii*) f_2-CNTs show a good linear dependence of the $\bar{r}_2$ with the CNTs concentration ($R^2 = 1$), which is a clear indication of a single type of (good) dispersion in alginate.

Going into detail, the behavior of $\bar{r}_2$ of f_1-CNTs in the first part of the concentration range (*i.e.* below 0.02%) is quite interesting. The alignment of the data points seems reasonably well linear, but, visually, with a higher slope than in water. A linear regression through the data points in aqueous alginate, in the first part of the concentration range, provides a satisfactory fitting, with slope = 0.33 and $R^2 = 0.9998$ (having used the $\bar{r}_2$ value of aqueous 2% alginate as the intercept). The value of the slope is 25.5% larger than in pure water. This result is at variance with the $\bar{r}_2$

value (derived from the initial $\overline{T_2}$) here above obtained at higher concentration (0.1%) and reported in Figure 15C. It points to the presence of a strong concentration dependence and suggests that, in very dilute conditions, alginate makes quaternarized f_1-CNTs favorably interact with water, rather than among themselves, to an extent larger than in pure water. Given the positive charge of f_1-CNTs, it is tempting to propose that an electrostatic association takes place between the cationic CNTs and the polyanion. Once attracted by the ionic polysaccharide, f_1-CNTs perceive a highly hydrated environment; at the same time, entropy will maximize the distribution of CNT-polymer contacts as well as the interpolymer distance because of polyanion-polyanion repulsion. The ensuing result will be an even better solvation of f_1-CNTs than in pure water, with complete annihilation of any possible aggregation. However, when the CNTs concentration increases electrostatic interactions may produce an opposite effect, since increased cationic CNT accumulation in the "condensation volume" of the polyanionic polyelectrolyte produces an increase of their local concentration and favor CNT association, with an ensuing decrease of $\overline{r_2}$. Although such clusters of aggregated CNTs are likely to be still associated with the polysaccharide chains, further experiments are required to verify this and to shed light on the topology of the macromolecular complexes. This association is observed for concentrations larger than about 0.03%. Use of the fitting parameters can be made much in the same way as it has been done DMEM case, *i.e.* allowing for the calculation of the $\overline{T_2}$-active (soluble) and the non-active (aggregated) fractions of CNTs, respectively. The results are reported in Figure 20.

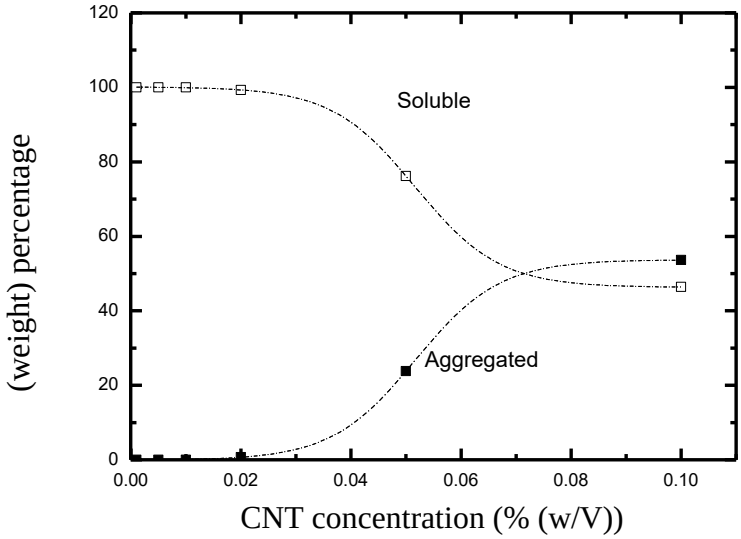

Figure 20. Concentration dependence of the soluble (void symbols) and the aggregated (full symbols) fractions of f_1-CNTs dispersed in 2% aqueous alginate.

From the graph, it can be observed that the presence of alginate favors solubility of f_1-CNTs at very low concentrations. Moreover, it can be appreciated the presence of two domains, with a sigmoid transition from the "soluble dispersion" regime to that of "aggregate".

Regarding the behavior of $\overline{r_2}$ of f_2-CNTs, it is similar to that of the dispersion in water and in DMEM, with a slope of 0.11 that indicate a "closed association" effect that is less extended respect to the case of DMEM (see Table 1). In the same way of what done for the DMEM dispersions, the $\overline{T_2}$-active (soluble) and the non-active (aggregated) fractions of CNTs can be calculated (Figure 21).

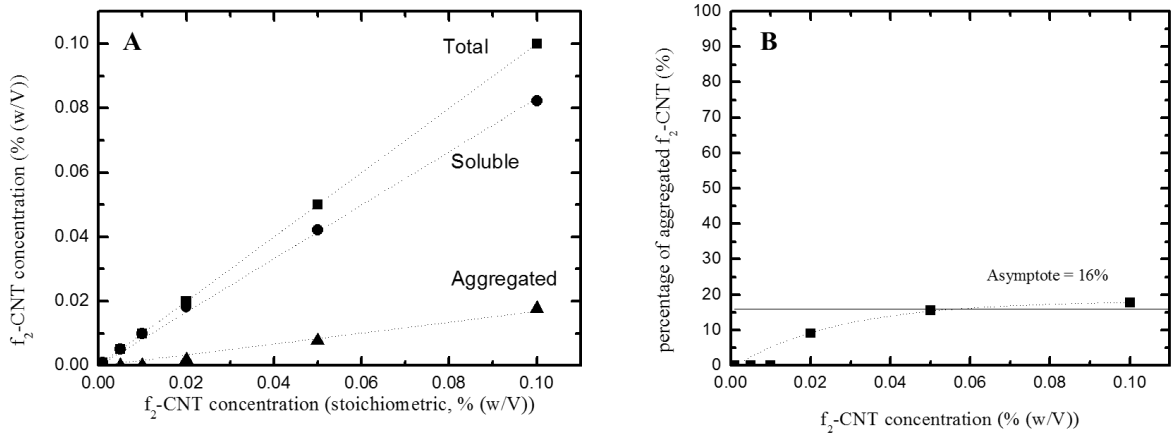

Figure 21. **A**) Concentration of active (soluble,●) and non-active (aggregated, ▲) components and of total f_2-CNTs (■) as a function of the total f_2-CNTs concentration dispersed in alginate. **B**) Percentage of aggregated f_2-CNTs as a function of f_2-CNTs concentration, dispersed in alginate.

Again, an asymptotic behavior of the aggregated fraction, as a function of the CNTs concentration, can be appreciated, although less marked than in the case of DMEM dispersions. Alginate seems to be able to bring out a different behavior between f_1-CNTs and f_2-CNTs, inasmuch as the former CNTs pass from a very hydrated microenvironment to a rather massive aggregation, depending upon their concentration (*i.e.* on the CNT/alginate ratio), whereas the interaction with alginate of the latter ones seem to give rise just to a (solubilizing) modulation of an otherwise persisting tendency to produce close-association complexes.

3.1.3 MECHANICAL AND SPECTROSCOPICAL CHARACTERIZATION OF ALGINATE/FUNTINALIZED CARBON NANOTUBES SOLUTIONS AND HYDROGELS

3.1.3.1 Characterization of alginate/f-CNTs solutions

Rheological behavior of alginate/f-CNTs solutions

Solutions of alginate (2% w/V) and f-CNTs (0.1 and 1% w/V, respectively) were characterized by means of steady state shear flow experiments. A shear thinning behavior was observed for all samples although at low values of the shear rate a variable tendency to conform to a Newtonian plateau was observed (Figure 22).

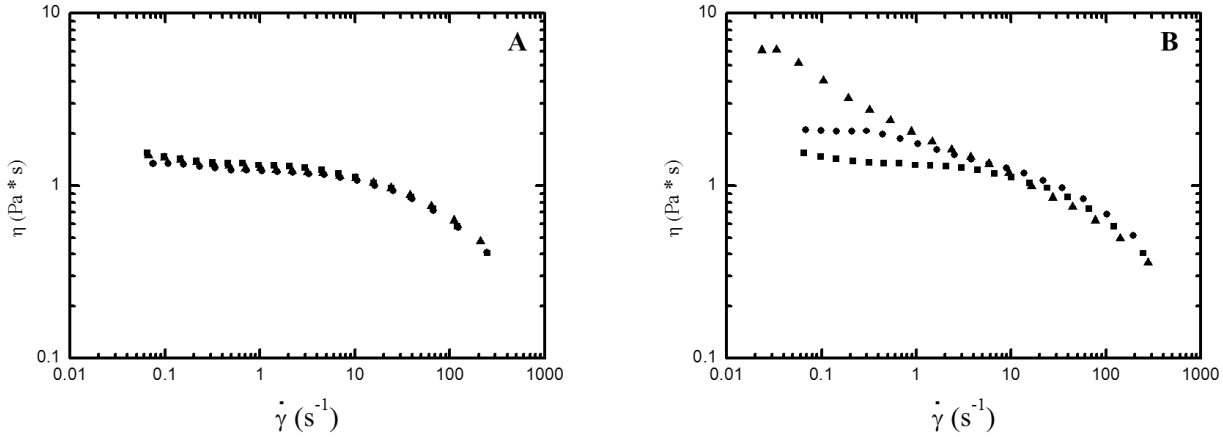

Figure 22. Flow curves for alginate alone (■) and with f_1-CNTs (●) and f_3-CNTs (▲) with a total concentration of CNTs of 0.1 % (w/V) (**A**) and 1 % (w/V) (**B**), respectively. In all cases, alginate concentration was 2 % (w/V).

It was found that the flow curve of the alginate solution was significantly affected by f-CNTs only at a concentration of 1% (Figure 22B) while at the concentration of 0.1% such influence on the rheological behavior of the polysaccharide was very small (Figure 22A).

Focusing on Figure 22B, the increase of the viscosity at low $\dot{\gamma}$ in the case of f_1-CNTs can be explained considering the electrostatic interactions between the protonated amino moieties[252] on nanotubes and the carboxylate groups of alginate. This is in line with recent observations on mixtures of oppositely charged polysaccharides.[193] The marked enhancement of η at low $\dot{\gamma}$ upon the addition of f_3-CNTs turns out to be more puzzlingly. Given the nature of the f_3-CNTs functionalization, it is possible that this type of CNTs is able to establish wider interactions with alginate chains, respect to f_1-CNTs. Moreover, it is possible that the carboxylic groups of f_3-CNTs form hydrogen bonds between each other, leading to a partial and local aggregation of CNTs.

Possible support to this hypothesis might derive from the observed higher deviation from the Cox-Merz rule (Figure 23) found in the latter case.[285] While this rule (which states that $\eta^*(\omega) = \eta(\dot{\gamma})$) typically holds for homopolymers solutions, it generally fails for nanocomposites.[286] In particular f_3-CNTs (Figure 23C) showed the highest deviation from the Cox-Merz rule suggesting a non-homogeneity of the solutions and the presence of microscopic aggregates that influence the viscosity.[287] The presence of an inhomogeneous system could also be responsible of the very marked shear thinning of the flow curve.

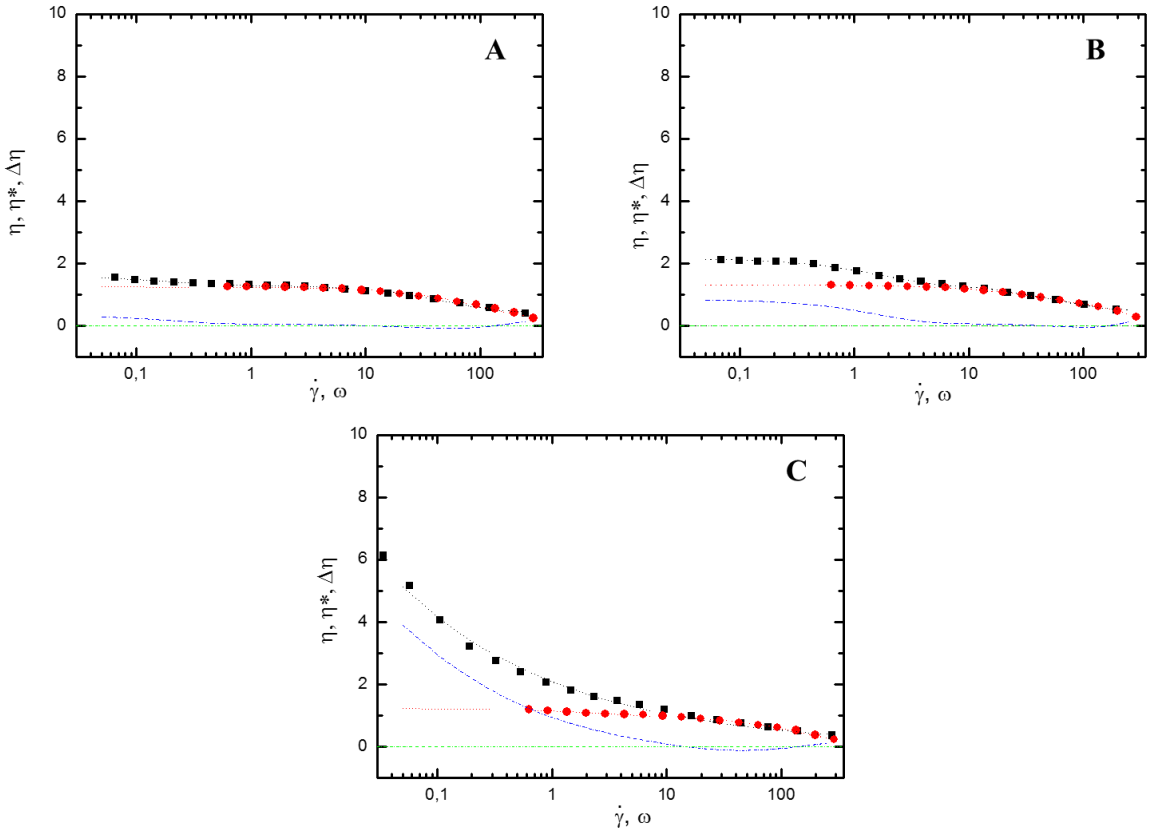

Figure 23. Comparison between the viscosity – shear rate (η - $\dot{\gamma}$, ■) and the complex viscosity- pulsation (η* - ω, ●) dependence (Cox-Merz rule) for alginate alone (**A**) and with the addition of f_1-CNTs (**B**) and f_3-CNTs (**C**). Same conditions as in Figure 1b. In the graphs is also reported the difference between η and η* as Δη (-·-), compared with the ideal trend (--).

NMR relaxometry of f-CNTs/alginate solutions

The behavior of alginate/f-CNTs solutions has been investigated through NMR relaxometry in order to get information about the dispersion stability and the organization of water molecules around CNTs. The time span from the preparation, up to 10 minutes was investigated and no prolonged time effect was investigated. In general terms, in the presence of f-CNTs a decrease of the relaxation time of the water molecules (Table 2) can be observed in the presence of f-CNTs in comparison with the solution of alginate alone ($\overline{T}_2$ = 1586.31 ms), showing that the effect of CNTs prevailed over the one of the polysaccharide.

Table 2. Average proton relaxation times ($\overline{T}_2$) of alginate solutions (2% w/V) in the presence of f-CNTs at 0.1% w/V and 1% w/V.

f-CNTs concentration	*f_1-CNTs*	*f_3-CNTs*
	$\overline{T}_2$ (ms)	
0.1% w/V	223.9	240.9
1% w/V	18.1	10.5

Alginate alone (2% w/V): $\overline{T}_2$ = 1586.3 ms.

In both cases, the average proton $\overline{T}_2$ decreased upon increasing the f-CNTs concentration. A 10-fold increase of concentration produced an about 12-fold decrease of $\overline{T}_2$ for f_1-CNTs and an almost double (23-fold) effect for f_3-CNTs.

The variation of $\overline{T}_2$ when the concentration of CNTs is increased seems to be related to the variation of viscosity. It can be observed that respect to the f_1-CNTs, with the f_2-CNTs there is a larger increase of viscosity and a larger decrease of $\overline{T}_2$. This can be an additional indication of the higher complexity of the system respect to the f_1-CNTs, due to the possible presence of micro-domains (namely, CNTs aggregates).

3.1.3.2 Characterization of alginate/f-CNTs hydrogels

Following the approach reported in the materials and methods section, highly homogeneous alginate hydrogels were obtained with a good dispersion of the f-CNTs.

Rheological characterization of alginate/f-CNTs hydrogels

Mechanical spectroscopy was used to determine the viscoelastic properties of the alginate/f-CNTs hydrogels under small oscillatory shear. Prior to the measurement, the linear viscoelastic range for each sample was determined for each sample by means of a stress sweep test.

The mechanical spectra (Figure 24) showed that in all cases the addition of f-CNTs did not modify at all the character of firm gels of the alginate-based systems, since G' is one order of magnitude higher than the G" and both are basically constant over three decades of frequency.[279] In addition, it was noticed that the presence of the f-CNTs at a concentration of 1% (w/V) reinforces the tridimensional structure in all cases.

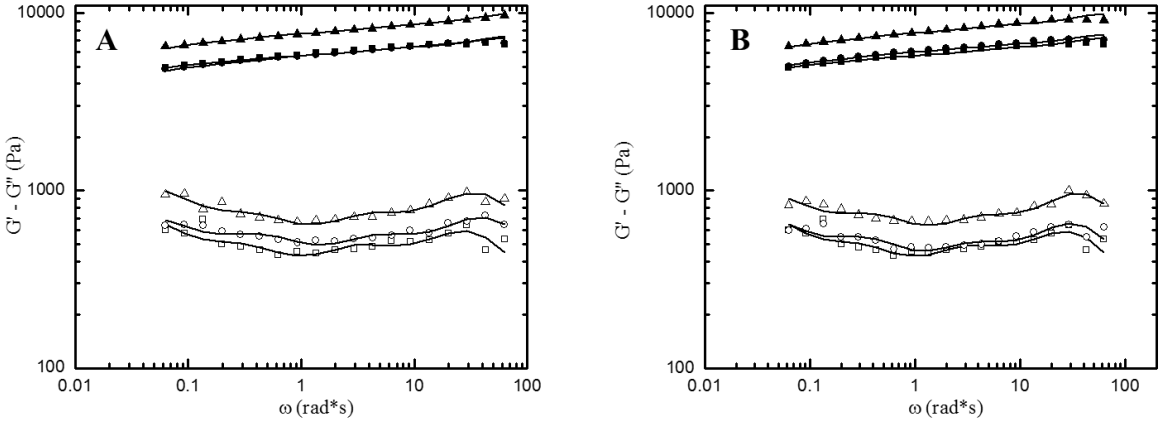

Figure 24. Mechanical spectra of calcium alginate hydrogels as such (black symbols) and in the presence of f_1-CNTs (**A**) and f_3-CNTs (**B**) at a total CNTs concentration of 0.1 % (w/V) (circle) and 1 % (w/V) (triangles), respectively. Full symbols indicates G' and void symbols indicates G".

The frequency sweep test were interpreted in terms of the generalized Maxwell model composed of a sequence of elements in parallel (spring and dashpot) to which an additional spring has been added:

$$G' = G_e + \sum_{i=1}^{n} G_i \frac{(\lambda_i \omega)^2}{1+(\lambda_i \omega)^2}; \qquad G_i = \eta_i / \lambda_i \tag{1}$$

$$G'' = \sum_{i=1}^{n} G_i \frac{\omega\ \lambda_i}{1+(\lambda_i \omega)^2} \tag{2}$$

where f is frequency, ω is pulsation ($= 2\pi f$), n is the number of Maxwell elements considered, G_i, η_i and λ_i represent, respectively, the spring constant, the dashpot viscosity and the relaxation time of the i^{th} Maxwell element while G_e is the spring constant of the last Maxwell element which is

supposed to be purely elastic. The fitting of the experimental data was performed assuming that relaxation times are not independent each other, but they are scaled by a factor 10.[279]

The number of the Maxwell elements was selected to minimize the product $\chi^2 * N_p$, where χ^2 is the sum of the squared errors while N_p (= n + 2; G_e, λ_1 plus G_i) indicates the number of fitting parameters. The experimental data were efficiently fitted by the generalized Maxwell model as reported in Figure 24. For all the hydrogels, four Maxwell elements were sufficient to describe the system and to determine the shear modulus G by summing the spring constants of the Maxwell elements (equation 3):

$$G = G_e + \sum_{i=1}^{n} G_i \qquad (3)$$

As previously determined on alginate hydrogels (2% w/V), the error associated with the shear modulus, calculated repeating the experiment on different replicates, is always less than 3%.[279]

The shear modulus G confirmed that the presence of f-CNTs at a concentration of 1% for all the f-CNTs slightly but neatly (about 33%) increased the mechanical properties of the hydrogels (Table 3).

Table 3. Shear modulus (G, in kPa) of alginate hydrogels (2% w/V) in the presence of f-CNTs at 0.1% w/V and 1% w/V.

f- CNTs concentration	*f_1-CNTs*	*f_3-CNTs*
	G (kPa)	
0.1% w/V	7.8 ± 0.1	7.9 ± 0.1
1% w/V	10.4 ± 0.1	10.5 ± 0.1

Alginate alone (2% w/V): G = 7.4 ± 0.2 kPa.

Uniaxial compression tests of alginate/f-CNTs hydrogels

Cylindrical shape hydrogels have been prepared in order to analyze their mechanical performance in the presence of carbon nanotubes under uniaxial compression test.

Compression tests showed that mechanical properties are influenced by the concentration and the type of functionalization of f-CNTs. In general, a decrease of the mechanical properties is observed in the presence of f-CNTs (Table 4). f_1-CNTs (1% w/V) turn out to be the best choice since the compression modulus value is very close to that of alginate one and the σ_{UCS} is the highest among the alginate/f-CNTs hydrogels analyzed. In the case of f_1-CNTs containing hydrogels, the increase in nanotube concentration from 0.1 % to 1 % led to an increase of both the ultimate compression strength (σ_{UCS}) and the energy at break. At variance, the opposite behavior was noticed when f_3-CNTs were used. It can be hypothesize that the increase of f_3-CNTs concentration plays a negative effect on the mechanical properties due to the presence of the CNTs aggregates and to the possible interaction between the carboxylic groups of the CNTs with the calcium ions competing with the carboxylic groups of the alginate chains.

Table 4. Ultimate compression strength (σ_{UCS}) and compression modulus (E) of alginate hydrogels (2% w/V) in the presence of f-CNTs at 0.1% w/V and 1% w/V.

f-CNTs concentration	*f_1-CNTs*		*f_3-CNTs*	
	σ_{UCS} (kPa)	E (kPa)	σ_{UCS} (kPa)	E (kPa)
0.1% w/V	240.3 ± 19.1	31.4 ± 1.1	390.9 ± 34.4	28.9 ± 1.5
1% w/V	383.1 ± 8.1	35.7 ± 1.8	248.5 ± 36.4	34.9 ± 2.9

Alginate alone (2% w/V): σ_{UCS} = 444.6 ± 29.6 kPa; E = 37.4 ± 1.9 kPa.

Small discrepancies were observed comparing rheology (shear modulus) and compression tests, which can be reasonably explained by taking into account the anisotropy typical of these complex materials.

NMR relaxometry of f-CNTs/alginate hydrogels

Alginate-based hydrogels containing f-CNTs have been characterized by LF-NMR water relaxometry. In general terms, the average relaxation time values of nanostructured hydrogels are lower than the alginate control ones ($\overline{T}_2$ = 156.81 ms) (Table 5). These results follow the same trend already reported for the f-CNTs/alginate solutions. Since rheological analyses suggested that the mesh size is not affected by the presence of CNTs (at least for 0.1 %), it was possible to assert

that the differences in the relaxometry behavior of the water molecules are related both to the concentration and to the functionalization of the carbon nanotubes.

Table 5. Average proton relaxation time ($\overline{T}_2$, in ms) of alginate hydrogels (2% w/V) in the presence of f-CNTs at 0.1% w/V and 1% w/V.

f-CNTs concentration	*f_1-CNTs*	*f_3-CNTs*
	$\overline{T}_2$ (ms)	
0.1% w/V	33.5	114.9
1% w/V	12.3	21.6

Alginate gel alone (2% w/V): $\overline{T}_2$ = 156.8 ms.

The effect of the gelation on the water relaxation time of the water can be evaluated from the ratio of the $\overline{T}_2$ relaxation rate of the hydrogel with the respective solution (Table 6).

The measured value of $\overline{T}_2$ is a combination of several factors, e.g. the mobility of the water protons (^{1}H), the concentration of macromolecules in the sample, the exchange of protons between the water and the macromolecules, as well as the local magnetic environment of the sample.[288]

Table 6. Ratio between the average $\overline{T}_2$ for the solutions and the average $\overline{T}_2$ for calcium hydrogels in the presence of f_1-CNTs or f_3-CNTs at a total CNTs concentration of 0.1 % and of 1 % (w/V).

f-CNTs concentration	*f_1-CNTs*	*f_3-CNTs*
0.1% w/V	6.7	2.1
1% w/V	1.5	0.5

Alginate alone (2% w/V): ratio = 10.1

Upon gelation, there is a general decrease of the $\overline{T}_2$ [279,288] in all cases except in the case of f_3-CNTs at 1% (w/V), for which a slight increase can be observed. The latter could be due to the aggregation

of CNTs already discussed, which impedes interactions with water. The presence of these aggregates (or interaction domains) could be proved by the decreased strength of this type of hydrogels (which formation is hindered by the presence of the aggregates)

As in the case of the solutions, the increase of the f-CNTs concentration in the hydrogels, leads to a decrease of the $\overline{T}_2$: a 10-fold increase of concentration produced a 2.7-fold decrease of $\overline{T}_2$ for f_1-CNTs and, likewise in the solutions, a 5.3-fold effect for f_3-CNTs. Also in this case this effect could be traced back to the presence of interaction domains and aggregates.

As in the case of the alginate/f-CNTs solutions, combining the data collected for the hydrogels, the organization of the CNTs and the polymer matrix can be inferred. In particular, the rheological analysis show that CNTs at 0.1% (w/V) do not affect the mechanical properties of the hydrogels and at 1% (w/V) there is a reinforcement of the structures; whereas the mechanical strength decreases with f_1-CNTs 0.1% (w/V) and with f_3-CNTs 1% (w/V). The hypothesis on the decrease in the case of f_3-CNTs seems confirmed by the LF-NMR analysis, which outcomes seem to indicate the presence of CNTs aggregates (that are not present at 0.1% w/V).

The low mechanical strength with f_1-CNTs 0.1% (w/V) is probably due to the interference of these f-CNTs with the coordination of calcium ions by alginate chains. However, if the concentration and hence, the solid fraction is increased, hydrogel strength is also increased.

The huge differences in the relaxation time with differently f-CNTs seem to point at strong interactions between water and f-CNTs suggesting an improvement of the wettability of the structures leading to better biological properties.[230]

3.1.4 CONCLUSIONS

The evaluation of dispersibility and aggregation tendency of different f-CNTs dispersed in aqueous media has been performed by LF-NMR: in particular, the analysis of $\overline{T_2}$ of water molecules allows for determining the aggregation of f-CNTs in water solutions, and a linear dependence between $\overline{r_2}$ and CNTs concentration for well dispersible f-CNTs, can be found when they are dispersed in water, and for all the f-CNTs (even the pristine CNTs) when they are dispersed in culture medium.

Moreover, LF-NMR is useful to analyze he effect of the addition of serum proteins (contained in DMEM) or alginate, as a dispersant, on suspensions of cationic and neutral f-CNTs. Serum proteins showed to be much more able to guarantee a good dispersion of all the f-CNTs overcoming the difficulties represented by the high hydrophobicity of the f_0-CNTs and the positive charges of the f_1-CNTs.

Alginate/f-CNTs solutions and hydrogels have been analyzed by means of LF-NMR, rheological measurements and uniaxial compression tests in order to determine the effects of the f-CNTs presence: the analysis revealed that f-CNTs are able to highly reduce the water protons relaxation time of both solutions and hydrogels, but their presence exerts a slight effect on the rheological properties in terms of an increase of solutions viscosity and hydrogels shear modulus, and a decrease of the mechanical properties of the hydrogels, depending on the chemical functionalization of the CNTs.

3.2 DEVELOPMENT OF A BRIDGING IMPLANT FOR THE SPINAL CORD INJURY TREATMENT

Natural biopolymers, and in particular polysaccharides, are being widely explored and investigated for the preparation of a bridging implant scaffold for the Spinal Cord Injury (SCI) treatment.[94] The strategy described and adopted in this work is based on tridimensional freeze-casted alginate scaffolds, whose biological properties were tailored by the addition of chitlac and of neurotrophines (NTs) expressed by engineered mesoangioblasts (MABs).

3.2.1 EVALUATION OF THE BIOLOGICAL PROPERTIES OF POLYSACCHARIDE-BASED SUBSTRATES (2D MODEL)

The evaluation of the biological properties of the polysaccharides employed has been performed analyzing the morphology, the differentiation and the electrophysiological activity of neural cell cultures, grown on the surface of polysaccharide-coated glass substrates. The effects of chitlac and of the combination of chitlac/alginate have been compared with the effect of chitosan and chitosan/alginate coatings (used as controls).

3.2.1.1 Preparation of polysaccharide-coated glass surfaces

The method for the preparation of the polysaccharide coatings is based on the electrostatic interactions between the polysaccharides and between them and the glass surface. The glass substrates have been treated to introduce negative charges, which were exploited to establish interactions between the glass surface and the amino groups of chitlac and chitosan. The approach based on the electrostatic interactions between polysaccharides and activated surfaces has been already successfully exploited to coat methacrylic surfaces[195,289] or alginate scaffolds with chitlac.[155] Various physical and chemical approaches have been tested for the activation of the glass surface: treatment with sulfuric acid, plasma cleaning and treatment with piranha solution. Preliminary studies pointed out that the treatment with piranha solution was the most effective in introducing negative charges on glass surface. The mixed layers have been prepared alternating chitlac or chitosan layers to alginate layers following the *layer-by-layer* deposition approach. Single layers of polycations (chitosan or chitlac) or mixed layers of polycation-polyanion-polycation (chitosan or chitlac with alginate) were obtained, as reported in Figure 25.

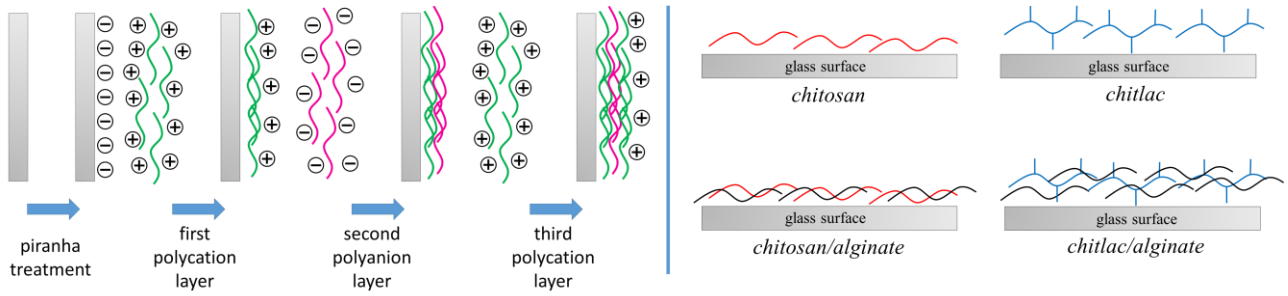

Figure 25. Scheme of the four different types of coatings based on the polysaccharides chitosan, chitlac and alginate.

The morphology of the layers was investigated by means of Confocal Laser Scanning Microscopy (CLSM), coating the glass substrates with fluorescein labelled chitosan (-fluo), chitlac (-fluo) and/or alginate (-fluo); in the case of the coatings composed of mixed layers (chitosan/alginate or chitlac/alginate) only one labelled polymer per sample was used. Figure 26 collects the confocal images of the four different surfaces.

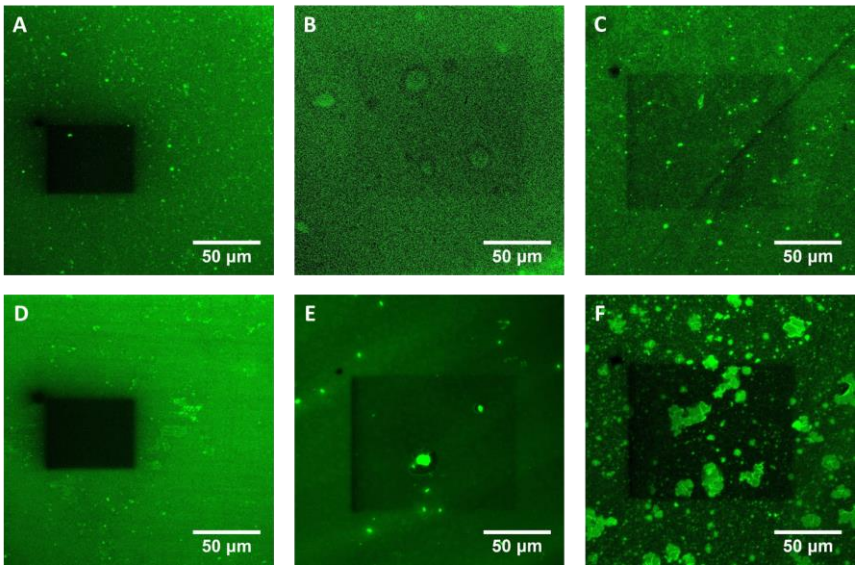

Figure 26. Confocal microscopy imaging (top view) of the four different polysaccharide-based coatings. **A**) Chitlac-fluo; **B**) chitlac-fluo/alginate; **C**) chitlac/alginate-fluo; **D**) chitosan-fluo; **E**) chitosan-fluo/alginate; **F**) chitosan/alginate-fluo.

The images point out the presence of fluorescent coatings all over the analyzed surfaces: putting the coated surfaces under intense laser irradiation results in bleached areas, which confirms the presence of a continuous fluorescent coating. Preliminary tests proved that the glass substrate does

not possess any auto-fluorescence (data not shown). The spots with more intense signals indicate surface areas where the fluorescently labelled polysaccharide accumulated upon drying the polymer solutions on the glass substrate. The thickness of the polysaccharide layers has been measured by means of Atomic Force Microscopy (AFM): to evaluate the thickness of the coatings a scratch was made on the coated surfaces. The values obtained are reported in Table 7.

Table 7. Thickness of the polysaccharide coatings, determined by AFM.

Polysaccharide coating	*Thickness (nm)*
Chitosan	104 ± 24
Chitlac	5 ± 2
Chitosan/alginate	213 ± 32
Chitlac/alginate	24 ± 18

The values indicates that there are differences in the polysaccharide adsorption onto glass surfaces: with chitosan, which possesses a high number of positive charges, is possible to obtain thicker coatings; moreover, the addition of alginate leads in both cases (chitlac and chitosan) to thicker coatings.

When biomaterials are implanted into the body, protein adsorption onto the foreign surface occurs within seconds from implantation, so that cells approaching the biomaterial surface interact with the adsorbed protein layer; surface properties like hydrophilicity, wettability and charge are key driving mechanisms for protein absorption processes, and thus, for the biological response;[290] these surface features can be expressed by studying surface free energy parameters.

Contact angle measurements were performed putting the four different polysaccharide-coated surfaces in contact with polar (water and ethylene glycol) and apolar (diiodomethane) liquids. The values obtained are reported in the Table 8: the contact angle values between water and the chitlac containing surfaces are lower than the chitosan containing ones, meaning that their wettability and hydrophilicity are higher. This result can be related to the chemical nature of chitlac and is in line with the recent findings of D'Amelio *et al.*,[197] who showed that the lactitol side-groups of chitlac determine a stronger interaction with water (solvation zone) with respect to chitosan.

Table 8. Contact angles of three reference liquids on the four different polysaccharide-based surfaces.

Polysaccharide coating	*Contact angles for liquids θ (°)*		
	Water (γ^{TOT} = 72.8 mJ/m^2)	Ethylene Glycol (γ^{TOT} = 48.0 mJ/m^2)	Diiodomethane (γ^{TOT} = 50.8 mJ/m^2)
Chitosan	58.5 ± 6.2	36.6 ± 6.9	42.4 ± 4.6
Chitlac	15.8 ± 4.3	11.9 ± 2.6	44.7 ± 3.1
Chitosan/alginate	67.8 ± 6.3	30.1 ± 4.4	36.7 ± 5.0
Chitlac/alginate	45.3 ± 5.3	13.9 ± 3.6	29.3 ± 3.1

From the contact angles data the surface free energy parameters were calculated; in fact, according to the Van Oss theory, it is possible to correlate contact angles with surface energy of a solid material by means of the Young-Duprè equation which enables to calculate the surface energies as a sum of the dispersive (LW) and acid-base (AB) contributions, which take into account the non-polar and polar interactions, respectively.[291] This approach was used to calculate surface free energy parameters and work of adhesion of the investigated surfaces (Table 9).

Table 9. Surface free energy parameters and work of adhesion parameters calculated by contact angle measurements. γ^{LW} is the apolar term of the specimens surface free energy; γ^{+} and γ^{-}, are respectively the acid and base terms of the specimens surface free energy; γ^{AB} is the polar term of the specimens surface free energy. γ^{TOT} is the total surface free energy of the specimen and is given by the sum of γ^{LW} and γ^{AB}. The polarity is the ratio between γ^{AB} and γ^{TOT}. Work of adhesion W^{AB} is due to acid-base interactions between polar liquids and surfaces and is reported as value and as percentage referred to the total work of adhesion. Contact angles of three reference liquids on the four different polysaccharide-based surfaces.

Polysaccharide coating	*Surface free energy parameters [mJ/m²]*					*polarity (%)*	*Work of adhesion*			
	γ^{LW}	γ^{+}	γ^{-}	γ^{AB}	γ^{tot}		W^{AB} H_2O [mJ/m²]	W^{AB} H_2O %	W^{AB} EG [mJ/m²]	W^{AB}% EG %
chitosan	38.41 ±2.47	0.23 ±0.21	22.69 ±1.31	4.57 ±2.09	42.97 ±3.26	10.63 ±4.93	53	37%	20	18%
chitlac	37.18 ±1.68	0.28 ±0.01	63.60 ±0.04	8.44 ±0.02	45.64 ±1.70	18.49 ±0.29	86	50%	29	25%
chitosan/alginate	41.21 ±2.47	0.73 ±0.12	9.84 ±1.17	5.36 ±0.54	46.56 ±2.56	11.51 ±1.32	40	31%	20	18%
chitlac/alginate	41.80 ±1.50	0.57 ±0.03	30.76 ±0.39	8.36 ±0.23	50.16 ±1.51	16.67 ±0.68	64	41%	26	22%

The total surface energy γ^{TOT} of the four different surfaces ranges from 42.97 to 50.16 mJ/m^2, in line with previous investigations on polysaccharide-coated methacrylic surfaces.[195] In the case of the chitlac coating, the higher value of the acid-base interactions (γ^{AB}) causes a considerable increase in the surface polarity with respect to the chitosan coating (chitlac: 18.49%, chitosan: 10.63%); the increase of surface polarity associated with chitlac is verified also in the case of the mixed layer with alginate (chitlac/alginate: 16.67%, chitosan/alginate: 11.51%). Table 9 shows also that the presence of chitlac is associated with a significant increase of acid−base interactions with water: from 53 mJ/m^2 to 86 mJ/m^2 for the monolayers and from 40 mJ/m^2 to 64 mJ/m^2 for mixed layers; while the dispersive contribution (γ^{LW}) is almost constant among all the surfaces. The increase of acid−base interactions with water can be ascribed to the higher density of polar functional groups of chitlac. This result stems from the different chemical structure of the macromolecules adsorbed on the surface, *i.e.* the presence of the lactose residues in the case of

chitlac, which determines a higher density of surface hydroxyl sites. These results suggest that surface energy parameters and interfacial interactions of polar liquids provide a reasonable description of the acid−base character of the polysaccharide-based surfaces. Conversely, the dispersive interactions did not vary between chitlac or chitosan containing surfaces. This finding is in line with what reported by Lamour *et al.*,[292] Assero *et al.*[293] and Hallab *et al.*[294] on similar polymer based coatings.

3.2.1.2 Biological effects of the polysaccharides in two-dimensional conditions

With the exception of the analyses performed to assess the involvement of galectin-1 in the biological effects of the polysaccharides, the evaluation of the biocompatibility and the biological effects of the polysaccharides has been performed by immunofluorescence staining and electrophysiological measurements in collaboration with prof. Laura Ballerini laboratories (SISSA, Trieste, Italy).

Polysaccharide biocompatibility

The biocompatibility of the polysaccharides has been assessed evaluating adhesion, morphology and viability of dissociated hippocampal neurons (as a simplified *in vitro* neuronal network model) grown on all the polysaccharide-coated substrates. Chitosan/alginate substrates have been excluded from the analyses because they were not able to sustain cell growth.

From the immunofluorescence images reported in Figure 27 it can be seen that the dissociated hippocampal cultures grew on all three substrates, but some differences in the network growth patterns can be appreciated: switching from chitosan to chitlac and to chitlac/alginate, neurons tend to grow in a widespread, uniform network without forming aggregates. The absence of aggregates can be the cause of the lower neuronal density on chitlac/alginate surfaces.

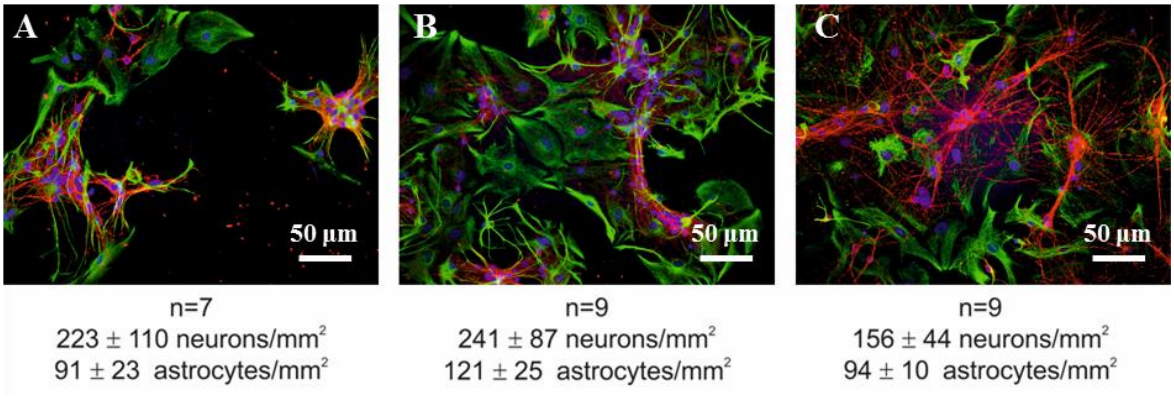

Figure 27. Representative images of hippocampal cultures after 8-10 days, on chitosan (**A**), chitlac (**B**) and chitlac/alginate (**C**) (n=number of coverslips; red: β-tubulin III (βtub III,) green: Glial Fibrillary Acid Protein **(**GFAP), blue: DAPI). Distribution and density have been evaluated from 5 culture series.

The health status of neuronal cells was further analysed by means of electrophysiological evaluation of neuronal passive membrane properties like membrane input resistance (R_{in}) and cell capacitance (C_m). These parameters are related to cell dimensions: a larger cell possesses a higher number of ion channels, thus a low resistance. The presence of higher number of ion channels on a larger cell means also a more extended conducting surface (which is opposed to the non-conducting membrane) that results in larger capacitance. Figure 28 shows the values of the measured parameters; no statistical differences can be observed between chitlac and chitlac/alginate; on the other hand, the resistance is higher and the capacitance is lower for neurons grown on chitosan. Altogether, the higher dimensions and the more spread neuronal network on chitlac and chitlac/alginate, indicate a healthier morphology of neurons in the presence of chitlac.

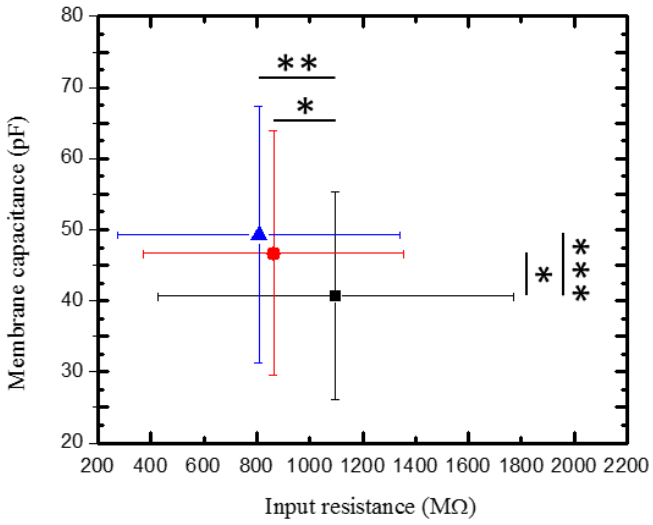

Figure 28. Plot showing membrane passive properties for chitosan (■, n=73), chitlac (●, n=102) and chitlac/alginate (▲, n=103) neurons, from 26 culture series. (*: P<0.05; **: P<0.01; ***: P<0.001)

The results obtained from the analysis of the membrane passive properties are confirmed by the measurement of the βtub III positive area (μm^2), reported in Figure 29, which is significantly higher in neurons grown on chitlac-based substrates, suggesting an increased neuronal arborisation since the number of neurons is unchanged (see Figure 27).

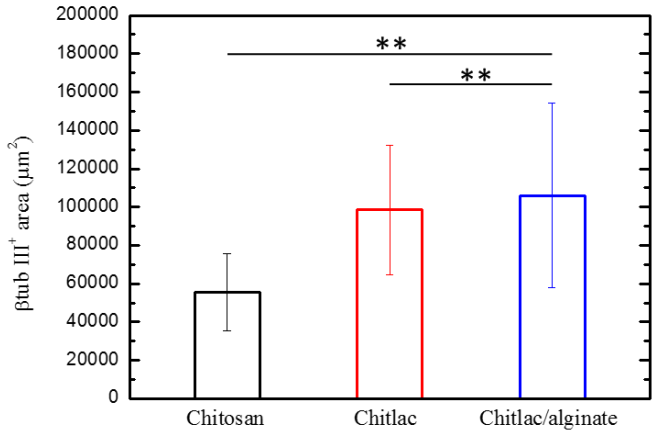

Figure 29. βtub III positive area (μm^2) of neurons grown on chitosan, chitlac and chitlac alginate. (*: P<0.05; **: P<0.01; ***: P<0.001).

Analyses of neuron functionality

In order to analyze the functionality and the formation of synaptic connections within the neuronal network, single-cell patch-clamp records were performed, and the occurrence of heterogeneous spontaneous postsynaptic currents (PSCs) was monitored; this is a widely accepted method for the identification of functional synapse formation.[295] Figure 30A shows sample traces of the PSCs for the three conditions. PSCs frequency was significantly increased (+ 62%) in the case of chitlac/alginate compared to the chitlac one, and it was even higher (+ 128%) when comparing it with the chitosan coating (Figure 30B). On the contrary, no significant differences were found between chitlac and chitosan neurons, even though an increasing trend was observed when neurons grew on chitlac. Similar results obtained by PSCs amplitude analysis are shown in Figure 30C: chitlac/alginate neurons displayed an increased (+ 36% and + 35% over chitlac and chitosan, respectively) PSCs amplitude.

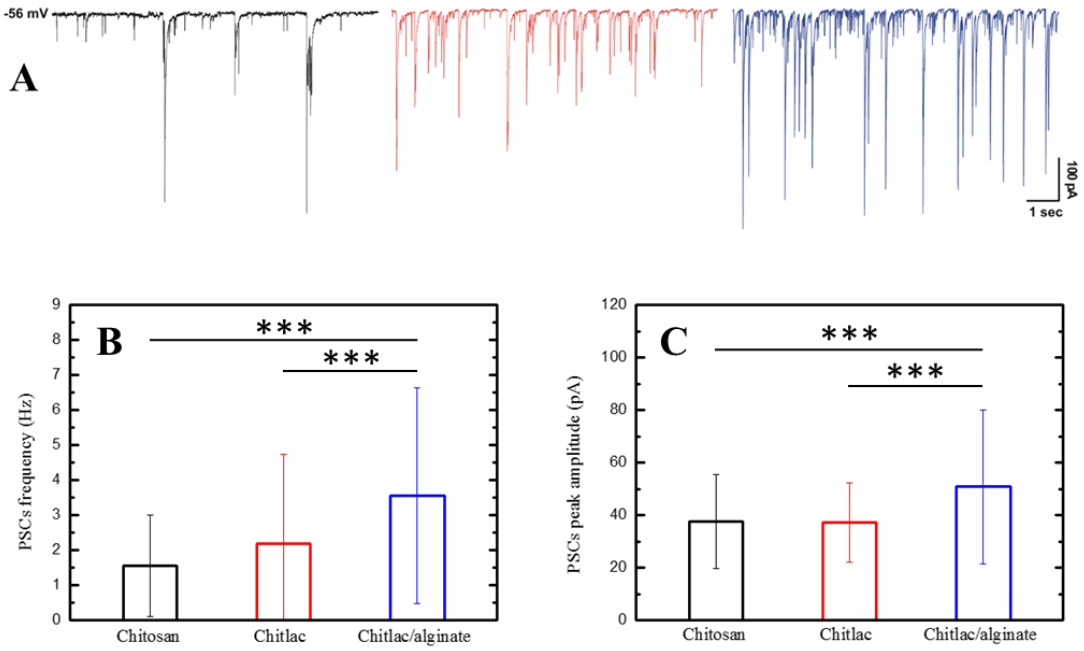

Figure 30. Spontaneous PSCs recorded from neurons sampled from the three experimental conditions. **A**) Representative traces recorded in voltage-clamp mode from chitosan (black, n=64), chitlac (red, n=85) and chitlac/alginate (blue, n=97) hippocampal neurons. **B**) Plot showing the increased PSCs frequency in the chitlac/alginate neurons compared to chitlac and chitosan neurons. **C**) PSCs amplitude plot showing the enhanced effect encountered in the chitlac/alginate condition over the chitlac and chitosan conditions. (*: P<0.05; **: P<0.01; ***: P<0.001).

In order to clarify whether the increased synaptic activity could be assigned to the neuronal network density or to neuritic arborisation and a possibly increased synaptogenesis, neurons have been marked with biocytin and the neurites have been counted right after their exit from the soma and at three increasing distances (25, 50 and 75 μm from the cell soma). Table 10 contains the results found. Due to the low number of stained neurons still adherent to the chitosan-coated substrate after the procedure, it was not possible to perform statistical analysis. Nevertheless, it can be suggested the presence of a decreased neuritic arborisation in the chitosan experimental group when compared to the other two groups, based on the obtained data.

Table 10. Values of neurites counting obtained from the biocytin labelled neurons from each experimental condition. Chitosan (n=2), chitlac (n=9), chitlac/alginate (n=11) (Analysis performed by Dr. Jummi Laishram).

Polysaccharide coating	*Neurites exiting the soma*	*Neurites at 25 μm from the soma*	*Neurites at 50 μm from the soma*	*Neurites at 75 μm from the soma*
Chitosan	4.0 ± 0.0	4.50 ± 0.71	7.0 ± 0.0	7.0 ± 1.14
Chitlac	5.0 ± 1.66	7.11 ± 3.14	10.22 ± 2.95	8.44 ± 3.40
Chitosan/alginate	5.60 ± 1.63	7.90 ± 4.06	8.70 ± 3.47	7.20 ± 4.94

Galectin-1 analyses

Considering the significant differences observed for the neurons grown on chitlac containing surfaces, the possible mechanism responsible for these differences has been further investigated. It has been shown that galectins, and in particular galectin-1, can be involved in the molecular recognition of chitlac and in the triggering of cellular processes.[198]

The presence of galecin-1 and the differences in its expression among the three conditions have been analyzed by means of ELISA assay, on the culture medium harvested after 8 days, and immunofluorescence staining of neurons after 8 days. The preliminary ELISA results (Figure 31) suggest an increased secretion of galectin-1 for cultures grown on supports functionalized with chitlac/alginate (although not statistically significant when comparing with chitosan and chitlac). The highest values observed in the case of the support coated with chitlac/alginate are probably

due to the larger amount of chitlac deposition in the presence of alginate, which probably contributes to an increased biological activity.

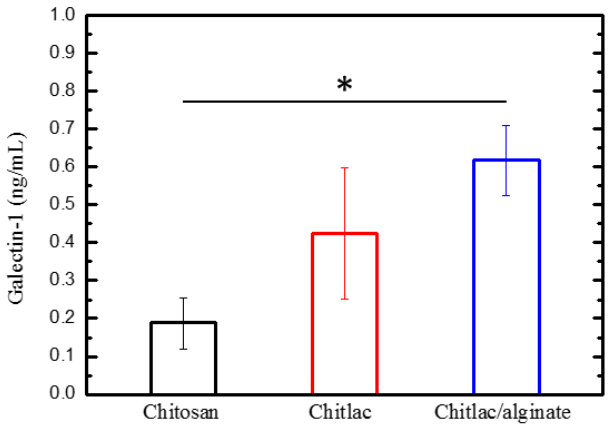

Figure 31. Galectin-1 quantification. Plot showing the significantly increased galectin-1 levels secreted by neurons belonging to the chitlac/alginate condition (number of supernatant samples analysed, n = 4, *: P<0.05)

The immunofluorescence staining (Figure 32) seems to confirm (preliminary results) the increased expression of galectin-1 in neurons grown on chitlac/alginate surfaces, which show several spots indicating the presence of galectin-1 molecules.

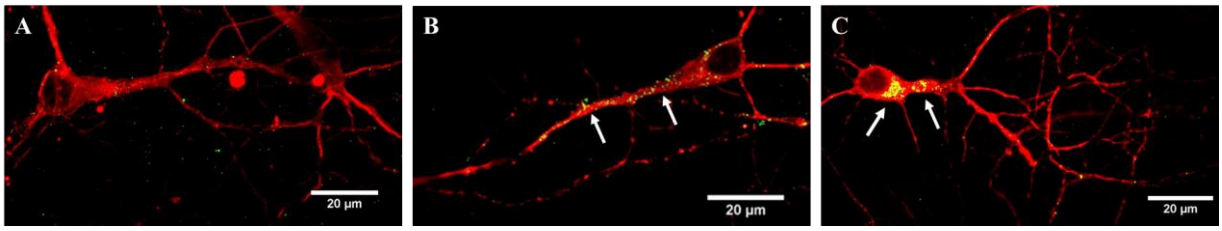

Figure 32. Immunofluorescence staining of neurons grown on chitosan (**A**), chitlac (**B**) and chitlac/alginate (**C**), showing the presence of galectin-1; red: βtub III, green: galectin-1. The arrows indicate the galecin-1 spots.

More in details, the analysis of the fluorescence intensity of the galectin-1 spots (calculated applying a threshold to the signal) shows that the intensity of the galectin-1 signals is higher on chitlac and chitlac alginate substrates (Figure 33).

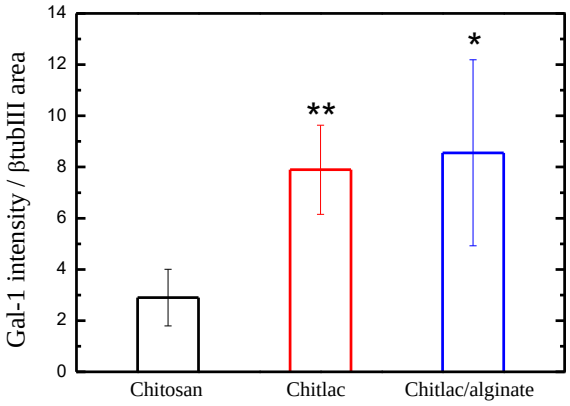

Figure 33. Galectin-1 fluorescence intensity spots normalized for the βtub III positive area. (number of images analysed, n = 4, *: P<0.05; **: P<0.01)

The involvement of galecin-1 in the nerve tissue regeneration processes is very complex: it regulates the embryonic development of nerve tissue; it can be secreted by growing axons and reactive Schwann cells, and trigger different responses depending on its red ox state: in the oxidized form galectin-1 stimulates the macrophages secretion of axonal regeneration promoting factors, while in the reduced form it induces astrocyte differentiation and enhanced their producton of BDNF, which plays an important role in the survival, differentiation, and synaptic plasticity of neurons.[296-298]

In this context, galectin-1 may thus be considered as a means for the prevention of neuronal loss in cases of injury to the CNS (Central Nervous System).[296] In this framework, the results of this work are particularly interesting, linking substrate interactions and galactin-1 expression with synaptic network reconstruction and activity, but further work is required in order to clarify the molecular mechanism that lies behind the galectin-1 involvement, and the possible involvement of other isoforms of this protein.

Effect of mesoangioblasts releasing neurotrophines on motoneuron progenitors differentiation

As previously anticipated, the strategy for the design of a spinal cord implant tackled in this work is based on the incorporation of engineered MABs secreting NTs, for a controlled and continuous release of NGF (Nerve Growth Factor) and BDNF (Brain Derived Neurotrophic Factor), whose

trophic effects have been tested in vitro on cultured neuronal cells and brain slices.[123] These MABs, due to their intrinsic high adhesin-dependent migratory capacity, can reach perivascular targets especially in damaged areas,[299] and thus could represent a suitable tool for spinal injury treatment based on cell replacement strategy. Both NGF and BDNF are important secretory proteins, regulators of survival, differentiation, and maintenance of nerve cells playing a pivotal role in neurodevelopment and neuroprotection. BDNF in particular supports the survival of existing neurons and encourages the growth and differentiation of new neurons and synapses through axonal and dendritic sprouting. In addition, several reports suggested a role for BDNF and NGF in the modulation of synaptic transmission.[300,301]

In order to determine the effects of both polysaccharides and neurotrophine expressing MABs, motoneuron progenitors (D7) have been co-cultured with MABs (here referred as D16), BDNF-expressing MABs (here referred as A9) or NGF-expressing MABs (here referred as F10), on the three different substrates. Control and NTs producing-MABs were able to efficiently grow on chitosan, chitlac and chitlac/alginate in a similar manner. When co-cultured with the three types of MABs on the different substrates and let differentiate, D7 progenitors gave rise to both neurons and astrocytes (data not shown). The percentage of choline acetyltransferase (ChAT) positive cells has been measured in order to determine the percentage of differentiated motoneurons, the results, showed in Figure 34, indicate more ChAT positive motoneurons when D7 progenitors are differentiated on chitlac/alginate.

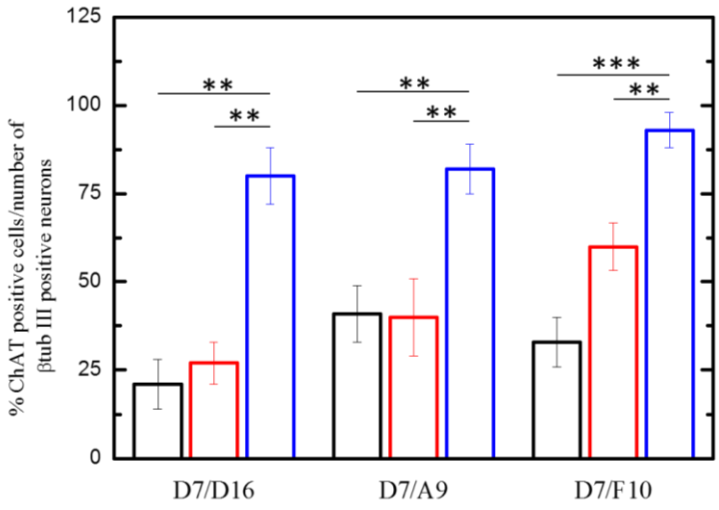

Figure 34. Percentage of D7 differentiation in the presence of MABs and NTs secreting MABs, in the three different conditions (chitosan, black; chitlac, red; chitlac/alginate, blue) (*: P<0.05; **: P<0.01; ***: P<0.001).

Effect of MABs releasing NTs on hippocampal network

Based on the previous results, the chitlac/alginate substrates (best performing in terms of network synaptic activities) have been chosen for an additional set of electrophysiological experiments in order to determine the effects of NTs secreting MABs on the neuronal activity of dissociated hippocampal cells. Figure 35 shows the passive membrane properties determined by electrophysiological recordings: these displayed a trend going from control to the D16 to F10 to A9 MABs co-cultures, reaching a statistical difference between the two extremities. Overall, the data indicate the good viability and activity of neurons and that the presence of MABs does not negatively affect health status and size of neurons.

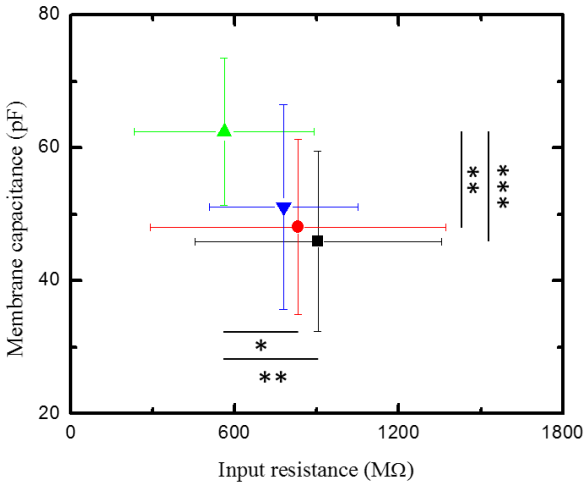

Figure 35. Plot showing membrane passive properties for neurons cultured alone (Ctrl, ■, n=18) and co-cultured with MABs D16 (●, n=29), A9 (▲, n=26) and F10 (▼, n=25). (*: P<0.05; **: P<0.01; ***: P<0.001).

The morphological analysis showed that neurons grew readily in all the four conditions and cell density counting analysis showed an almost identical neuronal density (data not shown). On the other hand, βtub III positive area was significantly higher in neurons grown together with all types of MABs compared to hippocampal neurons alone (Figure 36).

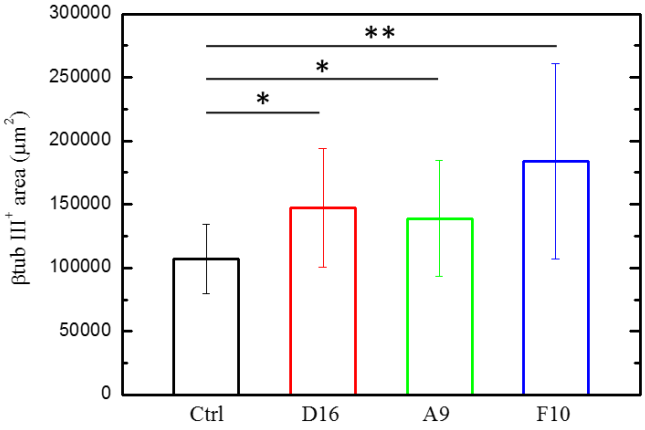

Figure 36. βtub III positive area (μm^2) of neurons alone (Ctrl) and co-cultured with D16, A9 and F10 MABs. (*: P<0.05; **: P<0.01; ***: P<0.001).

Regarding heterogeneous PSCs (Figure 37), both PSCs frequency and peak amplitude were further boosted by the presence of the NTs, while the peak amplitude was also increased when primary neurons were co-cultures with control MABs, meaning that MABs per se were able to interfere with the neuronal network formation. Taking together, the improvement in the synaptic activity driven by the chitlac/alginate substrate can be further implemented by the additional inclusion of NTs like BDNF and NGF.

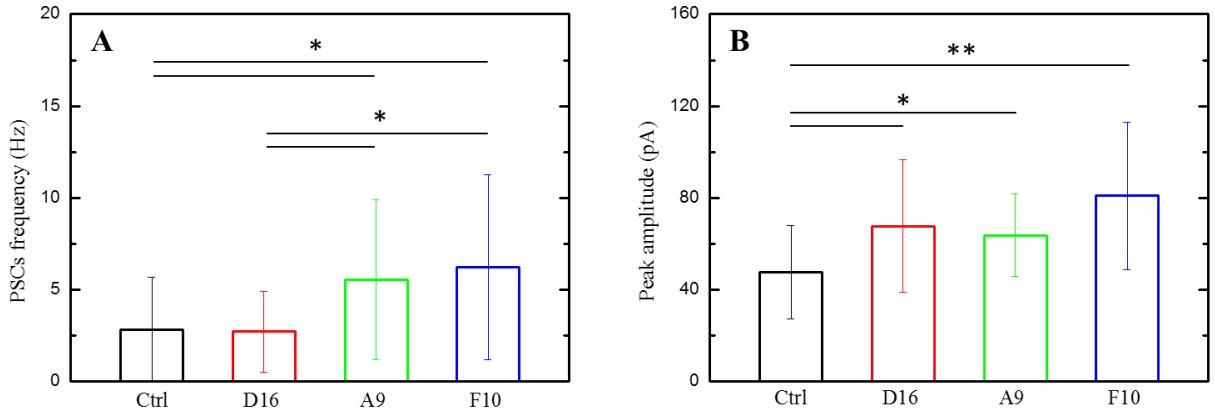

Figure 37. PSCs frequency (**A**) and PSCs amplitude (**B**) plots of voltage-clamped hippocampal neurons cultured in the four different conditions. (Ctrl, black, n=14; D16, red, n=20; A9, green, n=16; F10, blue, n=17).

From the results, it can be concluded that chitlac can exert a positive effect on the adhesion, the growth and the function of the cells analyzed. This key aspect of the work can be related to the chemical nature and differences between chitlac and chitosan, which lead to differences in the surface energies. It is widely accepted that neurons and cells in general, are able to sense the features of the growth substrate and actively respond to it.[302] Moreover, the findings of this work, are in line with previous reports by Lamour *et al.*[292] who recently pointed out how the arrangement of polar and apolar groups at the nanoscale level is a key factor in generating the surface energy gradients that PC12 cells are able to sense, thus suggesting that surface free-energy gradients are critical for biological processes such as nerve regeneration on biomaterials.

3.2.2 TRIDIMENSIONAL STRUCTURES FOR NEURAL TISSUE ENGINEERING

Driven by the positive biological results obtained with neurons and the combination of alginate and chitlac, which indicate that these polysaccharides are good candidates to be employed in the

bridging implant strategy, the work here described has proceeded with the development of alginate tridimensional scaffolds enriched with chitlac.

The general approach was to exploit the freeze-casting of alginate hydrogels, reticulated with calcium ions, in different conditions to prepare porous scaffolds with different pore morphology. In order to obtain a homogeneous gelation, an insoluble form of Ca^{2+} ($CaCO_3$) was dispersed within the alginate solution, and the calcium release was induced by the acidification of the medium triggered by the slow hydrolysis of δ-glucono lactone (GDL). The scaffolds obtained have been functionalized with chitlac by means of physical adsorption. Both isotropic and anisotropic porous scaffolds have been prepared and characterized in terms of material properties.

3.2.2.1 Preparation and characterization of alginate/chitlac scaffolds

Scaffolds with anisotropic pores were prepared by the Ice Segregation Induced Self Assembly (ISISA) process. This technique, based on the immersion of the hydrogel in liquid nitrogen at controlled speed, enabled to tailor the dimensions and the porosity of the structures by tuning the dimensions of the mold and the immersion speed in the liquid nitrogen bath.[110] The alginate hydrogels (contained in syringes) were frozen by the ISISA process to enable the formation of columnar ice crystals which, after freeze-drying (in vacuum conditions), left room for aligned anisotropic pores (Figure 38).

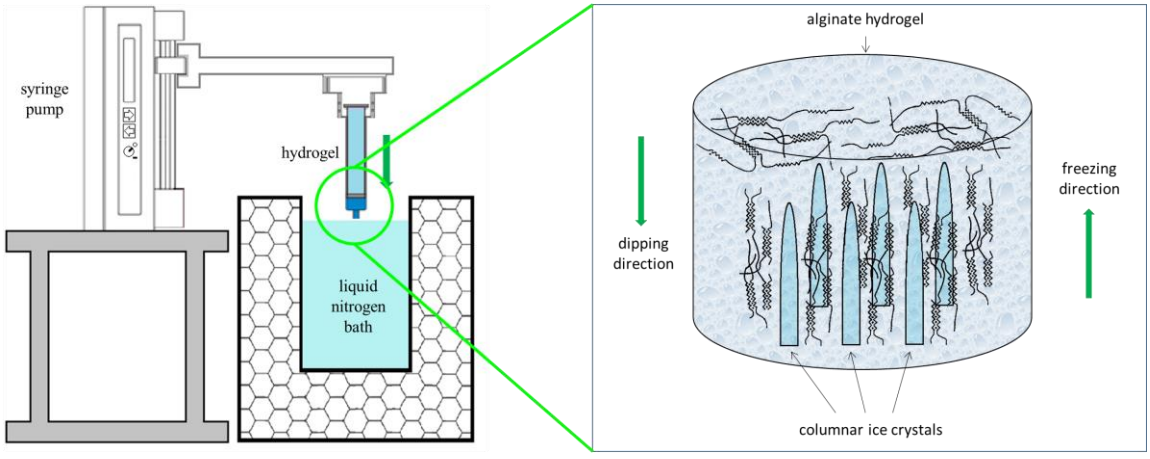

Figure 38. Left: schematic representation of the ISISA method in which a syringe containing alginate hydrogels is immersed at controlled speed in a liquid nitrogen bath. Right: formation of columnar ice crystals within alginate hydrogels.

The influence of the syringe diameter and of the immersion speed on the final porous structure was preliminarily assessed: the optimal conditions in terms of structural homogeneity were obtained with syringes of 13 mm diameter at a dipping speed of 8 mm/min. The characterization of the scaffolds obtained with the ISISA process (ISISAsc) was carried out as a direct comparison with scaffolds with the same formulation but with isotropic pores (here referred to as CRyo-Prepared IsOtropic scaffolds, CRIOsc); the manufacturing of CRIOsc was previously described[147,155] and is based on freezing the hydrogels at slow rate in a cryostat with a controlled temperature ramp. These procedures enabled to obtain freeze-dried scaffolds that can easily be cut and shaped with a scalpel, especially in the rehydrated form. Figure 39 reports the macroscopic images of the starting hydrogel and of the CRIOsc and ISISAsc obtained from it.

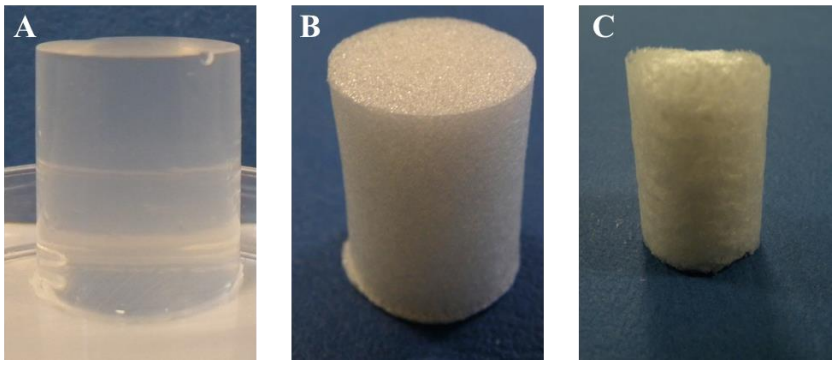

Figure 39. Images of the alginate hydrogel (**A**; h = 18 mm, ø = 16 mm) and the resulting structures obtained with the CRIO (**B**; h = 18 mm, ø = 16 mm) and the ISISA (**C**; h = 18 mm, ø = 11 mm) processes.

Morphological and physical-chemical characterization

The images point out the macroscopic homogeneity of the scaffolds obtained with the two different techniques. A deeper insight into the porous structure of the scaffolds was obtained by Scanning Electron Microscopy (SEM) imaging; Figure 40 reports the comparison between the two microstructures.

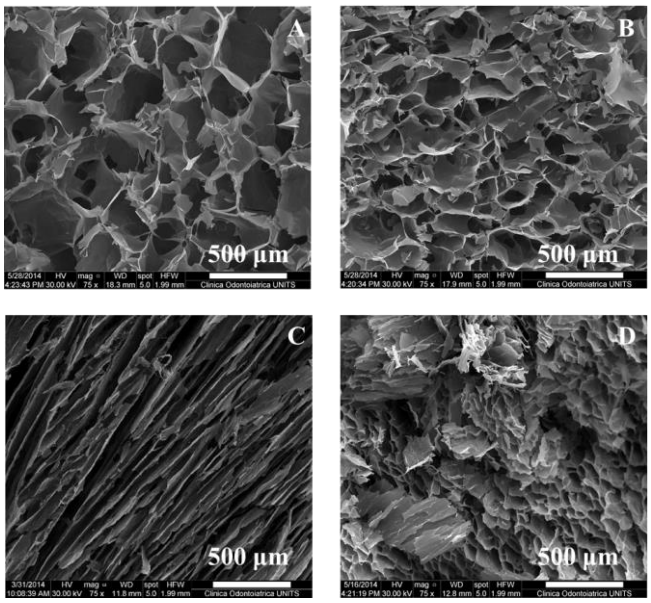

Figure 40. SEM micrographs of alginate scaffolds obtained with the CRIO process (**A**, longitudinal; **B**, cross sections) and with the ISISA process (**C**, longitudinal; **D**, cross sections).

SEM images point out the anisotropic porous structure of the ISISAsc, which display aligned columnar pores, at variance with the isotropic porosity of the CRIOsc; these columnar pores create large domains of aligned channels.

The processes here adopted for the preparation of tridimensional scaffolds from alginate hydrogels enable to achieve isotropic (CRIOsc) or anisotropic (ISISAsc) structures, in line with the results of several authors with materials of similar[94,147,155] or different nature.[107,152] In particular the ISISAsc, compared with other anisotropic structures reported in the literature,[105,152] showed a narrow distribution of pore dimensions and a pore morphology with a high degree of homogeneity.

For a quantitative analysis of the porous structures of ISISAsc and CRIOsc, micro-Computed Tomography (μ-CT) analyses were performed. The analysis of the μ-CT data was carried out according to a procedure previously described,[147] which made it possible to obtain quantitative data on the solid fraction (BV/TV: Solid Volume/Total Volume), on the thickness of the alginate structures delimitating the pores (Tb.Th.: Trabecular Thickness) and on the average dimension of the pores (Tb.Sp.: Trabecular Spacing). It was also possible to quantify both the interconnectivity

of the structures (expressed as Trabecular Number "Tb.N."[303,304] and their Degree of Anisotropy (DA). These latter parameters have been calculated by Equation (4) and (5):

$$Tb.N = \frac{1}{Tb.Th. + Tb.Sp.} \quad (4)$$

$$DA = 1 - \frac{short\ axis}{long\ axis} \quad (5)$$

The degree of anisotropy DA equals 0 for a perfectly isotropic structure and 1 for a perfectly anisotropic structure.

The reconstruction of the tridimensional structures shown in Figure 41 points out the different structure of scaffolds obtained with the two techniques.

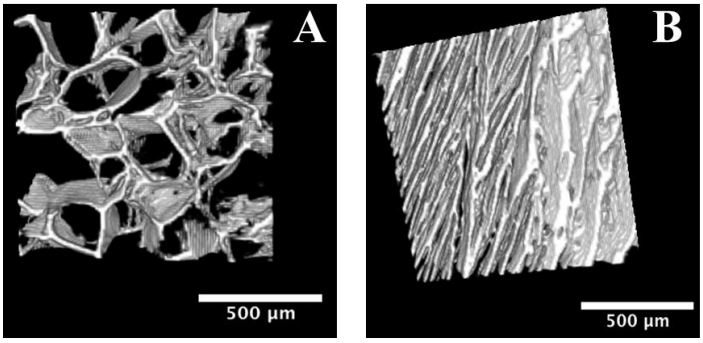

Figure 41. 3D reconstruction form μ-CT analysis of CRIOsc (**A**), and of ISISAsc (**B**).

Table 11 reports the quantitative analysis of the morphology of CRIOsc and ISISAsc; data show the differences in the morphology between the two types of scaffolds, being the DA of ISISAsc 1.7 times the DA of CRIOsc. Moreover, ISISAsc possess the proper porosity and pore size (Tb.Sp) to be used for neural tissue engineering applications.[94,99,100]

Table 11. Quantitative characterization of the microstructure of the alginate scaffolds. BV/TV: bone volume/total volume; Tb.Th.: trabecular thickness; Tb.Sp.: trabecular spacing; Tb.N: trabecular number; DA: degree of anisotropy.

Scaffold	*BV/TV*	*Porosity (%)*	*Tb.Th. (μm)*[a)]	*Tb.Sp. (μm)*[a)]	*Tb.N (mm^{-1})*	*DA*
CRIOsc	0.19 ± 0.04	81 ± 4	32.55 ± 0.19	178.12 ± 14.01	5.00 ± 2.35	0.52 ± 0.05
ISISAsc	0.40 ± 0.02	60 ± 2	31.71 ± 1.18	46.08 ± 18.10	12.86 ± 4.43	0.93 ± 0.02

[a)]In Tb.Th and Tb.Sp, linear dimensions are given ± std. dev. (6 experiments). Linear resolution is 8 μm.

Following a protocol already used for alginate scaffolds,[155] CRIOsc and ISISAsc have been incubated with chitlac solution in order to adsorb the chitlac on their surface. Figure 42A shows the adsorption kinetic of fluorescein labelled chitlac within the scaffolds, determined by fluorimetric measurements; Figure 42B shows the complete coating of both scaffolds structures and the deep permeation of the structure.

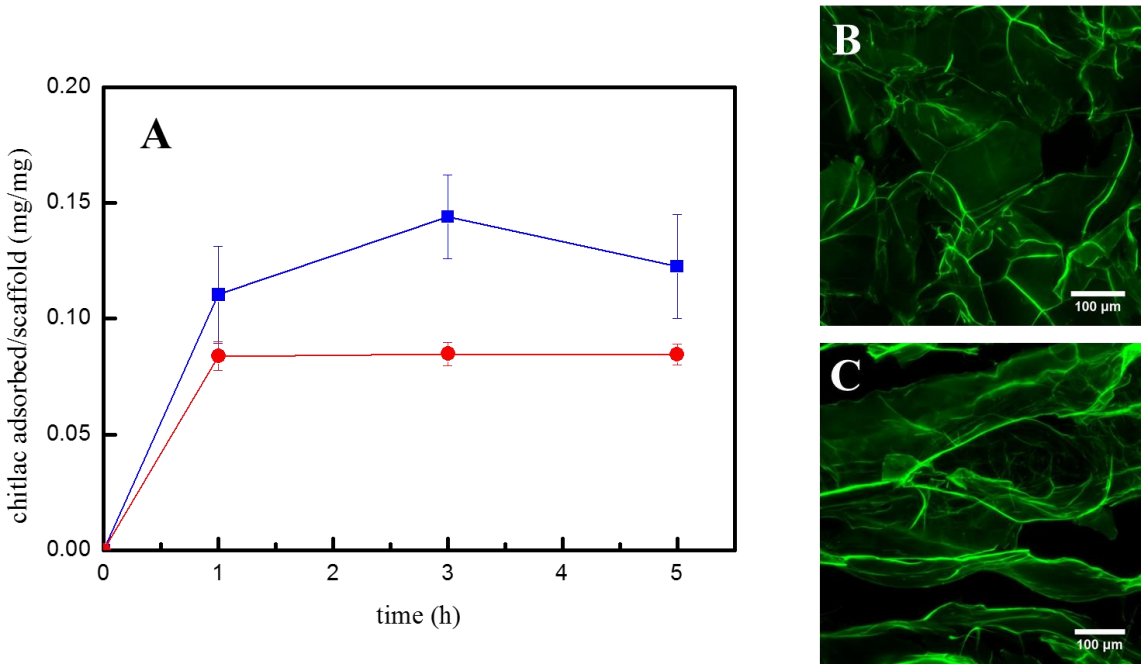

Figure 42. **A**) Adsorption kinetic of chitlac on alginate CRIOsc (■) and ISISAsc (●). 3D reconstruction of chitlac coated CRIOsc (**B**) and ISISAsc (**C**) from CLSM imaging.

The wettability and the initial swelling of the structures are important features influencing cell adhesion and colonization inside the structure. A biodegradable scaffold should favor cell adhesion

and proliferation while being gradually degraded at a rate which is synchronous with tissue regeneration; moreover, upon contact with body fluids, it should be able to withstand the initial swelling without exerting excessive compression towards the surrounding tissue, thus maintaining its original shape.[147,305] In order to characterize the swelling and degradation behavior, the scaffolds were incubated in simulated body fluid and these parameters were monitored as a function of time.

The time-dependent swelling behavior of the scaffolds in Simulated Body Fluid (SBF) is reported in Figure 43A. An initial rapid liquid uptake was observed in the first 10 minutes (up to ~3000% of swelling ratio); then the swelling remains almost constant. Despite the massive uptake of liquids, a small volume variation of the structures occurs (+ 1.9 ± 0.2 %). The considerable swelling of the scaffolds pointed out the high interconnectivity of the pores. The water uptake and the trend of swelling were found to be similar to the rates of swelling reported in the literature for tridimensional structures with isotropic[147,306] or anisotropic porosity.[107] As the swelling rate can be related to the hydrophilicity of the material,[305] these scaffolds can be considered as highly hydrophilic scaffolds. Moreover, these materials are able to absorb a large amount of fluids without losing their structural integrity, an important property that is known to affect the exchange of fluids, nutrients and catabolic products.[307,308]

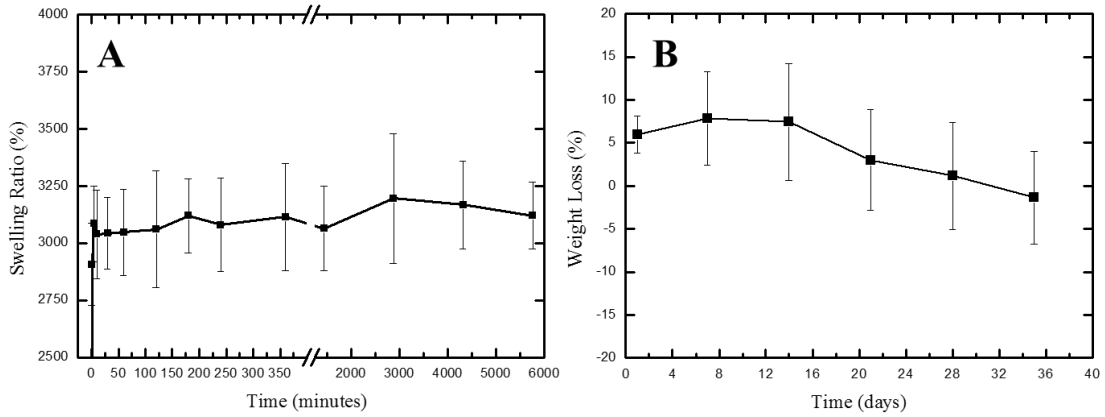

Figure 43. Weight variation of the ISISAsc during the swelling (**A**) and the degradation experiment (**B**). Data are averaged on three parallel runs.

Scaffolds proved also to be very stable in SBF (incubated at 37°C) during 35 days (Figure 43B), showing a weight decrease of only 1.36 %. Overall, these studies pointed out that the scaffolds swell instantaneously to a large extent and display a slow rate of degradation (*in vitro*) within the

first month of immersion in SBF; this behavior is particularly advantageous for neural tissue engineering applications, being the healing rate of neural tissue very low.

The stability of the scaffolds has been analyzed also in terms of release of the adsorbed chitlac in saline solution (NaCl 0.15 M). The graph reported in Figure 44 shows that the amount released from the scaffolds is very low over time and reaches rapidly a plateau, proving that the structures are able to retain chitlac within the polymer matrix.

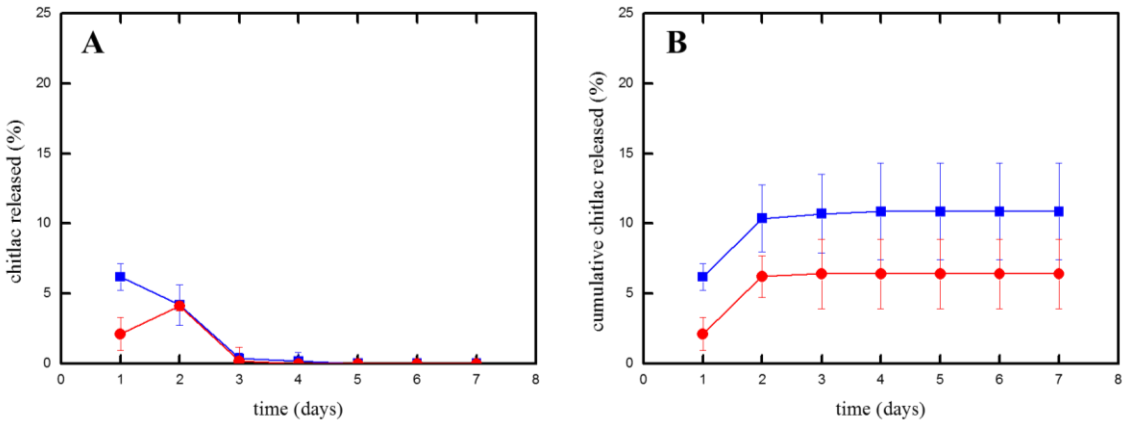

Figure 44. Chitlac-fluo release from CRIOsc (■) and ISISAsc (●) in saline solution expressed as percentage of the total chitlac-fluo contained: (**A**) release at given solution shift; (**B**) cumulative release. Data were averaged on three independent experiments

An important issue related to the use of calcium alginate hydrogel-derived scaffolds is the release of calcium ions in the extracellular environment and its possible toxicity.[31] The release of calcium ions from ISISAsc has been evaluated by soaking them in saline and measuring the calcium concentration with Induced Coupled Plasma – Optical Emission Spectroscopy (ICP-OES). The results are reported in the graphs of Figure 45. It can be noticed an initial burst of calcium release (approximately the 35 % of the total calcium content); after the first two saline changes, the calcium release reaches a plateau of low values. Thus, being the calcium release almost limited to the first two saline changes, curing the scaffolds in physiological medium could remove the excess of calcium without affecting the scaffold stability.

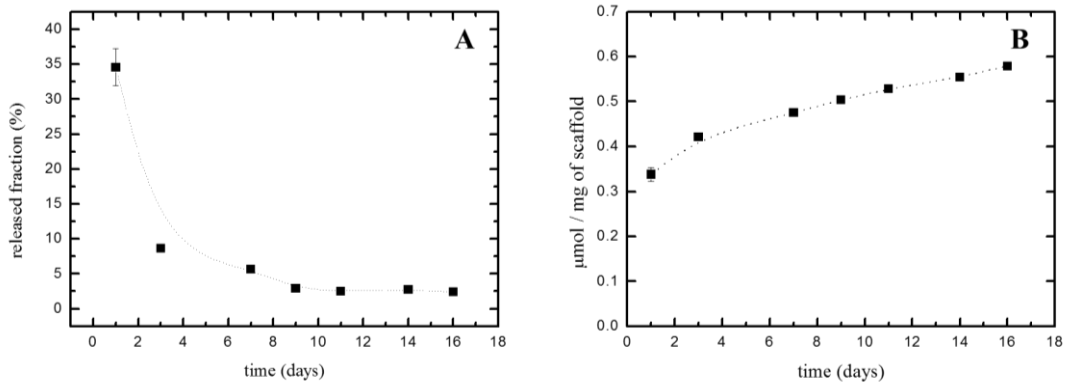

Figure 45. Release of calcium ions from ISISAsc reported as fraction released over the total calcium content (**A**) and as µmol of calcium per mg of scaffolds (**B**).

Scaffolds mechanical properties

In order to be suitable for neural tissue engineering (and in general for all the applications of tissue engineering) tridimensional scaffolds have to possess specific mechanical properties. In particular, in the case of neural tissue engineering, the scaffolds have to be soft enough to avoid mechanical stress to the tissue, without being too much weak. ISISAsc containing chitlac have been analyzed by means of uniaxial compression tests in order to determine their compression modulus. Figure 46 reports a representative stress/strain curve obtained from the mechanical analysis.

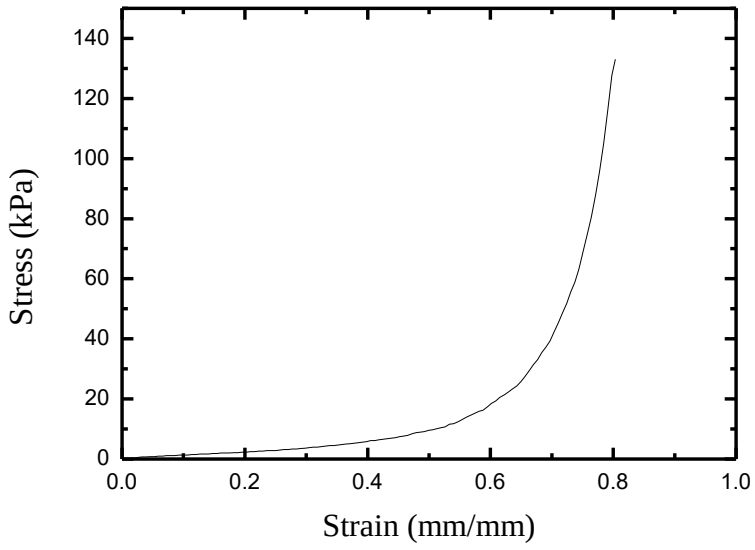

Figure 46. Representative stress/strain curve of ISISAsc analyzed by uniaxial compression tests.

Analyzing the data from the mechanical tests in the linear range of deformation, it was possible to calculate the compression modulus, which was found to be 14 kPa (± 1 kPa). The compression modulus for nerve tissue has been reported to be between 3 and 300 kPa,[6] in particular, Francis *et al.*[94] reported a compression modulus of 5 kPa for scaffolds to be employed in spinal cord tissue regeneration.

Altogether, data obtained from the morphological, physical-chemical and mechanical characterization indicate that the chitlac containing ISISAsc can be used for the development of a bridging implant strategy for spinal cord tissue regeneration.

3.2.3 CONCLUSIONS

Polysaccharide coated glass substrates have been prepared in order to analyze the biological effects of alginate, chitosan and chitlac on neural cell cultures. An effective strategy based on charge interactions was employed to prepare these polysaccharide-based coatings, whose thickness can be modulated by increasing the number of polysaccharide layers. The analysis of contact angles and of surface energies showed that the presence of the lactose branches on the chitosan backbone caused a considerable increase of surface hydrophilicity, polarity and acid-base work of adhesion.

Immunofluorescence and electrophysiological investigations showed that hippocampal derived neural cells were able to growth on all the substrates, but only on chitlac and chitlac/alginate substrates it was possible to observe the formation of a wide and interconnected neural network with a good electrophysiological activity. ELISA and immunofluorescence analyses of galectin-1 suggested that this protein is more expressed when neurons are grown on chitlac/alginate and chitlac substrates and that it has a possible biological role in the observed effects. Additional experimental evidence will be necessary to clarify whether the enhanced proliferation of neurons on chitlac-based substrates can be ascribed solely to the combined effect of the more hydrophilic and polar layer or also the biological activity of the polysaccharide.

In a similar way, chitlac/alginate substrates proved to be the best substrate for the differentiation of motoneuron progenitors in the presence of wild type and engineered MABs secreting NTs. The combination of NTs secreting MABs and the chitlac/alginate substrates has been tested for the culture of neuronal cells: the electrophysiological results showed that there is an improvement of

the neural activity when the neurons cultured on chitlac/alginate substrates are in the presence of NTs secreting MABs and that the development of alginate/chitlac scaffolds enriched with engineered MABs could be a good strategy for the preparation of a bridging implant for the spinal cord injury treatment.

Alginate/chitlac scaffolds have been prepared by embedding tridimensional alginate porous structures with chitlac. The porosity of the alginate structures has been tailored by using two different freezing methods, in order to obtain isotropic (spherical) and anisotropic (aligned) pores. The confocal microscopy imaging showed that the structures are completely embedded with chitlac. The swelling and stability behaviors as well as the mechanical properties of these constructs make them particularly appealing for neural tissue engineering applications.

3.3 DEVELOPMENT OF FILLERS FOR THE HEALING OF NON-CRITICAL BONE DEFECTS

The strategy tackled for the development of bone fillers has been focused on two different forms of materials, both based on polysaccharides (structural and bioactive components) and hydroxyapatite (HAp, osteoconductive component). The first form is represented by tridimensional porous structures, whose pore morphology has been tailored and studied with respect to the material properties. The second form is represented by injectable microparticles dispersed in polysaccharide mixtures.

3.3.1 TRIDIMENSINALS SCAFFOLDS: EVALUATION OF PORE MORPHOLOGY EFFECTS AND ENRICHMENT WITH FUNCTIONALIZED CARBON NANOTUBES

The scaffolds characterized in this work are designed to be employed in the filling and healing of non-critical bone defects. The first part of the work has been focused on the physical, mechanical and biological effects of different pore morphologies of the scaffolds, prepared applying the ISISA or the CRIO processes; the second part describes the biological characterization of differently functionalized carbon nanotubes and their use for the implementation of the scaffolds.

3.3.1.1 Characterization of scaffolds with different pore morphology

In order to prepare the bone scaffolds with different pore morphology, the methods previously described for the preparation of scaffolds for neural tissue engineering have been applied to alginate/HAp hydrogels. In fact, to improve both biological and mechanical properties of the scaffolds, HAp was employed for the preparation of the composite hydrogels.[147] The concentration of HAp needed to be optimized to avoid interference with the gelation and the freezing of the hydrogels; previous data showed that CRIOsc can be prepared with up to 3% w/V HAp without affecting the gelation process and the morphology of the porous structure.[147] In the present work, the ISISAsc were prepared with various concentrations of HAp and the resulting structures were evaluated; when HAp concentrations higher than 0.5% w/V where used, the homogeneity of the scaffold was negatively affected (data not shown). In contrast, with HAp 0.5% w/V the porous structure was not affected and therefore this initial concentration was selected.

Morphological and physical-chemical characterization

In order to compare the morphology of the constructs obtained with the two different techniques under the same conditions, both CRIOsc and ISISAsc were prepared with an initial concentration of solid HAp equal to 0.5% w/V, which, after dilution upon addition of GDL solution, reduces to 0.35% w/V. The final concentration of HAp lies into the range normally used for such kind of application and is considered sufficient to induce a biological effect.[107,309,310]

Figure 47 shows the SEM images of the two types of scaffolds containing HAp. The images show that, compared to the alginate-$CaCO_3$ scaffolds of Figure 40, the addition of HAp does not significantly affect the porous morphology of both scaffold.

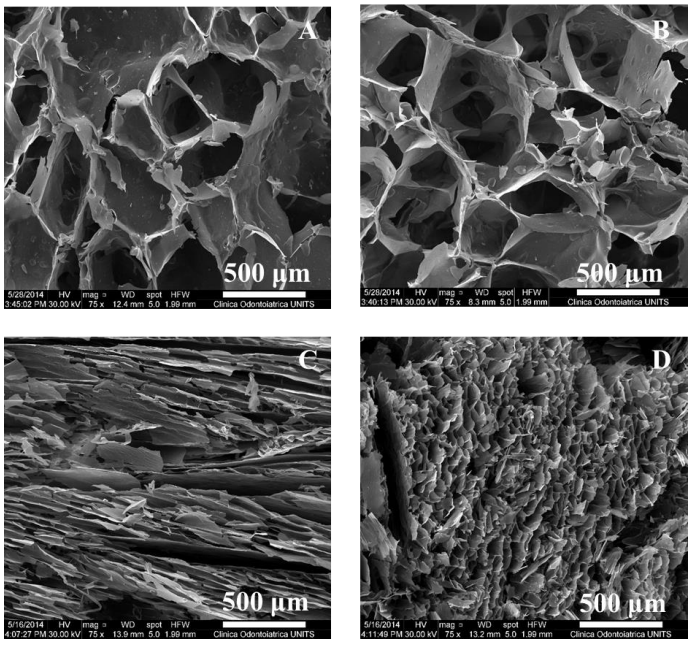

Figure 47. SEM micrographs of scaffolds with HAp obtained with the CRIO process (**A**, longitudinal; **B**, cross sections) and with the ISISA process (**C**, longitudinal; **D**, cross sections).

CRIOsc and ISISAsc have been analyzed by means of μ-CT in order to investigate their morphology and the differences with the scaffolds prepared with $CaCO_3$. The reconstruction of the tridimensional structures shown in Figure 48 points out the different structure of scaffolds obtained with the two techniques; moreover, it shows that the addition of HAp had a minor influence on the morphology of the structures.

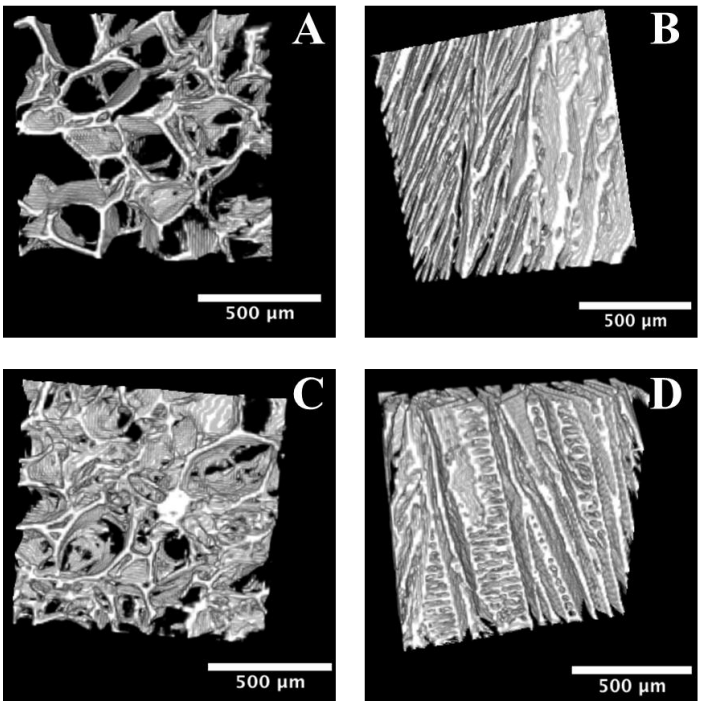

Figure 48. 3D reconstruction form μ-CT analysis of CRIOsc without HAp (**A**) or with HAp (**B**), and of ISISAsc without HAp (**C**) or with HAp (**D**).

Table 12 reports the quantitative analysis of the morphology of CRIOsc and ISISAsc. The use of HAp had a minor influence on the tridimensional properties of the scaffolds: in particular, the pore dimension and the porosity of both structures were not affected ($p > 0.05$) and the degree of anisotropy of the CRIOsc decreased by 27% ($p < 0.05$). The pore interconnectivity did not change significantly for the CRIOsc ($p > 0.05$) and it slightly decreased for the ISISAsc (-22%, $p < 0.01$).

Table 12. Quantitative characterization of the microstructure of the alginate scaffolds. BV/TV: bone volume/total volume; Tb.Th.: trabecular thickness; Tb.Sp.: trabecular spacing; Tb.N: trabecular number; DA: degree of anisotropy.

Scaffold	*BV/TV*	*Porosity (%)*	*Tb.Th. (μm)*[a)]	*Tb.Sp. (μm)*[a)]	*Tb.N (mm^{-1})*	*DA*
CRIOsc $CaCO_3$	0.19 ± 0.04	81 ± 4	32.55 ± 0.19	178.12 ± 14.01	5.00 ± 2.35	0.52 ± 0.05
CRIOsc HAp	0.20 ± 0.03	80 ± 3	33.82 ± 1.83	183.96 ± 15.22	4.61 ± 2.26	0.38 ± 0.03
ISISAsc $CaCO_3$	0.40 ± 0.02	60 ± 2	31.71 ± 1.18	46.08 ± 18.10	12.86 ± 4.43	0.93 ± 0.02
ISISAsc HAp	0.34 ± 0.04	66 ± 4	32.41 ± 0.78	67.85 ± 10.73	10.08 ± 5.07	0.90 ± 0.03

[a)]In Tb.Th and Tb.Sp, linear dimensions are given ± std. dev. (6 experiments). Linear resolution is 8 μm.

From the data obtained by SEM and μ-CT, it is possible to conclude that the structures match the requirements for osteoconductivity and bone tissue regeneration. Indeed, they present a high porosity, the values of which are similar to those claimed as good for bone scaffolds and fillers.[107,152,311,312] Moreover the interconnectivity of the pores, determined as the Tb.N. value, is very high and similar to that of osteoconductive scaffolds recently described.[147,155]

Swelling and degradation behaviors of both scaffolds have been evaluated in simulated body fluid. The possibility that HAp precipitates on the scaffold from the SBF solution was taken into account. Cursory X-ray Photoelectron Spectroscopy (XPS) experiments revealed traces of HAp on scaffolds made of alginate without HAp (data not reported). However, a conservative estimate of the theoretical maximum amount of HAp that could precipitate provides a very low value (about 1.4 mg), which becomes totally negligible if compared with the amount of adsorbed water (from 350 to 800 mg).

The time-dependent swelling behavior of the alginate/HAp scaffolds in SBF is reported in Figure 49A. The re-swelling behavior of the composite scaffolds did not significantly differ between CRIOsc and ISISAsc. An initial rapid liquid uptake was observed in the first 10 minutes (up to ~1900% of swelling ratio); then the swelling slightly increased up to ~2300% and ~2200% for the CRIOsc and the ISISAsc respectively. The lower swelling rate of the ISISAsc can be ascribed to the lower porosity of these scaffolds, in line with the results reported by Ghadiri *et al.*[306] Despite

the massive uptake of liquids, a small volume variation of the structures occurs only for the CRIOsc (+ 9%).

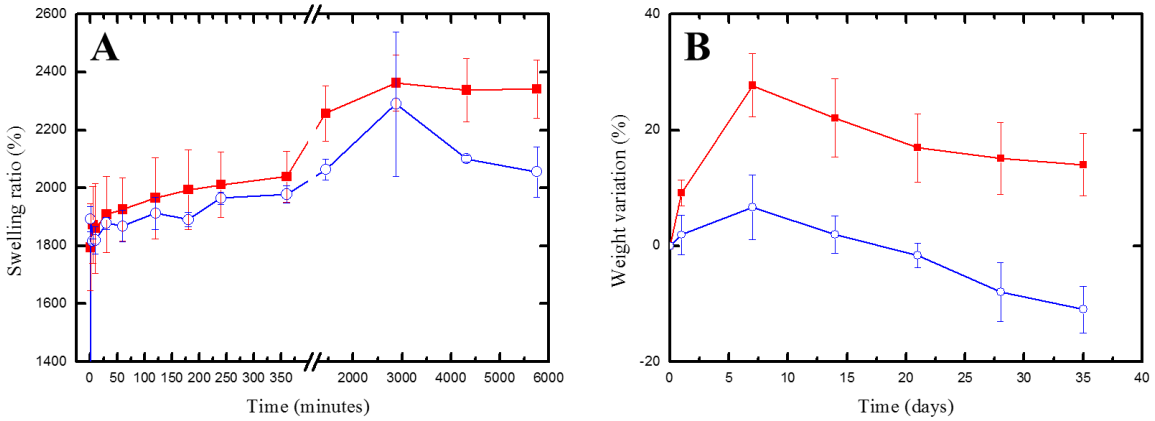

Figure 49. Weight variation of the CRIOsc (■) or the ISISAsc (○) during the swelling (a) and the degradation experiment (b). Data are averaged on three parallel runs.

Both scaffolds show good stability in SBF (incubated at 37°C) during 35 days (Figure 49B), showing no weight loss in the case of CRIOsc and a weight decrease of only 11% in the case of ISISAsc. In both cases, the degradation rate is lower than the one reported by Turco *et al.* with similar scaffolds:[147] this could be ascribed to the lower content of solid fraction (HAp) in both CRIOsc and ISISAsc, which hampers to a minor extent the reticulation of alginate.

Similarly to what has been observed for scaffolds containing $CaCO_3$, the swelling behavior of the HAp containing scaffolds is similar to that of scaffolds already discussed in literature[107,147] and indicates that these structures are highly hydrophilic; moreover, also in this case the scaffolds were able to maintain their structural integrity after the absorption of a large amount of fluids and proved to be very stable in simulated body fluid, showing important characteristics for the employment in the healing of bone defects.

Mechanical properties of the scaffolds

The scaffolds proposed in this work are meant to be used as temporary fillers to accelerate the repair of non-critical defects and small lesions of the bone tissue. Although these conditions are less demanding than those for load-bearing implants, it is nonetheless important to characterize the mechanical properties of the scaffolds, especially considering the implantation procedure, which

involves considerable compression forces during the surgical insertion. To this end, uniaxial compression tests in static and cyclic conditions on hydrogels and rehydrated scaffolds have been performed.

The results of Table 13 point to a marked improvement of the mechanical properties of the hydrogels in the presence of HAp: in particular, compression modulus, strength and toughness increased by 63%, 46% and 46% (respectively) with respect to $CaCO_3$ hydrogels, without affecting significantly the deformation at break of the hydrogels. The amount of calcium ions (responsible for the egg-box structure) in the $CaCO_3$ case (30 mM) is twice as large as in the case of HAp (15mM); therefore, the better mechanical properties shown in the case of HAp hydrogels must derive from the contribution of the dispersed solid and not from a larger number of gel junction structures. This finding is in full agreement with the results of Turco *et al.*[147] The undissolved fraction of HAp contributes to the mechanical strength of the hydrogel, while endowing the material with bioactive properties.

Table 13. Mechanical properties of hydrogels based con $CaCO_3$ or HAp, analyzed by means of uniaxial compression test.

Hydrogel	*E (kPa)*	*σ_{UCS} (kPa)*	*Toughness (kJ/m^3)*	*Deformation at break (%)*
$CaCO_3$	38.4 ± 6.3	177.9 ± 12.4	26.2 ± 1.8	52.6 ± 1.2
HAp	62.6 ± 3.2	260.5 ± 16.4	38.3 ± 2.7	53.0 ± 1.0

The freeze-dried scaffolds have been tested in the rehydrated state in order to simulate the stress conditions that the material undergoes after implantation in contact with body fluids.

It should be noticed that CRIOsc have an isotropic structure, which means that their mechanical properties are not dependent on the load direction; in contrast, ISISAsc have an anisotropic structure and the tests have been performed loading the samples along the main direction of pores.

Compression tests revealed that rehydrated CRIOsc possess higher modulus and toughness than rehydrated ISISAsc (Table 14).

Table 14. Mechanical properties of hydrogel based con $CaCO_3$ or HAp, analyzed by means of uniaxial compression test.

Rehydrated scaffold	*E (kPa)*	*Toughness (kJ/m^3)*
CRIOsc	155.5 ± 51.3	5.69 ± 0.38
ISISAsc	28.3 ± 9.1	2.63 ± 0.33

The inferior performance of the ISISAsc can be attributed to the sliding of the columnar trabeculae while applying compression forces (see Figure 47).

The mechanical properties of both types of scaffolds (in the wet state) are in line with those previously reported for biopolymer-based bone scaffolds.[147,313] Moreover, when rehydrated they display a "sponge-like" behavior and can be compressed up to 60% of their original dimensions without breaking the porous structure. It should be noticed that during the compression, absorbed water was observed to be released by both types of scaffolds and was eventually re-absorbed after the removal of the load.

Cyclic loading tests have been performed in order to investigate the response of the rehydrated scaffolds to cyclic loads. These tests were carried out by cyclically applying and removing a constant load to the rehydrated structures; upon removal of the load, scaffolds were able to reabsorb some of the water leaked during the compression and to partially recover their original shape (as sample height).

This peculiar behavior is shown in Figure 50. The load-displacement graphs (Figure 50A and B) show that at each compression the scaffolds displayed an initial elastic strain followed by a change of slope corresponding to the start of the water-release process; the graph highlights the considerable "shape-recovery" capability of the scaffold, which enabled the structure to re-expand at the end of each cycle when the load was removed. The recovery of the original shape is expressed in Figure 50C as the percentage of height regained after each cycle: as the number of cycles increased, the recovery progressively stabilized at about 85-88% of the initial scaffold height, which indicates that this mechanical feature was maintained during cyclic loads. The shape-

recovery ability of both scaffolds is comparable to that of scaffolds based on chitosan[314] and PCL[315] recently developed for bone tissue regeneration.

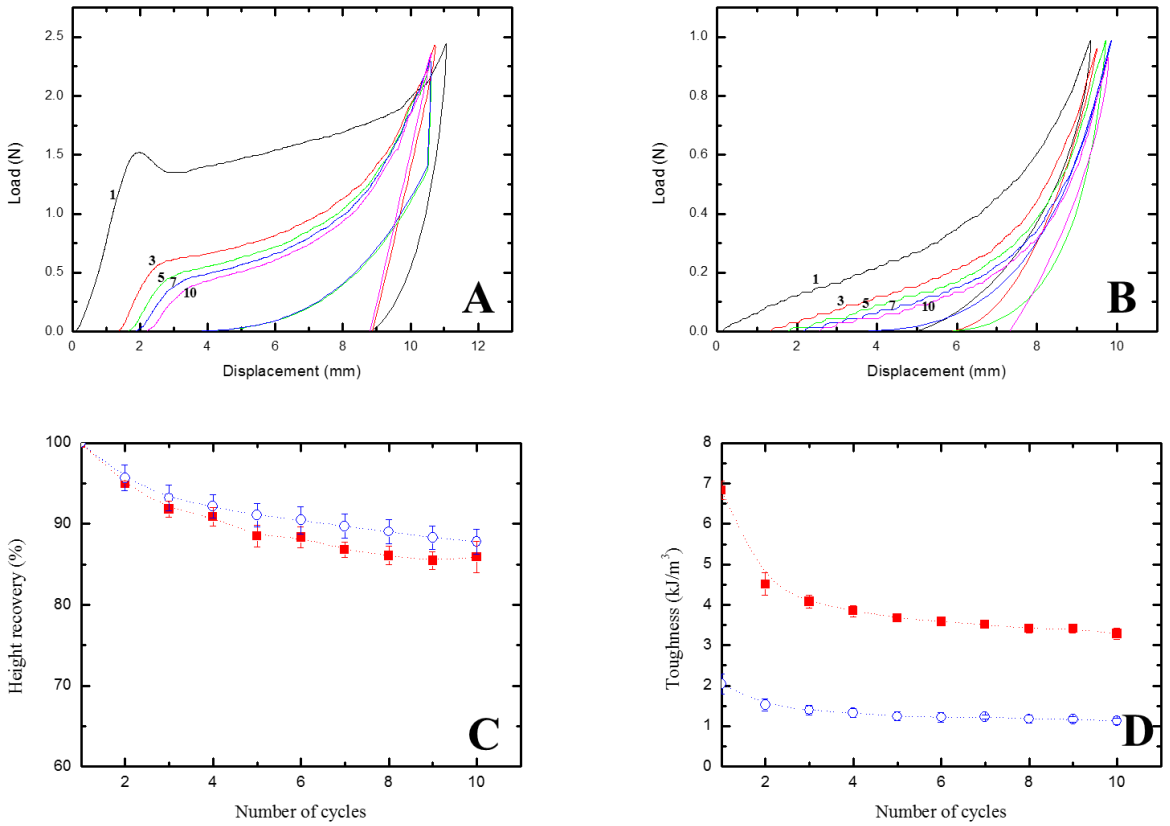

Figure 50. Load/displacement curve of the compression cycle performed in the cyclic loading test on CRIOsc (**A**) and ISISAsc (**B**). For clarity, only cycles 1, 3, 5, 7, 10 are reported. Variation of height recovered (**C**), toughness (**D**) of the CRIOsc (■) or the ISISAsc (○) during the cyclic loading test. Dotted lines have been drawn to guide the eye.

Besides highlighting the property of the material of displaying reversible deformations, the cyclic mechanical tests were also aimed at evaluating the variation of toughness (Figure 50D) of the scaffolds under repeated loads; after an initial decrease, in both cases the toughness values tend to stabilize around plateau values (~3.4 kJ/m^3 and ~1.2 kJ/m^3 for CRIOsc and ISISAsc respectively), in line with the shape-recovery trend.

Overall, the mechanical analysis indicates that, when rehydrated, both scaffolds behave as a "spongy" material that can be deformed to a large extent without breaking. They displayed a considerable recovery of the initial shape during cyclic loading, while toughness and stiffness

(modulus) of the material tended to reach progressively plateau values, higher for the CRIOsc than for the ISISAsc. This behavior can be particularly appealing for bone implants subjected to cyclic loadings (*e.g.* jawbone defects) and it matches the surgical need of cutting and shaping the scaffold before implantation to ensure a good fit within the defect cavity.[316,317]

Biological tests on scaffolds

The biocompatibility of the scaffolds depends on their ability to improve the adhesion and the proliferation of cells seeded onto the porous structures. In order to evaluate the effect of the pore arrangement and shape on these aspects, the viability, the osteocalcin expression and the alkaline phosphatase (ALP) activity of an osteoblast cell-line (MG63) seeded in the scaffolds have been studied.

The viability of cells was evaluated by means of a colorimetric assay (MTS) and the results are shown in Figure 51: for both scaffold types, the cells were viable and kept proliferating during the 3 weeks of test ($p < 0.01$ for day 21 compared to day 1). No significant difference in the proliferation rate was observed between the two different types of structures ($p > 0.05$).

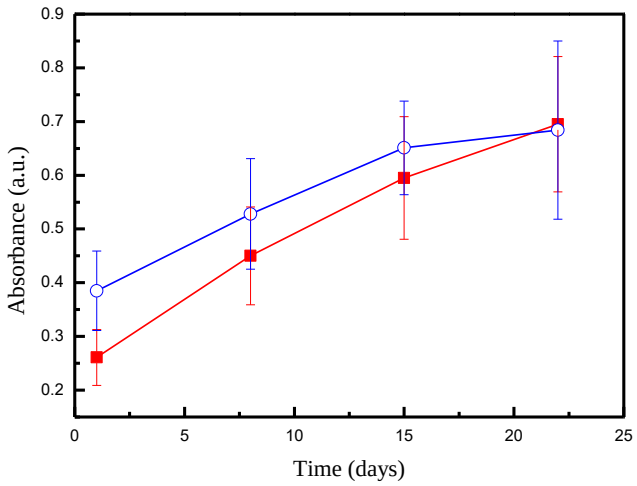

Figure 51. Proliferation rate of osteoblasts seeded on CRIOsc (■) and ISISAsc (○).

The osteocalcin expression and the ALP activity of the MG63 cells seeded inside the scaffold types were determined in order to evaluate a possible cellular differentiation. The analysis revealed that both parameters remained comparably low during the experiments and did not vary from day 1 to

day 21 regardless of the scaffold structure, which indicates that within this timeframe no differentiation processes occurred (data not shown).

The proliferation of the osteoblasts within the scaffolds was further investigated by carrying out SEM analysis on both types of structures (CRIOsc and ISISAsc). Figure 52 shows that, in both cases, the cells colonized the porous structures and were able to form clusters of numerous round-shaped osteoblasts which adhered to the scaffold walls, in agreement to what previously reported for osteoblasts on alginate based scaffolds.[306,308,318] The images point out the presence of extracellular matrix surrounding the clusters, which stresses the good cell viability and activity.

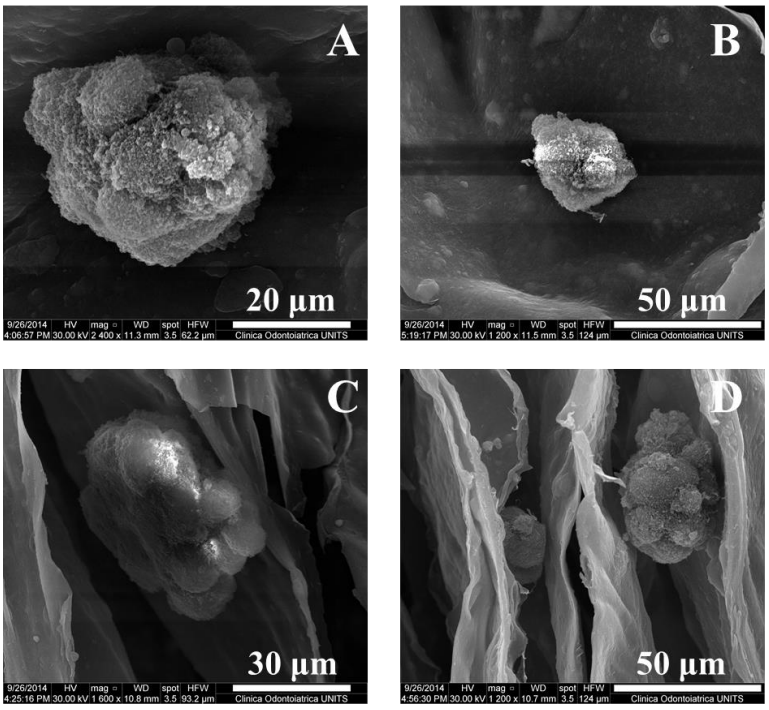

Figure 52. SEM micrographs of MG63 seeded on CRIOsc (**A**, **B**) and ISISAsc (**C**, **D**).

This investigation shows that, in the CRIOsc, the cell clusters were typically formed within the cavities of the isotropic pores, whereas in the ISISAsc the cell clusters adhered to the walls of the columnar pores, whose dimensions appear particularly suited for a widespread colonization of osteoblasts.

3.3.1.2 Scaffold enrichment with functionalized carbon nanotubes

In the perspective of tailoring the properties of the alginate/HAp scaffolds with CNTs, the effects of f_1 and f_3-CNTs (section 3.1.3), on the viability and the proliferation of MG63 cells have been analyzed. In the literature, several positive effects of CNTs have been reported, like the support to adhesion and growth of osteoblasts, the triggering of differentiation of human mesenchymal stem cells, the enhancing of deposition of HAp and extracellular matrix by osteoblasts and, in some cases, the inhibition of differentiation and activity of osteoclasts.[180,236]

The f-CNTs have been added to cultured cells at three different concentrations and the cell viability was evaluated after 24 and 72 hours of incubation.

It has been reported that CNTs can interfere with the routinely used colorimetric and fluorimetric assays[319-322] due to their absorbance and quenching capability; for these reasons the viability of the treated cells was evaluated through a modified version of the LDH assay proposed by Ali-Boucetta and coworkers in 2011.[319] The assay confirmed not to be influenced by the presence of the tested f-CNTs in these experimental conditions. The results (Figure 53) indicate that the levels of intracellular LDH are similar for the cells treated with f-CNTs and for untreated cells, which allows to conclude that the functionalized f-CNTs considered in this work did not show any toxicity for the MG63 cell line. Statistical analysis did not allow concluding for the presence of a dose-response mechanism.

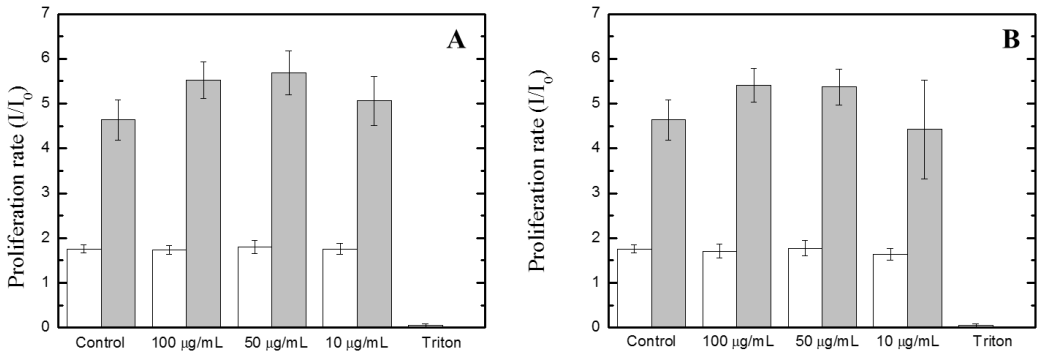

Figure 53. Viability of MG63 cells expressed as the ratio between cell number at day 0 and after 24 hours (white bars) or 72 hours (gray bars) in the presence of dispersed f_1-CNTs (**A**) or f_3-CNTs (**B**), at the concentration of 100, 50 or 10 µg/mL respectively. Control cells are seeded with DMEM and Triton X100 (0.01% V/V in DMEM) has been used as a positive control of toxicity.

After demonstrating the biocompatibility of the f-CNTs, these have been used to prepare alginate/HAp scaffolds for the evaluation of their ability of support the adhesion and growth of osteoblasts. For this application, CRIOsc containing HAp have been chosen, because of their better mechanical properties; f-CNTs have been dispersed in water (final concentration: 0.1% w/V) and added to the alginate/HAp solution prior to the gel formation.

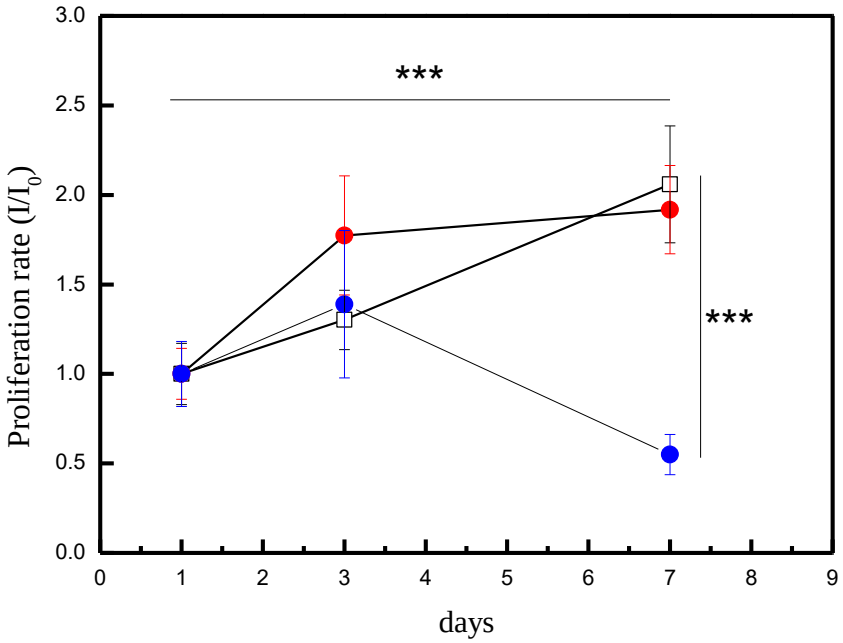

Figure 54. Viability of MG63 cells seeded in scaffolds of alginate (■), alginate/f_1-CNTs (●), alginate/f_3-CNTs (●); expressed as the ratio between cell number at day 1 and day 3 or 7. Statistical differences were determined by means of Student's t test. ***$P < 0.001$.

The proliferation trends in the alginate scaffolds are reported in Figure 54. Despite there were no differences in cell proliferation (Figure 53); when the f-CNTs are embedded within the scaffolds a different trend can be seen. At the concentration used for the preparation of the scaffolds, the f_1-CNTs did not affect the colonization and the proliferation of the cells, whereas, the f_3-CNTs, after 7 days were not able to sustain the proliferation of the osteoblasts (Figure 54). In the literature, no negative effects have been reported in the use of oxidized or, in general, negatively charged CNTs for the preparation of bone scaffolds.[209,323] The absence of any effect on the osteoblast adhesion and proliferation for the f_1-CNTs can be an intrinsic characteristic or a consequence of their low concentration. Regarding the f_3-CNTs it can be hypothesized that the wider interactions between

f_3-CNTs and alginate, and the presence of micro-domains affected the gelation and the scaffolds pore formation (discussed in section 3.1.3), leads to a structure less osteoconductive than the scaffolds prepared with f_1-CNTs or the scaffolds without f-CNTs.

3.3.2 INJECTABLE NANOCOMPOSITES IMPLEMENTED WITH ANTIMICROBIAL SILVER NANOPARTICLES AND BIOACTIVE COMPONENTS

A novel injectable bone filler is here described. The filler is based on alginate/HAp microbeads dispersed in a polysaccharide mixture in order to obtain an injectable formulation. The microbeads have been implemented in two different ways: i) by adding silver nanoparticles (nAg) in order to implement antimicrobial properties; ii) by embedding gelatin or chitlac in order to improve their bioactive properties.

3.3.2.1 Preparation and *in vitro* characterization of antimicrobial injectable bone fillers

Microbeads based on the mixture of the selected polysaccharides were prepared by exploiting the gel-forming properties of alginate: the rationale was to employ alginate as the structural component of the beads and to incorporate the bioceramic HAp to endow them with features suitable for the stimulation of bone tissue growth. To further implement the bioactivity of the beads, chitlac was added to the polymer mixture, also in the presence of antimicrobial nAg (chitlac-nAg). The hydrogel beads were prepared by dropping the aqueous mixtures of the biopolymers with HAp into an aqueous solution of $CaCl_2$; in order to control the size of the beads, an electrostatic generator was used (Figure 55).

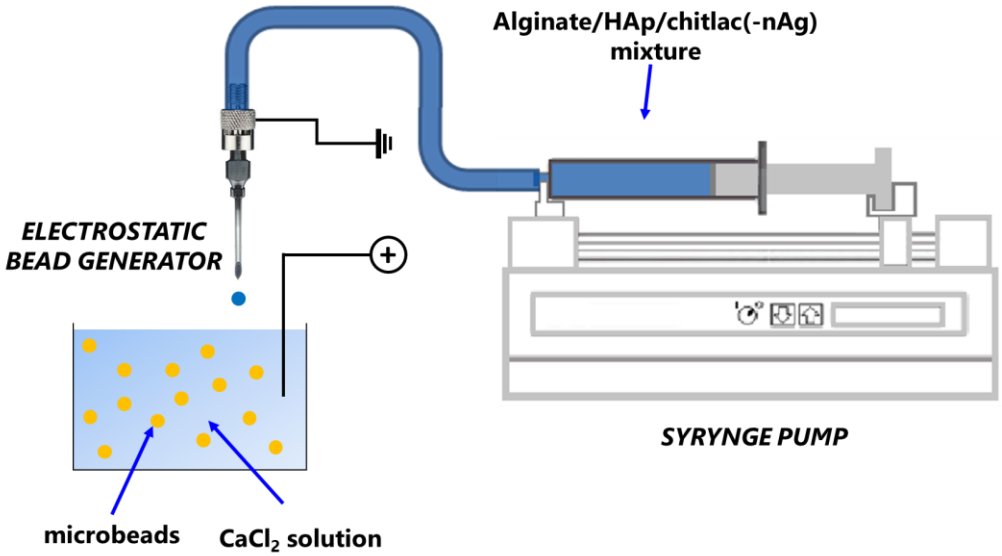

Figure 55. Schematic representation of the preparation of the microbeads: the alginate/HAp/chitlac(-nAg) solution is dropped in a $CaCl_2$ solution and a voltage is applied.

This method enabled to obtain hydrogel microbeads with a narrow size distribution and average size of 990 (± 60) µm, as determined by optical microscopy imaging; Figure 56A-C point out that the size distribution was similar for microbeads with (nAg-MB) or without (MB) silver nanoparticles.

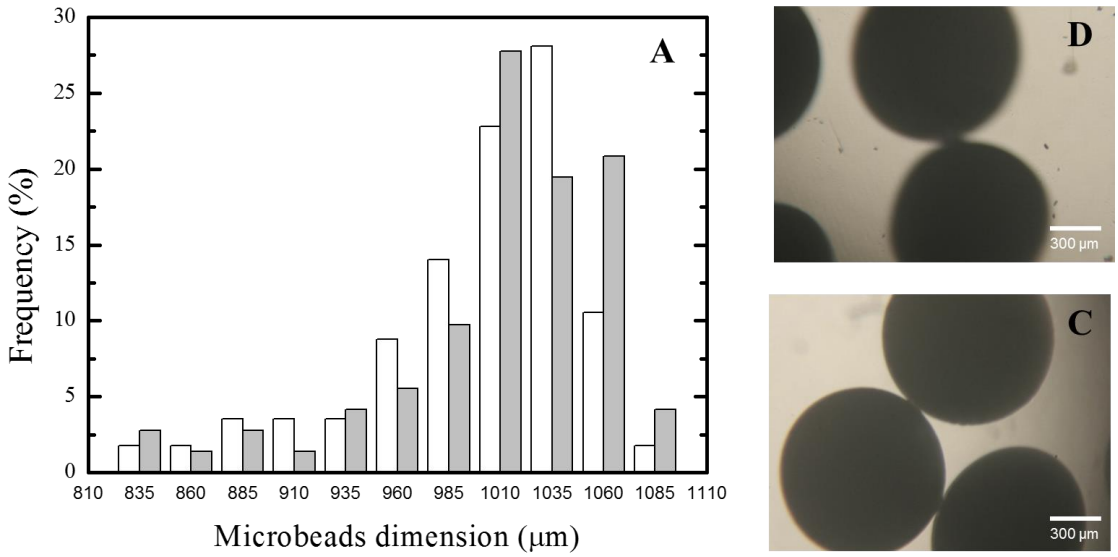

Figure 56. **A**) Dimension distribution of MB (white) and nAg-MB (grey). On the right, microbeads aspect: **B**), MB, **C**) nAg-MB.

The concentrations of alginate and HAp were optimized in order to reach a compromise between the maximization of the concentration of the osteoconductive component and the formation of a stable alginate mesh in the microbeads.[147]

Alginate microbeads have also been analyzed by means of confocal microscopy, using fluorescein-labelled chitlac, in order to evaluate the distribution of chitlac inside the alginate/hydroxyapatite matrix. Figure 57 shows the image of a sectioned microbead, which highlights the homogenous distribution of chitlac.

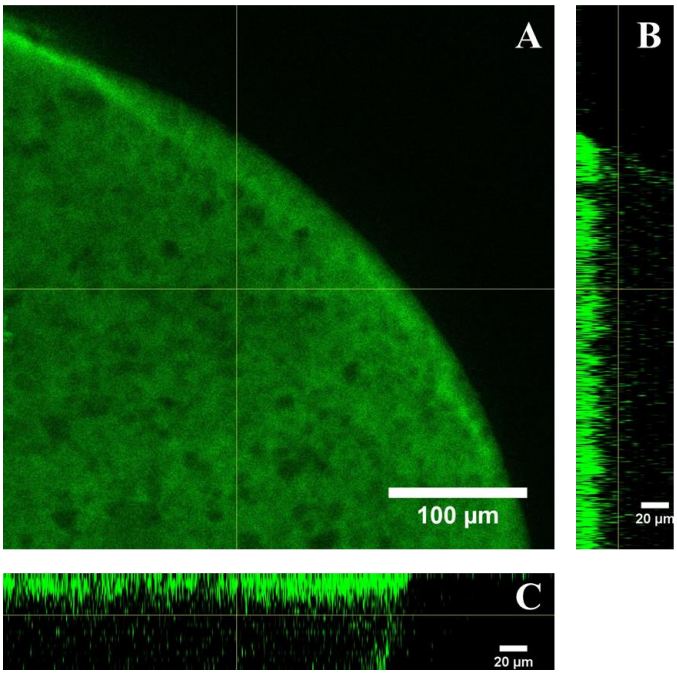

Figure 57. Confocal microscope images of alginate/HAp microbead containing fluorescein-labelled chitlac. **A**) xy top view; **B**) yz cross section; **C**) xz cross section.

Morphological and physical-chemical characterization

In order to obtain the dried composite powder required for the preparation of the injectable filler, the hydrogel beads were dehydrated by air flux, thus obtaining the dried composite particles. The dried particles were analyzed by SEM in order to evaluate size and morphology (Figure 58); as expected, drying the hydrogel microbeads led to a significant reduction of their dimensions (MB:

250 ± 40 µm; nAg-MB: 270 ± 40 µm). These values are in the range commonly employed for the preparation of composite bone fillers based on HAp or β-tricalcium phosphate (β-TCP).[172,324]

The SEM analysis enabled also to highlight how the bead surfaces are roughened by the presence of HAp crystals that protrude from both MB and nAg-MB particles (Figure 58B and D).

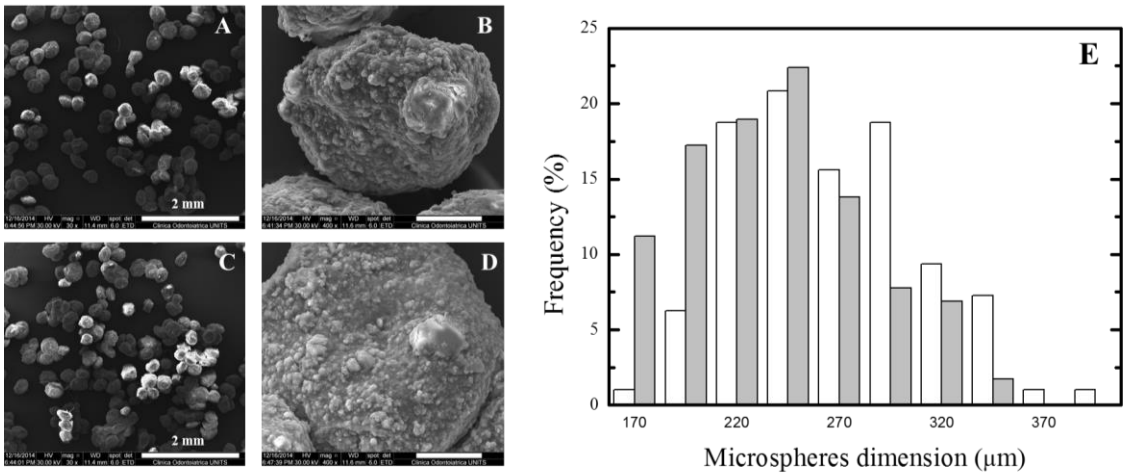

Figure 58. SEM micrographs of MB (**A**, **B**) and nAg-MB (**C**, **D**). **E**) Distribution of microbeads dimension: MB (white) and nAg-MB (grey).

The swelling behavior and stability were investigated by incubating the dried microbeads in SBF at 37 °C and replacing it at fixed days. The size variation of the particles over time is reported in Figure 59A: the data show how the microbeads underwent a considerable swelling that led to an increase of their dimension, owing to the presence of the hydrophilic polysaccharides. The microbeads rapidly (approximately 2 days) reached a swelling equilibrium, with an increase of the diameter of 3.5 times and of volume of about 43 times with respect to the initial dimension. The swelling rate of MB and nAg-MB was similar (Figure 59A) and did not affect the morphology of the microbeads (Figure 59 B and C).

The experiment, extended for 31 days, pointed out the excellent morphological stability of the microbeads, which did not show any significant degradation in physiological-like conditions.

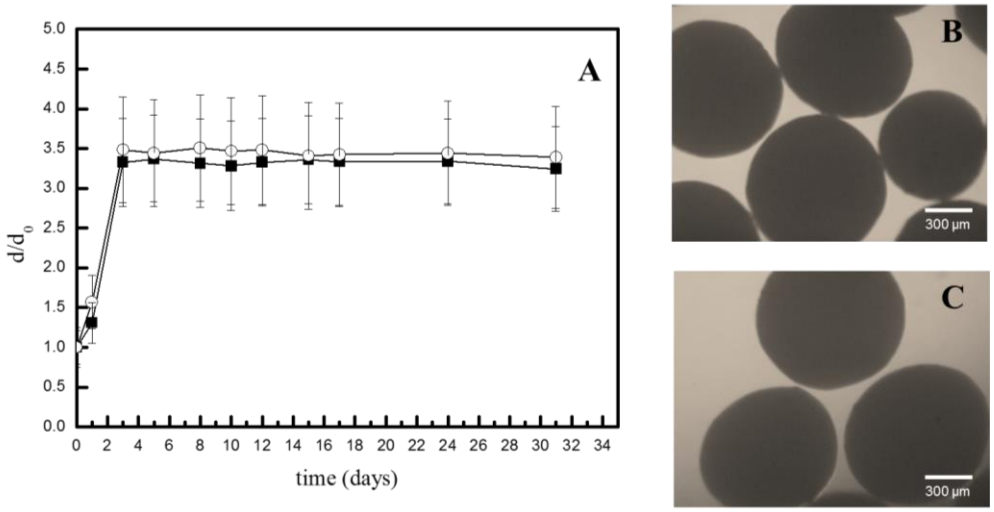

Figure 59. **A**) Diameter changes during the swelling/stability experiment: (■), MB, (○) nAg-MB. On the right, microbeads aspect after 12 days of experiment: **B**), MB, **C**) nAg-MB.

Considering the final application, the swelling and degradation behavior of the microbeads represent a positive feature of the material, enabling the injectable filler to adapt to the bone defect and firmly remain *in situ* for several weeks, thus assisting the natural bone regrowth process.

In fact, the prolonged stability of an injectable material is a key factor in the regeneration of the bone tissue,[325-327] as it takes several weeks to have new bone tissue formation.[328]

The amount of silver contained in the nAg-MB has been quantified by means of ICP-OES; the analysis revealed that 1 mg of microbeads contains 9.78 ± 1.46 ng of silver (data averaged on three samples).

The silver release from the nAg-MB has been measured by soaking the microbeads in deionized water and in saline solution (NaCl 0.15); in order to put the particles in contact with abundant liquid, the ratio between the volume of water/solution and the volume of microbeads was 10. To mimic real conditions, the solutions were changed every 24 h and the microbeads were subjected to mechanical agitation. The silver released from the microbeads over time was reported both as percentage of silver released each day (Figure 60A) or as cumulative release (Figure 60B).

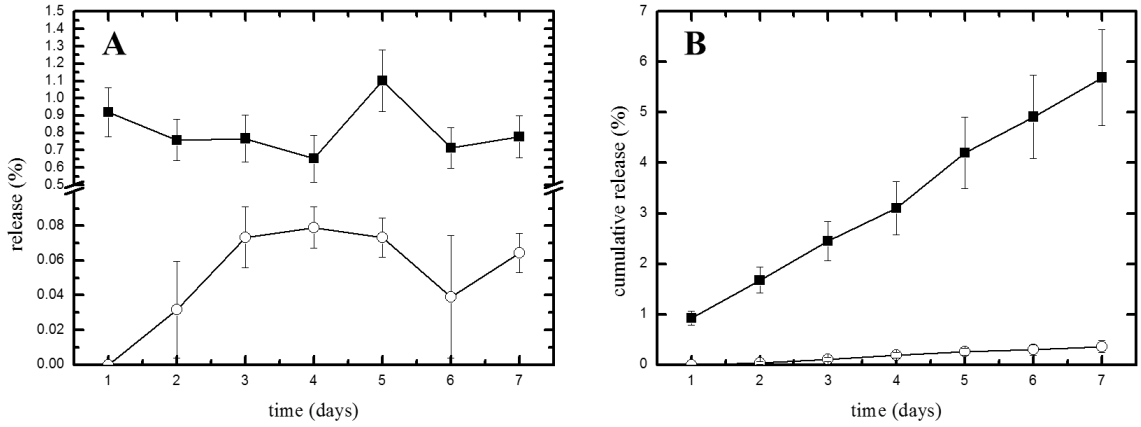

Figure 60. Silver released by the microbeads (nAg-MB) soaked in deionized water (○) or in saline solution (■) expressed as percentage of the total silver contained: (**A**) release at given solution shift; (**B**) cumulative release. Data were averaged on three independent experiments.

The data point out that for both water and saline solution the silver released upon daily shifts is typically lower than 1%, while after 7 days the cumulative silver release was (5.69 ± 0.95)% in saline solution and (0.36 ± 0.12)% in water. The higher release in saline is explainable considering that the presence of ions can accelerate the swelling of the polymer mesh, which increases the release of the entrapped nanoparticles. However, in both cases, the silver release was very low since only 0.56 ng per mg of beads is released after 7 days, which indicates the structural stability of the polymer mesh.

The profile of the silver released from the nAg-MB appears particularly appealing for bone tissue engineering applications, since it ensures a gradual long-term administration of the antimicrobial agent, thus avoiding a burst release of metal ions that could potentially be toxic for the cells of the surrounding tissues.

Antibacterial and biological properties of microbeads

The antimicrobial properties of nAg-MB were assessed in terms of inhibition of bacterial growth and eradication of biofilms produced by three bacterial strains: *S. aureus*, *P. aeruginosa* and *S. epidermidis*. These strains have been selected because of their role in bone-related infections and their antibiotic-resistance mechanisms.[329-333] The assays have been performed incubating the microbeads (nAg-MB or MB) in direct contact with bacteria for chosen times.

For *S. aureus* and *P. aeruginosa*, the growth inhibition assay was performed by incubating the bacterial suspension with the dried microbeads for 4 hours, after which the colony forming units (CFU) were measured; in both cases, the nAg-MB induced a significant decrease of the CFU, whose number was reduced by several orders of magnitude (Figure 61A-B).

In the case of *S. epidermidis*, no antibacterial effect was detected after 4 hours of incubation (data not shown). For this reason, the incubation was prolonged to 24 hours, which revealed to be a sufficient time for the nAg-MB to exert a bactericidal effect; in fact, a decrease of more than 4 orders of magnitude was found in the case of the silver-containing particles (Figure 61). The higher resistance of *S. epidermidis* was in line with the results reported in a previous work by Marsich *et al*.[155]

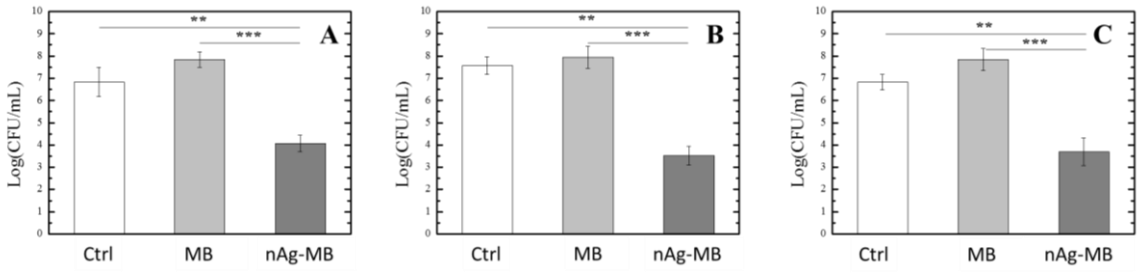

Figure 61. Growth inhibition assay of bacteria treated with microbeads (MB or nAg-MB), compared to the growth control (Ctrl). *S. aureus* (A), *P. aeruginosa* (B) were incubated for 4 hours, while *S. epidermidis* (C) were incubated for 24 h. Statistical differences were determined by means of Student's t test. **P < 0.01; ***P < 0.001.

Once verified the effectiveness of the silver-containing particles in inhibiting bacterial growth, a further test has been carried out to evaluate their effect towards pre-formed biofilms. This assay was performed on *S. aureus* and *P. aeruginosa* strains, since *S. epidermidis* does not produce a self-protecting biofilm; the bacteria biofilms were put in contact with the microbeads for four hours and the bacteria viability was quantified using the Green Biofilm Cell Stain assay, which exploits the fluorescence intensity of the biomass as an indicator of viable bacteria within the biofilm. The results are reported in Figure 62. In the case of *S. aureus*, the nAg-MB displayed a strong anti-biofilm activity, since a 69% decrease of the fluorescence intensity was measured with respect to the control. In the case of *P. aeruginosa* the nAg-MB determined a 26% of the biofilm fluorescence intensity; this milder effect could be ascribed to the high content of alginate in the *P. aeruginosa* biofilm, which represents a physical barrier towards antimicrobial agents.[334]

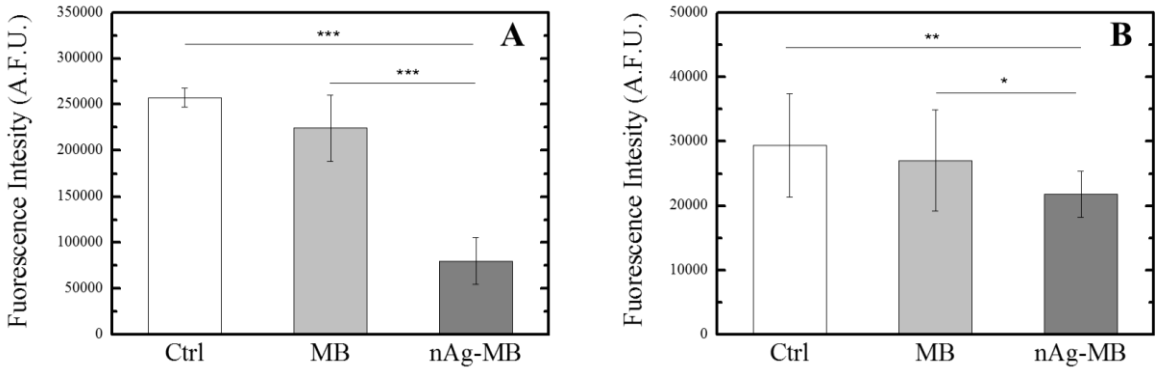

Figure 62. Effect of microbeads on biofilms of *S. aureus* (**A**) and *P. aeruginosa* (**B**) after 4 hours of contact with the materials (Green Biofilm Cell Stain assay). Ctrl: untreated biofilm; MB: biofilm treated with MB; nAg-MB: biofilm treated with nAg-MB. Statistical significance was evaluated by Student's t test. **P* < 0.05; ***P* < 0.01; ****P* < 0.001.

The viability of bacteria within biofilms was also evaluated by the Live/Dead assay, which, by means of a fluorescence microscope, enables to distinguish between viable cells (green) and dead cells (orange-red); Figure 63 collects the images of the biofilms after 4 hours of treatment with the particles, compared to untreated (control) biofilms.

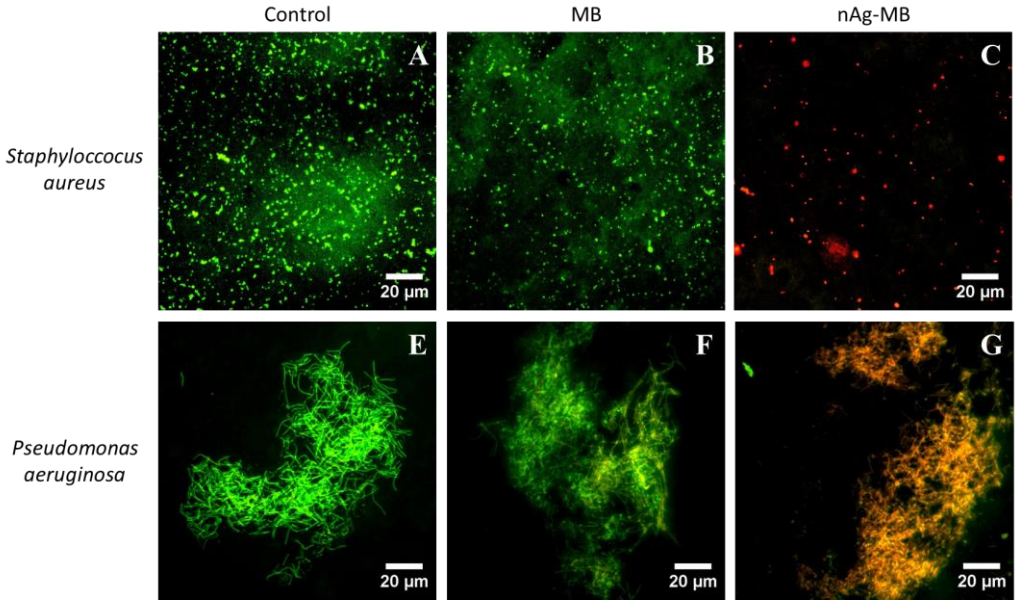

Figure 63. Effect of microbeads on biofilms of *S. aureus* (**A-C**) and *P. aeruginosa* (**E-G**) after 4 hours of contact with the materials (Live/Dead assay). Control: untreated biofilm; MB: biofilm treated with MB; nAg-MB: biofilm treated with nAg-MB. For all images, green fluorescence (SYTO® 9) indicates live cells whereas red fluorescence (Propidium iodide) refers to dead ones.

In the case of *S. aureus*, the images clearly show the abundance of viable bacteria (green) in the case of untreated (Figure 63A) and MB-treated biofilms (Figure 63B); at variance, the treatment with nAg-MB causes a clear inactivation of bacteria cells, appearing as red particles (Figure 63C).

In the case of *P. aeruginosa*, the antimicrobial effect of the nAg-MB can be inferred by the abundance of orange/red biomass (Figure 63G), at variance with control (Figure 63E) and MB-treated bacteria (Figure 63F).

Overall, the Live/Dead results are in line with the results of the Green Biofilm Cell Stain assay, both pointing out the antimicrobial effect of nAg-MB on pre-formed biofilms.

After studying the antimicrobial activity of the microbeads, their effect towards eukaryotic cells was evaluated by the lactate dehydrogenase (LDH) assay, which enables to quantify the release of the LDH enzyme due to cellular damage; the assay has been carried out by putting an osteoblasts cell line (MG63) in direct contact the cells with microbeads for 24 and 72 hours (accordingly to the ISO 10993−5 standard[335]). Figure 64 shows the results of this cytotoxicity study as well as a qualitative evaluation of the morphology of the cells in contact with the materials.

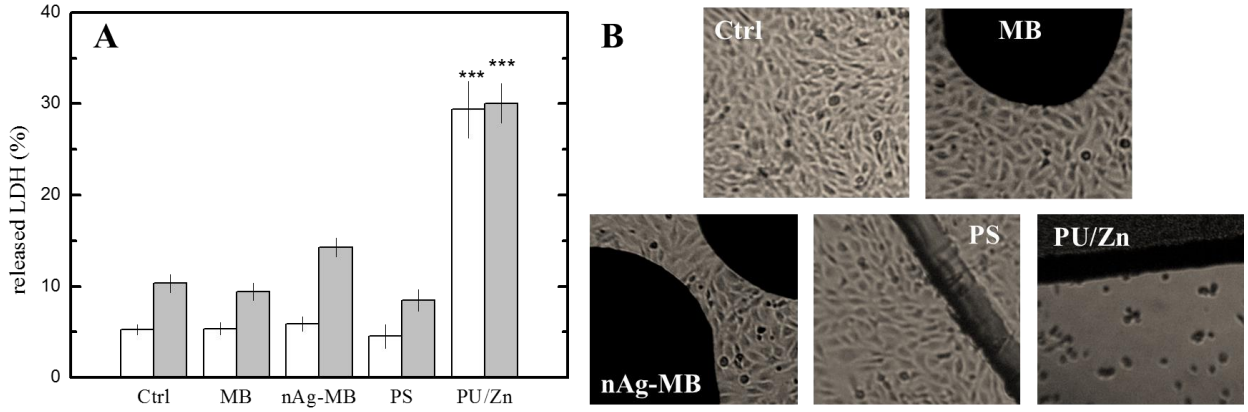

Figure 64. Evaluation of material cytotoxicity towards MG63 osteoblast-like cells. **A**) LDH assay after 24 h (white) and 72 h (grey) on cells in direct contact with the materials. Ctrl: adhesion control on multiwell, MB: cells in contact with MB, nAg-MB: cells in contact with nAg-MB, PS: cells in contact with polystyrene membrane (negative control), PU/Zn: cells in contact with polyurethane/zinc membranes (positive control). Statistical differences were determined by means of Student's t test. *$P < 0.05$; **$P < 0.01$. **B**) Microscopic image of the cells after 72 hours

The results of Figure 64A pointed out that both MB and nAg-MB particles were associated with low values (<15%) of LDH release, which remained significantly lower than the positive (cytotoxic) control (polyurethane/zinc); these quantitative data were confirmed by the qualitative investigation of cell morphology (Figure 64B), which highlighted the healthy conditions of the cells proliferated on the multiwell floor in direct contact with both types of microbeads.

Once verified the non-cytotoxicity of the material, a further *in vitro* study was carried out in order to evaluate the microbeads surface as substrate for osteoblast adhesion and proliferation; the test was performed by seeding the cells directly on the microbeads (Figure 65A) and measuring their proliferation with the Alamar Blue assay after 7 days.

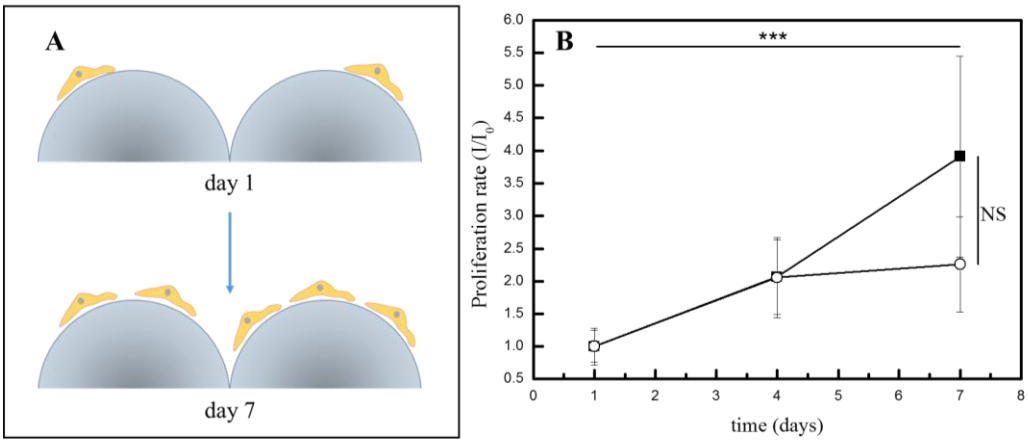

Figure 65. **A**) Schematic representation of the proliferation test performed by seeding MG63 cells on the surface of the microbeads; **B**) Proliferation rate of MG63 cells on the surface of MB (■) or nAg-MB (○); the rate was measured normalizing the intensity values (I) obtained at days 4 and 7 on the first culture day (I_0). Statistical differences were determined by means of Student's t test. *NS*: non significant; ****P* < 0.001.

The results reported in Figure 65B showed that the number of cells significantly increased after 1 week of culture on both MB and nAg-MB particles at a comparable rate. This result is particularly important keeping in mind the potential use of the material as a bone filler; in fact, the polysaccharide-HAp particles were proved to represent an efficient growth substrate for osteoblasts. This result is in line with previous investigations of some authors of the papers, which pointed out the excellent osteoconductive properties of chitlac-based substrates.[155,195,196]

Preparation of an injectable formulation

As soon as the composite microbeads were characterized, their ability to support osteoblasts proliferation assessed, and their antimicrobial activity (in the presence of silver nanoparticles) demonstrated, the material was employed for the preparation of an injectable system based on dried MB suspended in a liquid medium. The medium was selected through a preliminary screening of polysaccharide solutions by evaluating the homogeneity and stability over time of the paste resulting from the dispersion of the microbeads in the polysaccharide solution (data not shown); this screening study enabled to select alginate solution (4% w/V) with 30% w/w of microbeads as the best performing formulation, since this composition could be stored within syringes for 10 days maintaining the particles homogeneously distributed within the alginate medium (Figure 66A).

In order to assess the injectability of this formulation, the force required to extrude it through a syringe with a nozzle diameter of 2 mm was tested by means of a universal testing machine. This diameter nozzle is in the typical range for cannulas used for bone cement injections.[324] The results of the mechanical tests are reported in Figure 66B (blue line).

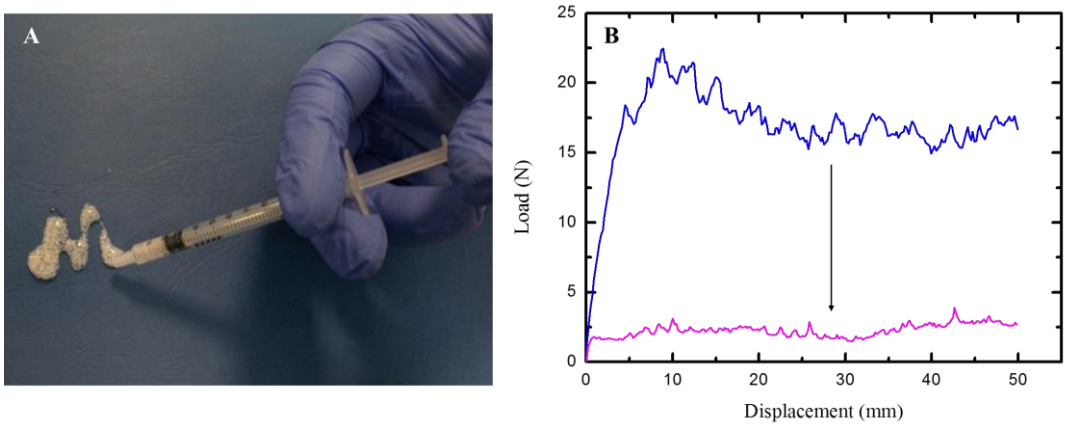

Figure 66. Injectability of MB microbeads dispersed in polysaccharide solutions. **A**) Image of the syringe employed to extrude the injectable pastes. **B**) Load-displacement (representative) curves recorded by compressing the plunger to extrude the paste out of the syringe. Blue line: 4% (w/V) alginate with 30% (w/w) microbeads; Magenta line: 3% (w/V) alginate / 1% hyaluronic acid with 30% (w/w) microbeads.

The data showed that it was possible to push the syringe plunger for the whole length of the syringe (50 mm) without stacking the particles or blocking the nozzle, thus achieving a 100% extrusion of the paste with an average compression load of 17 N (± 5 N). These values are in line with injectable

materials developed by other authors (Sohrabi *et al.*,[174] Sohrabi *et al.*,[336] Tadier *et al.*[324]) and highlight the capability of this bone filler to be injected in a surgical procedure: moreover, phase-separation phenomena were not observed during the extrusion.

In order to evaluate the morphology of the particles in the dispersion medium, a SEM investigation has been performed after withdrawing the microbeads from the alginate solution (Figure 67): the images qualitatively showed that the particles displayed a smoother surface than the native microbeads. This could be ascribed to the adsorption on the microbeads surface of some alginate from the solution.

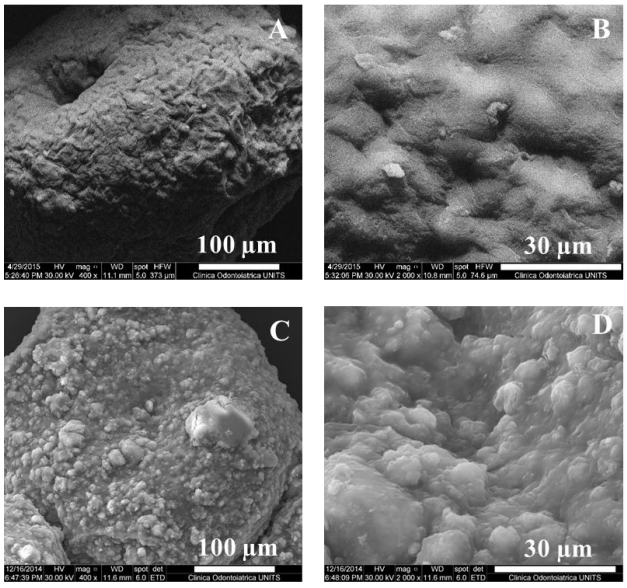

Figure 67. SEM micrographs of alginate-coated microbeads (**A**, **B**) and of native microbeads (**C**, **D**).

The confocal microscope images reported in Figure 68, of microbeads dispersed in 4% w/V alginate-fluo show how the alginate contained in the solution is adsorbed on the microbeads surface.

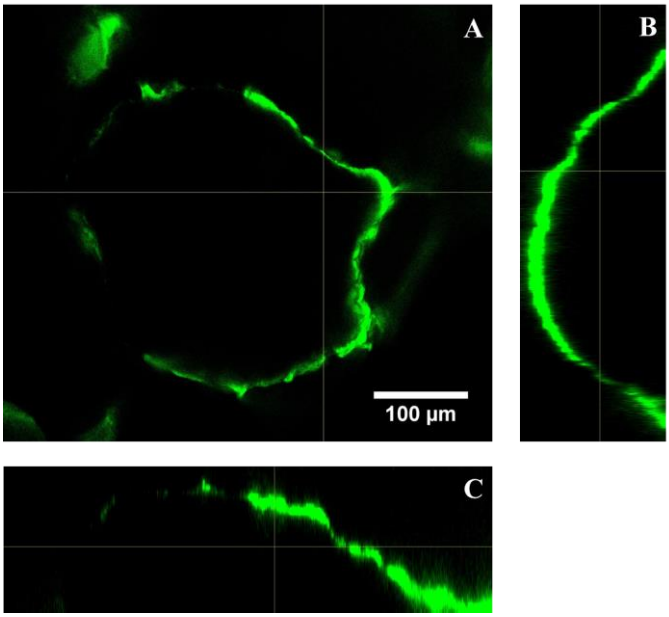

Figure 68. Confocal microscope images of alginate/HAp microbead containing fluorescein-labelled alginate. **A**) xy top view; **B**) yz cross section; **C**) xz cross section.

3.3.2.2 *In vivo* characterization of injectable filler biocompatibility and bioactivity

Optimization of material injectability

The primary goal of this experimental study is to compare osteoconductivity of the novel injectable bone-filler (with and without nAg) with that of commercial bone filler used in orthopedic surgery (HydroSet™, Stryker, NJ, USA).

Prior to the in vivo analysis, ex vivo experiments (performed on bones harvested from non-dedicated animals) have been performed in order to qualitatively evaluate the injectability of the formulation. Two problems had to be overcome regarding the material preparation: the phase separation between the microbeads and the alginate/hyaluronic acid mixture, and the stacking of the microbeads inside the syringes.

Preliminary evaluations allowed to select a paste prepared dispersing microbeads (30% w/w) in alginate solution (4% w/V). This type of paste was stable over time (no phase separation phenomena), but could be hardly applied into the bone defects; in fact this paste formulation was not easily injectable.

In a second attempt, a minor content of microbeads (15% w/V) have been dispersed in hyaluronic acid (3% w/V). Hyaluronic acid has been selected as the additional solution component, given its healing capability and lubricating properties.[337] This approach improved the injectability of the paste, although a separation between the two phases can be observed. The pastes need to be re-suspended and concentrated, discharging an uncontrolled amount of solution before their use.

After these preliminary attempts, several compositions of the liquid dispersant were prepared by mixing both polyanions (alginate and hyaluronic acid) and polycations (chitlac), as reported in Table 15. The resulting pastes obtained with 30% (w/w) microbeads were evaluated.

Table 15. List of the injectable formulations tested.

Formulation	*Composition of the liquid medium (to disperse 30% w/w microbeads)*
1	Alginate 4% w/V
2	Alginate 3% w/V; hyaluronic acid 1% w/V
3	Alginate 2% w/V; hyaluronic acid 2% w/V
4	Chitlac 3% w/V
5	Alginate 4% w/V; chitlac 1% w/V
6	Alginate 3% w/V; chitlac 1% w/V

In all the cases, except for formulations 1 and 2, a phase separation was observed, so all other formulations were discharged. Different syringes have been prepared dispersing microbeads with and without nAg (40% and ~30% w/w) in formulations 1 and 2. The best formulation was composed by 30% w/w microbeads dispersed in a mixed solution of alginate (3% w/V) and hyaluronic acid (1% w/V) (formulation 7). The mechanical tests revealed that the presence of hyaluronic acid led to a considerable decrease of the force required for the extrusion of the injectable filler, with an average compression load of 2 N (± 1N) required for the plunger to push the paste out of the syringe (Figure 66B, magenta line). This finding suggests that the addition of hyaluronic acid to the alginate-microbeads paste is able to lubricate the particles during the extrusion through the syringe, while implementing the bioactive properties of the injectable biomaterial.

Implantation procedures and preliminary μ-CT evaluation

Formulation 7 (microbeads 40% w/w dispersed in alginate/hyaluronic acid mixture 3% and 1% w/V respectively) has been used for the *in vivo* analysis. The evaluation of *in vivo* biocompatibility and osteoconductivity of fillers is based on a rabbit model of non-critical bone defects. Medial longitudinal defects have been created on the distal femur condyles as reported in Figure 69; these defects have been filled with the injectable formulations, with a positive control (HydroSet™, Stryker, NJ, USA) or left empty in order to compare the healing of treated defects with the normal healing rate of non-critical bone defects. The formulations tested showed to be easily injectable in the bone defects, achieving an optimal filling of defects, comparable with that of positive control. After implantation, animals showed a normal behavior, without movement impairing, infections or adverse and inflammatory reactions.

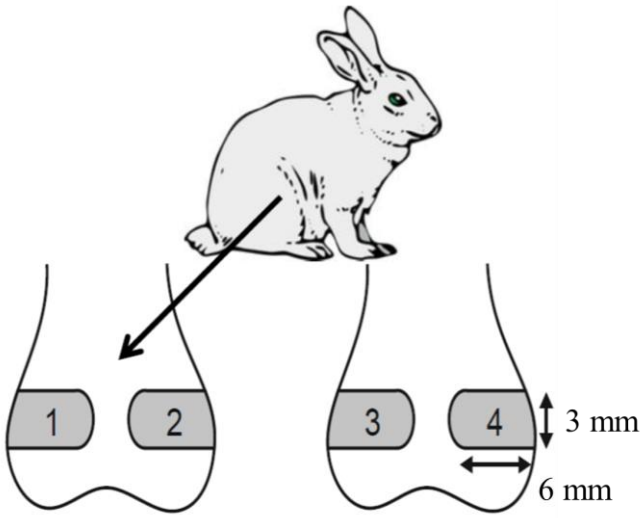

Figure 69. Schematic representation of the *in vivo* study design. In each rabbit lateral (1 and 4) and medial (2 and 3) defect were created on both the condyles and randomly filled with the materials or the controls, so each rabbit received all the treatments.

Following the indications reported by Urist *et al.*[328] the animals have been euthanized 6 and 12 weeks after implantation in order to evaluate: i) after 6 weeks: the earliest deposits of new bone from osteoprogenitor cells in the interior of well vascularized excavation chambers (that usually occurs at 4 to 6 weeks): ii) after 12 weeks: bone formation from proliferating connective-tissue

cells associated with vascularization calcification and replacement of the nests of cartilage by the typical route of endochondral ossification (that usually occurs at 8 to 16 weeks).

At the explantation of the knees no adverse tissue reaction have been observed. Preliminary μ-CT data have been collected by analyzing the bone defects as showed is Figure 70.

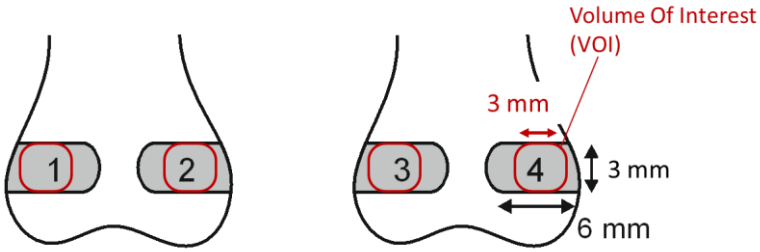

Figure 70. Schematic representation VOIs analyzed by μ-CT.

Figure 71 reports the cross-section views of the reconstructed μ-CT VOIs (Volume Of Interest) of the explant after 6 and 12 weeks. From these images it is possible to appreciate the optimal defect filling achieved with the materials tested if compared to the positive control.

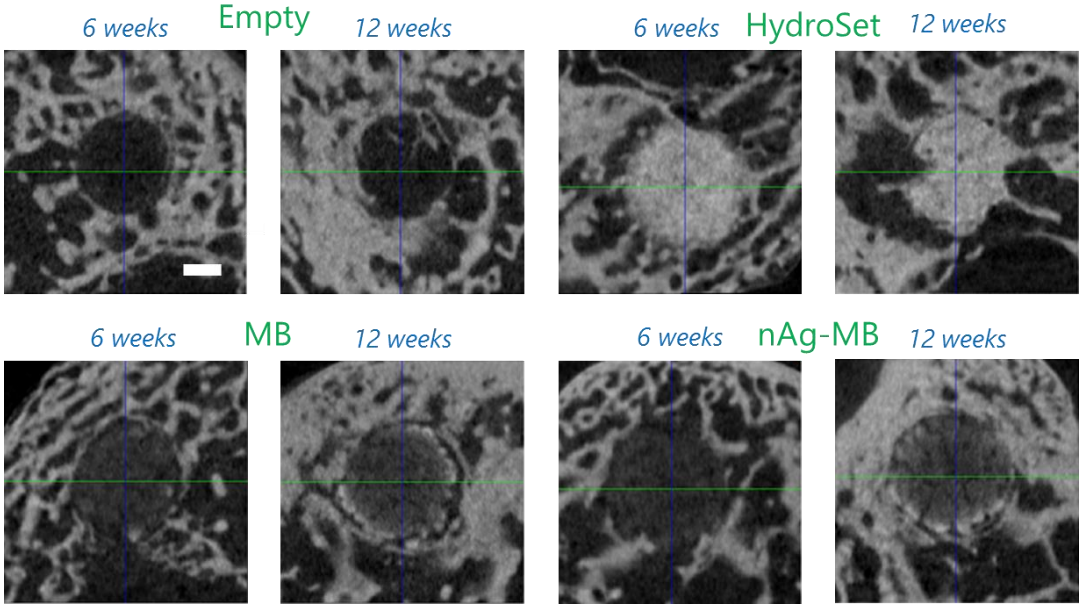

Figure 71. Cross section view of μ-CT reconstruction of VOIs. Dark regions represent areas in which is not present mineralized material (bone tissue or tested materials) (scale bar = 1 mm).

A preliminary evaluation of the μ-CT data has been performed by measuring, after a segmentation process and the application of thresholds, the percentage of dark volume over the total VOI analyzed. These values are an estimation of the volume that is not occupied by mineralized material (implants or new bone tissue). The values are reported in Figure 72.

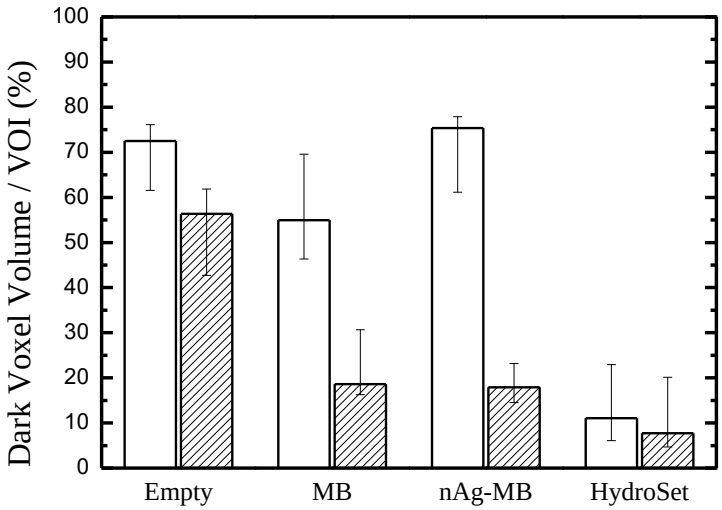

Figure 72. Percentage of Dark Voxel Volume over the total VOI analyzed at 6 weeks (empty bars) and 12 weeks (filled bars) after the implantation. Values are expressed as median and 25th and 75th percentiles.

From the graph reported in Figure 72 it is possible to observe that at 6 weeks the percentages of volume not occupied by mineralized matrix is comparable between void control and tested materials. Since Figure 71 shows that the defect are well filled by the tested materials, it is reasonable to think that the values at 6 weeks are affected by the low radio-opacity of the microbeads. Indeed, at 12 weeks, it is possible to appreciate similar values of volume occupied by mineral matrix between positive control and tested materials, which could suggest a possible regeneration of bone tissue in the presence of tested materials.

Despite these preliminary good results, it is necessary to evaluate the histology of the explants in order to distinguish between implanted biomaterials and bone tissue and to confirm the regeneration of bone tissue.

3.3.2.3 Implementation of bioactive properties

In order to tailor the bioactive properties of the alginate/HAp materials, the possibility of the addiction of bioactive components has been addressed. In preliminary experiments (data not showed) attempts to combine alginate and bovine tendon collagen have been performed. The difficulties to solubilize collagen and to mix it to alginate led to the choice of gelatin for the implementation of material bioactive properties. As discussed in the introduction, the denaturation process of collagen favors the exposition of RGD peptides and the decrease of collagen immunogenicity; moreover, it makes the gelatin more soluble and miscible with other polymers.[55,56,60,61]

In order to analyze the effects of gelatin on alginate/HAp material stability and biological properties, microbeads and scaffolds have been prepared using three different concentrations of gelatin.

The microbeads swelling and stability behavior has been analyzed, as previously reported, by soaking the microbeads in SBF and analyzing their diameter variation. Figure 73 shows that the microbeads are able to swell and uptake liquid form the environment and are stable over time. The swelling and stability behavior is different between these microbeads and the chitlac-containing microbeads, owing to the different macromolecular structure.

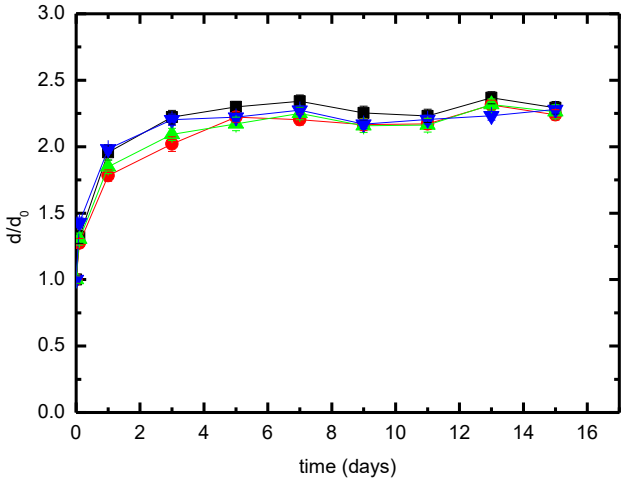

Figure 73. Diameter changes during the swelling/stability experiment for control microbeads (■) and microbeads containing gelatin 0.05% (●), gelatin 0.1% (▲) and gelatin 0.2% (▼).

Microbeads stability has also been analyzed in terms of the release of gelatin from the polymer matrix. The experiments have been performed in saline solution and the gelatin has been quantified by micro BCA (bicinchoninic acid) assay. The graphs reported in Figure 74 shows that the amount of gelatin released from the microbeads is very low (< 5% over the total gelatin content) and it reaches a plateau after few days. Comparing the release profile with the swelling behaviour it can be hypothesized that the release of gelatin is due to the initial swelling of the microbeads and that after this initial swelling an equilibrium is reached.

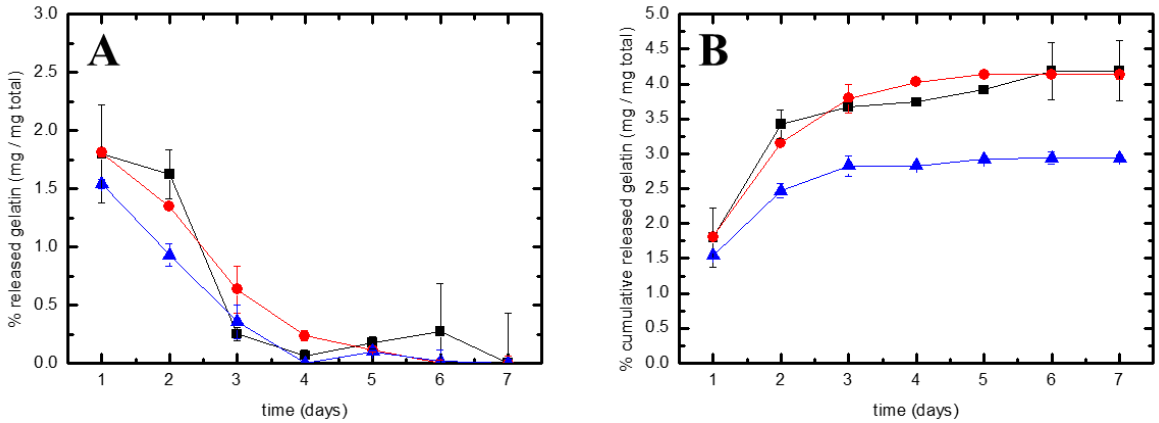

Figure 74. Gelatin release from microbeads containing gelatin 0.05% (■), gelatin 0.1% (●) and gelatin 0.2% (▲) in saline solution expressed as percentage of the total gelatin contained: (**A**) release at given solution shift; (**B**) cumulative release. Data were averaged on three independent experiments.

Finally, biological effects of gelatin-containing samples have been evaluated *in vitro* on osteoblasts grown into alginate/HAp/gelatin scaffolds. Data are reported in Figure 75 and show that there are no differences in the adhesion and proliferation of osteoblasts seeded in alginate/HAp scaffolds, with or without gelatin.

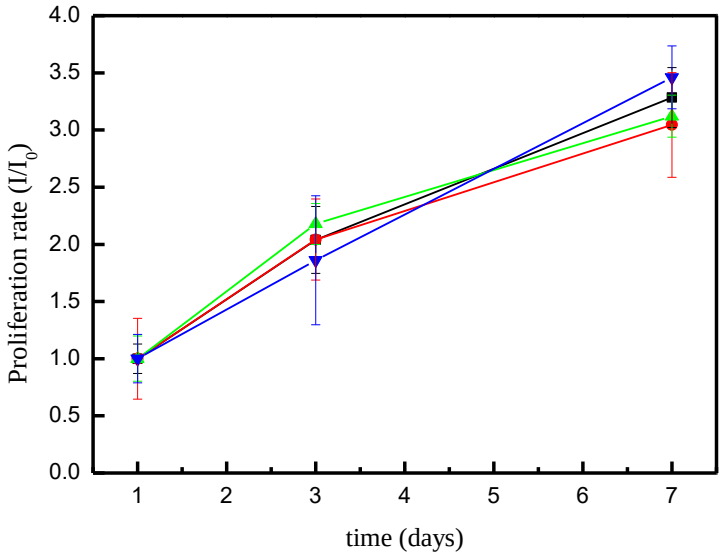

Figure 75. Proliferation rate of MG63 cells into alginate/HAp scaffolds (■) containing gelatin 0.05% (●), gelatin 0.1% (▲) and gelatin 0.2% (▼); the rate was measured normalizing the intensity values (I) obtained at days 3 and 7 on the first culture day (I_0).

Despite positive biological effects of gelatin have been reported for cells encapsulated in alginate/gelatin hydrogels,[56] in this work it was not possible to point out any positive effect of gelatin addition. It will be necessary to further evaluate the biological effects of gelatin in terms of morphology and metabolic activity of adhered osteoblasts.

3.3.3 CONCLUSIONS

Porous composite scaffolds were developed from alginate/HAp hydrogels by exploiting different freezing techniques (CRIO and ISISA) that enable to tailor the pores morphology/dimension. Upon contact with fluids, these materials are able to rapidly uptake large amounts of water and to maintain a structural integrity for several weeks. Moreover, after rehydrating the dried material, the scaffolds are able to withstand high deformations without breaking and display a peculiar shape-recovery behavior, which appears particularly advantageous when positioning and adapting the biomaterial to the bone defect cavity. *In vitro* biological tests proved that, on both types of scaffolds, osteoblasts are able to proliferate and to produce extracellular matrix, as a proof of the favorable microenvironment (alginate/HAp) and of the suitable porous structures. Interestingly,

osteoblasts seeded on ISISAsc were able to penetrate and proliferate within the columnar aligned pores.

The modified LDH employed, turned out to be a reliable method to evaluate the viability of cells in the presence of f-CNTs; the results so obtained demonstrated that for all dispersible (non-aggregating) f-CNTs, no detrimental effect on the viability of osteoblast-like MG63 cells was detected over three days in the range of concentration tested. The f-CNTs, embedded in a tridimensional structure showed different biological properties: positively charged f-CNTs were not able to affect the adhesion and the proliferation of the osteoblasts, whereas the negatively charged f-CNTs hampered the osteoblasts growth.

Microbeads based on hydroxyapatite, alginate, and chitlac-nAg were developed and characterized for the preparation of injectable bone fillers. The dried microbeads displayed a rapid swelling in contact with simulated body fluids and maintained their integrity for more than 30 days. The evaluation of silver leakage from the microbeads showed that the antimicrobial metal is slowly released in saline solution, with less than 6% of silver released after 1 week. *In vitro* antimicrobial tests proved that the microbeads displayed bactericidal effects toward *S. aureus*, *P. aeruginosa* and *S. epidermidis* and were also able to damage pre-formed bacterial biofilms. The microbeads did not exert any cytotoxic effect towards osteoblast-like cells, which were also able to colonize and proliferate on their surface. Upon suspension of the particles in alginate (or alginate/hyaluronic acid) solution, a homogenous and time-stable paste was obtained; mechanical tests enabled to quantify the extrusion forces from surgical syringes, pointing out the good injectability of the material. Moreover, the best injectable formulation has been successfully used for the *in vivo* evaluation of material biocompatibility and osteoconductivity on a rabbit model of non-critical bone defect.

4 CONCLUDING REMARKS

The present work describes the preparation and the characterization of polysaccharide-based nanocomposite biomaterials for bone and neural tissue engineering. Several analyses have been performed in order to characterize and optimize the materials. Moreover, the effects of the presence of functionalized carbon nanotubes (f-CNTs) and silver nanoparticles (nAg) in the polymer-based constructs have been analyzed.

4.1 CHARACTERIZATION OF FUNCTIONALIZED CARBON NANOTUBES (f-CNTs) DISPERSIONS AND NANOSYSTEMS

Low Field-Nuclear Magnetic Resonance (LF-NMR) has been used, for the first time, for the characterization of the dispersibility and aggregation tendency of f-CNTs: it was possible to correlate the aggregation behavior of f-CNTs with the $\overline{T_2}$ of water molecules and to discriminate the ability of different mediums (water, polymeric solutions, culture media) to disperse pristine and functionalized CNTs. Moreover, for well dispersible f-CNTs, a linear correlation between the water $\overline{r_2}$ and the f-CNTs concentration was found, suggesting that this technique could be used for the evaluation of the concentration of f-CNTs that, for example, are released from a material.

The investigation of the effects of the f-CNTs presence in polymer matrices (performed by spectroscopical, rheological and mechanical analyses of alginate-based solutions and hydrogels) showed that LF-NMR is a very sensitive technique that can be profitably flanked to the commonly used techniques, for a comprehensive characterization of CNTs based materials.

4.2 DEVELOPMENT OF A BRIDGING IMPLANT FOR THE SPINAL CORD INJURY TREATMENT

Alginate and chitlac proved to be good candidates for the preparation of tridimensional porous structures to be employed in the development of a bridging implant strategy for the spinal cord injury treatment. Chitlac alone and in combination with alginate showed to be biocompatible and to improve the physiological activity of neural cells. Moreover, a synergistic effect of the

combination of chitlac and neurotrophine secreting engineered mesoangioblasts was observed on neural cell morphology and activity. Altogether these results set the bases for the preparation of alginate-based tridimensional scaffolds enriched with chitlac and with neurotrophines secreting cells for the restoring of the lost synapses in spinal cord injury.

Alginate/chitlac scaffolds have been prepared with isotropic/spherical and aligned pores. The scaffold showed suitable properties for the employment in neural tissue engineering: in particular, swelling behavior and mechanical properties were found to be similar to the nerve tissue ones. *In vitro* experiments will be performed by seeding hippocampal-derived neurons on the scaffolds and analyzing their morphology and activity.

The introduction of f-CNTs will be adopted as a strategy for the implementation of scaffold electrical conductive properties and bioactivity. In order to evaluate the biological effects of f-CNTs they have been combined with chitlac for the preparation of chitlac/f-CNTs coated glass substrates that will be used for the growth of hippocampal derived neurons.

4.3 DEVELOPMENT OF FILLERS FOR NON-CRITICAL BONE DEFECTS HEALING

The pore morphology of alginate/HAp scaffolds has been tailored by applying two different freeze-drying techniques and the implications on stability, mechanical and biological properties of the constructs were analyzed. It was found that both structures possess similar stability and biological properties and different mechanical properties. Overall, both CRIOsc and ISISAsc represent advantageous solutions for the treatment of bone defects since they can be cut and press-fit into bone defects while maintaining shape and structural integrity. While isotropic scaffolds display higher mechanical properties, anisotropic scaffolds appear particularly suited to give a preferential directionality to cell colonization.

Antimicrobial injectable bone fillers have been developed by dispersing alginate/HAp microbeads containing nAg in polysaccharide solutions. The microbeads showed good stability and proved to be biocompatible and to exert antibacterial activity. The formulations, prepared by dispersing the microbeads in alginate and hyaluronic acid solutions and mixtures, could be easily injected and preliminary results on an on a rabbit *in vivo* model of non-critical bone defects showed that the

injectable fillers are biocompatible and osteoconductive. Overall, this novel antimicrobial bone-filler appears as a promising osteoconductive material for the treatment of bone defects, in particular when possible infections could compromise the bone-healing process.

5 MATERIALS AND METHODS

5.1 MATERIALS

LF1060 sodium alginate samples isolated from *Laminaria hyperborea* were provided by FMC BioPolymer AS (Norway). The (viscosity average) relative molecular mass ("molecular weight", MW) was found to be approximately 120000 as determined by capillary viscosimetry according to Vold *et al*.[338] The composition of the alginate sample was determined by means of ^{1}H-NMR[339,340] and resulted to be F_G = 0.68, F_M = 1 - F_G = 0.32, F_{GG} = 0.57, F_{GM+MG} = 0.22, F_{MM} = 0.21, $N_{G>1}$ = 14. K11675 sodium alginate samples isolated from *Laminaria hyperborea* was provided by Kerry Group (Ireland). The relative molar mass ("molecular weight", MW) was found to be 186600 ± 1100, as determined by capillary viscosimetry. The composition of this alginate sample was determined by means of ^{1}H-NMR and resulted to be F_G = 0.71, F_M = 0.29, F_{GG} = 0.55, F_{GM+MG} = 0.31, F_{MM} = 0.13, $N_{G>1}$ = 12.2. F_G and F_M denote the mole fraction of alginate monomers as α-L-guluronic acid (G) and β-D-mannuronic acid (M), respectively, F_{GG} indicates the fraction of G dimers, F_{MM} indicates the fraction of M dimers and F_{GM+MG} indicates the fraction of any mixed sequence of G and M (irrespective of sequence). $N_{G>1}$ is the number-average number ($\bar{n}_n$) of G monomer in homopolymeric sequences having $\bar{n}_n \geq 2$.

Hyaluronic acid samples (MW 1500000) were provided by FMC BioPolymer AS (Norway). Highly deacetylated chitosan (residual acetylation degree approximately 16 % as determined by means of ^{1}H-NMR), was purchased from Sigma-Aldrich (Chemical Co. USA). The relative MW of chitosan, determined by intrinsic viscosity measurements, was found to be around 690000.[181]

Chitlac (lactose modified chitosan, CAS registry number 85941-43-1) was prepared according to the procedure reported elsewhere starting from highly deacetylated chitosan.[181,192] The composition of chitlac was determined by means of ^{1}H-NMR and resulted to be: glucosamine residue 27 %, N-acetylglucosamine 18 % and 2-(lactit-1-yl)-glucosamine 55 %. The calculated relative MW of chitlac is around 1.5×10^6.

Hydroxyapatite (HAp) powder was from Fluka (U.S.A.). Silver nitrate ($AgNO_3$), ascorbic acid ($C_6H_8O_6$), $CaCO_3$, δ-gluconolactone (GDL), LDH (lactate dehydrogenase)-based TOX-7 kit,

in-vitro toxicology assay (Resazurin based, Alamar Blue) TOX-8 kit, phosphate buffered saline (PBS), Luria–Bertani (LB) broth, LB Agar and Brain Heart Infusion (BHI) were purchased from Sigma-Aldrich (Chemical Co. USA). Trypsin/EDTA solutions, Fetal Bovine Serum (FBS), penicillin streptomycin 100X, l-glutamine 100X and Dulbecco's modified Eagle's medium (DMEM) were purchased from EuroClone (Milan, Italy). FilmTracer™ FM® 1-43 Green Biofilm Cell Stain and FilmTracer Live/Dead biofilm viability kit were purchased from Invitrogen (U.S.A.). CellTiter Aqueous One Solution cell proliferation assay kit (MTS assay) was from Promega (U.S.A.). ELISA kits for human osteocalcin and mouse galectin-1 quantification were purchased from Invitrogen (U.S.A.). All other chemicals were of analytical grade.

5.2 PREPARATION OF POLYSACCHARIDES AND BIOMATERIALS

5.2.1 CHEMICAL MODIFICATION OF POLYSACCHARIDES AND SYNTHESIS OF NANOSTRUCTURES

5.2.1.1 Chemical modification of polysaccharides

Alginate-fluo

200 mg of alginate LF1060 were dissolved in 70 mL of MES buffer (50 mM; pH 5.5.). Fluoresceinamine (1 mg/mL in methanol) was added to the alginate solution to label 1/500 of available carboxylic groups. Then an amount of EDC (1.5 times the monomeric units of alginate) and of NHS (1:1 with EDC) were added to the solution. The reaction mixture was stirred 2 hours at room temperature. Then the mixture was dialyzed (dialysis membrane Spectrapore, MWCO 12000) three times against $NaHCO_3$ 0.05 M, two times against NaCl 0.1 M and against deionized water until the conductivity of the external solution was below 2 μS/cm at 4 °C. All procedures were carried out under dark condition. The pH was adjusted to 6.8 – 7.2 and then the solution was filtered through 0.45 μm filters and freeze-dried.

Chitosan-fluo

90 mg of chitosan in 30 mL of deionized water (pH was adjusted to 5.5 with HCl). Then 200 μL of a fluorescein isothiocyanate (FITC) solution (0.5 mg/mL in sodium carbonate buffer, 0.5 M) were added to the solution. The reaction mixture was stirred 24 hours at room temperature. Then

the mixture was dialyzed (dialysis membrane Spectrapore, MWCO 12000) three times against $NaHCO_3$ 0.05 M, two times against NaCl 0.1 M and against deionized water until the conductivity of the external solution was below 2 μS/cm at 4 °C. All procedures were carried out under dark condition. The pH was adjusted to 4.5 and then the solution was filtered through 0.45 μm filters and freeze dried.

Chitlac-fluo

200 mg of chitlac were dissolved in 70 mL sodium carbonate buffer (0.5 M). 20 μL of a FITC solution in the same buffer (5 mg/mL) were added drop wise to the chitlac solution to label 1/2000 of available amino groups. Then the mixture was dialyzed (dialysis membrane Spectrapore, MWCO 12000) three times against $NaHCO_3$ 0.05 M, two times against NaCl 0.1 M and against deionized water until the conductivity of the external solution was below 2 μS/cm at 4 °C. All procedures were carried out under dark condition. The solution was filtered through 0.45 μm filters and freeze dried.

5.2.1.2 Functionalization of carbon nanotubes

Multi-walled carbon nanotubes (MWCNTs) have been modified through two different kinds of reactions in order to achieve differently charged moieties on the carbon sidewall. Pristine MWCNTs (f_0-CNT; diameter 20-30 nm, length 0.5-2 μm) have been purchased from Nanostructured & Amorphous Materials Inc., with a degree of purity greater than 95%. Pristine MWCNTs have been directly analyzed (f_0-CNTs) or functionalized through the diazonium salt-based arylation reaction[252] (f_1-CNT), the 1,3-dipolar cycloaddition of azomethines ylides reaction[254] (f_2-CNT) and an oxidative reaction employing nitric acid[274] (f_3-CNT).

5.2.1.3 Preparation of silver nanoparticles

Silver nanoparticles (nAg) were obtained by reducing silver ions with ascorbic acid in chitlac solution. Freeze-dried chitlac was dissolved in deionized water to obtain a 4 g/L solution. Silver nitrate ($AgNO_3$) was added to chitlac at final concentration of 1 mM; then, ascorbic acid was added at final concentrations of 0.5 mM. The solution was kept for 4 hours at room temperature in darkness and then stored at 4 °C.

5.2.2 PREPARATION OF HYDROGELS AND SCAFFOLDS

5.2.2.1 Alginate/f-CNTs hydrogels and scaffolds

Homogeneous calcium hydrogels have been prepared by blending the alginate (K11675) solution (final concentration 2% w/V) with $CaCO_3$ (30mM) followed by the addition of the slowly hydrolyzing GDL (60mM). Gels with f-CNT were prepared by adding the suspended f-CNTs to the slurry prior to the addiction of the GDL. The suspension was degassed prior to the addition of GDL to avoid bubble formation. The Ca-polymer gelling solutions were cured in 24 wells tissue culture plates (Ø = 16 mm, h = 18 mm) (Costar, Cambridge, MA) or in a Petri dish (diameter = 3 mm, h = 18 mm) (Sarstedt, Newton, NC) for the rheological and mechanical tests, and directly in NMR tubes for relaxometry experiments.

For the preparation of f-CNTs alginate (K11675) scaffolds, HAp (final concentration 3% w/V) has been added to the alginate/f-CNTs solution. The reticulation has been triggered by the addiction of GDL and the Ca-polymer gelling solution was cured in 24 wells tissue culture plates (Ø = 16 mm, h = 18 mm) (Costar, Cambridge, MA). The hydrogels were then stepwise cooled by immersion in a liquid cryostat (circulating bath 28L, VWR, Radnor, PA, U.S.A.). Ethylene glycol in water (3:1) was used as refrigerant fluid. Temperature was decreased stepwise from 20 to -20 °C by 5 °C steps with 30 min intervals for equilibration; the samples were then freeze-dried (with an ALPHA 1-2 LD plus freeze-drier, CHRIST, Osterode am Harz, Germany), for 24 h to obtain porous scaffolds. This freezing process has been indicated as cryo-prepared isotropic, CRIO.

5.2.2.2 Preparation of alginate/HAp scaffolds with different pore morphology

Homogeneous calcium alginate hydrogels gels were prepared by blending the alginate (LF1060) solution (final concentration 2% w/V) with $CaCO_3$ (30 mM) or HAp (0.5% w/V) followed by the addition of GDL (60 mM). In the former case, a perfectly transparent hydrogel was obtained, confirming the complete dissolution of $CaCO_3$ (as anticipated by Ström *et al.*[341]), corresponding to free Ca^{2+} 30 mM. On the contrary, only 30% of total HAp was solubilized by GDL (corresponding to a concentration of free calcium 15 mM), leaving a total of 0.35% w/V as solid component. The suspension was degassed prior to the addition of GDL to avoid bubble formation. The Ca-polymer gelling solutions were cured in 24 well tissue culture plates (diameter = 16 mm, height = 18 mm)

(Costar, Cambridge, MA) or in syringes of different diameters (9 mm; 13 mm; 15.5 mm) (NiPro, Belgium). The gels were taken out from the mold after 24 h for the compression tests or freeze casted to obtain the scaffolds. The hydrogels in the tissue-culture plate were freeze-casted, as explained in the previous paragraph, to obtain isotropic porous scaffolds (CRIOsc). The syringes were cooled following the Ice Segregation Induced Self Assembly (ISISA) process, by immersion in a liquid nitrogen bath (-196 °C) at different speed (16.2, 8.04 and 3.24 mm/min) using a syringe pump with tunable speed. The samples were freeze-dried for 24 h to obtain anisotropic porous scaffolds (ISISAsc). The specimens were cylindrical in shape with an average thickness of 18 mm and 60 mm, and diameter of 16 mm and 11 mm, for the CRIOsc and the ISISAsc (upon preparation within the syringe) respectively; after preparation, the scaffolds were cut into the desired dimensions depending on the specific analysis.

5.2.2.3 Alginate/HAp scaffolds containing gelatin

Homogeneous calcium alginate hydrogels gels were prepared by mixing alginate (LF1060) (final concentration 2% w/V) and gelatin (final concentration 0.05% w/V, 0.1% w/V, 0.2% w/V) at 40° C in the presence of HEPES (final concentration 0.01 M) and NaCl (final concentration 0.15 M). HAp (final concentration 3% w/V) has been added to the polymeric mixtures followed by the addition of GDL (60 mM). The Ca-polymer gelling solutions were cured in 24 well tissue culture plates (diameter = 16 mm, height = 18 mm) (Costar, Cambridge, MA). The hydrogels were then freeze-casted, as explained in the previous paragraph, to obtain isotropic porous scaffolds.

5.2.2.4 Chitlac adsorption on alginate scaffolds

In order to quantify the amount of chitlac adsorbed in the scaffolds, CRIOsc and ISISAsc prepared with $CaCO_3$ (10 mm of diameter and height) have been incubated in chitlac-fluo (1.5 mL per scaffold, 0.2% w/V). At defined intervals of time, the solution was removed and the fluorescence was measured (λ_{exc} 485 nm, λ_{em} 520 nm, FLUOstar Omega, BMG LABTECH, Germany). The amount of adsorbed chitlac was calculated from the difference between the initial and the residual concentration of the chitlac-fluo solution, using a calibration curve obtained by solubilizing chitlac-fluo in water.

5.2.3 PREPARATION OF MICROBEADS

5.2.3.1 Alginate/HAp/chitlac-nAg microbeads

Microbeads were prepared following a well-defined protocol previously reported[184,194] Alginate/chitlac-nAg microbeads (nAg-MB) were obtained from alginate/chitlac-nAg mixtures (final concentrations: alginate (LF1060) 2% w/V, HAp 3% w/V, chitlac-nAg 0.2% w/V) in aqueous NaCl solution (final concentration 0.15 M) with HEPES (final concentration 0.01 M, pH 7.4). Control microbeads (MB) were prepared using chitlac 2 g/L (without nAg). The microbeads were obtained by dripping the polymer blend into a gelling solution (aqueous 0.05 M $CaCl_2$). The droplet size was controlled by use of a high voltage electrostatic bead generator (7.5 kV, 162 mL/h, steel needle with 0.7 mm outer diameter, 1 cm distance from the needle to the gelling solution) according to a procedure previously described.[184] The gel microbeads obtained were stirred for 30 min in the gelling solution, washed three times in deionized water and dried under air flux. Microbeads were sterilized for 1 h, under UV irradiation, before the use in the biological tests.

5.2.3.2 Alginate/HAp/gelatin microbeads

Alginate/gelatin microbeads were obtained from alginate/gelatin mixtures (final concentrations: alginate (LF1060) 2% w/V, HAp 3% w/V, gelatin 0.05% w/V, 0.1% w/V and 0.2% w/V) in aqueous NaCl solution (final concentration 0.15 M) with HEPES (final concentration 0.01 M, pH 7.4), solubilizing gelatin at 40 °C. The microbeads were obtained by dripping the polymer blend into a gelling solution (aqueous 0.05 M $CaCl_2$) in the same conditions used for the preparation of nAg-MB.

5.2.4 POLYSACCHARIDE COATING OF GLASS SUBSTRATES

Glass coverslips (O. Kindler GmbH) were treated with Piranha solution (H_2SO_4 : H_2O_2 (30% w/w) = 3 : 1) at 80 °C for 1h, thoroughly washed with deionized water and methanol and finally air-dried. Chitlac was solubilized in HCl (until pH 4.5), chitosan was solubilized in acetic acid 0.02 M and alginate was solubilized in deionized water. All polysaccharide solutions have been used at the concentration of 0.5 w/V. For each coating step, 200 μL of polymer solution were poured onto the activated glass coverslip.

In order to prepare the monolayer coated coverslips, after the activation with the piranha solution, chitlac or chitosan were placed on the coverslips. After 1 hour of incubation at room temperature, the excess of the solution was removed and the coverslips were washed twice for 1 hour with HEPES (10 mM, pH 7.4). The coverslips were washed with deionized water and air-dried.

In order to prepare the mixed layer coated coverslips, after the activation with the piranha solution, chitlac or chitosan were placed on the coverslips. After 1 hour of incubation at room temperature, the excess of the solution was removed and the coverslips were washed with deionized water (pH 4.5) or acetic acid 0.02 M respectively and dried in air. Then alginate was placed on the chitlac or chitosan coated coverslips and incubated at room temperature for 1 hour. The excess was removed and the coverslips were washed with deionized water and air-dried. Finally, additional chitlac or chitosan solution was placed on the coverslips. After 1 hour of incubation, the excess of the solution was removed and the coverslips were washed twice for 1 hour with HEPES (10 mM, pH 7.4). The coverslips were washed with deionized water and air-dried.

5.3 MORPHOLOGICAL, CHEMICAL AND PHYSICAL CHARACTERIZATION

5.3.1 LOW FIELD NUCLEAR MAGNETIC RESONANCE (LF-NMR)

LF-NMR characterization was performed by means of a Bruker Minispec mq20 (0.47 T). Transverse relaxation time (T_2) measurements were performed at 25 °C according to Carr-Purcell-Meiboom-Gill (CPMG) sequence with a 90°-180° pulse separation of 0.25 ms (number of scans 4; delay 5 s, from 500 to 1000 time intervals). The T_2 discrete distribution was determined by fitting the experimental time (t) decay of the signal, related to the extinction of the x-y component of the magnetization vector (M_{xy}), with the sum of exponential functions ($I(t)$):

$$I(t) = \sum_{i=1}^{m} A_i e^{-t/T_{2i}} \qquad (6)$$

where A_i are the (dimensionless) pre-exponential factors proportional to the number of protons relaxing with the relaxation time T_{2i}. This fitting allowed determining the different relaxation times (T_{2i}) of the water molecules subpopulations in the sample with the respective spin density (A_{2i}).

The chosen number of subpopulations was identified with that minimizing the product χ^2*Np, where χ^2 is data fitting chi-square value, and Np is the number of model parameters used, recalling that each exponential function introduced requires two parameters.[279] $\overline{T}_2$ and $\bar{r}_2$ are defined as:

$$\overline{T}_2 = \frac{\sum_i A_i \cdot T_{2i}}{\sum_i A_i} \quad (7) \qquad \bar{r}_2 = \frac{1}{\overline{T}_2} \quad (8)$$

LF-NMR characterization has been performed on f-CNTs dispersed, at different concentrations, in deionized water, in complete culture medium (DMEM) and in salt-free aqueous alginate solution (2% w/V in deionized water), and on alginate/f-CNTs hydrogels.

5.3.2 MORPHOLOGICAL ANALYSES

5.3.2.1 Scanning Electron Microscopy of scaffolds and microbeads

The microbeads were air-dried at room temperature for 24h and subsequently mounted on aluminum stubs covered with two-sides conductive carbon adhesive tape. Freeze-casted scaffold samples were sectioned at various planes mounted using the same set up used for microbeads.

Next, the samples were sputtered with gold (Sputter Coater K550X, Emitech, Quorum Technologies Ltd, UK) and immediately analyzed by means of a scanning electron microscope (Quanta250 SEM, FEI, Oregon, USA) operated in secondary electron detection mode. The working distance was adjusted in order to obtain the suitable magnification; the accelerating voltage was set to 30 kV.

5.3.2.2 Confocal Laser Scanning Microscopy of coated coverslips and microbeads

Coated glass coverslips were prepared labeling only one of the polymers composing the coating. The coverslips were prepared in dark conditions and mounted on microscope slides.

Microbeads have been prepared using the same protocol reported in the previous paragraphs, substituting chitlac with chitlac-fluo, in order to analyze the chitlac distribution within the microbeads.

IN order to analyze the distribution and the adsorption of the alginate contained in the dispersant solution, on the microbeads surface, microbeads (30% w/w) have been dispersed in an alginate-fluo solution (4% w/V).

Images were taken with a Nikon Eclipse C1 microscope, with an objective Nikon Plan Fluor 20X (2.10 WD, dry) using an argon laser (488 nm) and an acquisition channel of 515/30 nm. Images were analyzed with ImageJ software.

5.3.2.3 Micro-computed tomography

X-ray microcomputed tomography of samples was obtained by means of a custom made cone-beam system called TOMOLAB.[342] Samples were positioned onto the turn-table of the instrument and acquisitions were performed with the following parameters: distance source-sample (FOD), 100 mm; distance source-detector (FDD), 400 mm; magnification, 3.1×; binning, 2 × 2; resolution, 8 μm; tomography dimensions (pixels), 1984 × 1024; slices dimensions (pixels), 1984 × 1984; number of tomographies, 1440; number of slices, 864; E = 40 kV, I = 200 μA; exposure time, 1.8 s. The slices reconstruction process was achieved by means of commercial software (Cobra Exxim). Input projections and output slices are represented by files (one file per projection and one file per slice) using arrays of 16-bit integers. Custom produced MatLab code has been used to get a proper segmentation of the slices using Otsu's method[343] and to obtain numerical values of structural features like porosity, interconnection, pore, and trabecular size by means of parallel plate model.[344]

5.3.2.4 Atomic Force Microscopy (AFM)

AFM images have been acquired using a MFP-3D Stand Alone AFM (Asylum Research, Santa Barbara, CA). Measures were carried out at 25 °C working in dynamic mode. High-resolution images (1024 × 1024 pixels frames) were acquired at 0.75 lines/s scan speed. The polysaccharide coating thickness has been measured after removing the coating with a scratch.

5.3.2.5 Contact angle and surface energies

Contact angles of the surfaces were measured using a Microscope Leica MZ16 equipped with a camera Leica DFC320 using the sessile drop method.[345] Both polar (ultrapure water and ethylene glycol) and apolar (ultrapure di-iodomethane) liquids were used in order to allow surface energy

calculations. A droplet of liquid (4 μL) was placed on the surface. The profile of the water drop on the surface was recorded after 10 s to avoid time-dependent angle variations among samples. Contact angles were measured by means of an image analysis software (Image Pro Plus 6.2). For statistical analysis, 10 measurements for each surface type were averaged. The surface energy parameters were calculated from the contact angle values of the probe liquids according to the acid−base method proposed by Van Oss:[291] briefly, the values of the contact angles of the three liquids were used in the Young−Duprè equation ($(1 + \cos\theta)\gamma_l = 2[(\gamma_s^{LW}\gamma_l^{LW})1/2 + (\gamma_s^{+}\gamma_l^{-})^{1/2} + (\gamma_s^{-}\gamma_l^{+})^{1/2}]$), which enables to calculate the values of the Lifshitz-van der Waals contribution of surface tension γ^{LW} and the acid−base (AB) components γ^{+} and γ^{-} of the material. The surface polarity was calculated as the ratio between the AB contribution and the total surface tension ($\gamma^{tot} = \gamma^{LW} + \gamma^{AB}$, where $\gamma^{AB} = (\gamma s^{+}\gamma l^{-})^{1/2}$). Considering the thermodynamic work of adhesion between surface and liquids, the total work is given by $W^{T} = W^{AB} + W^{LW}$ where $W^{AB} = (1 + \cos\theta)\gamma_l - 2[(\gamma_s^{LW}\gamma_l^{LW})^{1/2}$ and $W^{LW} = 2[(\gamma_s^{LW}\gamma_l^{LW})^{1/2}$, while the W^{AB}% is obtained by dividing W^{AB} by W^{T}. More details on the calculations can be found in Travan *et al*.[195]

5.3.3 SWELLING, DEGRADATION AND RELEASE STUDIES

5.3.3.1 Preparation of Simulated Body Fluid

Evaluation of the in vitro scaffold stability was performed with SBF[346] with a pH of 7.40 and ion concentrations nearly equal to those of human blood plasma (Na^{+} 142.0, K^{+} 5.0, Mg^{2+} 1.5, Ca^{2+} 2.5, Cl^{-} 147.8, HCO_3^{-} 4.2, HPO_4^{2-} 1.0, SO_4^{2-} 0.5 mM). The SBF was prepared by dissolving reagent-grade chemicals of NaCl, $NaHCO_3$, KCl, K_2HPO_4, $MgCl_2{\cdot}6H_2O$, $CaCl_2$, Na_2SO_4 in distilled water and buffering at a pH of 7.40 with tris(hydroxymethyl)aminomethane $(CH_2OH)_3CNH_2$ and 1.0 M HCl at 36.5 °C.

5.3.3.2 Swelling and degradation behavior of scaffolds

Scaffold specimens were cylindrical in shape with an average thickness of 4 mm and diameter of 16 mm and 11 mm for the CRIOsc and the ISISAsc respectively. The swelling behavior was quantified by measuring the changes in sample weight as a function of sample immersion time in SBF. Wet weights were determined after blotting with a filter paper to remove the surface liquid and the swelling ratio was calculated using the Equation (9):

$$E_{sr}(\%) = \left(\frac{W_s - W_d}{W_d}\right) \times 100 \qquad (9)$$

where E_{sr} is the amount of absorbed water (weight percent) by the polymer matrix, and W_d and W_s are the weights of the samples in the dry and the swollen state, respectively. The results were taken as the mean values of three measurements. The dimensions of the dried scaffolds, and of the rehydrated scaffolds (at the end of the experiment) were measured with a caliper.

Structural stability and integrity in SBF was evaluated during 5 weeks at 37 °C. The samples were immersed in 8 mL of SBF. Wet weight was measured after 10 min equilibration and at 7, 14, 21, 28 and 35 days of immersion after blotting on filter paper. Soaking SBF was changed after each measurement. Weight variation was calculated using the Equation (10):

$$weight\ variation\ (\%) = \left(1 - \frac{W_{tn}}{W_{10min}}\right) \times 100 \qquad (10)$$

where W_{tn} and W_{10min} are the wet weights of the samples at the defined time and after 10 min of swelling, respectively.

5.3.3.3 Swelling and stability of microbeads

Each test was performed in triplicate on a known number of beads (70-100 range). The diameter variation of the microbeads was measured by collecting the images with a Pentax K100D camera mounted on an optical microscope (Olympus CK 2, Tokyo, Japan); the diameter of beads population was measured by means of an image analysis software (ImageJ, U.S.A.). The microbeads were analyzed every two days from the beginning of the swelling experiment. The soaking solution was changed every two days.

5.3.3.4 Evaluation of silver content and silver release

The total amount of silver in the nAg-MB and released from nAg-MB, soaked in saline or in deionized water, was determined by Inductively Coupled Plasma - Optical Emission Spectroscopy (ICP-OES) using an Optima 8000 ICP-OES Spectrometer (PerkinElmer, USA) equipped with an S10 Autosampler (PerkinElmer, USA). The analysis were conducted using a calibration curve obtained by dilution (range: 0–10 mg/L) of a silver standard solution (10.015 mg/mL) for ICP-OES analyses (Sigma-Aldrich, USA). The limit of detection (LOD) at the operative wavelength of

328.068 nm was 0.016 mg/L. The precision of the measurements as relative standard deviation for the analysis was always less than 5%.

The total amount of silver in the nAg-MB (ng Ag/mg beads) was measured upon treatment with concentrated H_2SO_4 and solubilization with concentrated HNO_3. About 9 mg of microbeads were degraded in 60 µL of H_2SO_4, than the volume was adjusted to 1.2 mL with HNO_3 to ensure the solubilization of silver precipitates. At the end, the volume was adjusted to 5 mL with deionized water. The average amount of silver was calculated as the mean of silver quantity measured in three samples.

For the quantification of silver released from the nAg-MB, about 50 mg of sample were incubated, in agitation, with a volume ratio solution/microbeads of 10. Every 24 h, supernatants from the microbeads suspensions were collected and analyzed and fresh solution was added to the microbeads. After the last solution change, the microbeads were washed with filtered deionized water to recover all the precipitated silver salts; the solution was then filtered (0.22 µm) and collected.

5.3.3.5 Calcium release from scaffolds

The total amount of calcium released from the scaffolds soaked in saline, was determined by ICP-OES, using the same equipment described before. The analysis were conducted using a calibration curve obtained by dilution (range: 0–100 mg/L) of a calcium standard solution (10 mg/mL) for ICP-OES analyses (Sigma-Aldrich, USA). The LOD at the operative wavelength of 317.933 was 0.02 mg/L. The precision of the measurements as relative standard deviation for the analysis was always less than 5%.

For the quantification of calcium released from the scaffolds, about 40 mg of sample were incubated, in agitation, with a volume ratio solution/scaffolds of 10. Every 24 h, supernatants were collected and analyzed and fresh solution was added to the scaffolds.

5.3.3.6 Release of gelatin from microbeads

For the quantification of the total content of gelatin, 300 mg of microbeads of each type were degraded in 50 mL of solving buffer (sodium citrate tribasic 0.05 M, NaCl 0.1 M, pH 7.4). The solution was then centrifuged at 16000×g for 5 min and the gelatin was quantified in the

supernatants after dilution 1:10 in NaCl 0.15 M. For the quantification of gelatin released from the microbeads, 300 mg of microbeads were incubated in agitation with 10 mL of NaCl 0.15 M. Every 24 h, supernatants were collected and analyzed and fresh solution was added to the microbeads.

Gelatin contained in the solutions obtained from the microbeads degradation and from the release experiments, has been quantified using Micro BCA^{TM} Protein Assay Kit (Thermo Fisher Scientific, Milan, Italy) using a calibration curve obtained by solubilizing gelatin in NaCl 0.15 M at the concentrations indicated in the kit protocol.

5.3.3.7 Release of chitlac from alginate scaffolds

For the quantification of chitlac released from the scaffolds, CRIOsc and ISISAsc scaffold samples containing chitlac-fluo (10 mm of diameter and height) were incubated in agitation with 5 mL of NaCl 0.15 M. Every 24 h, supernatants were collected and their fluorescence measured (λ_{exc} 485 nm, λ_{em} 520 nm, FLUOstar Omega, BMG LABTECH, Germany) and fresh solution was added to the scaffolds. Chitlac-fluo has been quantified using a calibration curve obtained by solubilizing chitlac-fluo in NaCl 0.15 M.

5.3.4 MECHANICAL CHARACTERIZATION OF MATERIALS.

5.3.4.1 Steady state shear flow viscosity and mechanical spectroscopy

Rheological characterization was performed by means of a controlled stress rheometer Haake Rheo-Stress RS150, operating at 25 °C. To avoid water evaporation from the systems, the measurements were led in a water saturated environment realized by using a glass bell (solvent trap) containing a wet cloth.

The linear viscoelastic range was determined for each sample by means of a stress sweep test consisting in measuring elastic (G') and viscous (G") moduli variation with increasing shear stress ($1\ Pa < \tau < 10^3\ Pa$) with a solicitation frequency of 1 Hz.

The analysis of the hydrogels was performed using a shagreened plate and plate apparatus (HPP20 profiliert: diameter = 20mm) as measuring device. The gap between the two plates was determined for each sample through a series of short stress sweep tests (f = 1 Hz; stress range 2-5 Pa; maximum deformation < 0.02%) until a constant value of the elastic modulus G' was achieved avoiding

excessive gel squeezing. The mechanical spectrum of hydrogels was determined by measuring the elastic (G') and viscous (G") moduli variation in the frequency range from 10 to 0.01 Hz at constant shear stress $\tau = 4$ Pa, well within the linear viscoelastic range that spans up to at least 50 Pa.

The analysis of the solutions was performed using a plate and cone apparatus (C60/1°) as a measuring device. The Newtonian plateau and the non-linear region were determined for each solution by steady state shear flow experiments with the applied shear stress ranging from 0.1 to 100 Pa.

5.3.4.2 Uniaxial compression tests of hydrogels and scaffolds

Compression tests have been performed with an Universal Testing Machine (Mecmesin MultiTest 2.5-I) equipped with a 100N Load Cell. A constant compression speed of 6 mm/min was used up to sample failure. For each type of hydrogel, 7 replicates were averaged. The compression modulus (E), the Ultimate Compression Strength (σ_{UCS}), the deformation at break and the toughness were determined. The compressive modulus was calculated from the initial linear range of the stress strain curves (from 2 to 5% of strain). The hydrogels were compressed up to sample failure, while the rehydrated scaffolds were compressed until 60% of strain

The cyclic loading tests were performed by applying 10 cycles of compression (with a constant load of 2.5 N and 1 N for CRIOsc and ISISAsc scaffolds respectively) at 6 mm/min followed by the removal of the load and a pause time of 2 min to allow uptake of the water loss and the shape-recovery of the scaffolds. The CRIOsc have been analyzed as prepared, while the ISISAsc were cut to obtain a height of 12.4 mm, to ensure the same aspect ratio (1.125) of CRIOsc. The rehydration of the scaffolds have been performed in deionized water at room temperature for 2 hours.

5.3.4.3 Preparation of the injectable bone-filler and injectability evaluation

The microbeads (30%w/w) were dispersed in the polysaccharide solution and transferred into syringes (1 mL, nozzle diameter 2 mm, Chemil, Italia). The solution was composed either by alginate (4% w/V) or by a mixture of alginate (3% w/V) and hyaluronic acid (1% w/V).

The injectability tests were performed by applying an axial compression load to the syringe plunger by means of a Universal Testing Machine (Mecmesin MultiTest 2.5-I) coupled with a 100 N load

cell, applying a compression rate of 15 mm/min, along 50 mm of plunger displacement and recording the load applied. For each formulation, 5 replicates have been used, the average load in the plateau region was measured and standard deviations calculated.

5.4 BIOLOGICAL CHARACTERIZATION

5.4.1 ANTIBACTERIAL PROPERTIES OF nAg-MB

The antibacterial activity of nAg-MB was evaluated using strains of *Staphylococcus epidermidis* (ATCC® 12228™), *Staphylococcus aureus* (ATCC® 25923™) and *Pseudomonas aeruginosa* (ATCC® 27853™), and using MB as a control.

5.4.1.1 Growth inhibition assay

Bacterial suspensions were prepared by adding 20 µL of bacteria, preserved in glycerol, to 5 mL of LB broth. The obtained suspensions were incubated overnight at 37 °C. After 24 h, 500 µL of bacterial suspension was diluted in 10 mL of broth and grown up for 90 min at 37 °C in order to restore an exponential growth phase. Bacterial concentration was measured by means of optical density (OD) at 600 nm. The bacterial suspension was then diluted in 10 % (v/v) LB broth in PBS to obtain a final concentration of 10^6 bacteria/mL. 1 mL of bacterial suspension was added to each microbeads sample (50 mg). *S. aureus* and *P. aeruginosa* were incubated at 37 °C for 4 h, *S. epidermidis* for 24 h. Tests were carried out in shaking condition at 140 revolutions per minute (rpm). At the end of incubation, bacterial suspension was collected and serially diluted in PBS (from 10^{-1} to 10^{-5}) and 25 µL of each suspension were plated on LB agar. After overnight incubation at 37 °C, the colony forming units (CFU) were counted. Outcomes were compared with a suspension of bacteria grown in liquid medium as control. Data are reported as the mean of three independent determinations.

5.4.1.2 Biofilm formation

Bacterial suspensions of *S. aureus* and *P. aeruginosa* were prepared by adding 20 µL of bacteria, preserved in glycerol, to 5 mL of BHI broth enriched with 3% w/v sucrose. The obtained suspensions were incubated overnight at 37 °C. After 24 h, bacteria were diluted 1:100 in the same broth and plated (200 µL/well) into 96-well plates. For confocal laser scanning microscopy

analyses, bacteria were plated on sterile 13 mm tissue culture coverslips (Sarstedt, USA) placed on the bottom of culture plate wells. Plates were incubated at 37 °C for 24 h allowing biofilm formation. After 24 h, broth was removed and formed biofilm was carefully rinsed with 100 µL of sterile PBS in order to remove non-adherent cells. 200 µL of 10% LB in PBS were then added to each well and microbeads were deposited on the bacterial layer. Biofilms treated with microbeads were then incubated at 37 °C for 4 h; then the viability of the biomass was assessed, as described in the following paragraph.

5.4.1.3 Viable biomass assessment

The test was performed staining the biofilm with the FilmTracer™ FM® 1-43 Green Biofilm Cell Stain. The staining solution was prepared by diluting 10 µL of stock solution into 990 µL of DMSO, followed by diluting 100 µL into 0.9 mL of filter-sterilized water. After the biofilm incubation period, microbeads and medium were gently removed from the plates and each well was carefully rinsed with filter-sterilized deionized water, in order to remove non-adherent cells. 20 µL of staining solution were placed into each well and the plates were incubated for 30 minutes under lightproof conditions at room temperature. After the incubation period, each well was washed with filter-sterilized deionized water; then 80 µL of deionized water were added and the fluorescence was read with a spectrofluorimeter (λ_{exc} 485 nm, λ_{em} 520 nm, FLUOstar Omega, BMG LABTECH, Germany). Outcomes were expressed as fluorescence units.

5.4.1.4 Live/Dead biofilm viability

Confocal laser scanning microscopy (CLSM) studies were addressed at detecting viability/death of bacteria grown in the biofilm community. FilmTracer Live/Dead biofilm viability kit was used. Dead cells were stained by propidium iodide, (red fluorescence: λ_{exc} 514 nm; λ_{em} 590 nm) whereas live cells by SYTO® 9 (green fluorescence: λ_{exc} 488 nm; λ_{em} 515 nm). Staining was performed on biofilms grown on coverslips as described above, according to the manufacture's protocol. Images were acquired on a Nikon Eclipse C1si confocal laser-scanning microscope with a Nikon Plan Fluor 20× as objective. Resulting stacks of images were analyzed using ImageJ software.

5.4.2 *IN VITRO* CHARACTERIZATION OF MATERIALS ON OSTEOBLASTS

Osteosarcoma MG-63 (ATCC® CRL-1427) human cell line was cultured in DMEM high glucose (Euro-Clone, Italy), 10 % heat-inactivated fetal bovine serum (Sigma Aldrich, Chemical Co. USA), 100 U/mL penicillin, 100 µg/mL-1 streptomycin and 2 mM L-glutamine in a humidified atmosphere of 5 % CO2 at 37 °C.

5.4.2.1 Modified lactate dehydrogenase test on f-CNTs

Cytotoxicity of dispersed f-CNTs at different concentration was evaluated on MG63 cells with a modified version of the lactate dehydrogenase cytotoxicity assay (*SIGMA TOX-7LDH assay*).[319]

f-CNTs were used as sterile stock solutions at 1 mg/mL in water. Stock dispersions were sonicated for 30 min prior to use in cell culture studies and used at final concentration of 10, 50 and 100 µg/mL diluting the stock solution in complete DMEM. 500 µL of f-CNTs/DMEM solutions were used for each well. Cells were seeded into 24-well plates (30000 cells per well) and incubated 24 hours before the cytotoxicity test. The experiments were performed in triplicate. Cells were than incubated for 24 and 72 hours with f-CNTs (f_1, and f_3) diluted with medium at the different concentrations After 24 and 72 hours the medium was removed and cells were lysed with 10 µL of lysis buffer (of the SIGMA TOX-7 kit) mixed with 100 µL serum free media for 45 min at 37 °C. The cell lysate was then diluted with 800 µL of serum free media and centrifuged at 16100×g for 5 min to allow the precipitation of the f-CNTs. 45 µL of the supernatant was mixed with 90 µL of LDH substrate mix in a 96-well plate and incubated for 20 min at R.T. in light-proof conditions. The colorimetric reaction was quenched by adding 13.5 µL of HCl 1N. The absorbance was measured at 490 nm (A_{490}) and 690 nm (A_{690}), with a *Tecan Nano Quant Infinite M200 Pro* plate reader. The proliferation rate of the cells was calculated using the following equation:

$$Proliferation\ Rate = \frac{(A_{490} - A_{690} treated\ and\ untreated\ cells) - (A_{490} - A_{690} medium\ alone)}{(A_{490} - A_{690} untreated\ cells) - (A_{490} - A_{690} medium\ alone)} \quad (11)$$

5.4.2.2 Lactate dehydrogenase test on microbeads

In vitro cytotoxicity of nAg-MB was evaluated by using lactate dehydrogenase cytotoxicity assay (SIGMA TOX-7LDH assay), and using MB as a control. UV-sterilized microbeads were placed in Dulbecco's modified Eagle's medium, inactivated fetal bovine serum 10 %, penicillin 100 U/mL,

streptomycin 100 µg/mL and L-glutamine 2 mM for 24 h. After 24 h of incubation, the cytotoxicity test was performed by direct contact of the cells with the swollen microbeads (20 mg per well). Cells were seeded into 24-well plates (30000 cells per well) and incubated 24 hours before the cytotoxicity test. The experiments were performed in triplicate. Cells were than incubated for 24 and 72 hours with microbeads. After 24 and 72 hours, the medium was collected and the test was performed following the manufacturer's protocol. The absorbance was measured at 490 nm and 690 nm, with a Tecan Nano Quant Infinite M200 Pro plate reader. The cytotoxicity was calculated using the following equation:

$$\%\, LDH\ release = 100 \times \frac{(A_{490} - A_{690} treated\ cells) - (A_{490} - A_{690} medium)}{(A_{490} - A_{690} cell\ lysate) - (A_{490} - A_{690} medium)} \qquad (12)$$

normalizing the values for the total LDH of the control cell lysate. Polystyrene (PS) was used as a negative control; zinc embedded polyurethane (PU/Zn) membrane was used as positive control.

5.4.2.3 Viability of osteoblasts seeded into alginate scaffolds

For cell seeding onto scaffolds, porous freeze-casted scaffolds (prepared with HAp 0.5% w/V, gelatin or f-CNTs) were cut to obtain samples with similar dimension (diameter = 11 mm; height = 10 mm), sterilized under UV light (3 × 20 minutes), rehydrated in 5 mM $CaCl_2$ for 10 minutes and immersed in complete cell culture medium for 24 h in 24-well culture plates to ensure chemical equilibration. Osteosarcoma cells, suspended in 40 µL of medium, were loaded on the scaffolds. After 4 h, the scaffolds were placed into fresh, sterile 24-well culture plates and 1.5 mL of complete medium was added.

The viability and growth rate of MG63 osteosarcoma human cell line on Alg/HAp scaffolds was assessed as a function of time using the MTS assay according to the protocol provided by the manufacturer (CellTiter Aqueous One Solution cell proliferation assay kit from Promega). 40000 cells suspended in 40 µL of culture medium were seeded on UV-sterilized scaffolds and incubated at 37 °C in a humidified air atmosphere of containing 5% CO_2. MTS assays were performed at different endpoint from cell seeding. Briefly, after 4 h of incubation with the MTS reagent in a humidified 5% pCO_2 atmosphere, the medium was collected from the scaffolds and absorbance was measured with a *Nano Quant Infinite M200 Pro* (Tecan, Swiss) plate reader at a

wavelength of 490 nm. The background absorbance obtained from an empty scaffold (blank) was subtracted from the sample values.

5.4.2.4 Cell imaging by Scanning Electron Microscopy

Scaffolds seeded with cells were rinsed with 10 mM HEPES, pH 7.4, containing 10 mM $CaCl_2$, 100 mM NaCl, and 5 mM glucose and fixed with 10% glutaraldehyde in PBS for 1 h at room temperature. Samples were then washed three times with the same buffer described above, dehydrated by stepwise treatment with ethanol, and finally dried with a critical point dryer, sputter-coated with gold, and visualized by electron microscopy.

5.4.2.5 Cell viability on microbeads

UV-sterilized microbeads (nAg-MB and MB) were incubated in complete DMEM for 72 h. About 10 microbeads were put in each well of a Microtest Plate 96-well (Sarstedt, non-treated for cell adhesion); 5000 cells were placed in each well and left for 24 h in a humidified atmosphere of 5 % CO2 at 37 °C. Cellular adhesion and growth were tested by means of Alamar Blue™ assay: microbeads were washed with PBS and incubated with 100 uL of 10% Alamar Blue™ in DMEM, for 5 hours in darkness, at 37°C. After the time indicated the medium was removed from each well and replaced with fresh medium; the fluorescence of the collected medium was measured (λ_{exc}= 544 nm; λ_{em}= 590 nm) with a spectrofluorimeter (FLUOstar Omega, BMG LABTECH, Germany). As a control, beads without cells were incubated at the same conditions and analyzed.

5.4.2.6 Determination of alkaline phosphatase activity

A suspension of MG63 cells (100000 cells) was seeded on the scaffolds and maintained in culture in complete medium at 37 °C in a 5% pCO_2 atmosphere. At different days, scaffolds were washed at r.t. for 30 min in a buffer 10 mM HEPES, pH 7.4, containing 10 mM $CaCl_2$, 100 mM NaCl, 5 mM glucose, and finally dissolved in a sodium citrate solution (50 mM sodium citrate, 100 mM NaCl, 10 mM glucose, pH 7.4). Cells were collected by centrifugation at 800 rpm for 5 minutes and lysed in a TritonX-100 solution (0.2% w/w TritonX-100 in 100 mM Tris/HCl buffer, pH 9.8) keeping them for 30 minutes at -80 °C and transferring at 37 °C for two times. Enzymatic activity was measured in a solution of 6 mM *para*-nitro-phenyl-phosphate and 1 mM $MgCl_2$ in Tris-HCl, 100 mM, pH 9.8, after 60 min of incubation at 37 °C. Absorbance was measured at 410

nm with a *Tecan Nano Quant Infinite M200 Pro* plate reader. The results were normalized to the amount of protein content in the cellular extract calculated by means of BCA method according to the manufacturer's protocol (Sigma). All tests were performed in quadruplicate.

5.4.2.7 Quantification of osteocalcin expression

40000 cells suspended in 40 µL of culture medium were seeded on UV-sterilized scaffolds (CRIOsc and ISISAsc containing 0.5% w/V HAp) and incubated at 37 °C in a humidified air atmosphere of containing 5% CO_2. At 1, 7, 14, 21 days culture medium was harvested and the osteocalcin was quantified using the Osteocalcin ELISA Kit, Human (Thermo Fisher Scientific, Milan, Italy), according to the protocol, and normalizing the values for the viability data, determined by MTS assay (as described in the previous paragraph).

5.4.3 *IN VITRO* CHARACTERIZATION OF MATERIALS ON NEURAL CELLS

5.4.3.1 Cell cultures and co-cultures on coated coverslips

Primary cultures of hippocampal neurons were obtained from postnatal (P2-P3) rat pups (of either sex) as previously reported.[99,238,347,348] Briefly, hippocampi were isolated from the rest of the brain and cells were dissociated enzymatically and mechanically. Cells were plated (150 µl of cell suspension) on three different substrates: Chitosan monolayer, chitlac monolayer and chitlac/alginate three-layers (see Material synthesis). Plating was carried out at a nominal density of 200000 ± 16000 cells/mL (n=4 different series of cultures) meaning that ~ 30000 cells were plated on each coverslip (12 x 24 mm^2, 0.13-0.16 mm thick, Kindler, EU). Cultures were incubated at 37ºC, in a humidified atmosphere with 5% CO_2 in culture medium, consisting of MEM (Gibco) supplemented with 35 mM glucose (CarloErba Reagents), 15 mM HEPES, 1 mM Apo-Transferrin, 48 µM Insulin, 3 µM Biotin, 1 mM Vitamin B12 (Sigma-Aldrich) and 500 nM Gentamicin (Gibco) in the presence of 10% dialysed fetal bovine serum (FBS, Invitrogen). Culture medium (supplemented with the proliferation inhibitor cytosine arabinoside (Ara C) and with a lower concentration of serum (5%)) was renewed (~60%) after two days from seeding and hereafter changed every two days. Cultures were then used for experiments after 8-10 days *in vitro*.

D7 motor neuron (MN) progenitors were derived from embryonic spinal cord as described by Su *et al*.[123] Cells were cultured as neurospheres in DMEM/F12 medium supplemented with B27 (Invitrogen), EGF and bFGF (20 and 10 ng/ml, respectively; Peprotech) (growing medium) in a humidified incubator at 37°C in 5% CO_2.

To assess for differentiation, neurospheres were dissociated into single cells and transferred onto chitosan, chitlac or chitlac/alginate glass coverslips (12 mm diameter) in differentiating medium (growth medium without EGF and FGF) at 50000 cells density, in co-culture with control or neurotrophins producing MABs at the same cell density. Seven days after plating, cultures were fixed in 4% paraformaldehyde and processed for immunocytochemistry.

GFP-expressing MABs D16 were grown in DMEM plus 10% FBS as described by Galvez *et al*.[349] NGF-expressing MABs (D16-NGF, clone F10) and BDNF-expressing MABs (D16-BDNF, clone A9) have been obtained upon stable transfection of D16 cells and single clone selection, as described in Su *et al.*[123] F10 and A9 MABs produce 36 ng/ml/day/10^6 cells of NGF and 30 ng/ml/day/10^6 cells of BDNF, respectively.

In co-culture between primary neurons and control or neurotrophines producing MABs, hippocampal neurons were cultured as previously described. A 1:1 ratio between the two cell populations was maintained. Therefore, 30000 cells for each type of MABs were dissolved into the dissociated hippocampal neuron medium. These co-cultures were tested on the chitlac/alginate substrate. In this set of experiments control, D16-MABs, A9-MABs BDNF and F10-MABs NGF refer to dissociated hippocampal cultures alone, co-culture with control MABs, co-culture with BDNF-producing MABs and co-culture with NGF-producing MABs, respectively.

All animal procedures were conducted in accordance with the National Institutes of Health, international and institutional standards for the care and use of animals in research, and after consulting with a veterinarian. All experiments were performed in accordance with the EU guidelines (2010/63/UE) and Italian law (decree 26/14) and were approved by the local authority veterinary service. All efforts were made to minimize animal suffering and to reduce the number of animal used. Animals use was approved by the Italian Ministry of Health, in agreement with the EU Recommendation 2007/526/CE.

5.4.3.2 Electrophysiological recordings

For patch clamp recordings (whole-cell, voltage clamp mode), the samples were positioned in a recording chamber, mounted on an inverted microscope and continuously superfused with control Krebs solution containing (in mM): 150 NaCl, 4 KCl, 2 $CaCl_2$, 1 $MgCl_2$, 10 HEPES and 10 glucose. The pH was adjusted to 7.4 with NaOH (osmolarity 300 mOsm). Cells were patched with pipettes (4-7 MΩ) filled with a solution of the following composition (in mM): 120 K gluconate, 20 KCl, 2 $MgCl_2$, 2 Na_2ATP, 10 HEPES and 10 EGTA. The pH was adjusted to 7.3 with KOH (osmolarity 295 mOsm). Voltage values indicated in the text and in figures are not corrected for the liquid junction potential, estimated to be ~ 14 mV. Electrophysiological responses were amplified (EPC-7, HEKA; Multiclamp 700B, Axon Instruments), sampled and digitized at 10 kHz with the pClamp software (Axon Instruments) for offline analysis. Single spontaneous synaptic events were detected by the use of the AxoGraph X (Axograph Scientific) event detection program (Clements & Bekkers, 1997). On average, ≥ 400 events were analysed for each cell in order to obtain mean amplitude parameter. Neuronal passive properties were measured by repeated (80 times) stimulation of cells with a 100 ms lasting hyperpolarizing stimulus (5 mV). The area below capacitative transients was computed and normalized for voltage transient amplitude to calculate cell capacitance (C_m); input resistance (R_{in}) was obtained through Ohm's law, by measuring the amplitude of steady state current generated by the voltage transient.

5.4.3.3 Immunofluorescence: cell morphology analyses

Immunolabelling on dissociated hippocampal neurons was performed after fixation with 4% paraformaldehyde (PFA) in PBS for 20 min at room temperature. Cells were permeabilized and blocked in 5% FBS and 0.3% Triton X-100 for at least 30 min at room temperature and incubated with the following primary antibodies for 30 min: rabbit polyclonal anti- β-Tubulin III (Sigma-Aldrich, T2200, 1:500) and mouse monoclonal anti-GFAP (Sigma-Aldrich, G3893, 1:250). Upon washing, cells were then incubated for 30 min with the following secondary antibodies: goat anti-rabbit Alexa 594 (Invitrogen, A-11012, 1:500), goat anti-mouse Alexa 488 (Invitrogen, A-11001, 1:500) and 4,6-diamidine-2-phenylindole dihydrochloride (DAPI, Invitrogen, D1306, 1:200) to label the nuclei. Finally, samples were washed in PBS and quickly rinsed with milliQ water to remove the PBS salt residual and mounted on glass microscope slides

using Vectashield hardset mounting medium (Vector Laboratories). Fluorescence images were acquired using a Leica DM6000 upright microscope with a 20X dry objective. Identical binning, gains and exposure times were used for all images of the same marker. Image analysis was performed using the professional image analysis software Volocity (PerkinElmer). For the quantification of the β-Tubulin positive area, a threshold was set for both intensity and object size, thus ensuring that the observed signal indicates the presence of genuine β-Tubulin positive labelling. Cell density counting analysis (number of cells/mm^2) was obtained from at least three fields randomly selected from each sample per condition.

Immunolabelling on MN progenitors was performed after fixation in 4% PFA for 10 min at RT. Upon fixation, cells were permeabilized in 0.1% Triton X-100 in PBS and then incubated with the following primary antibodies: rabbit polyclonal anti-GFAP (DakoCytomation, Z0334, 1:250), mouse monoclonal anti-Neuronal class III β-Tubulin (Covance; MMS-435P, 1:250), goat polyclonal anti-choline acethyltransferase (ChAT) (Merck Millipore, AB144P, 1:200) and then secondary antibodies: goat-anti rabbit antiserum conjugated to Alexa 488 (Invitrogen), goat-anti mouse antiserum conjugated to Alexa 594 (Invitrogen), donkey anti-goat conjugated to Alexa 647 (Invitrogen). Immunolabelled cells were mounted in Aqua-Poly/Mount (Polysciences, Inc.) and analyzed at confocal microscopy, using a TCS SP5 microscope (Leica Microsystem). Z-stacks images were captured at 1 μm intervals with a 40X or 63X objectives and a pinhole of 1.0 Airy unit. Analyses were performed in sequential scanning mode to rule out cross-bleeding between channels. Fluorescence intensity quantification of β-tubulin was performed with ImageJ software. To quantify the percentage of differentiation, the number of β-tubulin (Tuj1) and glial fibrillary acid protein (GFAP) immunoreactive cells was counted in at least ten non-overlapping fields in each sample, for a total of >1000 cells per sample. The total number of cells in each field was determined by counterstaining cell nuclei with DAPI (Sigma-Aldrich, 50 mg/ml in PBS for 15 min at RT). The average percentage of differentiated cells for each sample was then calculated by dividing the number of Tuj1 and GFAP positive cells by the total number of cells for each field. For motor neuron differentiation, the average percentage of ChAT positive cells was calculated by dividing the number of C*h*AT immunoreactive cells a by the total number of Tuj1 positive cells for each field. Data are the mean ± standard error of the mean of three independent cultures, three independent experiments for each culture.

5.4.3.4 Statistical analyses

Results are presented as mean ± standard deviation; n is the number of neurons, if not otherwise indicated. Statistically significant difference between groups was assessed by Student's *t* test (after checking variances homogeneity by Levene's test) for parametric data and by Mann-Whitney's test for non-parametric ones. A p-value below 0.05 was accepted as indicative of a statistically significant difference.

5.4.3.5 Galectin-1 quantification (ELISA)

Galectin-1 quantification was performed by the enzyme-linked immunosorbent assay (ELISA). The quantification was performed on the culture medium, subtracted 2 times from the culture dish (the first one at the last medium change before the electrophysiological experiment and the second at the day of the experiment), to determine the amount of protein secreted by the cells. The ELISA kit Galectin 1 Mouse abcam® Company (Cambridge, UK) was used.

5.4.3.6 Immunofluorescence: localization of Galectin-1

Immunolabelling on dissociated hippocampal neurons was performed after fixation with 4% paraformaldehyde (PFA) in PBS for 20 min at room temperature. Cells were permeabilized and blocked in 5% FBS and 0.3% Triton X-100 for at least 30 min at room temperature and incubated with the following primary antibodies for 30 min: rabbit polyclonal anti-β-Tubulin III (Sigma-Aldrich, T2200, 1:500) and mouse monoclonal anti-Galectin 1 Antibody (Invitrogen, 6C8.4-1, 1:250). Upon washing, cells were then incubated for 30 min with the following secondary antibodies: goat anti-rabbit Alexa 568 (Invitrogen, A-11011, 1:400) and goat anti-mouse Alexa 488 (Invitrogen, A-11001, 1:200). Finally, samples were washed in PBS and quickly rinsed with milliQ water to remove the PBS salt residual and mounted on glass microscope slides using Mowiol mounting medium (Sigma Aldrich). Images were taken with a Nikon Eclipse C1 microscope, with an objective Nikon 60X Plan using an argon laser (488 nm) and a diode laser (568 nm), an acquisition channel of 515/30 nm and of 590/50 nm. Identical binning, gains and exposure times were used for all images of the same marker. Image analysis was performed using the ImageJ software. For the quantification of the Galectin-1 and the β-Tubulin positive areas, a threshold was

set for both intensity and object size, thus ensuring that the observed signal indicates the presence of genuine positive labelling.

5.5 *IN VIVO* CHARACTERIZATION OF INJECTABLE BONE FILLERS

5.5.1 ANIMAL MODEL

A total of 12 New Zealand white rabbits, body weight 3.9 ± 0.3 kg, age 6.9 ± 0.6 months, were used for this study. The selected animal model is well-established and recommended for use in biomaterial research.[231] Two groups of animals (6 rabbits per group) were created; scaffolds were implanted in one group for 6 weeks and in the other for 12 weeks.

5.5.2 MATERIALS PREPARATION

Three types of materials have been tested: i) alginate microbeads containing chitlac/nAg, dispersed in alginate/hyaluronic acid; ii) alginate microbeads containing chitlac, dispersed in alginate/hyaluronic acid; iii) HydroSet™, Stryker, NJ, USA (LOT n. T45SB IC01996 and LOT n. T45SK IC02000), as positive control.

The microbeads have been prepared as reported in the previous paragraphs using sterile instrumentation, autoclaved alginate, HAp and hyaluronic acid solutions and dispersions, and filtered chitac and chitlac/nAg solutions. Briefly, once the microbeads are formed, they are sterilized with UV irradiation and mixed with the autoclaved anionic polysaccharide (alginate 3% w/V; hyaluronic acid 1% w/V) solution. Autoclaved sterilized syringes have been loaded in sterile condition with the injectable formulation and sterile packaged.

The positive control material was previously divided into one syringe per rabbit. The liquid and the powder were mixed together right before the drilling of the holes, and the resulting material was used right after.

5.5.3 ANIMAL EXPERIMENTS

The animal experiments have been carried out in the Central Animal Laboratory of the University of Turku which is managed according to the Act and Decrees on the Protection of Animals used for Scientific and Educational purposes in Finland (497/2013; 564/2013; 565/2013) and the EU Directive 2010/63/EU, the Decrees 1076/85 §3 and 1360/90. The Central Animal Laboratory has

the statement of GLP Compliance to OECD Principles, is included in the national GLP-Compliance Program and is inspected on a regular basis. The animal study protocols have been planned according to the 3Rs principles (Replacement, Reduction and Refinement). The Federation of Laboratory Animal Science Associations (FELASA) guidelines on pain and distress in laboratory rodents and lagomorphs and Recommendations for euthanasia of experimental animals as well as humane endpoint have been followed up in the procedures of the experiments.

5.5.3.1 Implantations

The procedure has been designed to simulate clinical filling of a non-critical bone defect. A well-established rabbit bilateral femoral defect model has been applied. The animal model includes a creation of non-critical size medial longitudinal defects, 3 mm of diameter and 6 mm of depth, in both the left and right femoral condyles of the rabbit under general anesthesia. The anatomic location for the implantation (cancellous bone of the distal femur) provided similar structural and biomechanical conditions for the healing of multiple implants.

Two scaffold formulations and injectable bone void filler have been randomly implanted. Randomization has been performed by drawings of the lots. The codes for the compositions has not been opened before the final data analysis (blinded analysis). In addition, one bone defect in each rabbit has been left unfilled to allow evaluation of a possible trend for osteoinduction of tested materials. After surgery, the functional activity of the animals is not restricted and the animals receive a post-operative pain medication. The animals have been euthanized 6 and 12 weeks after implantation in order to evaluate bone tissue healing and the replacement of materials.

5.5.3.2 Micro-computed tomography (μ-CT) imaging

The imaging was performed by SkyScan 1072 scanner (Skyscan N.V. Kontich, Belgium). One knee containing two implants was imaged in each imaging session. In the μ-CT imaging, the imaging step angle was 0.45 degrees, within a full angle of 180 degrees. The source voltage was 61 kV, the source current was 163 μA, and no filters were used. In image acquisition, a single 16-bit grayscale shadow projection image was obtained for each step angle as an average of two consequent images. Image averaging resulted in the improved quality of the images. The acquired shadow projection images were reconstructed into an array of cross-sectional 8 bit grayscale

images using NRecon software (version v.1.4.3, Skyscan N.V. Kontich, Belgium). Automatic post-alignment and beam hardening correction were used in the reconstruction. The resulting spatial resolution of the cross-sectional images was 18.9 μm per pixel.

5.5.3.3 Analysis of the μ-CT data

The arrays of the reconstructed cross-sectional images were loaded into DataViewer software (version v.1.4.4 64 bit, Skyscan N.V. Kontich, Belgium). For each of the two implants, the images were repositioned along the long axis of the implant (drilling direction) and cropped in a standardized way leaving sufficient amount of per-implant bone visible. This operation resulted in the creation of separate data arrays for each implant. These data arrays were characterized using CT analyzer software (CTAn version 1.5.0.0. Skyscan N.V. Kontich, Belgium). For each implant, a standard cylindrical volume of interest (VOI) with the diameter of 3 mm and the height of 3 mm was created within the implant volume.

In the analysis, local thresholding procedure (adaptive mean) with pre-thresholding (50 - 255 grayscale levels) was applied to segment the pixels containing bone and or implants from non-mineralized tissues and voids. The selection was inverted to obtain dark grayscale pixels, which represented the non-mineralized tissues and voids. The total amount of dark grayscale pixels was counted within the VOI and expressed as percentage of the total area of the VOI. These dark grayscale pixels were expected to give an estimate of the volumes not occupied by the mineralized bone.

6 BIBLIOGRAPHY

1. Langer, R.; Vacanti, J. P. Tissue engineering. *Science* **1993,** *260* (5110), 920-926.

2. Salgado, A. J.; Oliveira, J. M.; Martins, A.; Teixeira, F. G.; Silva, N. A.; Neves, N. M.; Sousa, N.; Reis, R. L. Tissue engineering and regenerative medicine: past, present, and future. *Int. Rev. Neurobiol.* **2013,** *108* (1), 1-33.

3. Danie Kingsley, J.; Ranjan, S.; Dasgupta, N.; Saha, P. Nanotechnology for tissue engineering: need, techniques and applications. *J. Pharm. Res.* **2013,** *7* (2), 200-204.

4. Chen, C. Y.; Ke, C. J.; Yen, K. C.; Hsieh, H. C.; Sun, J. S.; Lin, F. H. 3D porous calcium-alginate scaffolds cell culture system improved human osteoblast cell clusters for cell therapy. *Theranostics* **2015,** *5* (6), 643-655.

5. Porter, J. R.; Ruckh, T. T.; Popat, K. C. Bone tissue engineering: a review in bone biomimetics and drug delivery strategies. *Biotechnol. Progress* **2009,** *25* (6), 1539-1560.

6. Straley, K. S.; Foo, C. W.; Heilshorn, S. C. Biomaterial design strategies for the treatment of spinal cord injuries. *J. Neurotrauma* **2010,** *27* (1), 1-19.

7. Lee, K.; Silva, E. A.; Mooney, D. J. Growth factor delivery-based tissue engineering: general approaches and a review of recent developments. *J. R. Soc. Interface* **2011,** *6* (8), 153-170.

8. He, J.; Zhong, C.; Mi, J. Modeling of drug release from bioerodible polymer matrices. *Drug Deliv.* **2005,** *12* (5), 251-259.

9. Ulijn, R. V.; Bibi, N.; Jayawarna, V.; Thornton, P. D.; Todd, S. J.; Mart, R. J.; Smith, A. M.; Gough, J. E. Bioresponsive hydrogels. *Mater. Today* **2007,** *10* (4), 40-48.

10. Michel, J.; Penna, M.; Kochen, J.; Cheung, H. Recent advances in hydroxyapatite scaffolds containing mesenchymal stem cells. *Stem Cells Int.* **2015,** *2015*, 305217.

11. Giuliani, J.; Pickett, A. Cell-based chondral restoration. *Curr. Rev. Musculoskelet. Med.* **2015,** *8* (4), 436-442.

12. Fallahiarezoudar, E.; Ahmadipourroudposht, M.; Idris, A.; Mohd Yusof, N. A review of: application of synthetic scaffold in tissue engineering heart valves. *Mater. Sci. Eng., C* **2015,** *48*, 556-565.

13. Markeson, D.; Pleat, J. M.; Sharpe, J. R.; Harris, A. L.; Seifalian, A. M.; Watt, S. M. Scarring, stem cells, scaffolds and skin repair. *J. Tissue. Eng. Regener. Med.* **2015,** *9* (6), 649-668.

14. Shrestha, B.; Coykendall, K.; Li, Y.; Moon, A.; Priyadarshani, P.; Yao, L. Repair of injured spinal cord using biomaterial scaffolds and stem cells. *Stem Cell Res. Ther.* **2014,** *5* (4), 1-11.

15. Gladysz, D.; Hozyasz, K. K. Stem cell regenerative therapy in alveolar cleft reconstruction. *Arch. Oral Biol.* **2015,** *60* (10), 1517-1532.

16. Davies, B. M.; Morrey, M. E.; Mouthuy, P. A.; Baboldashti, N. Z.; Hakimi, O.; Snelling, S.; Price, A.; Carr, A. Repairing damaged tendon and muscle: are mesenchymal stem cells and scaffolds the answer? *Regen. Med.* **2013,** *8* (5), 613-620.

17. Wahl, E. A.; Fierro, F. A.; Peavy, T. R.; Hopfner, U.; Dye, J. F.; Machens, H. G.; Egana, J. T.; Schenck, T. L. In vitro evaluation of scaffolds for the delivery of mesenchymal stem cells to wounds. *Biomed. Res. Int.* **2015,** *2015*, 108571.

18. El-Amin, S. F.; Lu, H. H.; Khan, Y.; Burems, J.; Mitchell, J.; Tuan, R. S.; Laurencin, C. T. Extracellular matrix production by human osteoblasts cultured on biodegradable polymers applicable for tissue engineering. *Biomaterials* **2003,** *24* (7), 1213-1221.

19. Laurencin, C. T.; Attawia, M. A.; Lu, L. Q.; Borden, M. D.; Lu, H. H.; Gorum, W. J.; Lieberman, J. R. Poly(lactide-co-glycolide)/hydroxyapatite delivery of BMP-2-producing cells: a regional gene therapy approach to bone regeneration. *Biomaterials* **2001,** *22* (11), 1271-1277.

20. Geiger, F.; Lorenz, H.; Xu, W.; Szalay, K.; Kasten, P.; Claes, L.; Augat, P.; Richter, W. VEGF producing bone marrow stromal cells (BMSC) enhance vascularization and resorption of a natural coral bone substitute. *Bone* **2007,** *41* (4), 516-522.

21. Rezwan, K.; Chen, Q. Z.; Blaker, J. J.; Boccaccini, A. R. Biodegradable and bioactive porous polymer/inorganic composite scaffolds for bone tissue engineering. *Biomaterials* **2006,** *27* (18), 3413-3431.

22. Donati, I.; Paoletti, S. Material properties of alginates. In *Alginates: biology and applications*, 13 ed.; Rehm, B. H. A., Ed.; Springer Berlin Heidelberg: **2009**; pp 1-53.

23. Morris, E. R.; Rees, D. A.; Thom, D.; Boyd, J. Chiroptical and stoichiometric evidence of a specific, primary dimerisation process in alginate gelation. *Carbohydr. Res.* **1978,** *66* (1), 145-154.

24. Smidsrod, O. Molecular basis for some physical properties of alginates in the gel state. *Faraday Discuss Chem. Soc.* **1974,** *57*, 263-274.

25. Haug, A.; Smidsrod, O. Selectivity of some anionic polymers for divalent metal ions. *Acta Chem. Scand.* **1970,** *24*, 843-854.

26. Sayag, J.; Meaume, S.; Bohbot, S. Healing properties of calcium alginate dressings. *J. Wound. Care* **1996,** *5* (8), 357-362.

27. Blair, S. D.; Jarvis, P.; Salmon, M.; McCollum, C. Clinical trial of calcium alginate haemostatic swabs. *Br. J. Surg.* **1990,** *77* (5), 568-570.

28. Maggiori, L.; Rullier, E.; Meyer, C.; Portier, G.; Faucheron, J. L.; Panis, Y. Randomixed controlled trial of pelvic calcium alginate following rectal cancer surgery. *Br. J. Surg.* **2010,** *97* (4), 479-484.

29. Sun, J.; Tan, H. Alginate-based biomaterials for regenerative medicine applications. *Materials* **2013,** *6* (4), 1285-1309.

30. Porrelli, D.; Travan, A.; Turco, G.; Marsich, E.; Borgogna, M.; Paoletti, S.; Donati, I. Alginate-hydroxyapatite bone scaffolds with isotropic or anisotropic pore Structure: material properties and biological behavior. *Macromol. Mater. Eng.* **2015,** *300* (10), 989-1000.

31. McKay, C. A.; Pomrenke, R. D.; McLane, J. S.; Schaub, N. J.; DeSimone, E. K.; Ligon, L. A.; Gilbert, R. J. An injectable, calcium responsive composite hydrogel for the treatment of acute Spinal Cord Injury. *ACS Appl. Mater. Interfaces* **2014,** *6* (3), 1424-1438.

32. Kumar, P.; Choonara, Y. E.; Toit, L. C.; Modi, G.; Naidoo, D.; Pillay, V. Novel high-viscosity polyacrylamidated chitosan for neural tissue engineering: fabrication of anisotropic neurodurable scaffold via molecular disposition of persulfate-mediated polymer slicing and complexation. *Int. J. Mol. Sci.* **2012,** *13*, 13966-13984.

33. Dodane, V.; Vilivalam, V. D. Pharmaceutical applications of chitosan. *Pharm. Sci. Technol. Today* **1998,** *1* (6), 246-253.

34. Chandy, T.; Sharma, C. P. Chitosan as a biomaterial. *Biomater. Artif. Cells Artif. Organs* **1990,** *18* (1), 1-24.

35. Kim, I. Y.; Seo, S. J.; Moon, H. S.; Yoo, M. K.; Park, I. Y.; Kim, B. C.; Cho, C. S. Chitosan and its derivatives for tissue engineering applications. *Biotechnol. Adv.* **2008,** *26* (1), 1-21.

36. Kogan, G.; Soltes, L.; Stern, R.; Gemeiner, P. Hyaluronic acid: a natural biopolymer with a broad range of biomedical and industrial applications. *Biotechnol. Lett.* **2007,** *29*, 17-25.

37. Tang, S.; Vickers, S. M.; Hsu, H. P.; Spector, M. Fabrication and characterization of porous hyaluronic acid-collagen composite scaffolds. *J. Biomed. Mater. Res. A* **2007,** *82* (2), 323-335.

38. John, H. E.; Price, R. D. Perspectives in the selection of hyaluronic acid fillers for facial wrinkles and aging skin. *Patient Prefer Adherence* **2009,** *3*, 225-230.

39. Jiang, D.; Liang, J.; Noble, P. W. Hyaluronan in tissue injury and repair. *Annu. Rev. Cell Dev. Biol.* **2007,** *23*, 435-461.

40. Burdick, J. A.; Prestwich, G. D. Hyaluronic acid hydrogels for biomedical applications. *Adv. Mater.* **2011,** *23* (12), H41-H56.

41. Valentine, R.; Wormald, P. J.; Sindwani, R. Advances in absorbable biomaterials and nasal packing. *Otolaryngol. Clin. North Am.* **2009,** *42* (5), 813-828.

42. Saska, S.; Teixeira, L. N.; Tambasco de Oliveira, P.; Minarelli Gaspar, A. M.; Lima Ribeiro, S. J.; Messaddeq, Y.; Marchetto, R. Bacterial cellulose-collagen nanocomposite for bone tissue engineering. *J. Mater. Chem.* **2012,** *22* (41), 22102-22112.

43. Sakai, S.; Hashimoto, I.; Kawakami, K. Synthesis of an agarose-gelatin conjugate for use as a tissue engineering scaffold. *J. Biosci. Bioeng.* **2007,** *103* (1), 22-26.

44. Alaminos, M.; Sànchez-Quevedo, M. D. C.; Muñoz-Ávila, J. I.; Serrano, D.; Medialdea, S.; Carreras, I.; Campos, A. Construction of a complete rabbit cornea substitute using a fibrin-agarose scaffold. *Invest. Ophthalmol. Vis. Sci.* **2006,** *47* (8), 3311-3317.

45. Yu, X.; Dillon, G. P.; Bellamkonda, R. V. A laminin and nerve growth factor-laden three-dimensional scaffold for enhanced neurite extension. *Tissue Eng.* **1999,** *5* (4), 291-304.

46. Klaver, C. L.; Caplan, M. R. Bioactive surface for neural electrodes: Decreasing astrocyte proliferation via transforming growth factor-β1. *J. Biomed. Mater. Res.* **2007,** *81A* (4), 1011-1016.

47. Massia, S. P.; Holecko, M. M.; Ehteshami, G. R. In vitro assessment of bioactive coatings for neural implant applications. *J. Biomed. Mater. Res.* **2004,** *68A* (1), 177-186.

48. Patel, H.; Bonde, M.; Srinivasan, G. Biodegradable polymer scaffold for tissue engineering. *Trends Biomater. Artif. Organs* **2011,** *25* (1), 20-29.

49. Alberts, S.; Johnson, A.; Lewis, J.; Raff, M.; Roberts, K.; Walter, P. *Molecular biology of the cell;* Garland Science: New York, **2002**.

50. Shoulders, M. D.; Raines, R. T. Collagen structure and stability. *Annu. Rev. Biochem.* **2009,** *78*, 929-958.

51. Okuyama, K.; Hongo, C.; Fukushima, R.; Wu, G.; Narita, H.; Noguchi, K.; Tanaka, Y.; Nishino, N. Crystal structures of collagen model peptides with Pro-Hyp-Gly repeating sequence at 1.26 Å resolution: implications for proline ring puckering. *Biopolymers* **2004,** *76* (5), 367-377.

52. Chattopadhyay, S.; Raines, R. T. Review collagen-based biomaterials for wound healing. *Biopolymers* **2014,** *101* (8), 821-833.

53. Badylak, S. F. Xenogeneic extracellular matrix as a scaffold for tissue reconstruction. *Transplant Immunol.* **2004,** *12* (3-4), 367-377.

54. Rutschmann, C.; Baumann, S.; Cabalzar, J.; Luther, K.; Hennet, T. Recombinant expression of hydroxylated human collagen in Escherichia coli. *Appl. Microbiol. Biotechnol.* **2014,** *98* (10), 4445-4455.

55. Perez, R. A.; Kim, H. W.; Ginebra, M. P. Polymeric additives to enhance the functional properties of calcium phosphate cements. *J. Tissue Eng.* **2012,** *3* (1).

56. Grigore, A.; Sarker, B.; Fabry, B.; Boccaccini, A. R.; Detsch, R. Behavior of encapsulated MG-63 cells in RGD and gelatine-modified alginate hydrogels. *Tissue Eng., Part A* **2014,** *20* (15-16), 2140-2150.

57. Bernhardt, A.; Despang, F.; Lode, A.; Demmler, A.; Hanke, T.; Gelinsky, M. Proliferation and osteogenic differentiation of human bone marrow stromal cells on alginate-gelatine-hydroxyapatite scaffolds with anisotropic pore structure. *J. Tissue Eng. Regen. Med.* **2009,** *3* (1), 54-62.

58. Huang, Y.; Onyeri, S.; Siewe, M.; Moshfeghian, A.; Madihally, S. V. In vitro characterization of chitosan-gelatin scaffolds for tissue engineering. *Biomaterials* **2005,** *26* (36), 7616-7627.

59. Ferreira Almeida, P.; Almeida, A. J. Cross-linked alginate-gelatine beads: a new matrix for controlled release of pindolol. *J. Control. Rel.* **2004,** *97* (3), 431-439.

60. Augst, A. D.; Kong, H. J.; Mooney, D. J. Alginate hydrogels as biomaterials. *Macromol. Biosci.* **2006,** *6* (8), 623-633.

61. Drury, J. L.; Mooney, D. J. Hydrogels for tissue engineering: scaffold design variables and applications. *Biomaterials* **2003,** *24* (24), 4337-4351.

62. Faury, G. Function-structure relationship of elastic arteries in evolution: from microfibrils to elastin and elastic fibres. *Pathol. Biol.* **2001,** *49* (4), 310-325.

63. Martyn, C.; Greenwald, S. A Hypothesis about a mechanism for the programming of blood pressure and vascular disease in early life. *Clin. Exp. Pharmacol. Physiol.* **2001,** *28* (11), 948-951.

64. Pasquali-Ronchetti, I.; Baccarani-Contri, M. Elastic fiber during development and aging. *Microsc. Res. Tech.* **1997,** *38* (4), 428-435.

65. Nivison-Smith, L.; Weiss, A. Elastin based constructs. In *Regen. Med. Tissue Eng. Biomater.*, InTech ed.; Eberli, D., Ed.; **1997**; pp 323-340.

66. Daamen, W. F.; Veerkamp, J. H.; van Hest, J. C. M.; van Kuppevelt, T. H. Elastin as a biomaterial for tissue engineering. *Biomaterials* **2007,** *28* (30), 4378-4398.

67. Ahmed, T. A.; Dare , E. V.; Hincke, M. Fibrin: a versatile scaffold for tissue engineering applications. *Tissue. Eng., Part B Rev.* **2008,** *14* (2), 199-215.

68. Sakiyama, S. E.; Schense, J. C.; Hubbell, J. A. Incorporation of heparin-binding peptides into fibrin gels enhances neurite extension: an example of designer matrices in tissue engineering. *FASEB J* **1999,** *13*, 2214-2224.

69. Yun, Y. R.; Hang Pham, L. B.; Yoo, Y. R.; Lee, S.; Kim, H. W.; Jang, J. H. Engineering of self-assembled fibronectin matrix protein and its effects on mesenchymal stem cells. *Int. J. Mol. Sci.* **2015,** *16* (8), 19645-19656.

70. Kang, W.; Park, S.; Jang, J. H. Kinetic and functional analysis of the heparin-binding domain of fibronectin. *Biotechnol. Lett.* **2008,** *30* (1), 55-59.

71. Hynes, R. O. Integrins: bidirectional, allosteric signaling machines. *Cell.* **2002,** *110* (6), 673-687.

72. Yamada, Y.; Hozumi, K.; Aso, A.; Hotta, A.; Toma, K.; Katagiri, F.; Kikkawa, Y.; Nomizu, M. Laminin active peptide/agarose matrices as multifunctional biomaterials for tissue engineering. *Biomaterials* **2012,** *33* (16), 4118-4125.

73. Junka, R.; Valmikinathan, C. M.; Kalyon, D. M.; Yu, X. Laminin functionalized biomimetic nanofibers for nerve tissue engineering. *J. Biomater. Tissue Eng.* **2013,** *3* (4), 494-502.

74. Stabenfeldt, S. E.; García, A. J.; LaPlaca, M. C. Thermoreversible laminin-functionalized hydrogel for neural tissue engineering. *J. Biomed. Mater. Res.* **2006,** *77A* (4), 718-725.

75. Mottaghitalab, F.; Hosseinkhani, H.; Shokrgozar, M. A.; Mao, C.; Yang, M.; Farokhi, M. Silk as a potential candidate for bone tissue engineering. *J. Control. Rel.* **2015,** *215*, 112-128.

76. Han, K. S.; Song, J.; Tripathy, N.; Kim, H.; Moon, B.; Park, C.; Khang, G. Effect of pore sizes of silk scaffolds for cartilage tissue engineering. *Macromol. Res.* **2015**.

77. Hochman, S. Spinal cord. *Curr. Biol.* **2007,** *17* (22), R950-R955.

78. Bradbury, E. J.; McMahon, S. B. Spinal cord repair strategies: why do they work? *Nat. Rev. Neurosci.* **2006,** *7* (8), 644-653.

79. Steward, M.; Sridhar, A.; Meyer, J. Neural regeneration. In *New perspectives in regeneration*, 367 ed.; Heber-Katz, E., Stocum, D. L., Eds.; Springer Berlin Heidelberg: **2013**; pp 163-191.

80. Wang, M.; Zhai, P.; Chen, X.; Schreyer, D. J.; Sun, X.; Cui, F. Bioengineered scaffolds for spinal cord repair. *Tissue Eng., Part B Rev.* **2011,** *17*, 177-194.

81. Cosar, S. N. S.; Yemisci, O. U.; Oztop, P.; Cetin, N.; Sarifakioglu, B.; Yalbuzdag, S. A.; Ustaomer, K.; Karatas, M. Demographic characteristics after traumatic and non-traumatic spinal cord injury: a retrospective comparison study. *Spinal Cord* **2010,** *48* (12), 862-866.

82. Guilcher, S. J.; Munce, S. E.; Couris, C. M.; Fung, K. Health care utilization in non-traumatic and traumatic spinal cord injury: a population-based study. *Spinal Cord* **2010,** *48* (1), 45-50.

83. Singh, A.; Tetreault, L.; Kalsi-Ryan, S.; Nouri, A.; Fehlings, M. G. Global prevalence and incidence of traumatic spinal cord injury. *Clin. Epidemiol.* **2014,** *6*, 309-331.

84. Beattie, M. S.; Hermann, G. E.; Rogers, R. C.; Bresnahan, J. C. Cell death in models of spinal cord injury. In *Progress in brain research spinal cord trauma: regeneration, neural repair and Functional Recovery*, Chapter 4, Volume 137 ed.; McKerracher, L., Ed.; Elsevier: **2002**; pp 37-47.

85. Tator, C. H. Update on the pathophysiology and pathology of acute spinal cord injury. *Brain Pathol.* **1995,** *5* (4), 407-413.

86. Yiu, G.; He, Z. Glial inhibition of CNS axon regeneration. *Nat. Rev. Neurosci.* **2006,** *7* (8), 617-627.

87. Pasterkamp, R. J.; Giger, R. J.; Ruitenberg, M. J.; Holtmaat, A. J. G. D.; De Wit, J.; De Winter, F.; Verhaagen, J. Expression of the gene encoding the chemorepellent semaphorin III is induced in the fibroblast component of neural scar tissue formed following injuries of adult but not neonatal CNS. *Mol. Cell. Neurosci.* **1999,** *13* (2), 143-166.

88. Hynds, D. L.; Snow, D. M. Neurite outgrowth inhibition by chondroitin sulfate proteoglycan: stalling/stopping exceeds turning in human neuroblastoma growth cones. *Exp. Neurol.* **1999,** *160* (1), 244-255.

89. Ji, W.; Hu, S.; Zhou, J.; Wang, G.; Wang, K.; Zhang, Y. Tissue engineering is a promising method for the repair of spinal cord injuries (Review). *Exp. Ther. Med.* **2014,** *7* (3), 523-528.

90. Musienko, P.; Heutschi, J.; Friedli, L.; den Brand, R. v.; Courtine, G. g. Multi-system neurorehabilitative strategies to restore motor functions following severe spinal cord injury. *Exp. Neurol.* **2012,** *235* (1), 100-109.

91. Thuret, S.; Moon, L. D. F.; Gage, F. H. Therapeutic interventions after spinal cord injury. *Nat. Rev. Neurosci.* **2006,** *7* (8), 628-643.

92. Ramer, L. M.; Ramer, M. S.; Steeves, J. D. Setting the stage for functional repair of spinal cord injuries: a cast of thousands. *Spinal Cord* **2005,** *43* (3), 134-161.

93. Geller, H. M.; Fawcett, J. W. Building a bridge: engineering spinal cord repair. *Exp. Neurol.* **2002,** *174* (2), 125-136.

94. Francis, N. L.; Hunger, P. M.; Donius, A. E.; Riblett, B. W.; Zavaliangos, A.; Wegst, U. G. K.; Wheatley, M. A. An ice-templated, linearly aligned chitosan-alginate scaffold for neural tissue engineering. *J. Biomed. Mater. Res.* **2013,** *101* (12), 3493-3503.

95. Fabbro, A.; Bosi, S.; Ballerini, L.; Prato, M. Carbon nanotubes: artificial nanomaterials to engineer single neurons and neuronal networks. *ACS Chem. Neurosci.* **2012,** *3* (8), 611-618.

96. Dvir, T.; Timko, B. P.; Kohane, D. S.; Langer, R. Nanotechnological strategies for engineering complex tissues. *Nat. Nanotech.* **2011,** *6*, 13-22.

97. Oakland, R. J.; Hall, R. M.; Wilcox, R. K.; arton, D. C. The biomechanical response of spinal cord tissue to uniaxial loading. *Proc. Inst. Mec. Eng. H.* **2006,** *220* (4), 489-492.

98. Stokols, S.; Tuszynski, M. H. Freeze-dried agarose scaffolds with uniaxial channels stimulate and guide linear axonal growth following spinal cord injury. *Biomaterials* **2006,** *27* (3), 443-451.

99. Bosi, S.; Rauti, R.; Laishram, J.; Turco, A.; Lonardoni, D.; Nieus, T.; Prato, M.; Scaini, D.; Ballerini, L. From 2D to 3D: novel nanostructured scaffolds to investigate signalling in reconstructed neuronal networks. *Sci. Rep.* **2015,** *5*, 9562.

100. Huang, J.; Lu, L.; Zhang, J.; Hu, X.; Zhang, Y.; Liang, W.; Wu, S.; Luo, Z. Electrical stimulation to conductive scaffold promotes axonal regeneration and remyelination in a rat model of large nerve defect. *PLoS ONE* **2012,** *7* (6), e39526.

101. Dittrich, R.; Tomandl, G.; Despang, F.; Bernhardt, A.; Hanke, T.; Pompe, W.; Gelinsky, M. Scaffolds for hard tissue engineering by ionotropic gelation of alginate-influence of selected preparation parameters. *J. Am. Ceram. Soc.* **2007,** *90* (6), 1703-1708.

102. Gnanaprakasam Thankam, F.; Muthu, J. Alginate based hybrid copolymer hydrogels-Influence of pore morphology on cell-material interaction. *Carbohydr. Polym.* **2014,** *112*, 235-244.

103. Mathieu, L. M.; Mueller, T. L.; Bourban, P. E.; Pioletti, D. P.; Müller, R.; Månson, J. A. Architecture and properties of anisotropic polymer composite scaffolds for bone tissue engineering. *Biomaterials* **2006,** *27* (6), 905-916.

104. He, F.; Chen, Y.; Li, J.; Lin, B.; Ouyang, Y.; Yu, B.; Xia, Y.; Yu, B.; Ye, J. Improving bone repair of femoral and radial defects in rabbit by incorporating PRP into PLGA/CPC composite scaffold with unidirectional pore structure. *J. Biomed. Mater. Res.* **2015,** *103* (4), 1312-1324.

105. Qi, X.; Ye, J.; Wang, Y. Alginate/poly (lactic-co-glycolic acid)/calcium phosphate cement scaffold with oriented pore structure for bone tissue engineering. *J. Biomed. Mater. Res.* **2009,** *89A* (4), 980-987.

106. Serrano, M. C.; Nardecchia, S.; García-Rama, C.; Ferrer, M. L.; Collazos-Castro, J. E.; del Monte, F.; Gutiérrez, M. C. Chondroitin sulphate-based 3D scaffolds containing MWCNTs for nervous tissue repair. *Biomaterials* **2014,** *35* (5), 1543-1551.

107. Fonseca-García, A.; Mota-Morales, J. D.; Quintero-Ortega, I. A.; García-Carvajal, Z. Y.; Martínez-López, V.; Ruvalcaba, E.; Solis, L.; Ibarra, C.; Gutiérrez, M. C.; Terrones, M.; Sanchez, I. C.; del Monte, F.; Velasquillo, M. C.; Luna-Bárcenas, G. Effect of doping in carbon nanotubes on the viability of biomimetic chitosan-carbon nanotubes-hydroxyapatite scaffolds. *J. Biomed. Mater. Res.* **2013,** *102* (10), 3341-3351.

108. Kwon, S. M.; Kim, H. S.; Jin, H. J. Multiwalled carbon nanotube cryogels with aligned and non-aligned porous structures. *Polymer* **2009,** *50* (13), 2786-2792.

109. Yao, X.; Yao, H.; Li, Y. Hierarchically aligned porous scaffold by ice-segregation-induced self-assembly and thermally triggered electrostatic self-assembly of oppositely charged thermosensitive microgels. *J. Mater. Chem.* **2009,** *19* (36), 6516-6520.

110. Deville, S.; Saiz, E.; Nalla, R. K.; Tomsia, A. P. Freezing as a path to build complex composites. *Science* **2006,** *311* (5760), 515-518.

111. Nardecchia, S.; Serrano, M. C.; Gutiérrez, M. C.; Ferrer, M. L.; Monte, F. d. Modulating the cytocompatibility of tridimensional carbon nanotube-based scaffolds. *J. Mater. Chem. B* **2013,** *1* (24), 3064-3072.

112. Kuo, Y. C.; Wang, C. C. Guided differentiation of induced pluripotent stem cells into neuronal lineage in alginate-chitosan-gelatin hydrogels with surface neuron growth factor. *Colloids Surf., B* **2013,** *104*, 194-199.

113. Xiao, W.; Hu, X. Y.; Zeng, W.; Huang, J. H.; Zhang, Y. G.; Luo, Z. J. Rapid sciatic nerve regeneration of rats by a surface modified collagen-chitosan scaffold. *Injury* **2013,** *44* (7), 941-946.

114. Yi, X.; Jin, G.; Tian, M.; Mao, W.; Qin, J. Porous chitosan scaffold and NGF promote neuronal differentiation of neural stem cells in vitro. *Neuro. Endocrinol. Lett.* **2011,** *32* (5), 705-710.

115. Khaing, Z. Z.; Schmidt, C. E. Advances in natural biomaterials for nerve tissue repair. *Neurosci. Lett.* **2012,** *519* (2), 103-114.

116. Wei, Y. T.; He, Y.; Xu, C. L.; Wang, Y.; Liu, B. F.; Wang, X. M.; Sun, X. D.; Cui, F. Z.; Xu, Q. Y. Hyaluronic acid hydrogel modified with nogo-66 receptor antibody and poly-L-lysine to promote axon regrowth after spinal cord injury. *J. Biomed. Mater. Res. B Appl. Biomater.* **2010,** *95* (1), 110-117.

117. Johnson, P. J.; Parker SR FAU - Sakiyama-Elbert, S.; Sakiyama-Elbert, S. E. Controlled release of neurotrophin-3 from fibrin-based tissue engineering scaffolds enhances neural fiber sprouting following subacute spinal cord injury. *Biotechnol. Bioeng.* **2009,** *104* (6), 1207-1214.

118. King, V. R.; Henseler, M.; Brown, R. A.; Priestley, J. V. Mats made from fibronectin support oriented growth of axons in the damaged spinal cord of the adult rat. *Exp. Neurol.* **2003,** *182* (2), 383-398.

119. Sasaki, M.; Radtke, C.; Tan, A. M.; Zhao, P.; amada, H.; oukin, K.; onmou, O.; ocsis, J. D. BDNF-hypersecreting human mesenchymal stem cells promote functional recovery, axonal sprouting, and protection of corticospinal neurons after spinal cord injury. *J. Neurosci.* **2009,** *29* (47), 14932-14941.

120. Hwang, D. H.; Kim, H. M.; Kang, Y. M.; Joo, I. S.; Cho, C. S.; Yoon, B. W.; Kim, S. U.; Kim, B. G. Combination of multifaceted strategies to maximize the therapeutic benefits of neural stem cell transplantation for spinal cord repair. *Cell Transplant.* **2011,** *20* (9), 1361-1379.

121. Sampaolesi, M.; Blot, S.; D'Antona, G.; Granger, N.; Tonlorenzi, R.; Innocenzi, A.; Mognol, P.; Thibaud, J. L.; Galvez, B. G.; Barthelemy, I.; Perani, L.; Mantero, S.; Guttinger, M.; Pansarasa, O.; Rinaldi, C.; Cusella De Angelis, M. G.; Torrente, Y.; Bordignon, C.; Bottinelli, R.; Cossu, G. Mesoangioblast stem cells ameliorate muscle function in dystrophic dogs. *Nature* **2006,** *444* (7119), 574-579.

122. Morosetti, R.; Mirabella, M.; Gliubizzi, C.; Broccolini, A.; Sancricca, C.; Pescatori, M.; Gidaro, T.; Tasca, G.; Frusciante, R.; Tonali, P. A.; Cossu, G.; Ricci, E. Isolation and characterization of mesoangioblasts from facioscapulohumeral muscular dystrophy muscle biopsies. *Stem Cells* **2007,** *25* (12), 3173-3182.

123. Su, T.; Scardigli, R.; Fasulo, L.; Paradiso, B.; Barbieri, M.; Binaschi, A.; Bovolenta, R.; Zucchini, S.; Cossu, G.; Cattaneo, A.; Simonato, M. Bystander effect on brain tissue of mesoangioblasts producing neurotrophins. *Cell Transplant.* **2012,** *21* (8), 1613-1627.

124. Wu, S.; Liu, X.; Yeung, K. W. K.; Liu, C.; Yang, X. Biomimetic porous scaffolds for bone tissue engineering. *Mater. Sci. Eng., R* **2014,** *80*, 1-36.

125. Jang, J. H.; Castano, O.; Kim, H. W. Electrospun materials as potential platforms for bone tissue engineering. *Adv. Drug Deliv. Rev.* **2009,** *61* (12), 1065-1083.

126. Shi, S.; Kirk, M.; Kahn, A. J. The role of type I collagen in the regulation of the osteoblast phenotype. *J. Bone Miner. Res.* **1996,** *11* (8), 1139-1145.

127. Elliott, S. R.; Robinson, R. A. The water content of bone. I. The mass of water, inorganic crystals, organic matrix, and CO_2 space components in a unit volume of the dog bone. *J. Bone Joint Surg. Am.* **1957,** *39 A* (1), 167-188.

128. Rho, J. Y.; Kuhn-Spearing, L.; Zioupos, P. Mechanical properties and the hierarchical structure of bone. *Med. Eng. Phys.* **1998,** *20* (2), 92-102.

129. Reilly, D. T.; Burstein, A. H. The elastic and ultimate properties of compact bone tissue. *J. Biomech.* **1975,** *8* (6), 393-405.

130. Misch, C. E.; Qu, Z.; Bidez, M. W. Mechanical properties of trabecular bone in the human mandible: Implications for dental implant treatment planning and surgical placement. *J, Oral Maxillofac. Surg.* **1999,** *57* (6), 700-706.

131. Mauffrey, C.; Barlow, B. T.; Smith, W. Management of segmental bone defects. *J. Am. Acad. Orthop. Surg.* **2015,** *23* (3), 143-153.

132. Yang, Y. G.; Sykes, M. Xenotransplantation: current status and a perspective on the future. *Nat. Rev. Immunol.* **2007,** *7* (7), 519-531.

133. Mankin, H. J.; Hornicek, F. J.; Raskin, K. A. Infection in massive bone allografts. *Clin. Orthop. Relat. Res.* **2005,** (432), 210-216.

134. Hou, C. H.; Yang, R. S.; Hou, S. M. Hospital-based allogenic bone bank-10-year experience. *J. Hosp. Infect.* **2005,** *59* (1), 41-45.

135. Heary, R. F.; Schlenk, R. P.; Sacchieri, T. A.; Barone, D.; Brotea, C.; Fessler, R. G.; Sonntag, V. K. H.; Ratliff, J.; Cooper, P. R.; Kaiser, M.; McCormick, P. C. Persistent iliac crest donor site pain: independent outcome assessment. *Neurosurg.* **2002,** *50* (3), 510-517.

136. Arrington, E. D.; Smith, W. J.; Chambers, H. G.; Bucknell, A. L.; Davino, N. A. Complications of iliac crest bone graft harvesting. *Clin. Orthop. Relat. Res.* **1996,** *329*, 300-309.

137. Banwart, J. C.; Asher, M. A.; Hassanein, R. S. Iliac crest bone graft harvest donor site morbidity: A statistical evaluation. *Spine* **1995,** *20* (9), 1055-1066.

138. Holzwarth, J. M.; Ma, P. X. Biomimetic nanofibrous scaffolds for bone tissue engineering. *Biomaterials* **2011,** *32* (36), 9622-9629.

139. Page, J. M.; Harmata, A. J.; Guelcher, S. A. Design and development of reactive injectable and settable polymeric biomaterials. *J. Biomed. Mater. Res.* **2013,** *101* (12), 3630-3645.

140. Jawad, M. U.; Fritton, K. E.; Ma, T.; Ren, P. G.; Goodman, S. B.; Ke, H. Z.; Babij, P.; Genovese, M. C. Effects of sclerostin antibody on healing of a non-critical size femoral bone defect. *J. Orthop. Res.* **2013,** *31* (1), 155-163.

141. Lewis, G. Viscoelastic properties of injectable bone cements for orthopaedic applications: state-of-the-art review. *J. Biomed. Mater. Res., B* **2011,** *98B* (1), 171-191.

142. Oliveira, S. M.; Barrias, C. C.; Almeida, I. F.; Costa, P. C.; Ferreira, M. R.; Bahia, M. F.; Barbosa, M. A. Injectability of a bone filler system based on hydroxyapatite microspheres and a vehicle with in situ gel-forming ability. *J. Biomed. Mater. Res., B* **2008,** *87* (1), 49-58.

143. Woodruff, M. A.; Hutmacher, D. W. The return of a forgotten polymer: polycaprolactone in the 21st century. *Prog. Polym. Sci.* **2010,** *35* (10), 1217-1256.

144. Ward, B.; Brown, S.; Krebsbach, P. H. Bioengineering strategies for regeneration of craniofacial bone: a review of emerging technologies. *Oral Dis.* **2010,** *16* (8), 709-716.

145. Shrivats, A. R.; McDermott, M. C.; Hollinger, J. O. Bone tissue engineering: state of the union. *Drug Disc. Today* **2014,** *19* (6), 781-786.

146. Joschek, S.; Nies, B.; Krotz, R.; Göpferich, A. Chemical and physicochemical characterization of porous hydroxyapatite ceramics made of natural bone. *Biomaterials* **2000,** *21* (16), 1645-1658.

147. Turco, G.; Marsich, E.; Bellomo, F.; Semeraro, S.; Donati, I.; Brun, F.; Grandolfo, M.; Accardo, A.; Paoletti, S. Alginate/hydroxyapatite biocomposite for bone ingrowth: a trabecular structure with high and isotropic connectivity. *Biomacromolecules* **2009,** *10* (6), 1575-1583.

148. Lin, H. R.; Yen, Y. J. Porous alginate/hydroxyapatite composite scaffolds for bone tissue engineering: Preparation, characterization, and in vitro studies. *J. Biomed. Mater. Res., B* **2004,** *71* (1), 52-65.

149. Rossi, F.; Santoro, M.; Perale, G. Polymeric scaffolds as stem cell carriers in bone repair. *J. Tissue. Eng. Regen. Med.* **2015,** *9* (10), 1093-1119.

150. Ravichandran, R.; Sundarrajan, S.; Venugopal, J. R.; Mukherjee, S.; Ramakrishna, S. Advances in polymeric systems for tissue engineering and biomedical applications. *Macromol. Biosci.* **2012,** *12* (4), 286-311.

151. Despang, F.; Dittrich, R.; Gelinsky, M. Novel biomaterials with parallel aligned pore channels by directed ionotropic gelation of alginate: mimicking the anisotropic structure of bone tissue. In *Advances in Biomimetic*, **2011**; pp 349-372.

152. Deville, S.; Saiz, E.; Tomsia, A. P. Freeze casting of hydroxyapatite scaffolds for bone tissue engineering. *Biomaterials* **2006,** *27* (32), 5480-5489.

153. Itälä, A. I.; Ylänen, H. O.; Ekholm, C.; Karlsson, K. H.; Aro, H. T. Pore diameter of more than 100 mm is not requisite for bone ingrowth in rabbits. *J. Biomed. Mater. Res.* **2001,** *58* (6), 679-683.

154. Lee, S. H.; Shin, H. Matrices and scaffolds for delivery of bioactive molecules in bone and cartilage tissue engineering. *Adv. Drug Deliv. Rev.* **2007,** *59* (4-5), 339-359.

155. Marsich, E.; Bellomo, F.; Turco, G.; Travan, A.; Donati, I.; Paoletti, S. Nano-composite scaffolds for bone tissue engineering containing silver nanoparticles: preparation, characterization and biological properties. *J. Mater. Sci., Mater. Med.* **2013,** *24* (7), 1799-1807.

156. Suárez-González, D.; Barnhart, K.; Saito, E.; Vanderby, R.; Hollister, S. J.; Murphy, W. L. Controlled nucleation of hydroxyapatite on alginate scaffolds for stem cell-based bone tissue engineering. *J. Biomed. Mater. Res.* **2010,** *95A* (1), 222-234.

157. Kanczler, J. M.; Ginty, P. J.; White, L.; Clarke, N. M. P.; Howdle, S. M.; Shakesheff, K. M.; Oreffo, R. O. C. The effect of the delivery of vascular endothelial growth factor and bone morphogenic protein-2 to osteoprogenitor cell populations on bone formation. *Biomaterials* **2010,** *31* (6), 1242-1250.

158. Kolambkar, Y. M.; Boerckel, J. D.; Dupont, K. M.; Bajin, M.; Huebsch, N.; Mooney, D. J.; Hutmacher, D. W.; Guldberg, R. E. Spatiotemporal delivery of bone morphogenetic protein enhances functional repair of segmental bone defects. *Bone* **2011,** *49* (3), 485-492.

159. Schloßmacher, U.; der, H. C.; Wang, X.; Feng, Q.; Diehl-Seifert, B.; Neumann, S.; Trautwein, A.; ller, W. E. G. Alginate/silica composite hydrogel as a potential morphogenetically active scaffold for three-dimensional tissue engineering. *RSC Adv.* **2013,** *3* (28), 11185-11194.

160. Wang, L.; Stegemann, J. P. Thermogelling chitosan and collagen composite hydrogels initiated with b-glycerophosphate for bone tissue engineering. *Biomaterials* **2010,** *31* (14), 3976-3985.

161. Wang, L.; Stegemann, J. P. Glyoxal crosslinking of cell-seeded chitosan/collagen hydrogels for bone regeneration. *Acta Biomater.* **2011,** *7* (6), 2410-2417.

162. Hoemann, C. D.; Chenite, A.; Sun, J.; Hurtig, M.; Serreqi, A.; Lu, Z.; Rossomacha, E.; Buschmann, M. D. Cytocompatible gel formation of chitosan-glycerol phosphate solutions supplemented with hydroxyl ethyl cellulose is due to the presence of glyoxal. *J. Biomed. Mater. Res.* **2007,** *83A* (2), 521-529.

163. Wang, L.; Li, C. Preparation and physicochemical properties of a novel hydroxyapatite/chitosan-silk fibroin composite. *Carbohydr. Polym.* **2007,** *68* (4), 740-745.

164. Qu, Z.; Yan, J.; Li, B.; Zhuang, J.; Huang, Y. Improving bone marrow stromal cell attachment on chitosan/hydroxyapatite scaffolds by an immobilized RGD peptide. *Biomed. Mater.* **2010,** *5* (6).

165. Yu, H. S.; Won, J. E.; Jin, G. Z.; Kim, H. W. Construction of mesenchymal stem cell-containing collagen gel with a macrochanneled polycaprolactone scaffold and the flow perfusion culturing for bone tissue engineering. *Biores. Open Access* **2012,** *1* (3), 124-136.

166. Xu, C.; Su, P.; Chen, X.; Meng, Y.; Yu, W.; Xiang, A. P.; Wang, Y. Biocompatibility and osteogenesis of biomimetic bioglass-collagen-phosphatidylserine composite scaffolds for bone tissue engineering. *Biomaterials* **2011,** *32* (4), 1051-1058.

167. Schneider, R. K.; Puellen, A.; Kramann, R.; Raupach, K.; Bornemann, J.; Knuechel, R.; Pérez-Bouza, A.; Neuss, S. The osteogenic differentiation of adult bone marrow and perinatal umbilical mesenchymal stem cells and matrix remodelling in three-dimensional collagen scaffolds. *Biomaterials* **2010,** *31* (3), 467-480.

168. Low, K. L.; Tan, S. H.; Zein, S. H. S.; Roether, J. A.; Mouriño, V.; Boccaccini, A. R. Calcium phosphate-based composites as injectable bone substitute materials. *J. Biomed. Mater. Res., B* **2010,** *94B* (1), 273-286.

169. Bonher, M. Design of ceramic-based cements and putties for bone graft substitution. *Eur. Cell Mater.* **2010,** *20*, 1-12.

170. Gauthier, O.; Bouler, J. M.; Aguado, E.; Pilet, P.; Daculsi, G. Macroporous biphasic calcium phosphate ceramics: influence of macropore diameter and macroporosity percentage on bone ingrowth. *Biomaterials* **1998,** *19* (1GÇô3), 133-139.

171. Bongio, M.; van den Beucken, J. J. J. P.; Leeuwenburgh, S. C. G.; Jansen, J. A. Preclinical evaluation of injectable bone substitute materials. *J. Tissue Eng. Regen. Med.* **2015,** *9* (3), 191-209.

172. Suzuki, K.; Anada, T.; Miyazaki, T.; Miyatake, N.; Honda, Y.; Kishimoto, K. N.; Hosaka, M.; Imaizumi, H.; Itoi, E.; Suzuki, O. Effect of addition of hyaluronic acids on the osteoconductivity and biodegradability of synthetic octacalcium phosphate. *Acta Biomater.* **2014,** *10* (1), 531-543.

173. Nejadnik, M. R.; Yang, X.; Bongio, M.; Alghamdi, H. S.; van den Beucken, J. J. J. P.; Huysmans, M. C.; Jansen, J. A.; Hilborn, J.; Ossipov, D.; Leeuwenburgh, S. C. G. Self-healing hybrid nanocomposites consisting of bisphosphonated hyaluronan and calcium phosphate nanoparticles. *Biomaterials* **2014,** *35* (25), 6918-6929.

174. Sohrabi, M.; Hesaraki, S.; Kazemzadeh, A. Injectable bioactive glass/polysaccharide polymers nanocomposites for bone sostitution. *Key Eng. Mater.* **2014,** *614*, 41-46.

175. Kurien, T.; Pearson RG, F. A. U.; Scammell, B. E. Bone graft substitutes currently available in orthopaedic practice: the evidence for their use. *Bone Joint J.* **2013,** *95* (5), 583-597.

176. No, Y. J.; Roohani-Esfahani, S. I.; Zreiqat, H. Nanomaterials: the next step in injectable bone cements . *Nanomedicine* **2014,** *9* (11), 1745-1764.

177. Norowski, P. A.; Bumgardner, J. D. Biomaterial and antibiotic strategies for peri-implantitis: a review. *J. Biomed. Mater. Res., Part B* **2009,** *88B* (2), 530-543.

178. Campoccia, D.; Montanaro, L.; Arciola, C. R. The significance of infection related to orthopedic devices and issues of antibiotic resistance. *Biomaterials* **2006,** *27* (11), 2331-2339.

179. Campoccia, D.; Montanaro, L.; Speziale, P.; Arciola, C. R. Antibiotic-loaded biomaterials and the risks for the spread of antibiotic resistance following their prophylactic and therapeutic clinical use. *Biomaterials* **2010,** *31* (25), 6363-6377.

180. Ku, S. H.; Lee, M.; Park, C. B. Carbon-based nanomaterials for tissue engineering. *Adv. Healthc. Mater.* **2013,** *2* (2), 244-260.

181. Donati, I.; Stredanska, S.; Silvestrini, G.; Vetere, A.; Marcon, P.; Marsich, E.; Mozetic, P.; Gamini, A.; Paoletti, S.; Vittur, F. The aggregation of pig articular chondrocyte and synthesis of extracellular matrix by a lactose-modified chitosan. *Biomaterials* **2005,** *26* (9), 987-998.

182. Chung, B. G.; Kang, L.; Khademhosseini, A. Micro- and nanoscale technologies for tissue engineering and drug discovery applications. *Expert Opin. Drug Discov.* **2007,** *2* (12), 1653-1668.

183. Mata, D.; Horovistiz, A. L.; Branco, I.; Ferro, M.; Ferreira, N. M.; Belmonte, M.; Lopes, M. A.; Silva, R. F.; Oliveira, F. J. Carbon nanotube-based bioceramic grafts for electrotherapy of bone. *Mater. Sci. Eng., C* **2014,** *34*, 360-368.

184. Travan, A.; Pelillo, C.; Donati, I.; Marsich, E.; Benincasa, M.; Scarpa, T.; Semeraro, S.; Turco, G.; Gennaro, R.; Paoletti, S. Non-cytotoxic silver nanoparticle-polysaccharide nanocomposites with antimicrobial activity. *Biomacromolecules* **2009,** *10* (6), 1429-1435.

185. Tran, P. A.; Zhang, L.; Webster, T. J. Carbon nanofibers and carbon nanotubes in regenerative medicine. *Adv. Drug Deliv. Rev.* **2009,** *61* (12), 1097-1114.

186. Bianco, A.; Kostarelos, K.; Partidos, C. D.; Prato, M. Biomedical applications of functionalised carbon nanotubes. *Chem. Commun.* **2005,** (5), 571-577.

187. Vindigni, V.; Cortivo, R.; Iacobellis, L.; Abatangelo, G.; Zavan, B. Hyaluronan benzyl ester as a scaffold for tissue engineering. *Int. J. Mol. Sci.* **2009,** *10* (7), 2972-2985.

188. Benedetti, L.; Cortivo, R.; Berti, T.; Berti, A.; Pea, F.; Mazzo, M.; Moras, M.; Abatangelo, G. Biocompatibility and biodegradation of different hyaluronan derivatives (Hyaff) implanted in rats. *Biomaterials* **1993,** *14* (15), 1154-1160.

189. Riva, R.; Ragelle, H.; des Rieux, A.; Duhem, N.; Jérome, C.; Préat, V. Chitosan and chitosan derivatives in drug delivery and tissue engineering. In *Chitosan for biomaterials II*, 244 ed.; Jayakumar, R., Prabaharan, M., Muzzarelli, R. A. A., Eds.; Springer Berlin Heidelberg: **2011**; pp 19-44.

190. Francesko, A.; Tzanov, T. Chitin, chitosan and derivatives for wound healing and tissue engineering. In *Biofunctionalization of polymers and their applications*, 125 ed.; Nyanhongo, G. S., Steiner, W., Gübitz, G., Eds.; Springer Berlin Heidelberg: **2011**; pp 1-27.

191. Sashiwa, H.; Aiba, S. i. Chemically modified chitin and chitosan as biomaterials. *Prog. Polym. Sci.* **2004,** *29* (9), 887-908.

192. Yalpani, M.; Hall, L. D.; Tung, M. A.; Brooks, D. E. Unusual rheology of a branched, water-soluble chitosan derivative. *Nature* **1983,** *302* (5911), 812-814.

193. Marsich, E.; Travan, A.; Feresini, M.; Lapasin, R.; Paoletti, S.; Donati, I. Polysaccharide-based polyanion-polycation-polyanion ternary systems in the concentrated regime and hydrogel form. *Macromol. Chem. Phys.* **2013,** *214* (12), 1309-1320.

194. Marsich, E.; Borgogna, M.; Donati, I.; Mozetic, P.; Strand, B. L.; Salvador, S. G.; Vittur, F.; Paoletti, S. Alginate/lactose-modified chitosan hydrogels: a bioactive biomaterial for chondrocyte encapsulation. *J. Biomed. Mater. Res.* **2008,** *84A* (2), 364-376.

195. Travan, A.; Marsich, E.; Donati, I.; Foulc, M. P.; Moritz, N.; Aro, H. T.; Paoletti, S. Polysaccharide-coated thermosets for orthopedic applications: from material characterization to in vivo tests. *Biomacromolecules* **2012,** *13* (5), 1564-1572.

196. Marsich, E.; Travan, A.; Donati, I.; Turco, G.; Kulkova, J.; Moritz, N.; Aro, H. T.; Crosera, M.; Paoletti, S. Biological responses of silver-coated thermosets: an in vitro and in vivo study. *Acta Biomater.* **2013,** *9* (2), 5088-5099.

197. D`Amelio, N.; Esteban, C.; Coslovi, A.; Feruglio, L.; Uggeri, F.; Villegas, M.; Benegas, J.; Paoletti, S.; Donati, I. Insight into the molecular properties of chitlac, a chitosan derivative for tissue engineering. *J. Phys. Chem. B* **2013,** *117* (43), 13578-13587.

198. Marcon, P.; Marsich, E.; Vetere, A.; Mozetic, P.; Campa, C.; Donati, I.; Vittur, F.; Gamini, A.; Paoletti, S. The role of Galectin-1 in the interaction between chondrocytes and a lactose-modified chitosan. *Biomaterials* **2005,** *26* (24), 4975-4984.

199. Kopitz, J.; Von Reitzenstein, C.; Burchert, M.; Cantz, M.; Gabius, H. J. Galectin-1 is a major receptor for ganglioside GM1, a product of the growth-controlling activity of a cell surface ganglioside sialidase, on human neuroblastoma cells in culture. *J. Biol. Chem.* **1998,** *273* (18), 11205-11211.

200. Hernandez, J. D.; Baum, L. G. Ah, sweet mystery of death! Galectins and control of cell fate. *Glycobiol.* **2002,** *12* (10), 127R-136R.

201. Parlato, M.; Yeretssian, G. NOD-Like receptors in intestinal homeostasis and epithelial tissue repair. *Int. J Mol. Sci.* **2014,** *15* (6), 9594-9627.

202. Viguier, M.; Advedissian, T.; Delacour, D.; Poirier, F.; Deshayes, F. Galectins in epithelial functions. *Tissue Barriers* **2014,** *2*, e29103.

203. Gaudet, A. D.; Steeves, J. D.; Tetzlaff, W.; Ramer, M. S. Expression and functions of galectin-1 in sensory and motoneurons. *Curr. Drug. Targets* **2005,** *6*, 419-425.

204. Bigdeli, A. K.; Lyer, S.; Detsch, R.; Boccaccini, A. R.; Beier, J. P.; Kneser, U.; Horch, R. E.; Arkudas, A. Nanotechnologies in tissue engineering. **2013,** *2* (4), 411-425.

205. Smith, I. O.; Liu, X. H.; Smith, L. A.; Ma, P. X. Nanostructured polymer scaffolds for tissue engineering and regenerative medicine. *WIREs Nanomed. Nanobiotechnol.* **2009,** *1* (2), 226-236.

206. Ma, Z.; Kotaki, M.; Inai, R.; Ramakrishna, S. Potential of nanofiber matrix as tissue-engineering scaffolds. *Tissue Eng.* **2005,** *11*, 101-109.

207. Izadifar, M.; Haddadi, A.; Chen, X.; Kelly, M. E. Rate-programming of nano-particulate delivery systems for smart bioactive scaffolds in tissue engineering. *Nanotechnol.* **2015,** *26* (1).

208. Chen, J.; Wang, F.; Liu, Q.; Du, J. Antibacterial polymeric nanostructures for biomedical applications. *Chem. Commun.* **2014,** *50* (93), 14482-14493.

209. Shin, U. S.; Yoon, I. K.; Lee, G. S.; Jang, W. C.; Knowles, J. C.; Kim, H. W. Carbon nanotubes in nanocomposites and hybrids with hydroxyapatite for bone replacements. *J. Tissue Eng.* **2011,** *2* (1), 1-10.

210. Iijima, S. Helical microtubules of graphitic carbon. *Nature* **1991,** *354* (6348), 56-58.

211. Li, W. Z.; Wen, J. G.; Ren, Z. F. Straight carbon nanotube Y junctions. *Appl. Phys. Lett.* **2001,** *79*, 1879-1881.

212. Iijima, S.; Ichihashi, T. Single-shell carbon nanotubes of 1-nm diameter. *Nature* **1993,** *363* (6430), 603-605.

213. Zhang, X.; Meng, L.; Lu, Q. Cell behaviors on polysaccharide-wrapped single-wall carbon nanotubes: a quantitative study of the surface properties of biomimetic nanofibrous scaffolds. *ACS Nano* **2009,** *3* (10), 3200-3206.

214. Yu, M.-F.; Files, B. S.; Arepalli, S.; Ruoff, R. S. Tensile loading of ropes of single wall carbon nanotubes and their mechanical properties. *Phys. Rev. Lett.* **2000,** *84* (24), 5552-5555.

215. Yu, M.-F.; Lourie, O.; Dyer, M. J.; Moloni, K.; Kelly, T. F.; Ruoff, R. S. Strength and breaking mechanism of multiwalled carbon nanotubes under tensile load. *Science* **2000,** *287* (5453), 637-640.

216. Wong, E. W.; Sheehan, P. E.; Lieber, C. M. Nanobeam mechanics: elasticity, strength, and toughness of nanorods and nanotubes. *Science* **1997,** *277* (5334), 1971-1975.

217. Treacy, M. M. J.; Ebbesen, T. W.; Gibson, J. M. Exceptionally high Young's modulus observed for individual carbon nanotubes. *Nature* **1996,** *381* (6584), 678-680.

218. Louie, S. Electronic properties, junctions, and defects of carbon nanotubes. In *Carbon Nanotubes*, 80 ed.; Dresselhaus, M., Dresselhaus, G., Avouris, P., Eds.; Springer Berlin Heidelberg: **2001**; pp 113-145.

219. Yao, Z.; Kane, C. L.; Dekker, C. High-field electrical transport in single-wall carbon nanotubes. *Phys. Rev. Lett.* **2000,** *84* (13), 2941-2944.

220. Liang, W.; Bockrath, M.; Bozovic, D.; Hafner, J. H.; Tinkham, M.; Park, H. Fabry-Perot interference in a nanotube electron waveguide. *Nature* **2001,** *411* (6838), 665-669.

221. Mehra, N. K.; Jain, K.; Jain, N. K. Pharmaceutical and biomedical applications of surface engineered carbon nanotubes. *Drug Discov. Today* **2015,** *20* (6), 750-759.

222. Wang, W.; Zhu, Y.; Liao, S.; Li, J. Carbon nanotube reinforced composites for biomedical applications. *Biomed. Res. Int.* **2014,** *2014*, 518609.

223. Roldo, M.; Fatouros, D. G. Biomedical applications of carbon nanotubes. *Annu. Rep. Prog. Chem. , Sect. C: Phys. Chem.* **2013,** *109*, 10-35.

224. Boguslavsky, Y.; Fadida, T.; Talyosef, Y.; Lellouche, J. P. Controlling the wettability properties of polyester fibers using grafted functional nanomaterials. *J. Mater. Chem.* **2011,** *21* (28), 10304-10310.

225. Mitra, J.; Tripathi, G.; Sharma, A.; Basu, B. Scaffolds for bone tissue engineering: role of surface patterning on osteoblast response. *RSC Adv.* **2013,** *3* (28), 11073-11094.

226. Calvert, P. Nanotube composites: a recipe for strength. *Nature* **1999,** *399* (6733), 210-211.

227. Wang, W.; Ciselli, P.; Kuznetsov, E.; Peijs, T.; Barber, A. H. Effective reinforcement in carbon nanotube-polymer composites. *Philos. Trans. R. Soc., A* **2008,** *366* (1870), 1613-1626.

228. Bosi, S.; Ballerini, L.; Prato, M. Carbon nanotubes in tissue engineering. In *Making and exploiting fullerenes, graphene, and carbon nanotubes*, 348 ed.; Marcaccio, M., Paolucci, F., Eds.; Springer Berlin Heidelberg: **2014**; pp 181-204.

229. Stankova, L.; Fraczek-Szczypta, A.; Blazewicz, M.; Filova, E.; Blazewicz, S.; Lisa, V.; Bacakova, L. Human osteoblast-like MG 63 cells on polysulfone modified with carbon nanotubes or carbon nanohorns. *Carbon* **2014,** *67*, 578-591.

230. McMahon, R. E.; Wang, L.; Skoracki, R.; Mathur, A. B. Development of nanomaterials for bone repair and regeneration. *J. Biomed. Mater. Res., B* **2013,** *101* (2), 387-397.

231. Sitharaman, B.; Shi, X.; Walboomers, X. F.; Liao, H.; Cuijpers, V.; Wilson, L. J.; Mikos, A. G.; Jansen, J. A. In vivo biocompatibility of ultra-short single-walled carbon nanotube/biodegradable polymer nanocomposites for bone tissue engineering. *Bone* **2008,** *43* (2), 362-370.

232. Zanello, L. P.; Zhao, B.; Hu, H.; Haddon, R. C. Bone cell proliferation on carbon nanotubes. *Nano Lett.* **2006,** *6* (3), 562-567.

233. Xiao, Y.; Gong, T.; Zhou, S. The functionalization of multi-walled carbon nanotubes by in situ deposition of hydroxyapatite. *Biomaterials* **2010,** *31* (19), 5182-5190.

234. Akasaka, T.; Watari, F.; Sato, Y.; Tohji, K. Apatite formation on carbon nanotubes. *Mater. Sci. Eng., C* **2006,** *26* (4), 675-678.

235. Zhao, B.; Hu, H.; Mandal, S. K.; Haddon, R. C. A bone mimic based on the self-assembly of hydroxyapatite on chemically functionalized single-walled carbon nanotubes. *Chem. Mater.* **2005,** *17* (12), 3235-3241.

236. Narita, N.; Kobayashi, Y.; Nakamura, H.; Maeda, K.; Ishihara, A.; Mizoguchi, T.; Usui, Y.; Aoki, K.; Simizu, M.; Kato, H.; Ozawa, H.; Udagawa, N.; Endo, M.; Takahashi, N.; Saito, N. Multiwalled carbon nanotubes specifically inhibit osteoclast differentiation and function. *Nano Lett.* **2009,** *9* (4), 1406-1413.

237. Fabbro, A.; Villari, A.; Laishram, J.; Scaini, D.; Toma, F. M.; Turco, A.; Prato, M.; Ballerini, L. Spinal cord explants use carbon nanotube interfaces to enhance neurite outgrowth and to fortify synaptic inputs. *ACS Nano* **2012,** *6* (3), 2041-2055.

238. Cellot, G.; Toma, F. M.; Varley, Z. K.; Laishram, J.; Villari, A.; Quintana, M.; Cipollone, S.; Prato, M.; Ballerini, L. Carbon nanotube scaffolds tune synaptic strength in cultured neural circuits: novel frontiers in nanomaterial-tissue interactions. *J. Neurosci.* **2011,** *31* (36), 12945-12953.

239. Buzea, C.; Pacheco, I. I.; Robbie, K. Nanomaterials and nanoparticles: sources and toxicity. *Biomaterials* **2007,** *2* (4), MR17-MR71.

240. Madani, S. Y.; Mandel, A.; Seifalian, A. M. A concise review of carbon nanotube's toxicology. *Nano Rev.* **2013,** *4*.

241. Li, R.; Wang, X.; Ji, Z.; Sun, B.; Zhang, H.; Chang, C. H.; Lin, S.; Meng, H.; Liao, Y. P.; Wang, M.; Li, Z.; Hwang, A. A.; Song, T. B.; Xu, R.; Yang, Y.; Zink, J. I.; Nel, A. E.; Xia, T. Surface charge and cellular processing of covalently functionalized multiwall carbon nanotubes determine pulmonary toxicity. *ACS Nano* **2013,** *7* (3), 2352-2368.

242. Salvador-Morales, C.; Basiuk, E. V.; Basiuk, V. A.; Green, M. L.; Sim, R. B. Effects of covalent functionalization on the biocompatibility characteristics of multi-walled carbon nanotubes. *J. Nanosci. Nanotechnol.* **2007,** *8*, 1-10.

243. Dumortier, H.; Lacotte, S.; Pastorin, G.; Marega, R.; Wu, W.; Bonifazi, D.; Briand, J. P.; Prato, M.; Muller, S.; Bianco, A. Functionalized carbon nanotubes are non-cytotoxic and preserve the functionality of primary immune cells. *Nano Lett.* **2006,** *6* (7), 1522-1528.

244. Liu, Y.; Chipot, C.; Shao, X.; Cai, W. Solubilizing carbon nanotubes through noncovalent functionalization. Insight from the reversible wrapping of alginic acid around a single-walled carbon nanotube. *J. Phys. Chem. B* **2010,** *114* (17), 5783-5789.

245. Schipper, M. L.; Nakayama-Ratchford, N.; Davis, C. R.; Kam, N. W. S.; Chu, P.; Liu, Z.; Sun, X.; Dai, H.; Gambhir, S. S. A pilot toxicology study of single-walled carbon nanotubes in a small sample of mice. *Nat. Nanotech.* **2008,** *3* (4), 216-221.

246. Lee, H. J.; Park, J.; Yoon, O. J.; Kim, H. W.; Lee, D. Y.; Kim, D. H.; Lee, W. B.; Lee, N. E.; Bonventre, J. V.; Kim, S. S. Amine-modified single-walled carbon nanotubes protect neurons from injury in a rat stroke model. *Nat. Nanotech.* **2011,** *6* (2), 121-125.

247. Gaillard, C.; Cellot, G.; Li, S.; Toma, F. M.; Dumortier, H.; Spalluto, G.; Cacciari, B.; Prato, M.; Ballerini, L.; Bianco, A. Carbon nanotubes carrying cell-adhesion peptides do not interfere with neuronal functionality. *Adv. Mater.* **2009,** *21* (28), 2903-2908.

248. Bianco, A.; Kostarelos, K.; Prato, M. Making carbon nanotubes biocompatible and biodegradable. *Chem. Commun.* **2011,** *47* (37), 10182-10188.

249. Dresselhaus, M. S.; Dresselhaus, G.; Eklund, P. C. Synthesis, extraction, and purification of fullerenes. In *Science of Fullerenes and Carbon Nanotubes*, Dresselhaus, M. S., Dresselhaus, G., Eklund, P. C., Eds.; Academic Press: San Diego, **1996**; pp 110-142.

250. Hsiao, A. E.; Tsai, S. Y.; Hsu, M. W.; Chang, S. J. Decoration of multi-walled carbon nanotubes by polymer wrapping and its application in MWCNT/polyethylene composites. *Nanoscale Res. Lett.* **2012,** *7* (1), 1-5.

251. Wang, Y.; Iqbal, Z.; Mitra, S. Rapidly functionalized, water-dispersed carbon nanotubes at high concentration. *J. Am. Chem. Soc.* **2005,** *128* (1), 95-99.

252. Bahr, J. L.; Tour, J. M. Covalent chemistry of single-wall carbon nanotubes. *J. Mater. Chem.* **2002,** *12* (7), 1952-1958.

253. Price, B. K.; Tour, J. M. Functionalization of single-walled carbon nanotubes on water. *J. Am. Chem. Soc.* **2006,** *128* (39), 12899-12904.

254. Georgakilas, V.; Tagmatarchis, N.; Pantarotto, D.; Bianco, A.; Briand, J. P.; Prato, M. Amino acid functionalisation of water soluble carbon nanotubes. *Chem. Commun.* **2002,** *24*, 3050-3051.

255. Chen, J. P. Late angiographic stent thrombosis (LAST): the cloud behind the drug-eluting stent silver lining? *J. Invasive. Cardiol.* **2007,** *19* (9), 395-400.

256. Marambio-Jones, C.; Hoek, E. V. A review of the antibacterial effects of silver nanomaterials and potential implications for human health and environment. *J. Nanopart. Res.* **2010,** *12* (5), 1531-1551.

257. Elechiguerra, J.; Burt, J.; Morones, J.; Camacho-Bragado, A.; Gao, X.; Lara, H.; Yacaman, M. Interaction of silver nanoparticles with HIV-1. *J. Nanobiotechnol.* **2005,** *3* (1), 6.

258. Clement, J. L.; Jarrett, P. S. Antibacterial silver. *Met. Based. Drugs* **1994,** *1* (5-6), 467-482.

259. Sondi, I.; Salopek-Sondi, B. Silver nanoparticles as antimicrobial agent: a case study on E. coli as a model for Gram-negative bacteria. *J. Colloid Interface Sci.* **2004,** *275*, 177-182.

260. Rai, M.; Yadav, A.; Gade, A. Silver nanoparticles as a new generation of antimicrobials. *Biotechnol. Adv.* **2001,** *27* (1), 76-83.

261. Feng, Q. L.; Wu, J.; Chen, G. Q.; Cui, F. Z.; Kim, T. N.; Kim, J. O. A mechanistic study of the antibacterial effect of silver ions on Escherichia coli and Staphylococcus aureus. *J Biomed. Mater. Res* **2000,** *52* (4), 662-668.

262. Alt, V.; Bechert, T.; Steinrucke, P.; Wagener, M.; Seidel, P.; Dingeldein, E.; Scheddin, D.; Domann, E.; Schnettler, R. Nanoparticulate silver. a new antimicrobial substance for bone cement. *Orthopade* **2004,** *33* (8), 885-892.

263. Morones, J. R.; Elechiguerra, J. L.; Camacho, A.; Holt, K.; Kouri, J. B.; Ramirez, J. T.; Yacaman, M. J. The bactericidal effect of silver nanoparticles. *Nanotechnol.* **2005,** *16* (10), 2346-2353.

264. Hwang, I.; Hwang, J. H.; Choi, H.; Kim, K.-J.; Lee, D. G. Synergistic effects between silver nanoparticles and antibiotics and the mechanisms involved. *J. Med. Microbiol.* **2012,** *61* (1719), 1726.

265. Shi, X.; Hudson, J. L.; Spicer, P. P.; Tour, J. M.; Krishnamoorti, R.; Mikos, A. G. Injectable nanocomposites of single-walled carbon nanotubes and biodegradable polymers for bone tissue engineering. *Biomacromolecules* **2006,** *7* (7), 2237-2242.

266. Lubick, N. Nanosilver toxicity: ions, nanoparticles - or both? *Environ. Sci. Technol.* **2008,** *42* (23), 8617.

267. Lin, M. T.; Beal, M. F. Mitochondrial dysfunction and oxidative stress in neurodegenerative diseases. *Nature* **2006,** *443* (7113), 787-795.

268. Gilca, M.; Stoian, I.; Atanasiu, V.; Virgolici, B. The oxidative hypothesis of senescence. *J. Postgrad. Med.* **2007,** *53* (3), 207-213.

269. Martinez-Castanon, G. A.; Nino-Martinez, N.; Martinez-Gutierrez, F.; Martinez-Mendoza, J. R.; Ruiz, F. Synthesis and antibacterial activity of silver nanoparticles with different sizes. *J. Nanopart. Res.* **2008,** *10*, 1343-1348.

270. Nganga, S.; Travan, A.; Marsich, E.; Donati, I.; Söderling, E.; Moritz, N.; Paoletti, S.; Vallittu, P. In vitro antimicrobial properties of silver-polysaccharide coatings on porous fiber-reinforced composites for bone implants. *J. Mater. Sci., Mater. Med.* **2013,** *24* (12), 2775-2785.

271. Wang, X.; Xia, T.; Ntim, S. A.; Ji, Z.; George, S.; Meng, H.; Zhang, H.; Castranova, V.; Mitra, S.; Nel, A. E. Quantitative techniques for assessing and controlling the dispersion and biological effects of multiwalled carbon nanotubes in mammalian tissue culture cells. *ACS Nano* **2010,** *4* (12), 7241-7252.

272. Delogu, L. G.; Vidili, G.; Venturelli, E.; Ménard-Moyon, C.; Zoroddu, M. A.; Pilo, G.; Nicolussi, P.; Ligios, C.; Bedognetti, D.; Sgarrella, F.; Manetti, R.; Bianco, A. Functionalized multiwalled carbon nanotubes as ultrasound contrast agents. *Proc. Natl. Acad. Sci.* **2012,** *109* (41), 16612-16617.

273. Georgakilas, V.; Kordatos, K.; Prato, M.; Guldi, D. M.; Holzinger, M.; Hirsch, A. Organic functionalization of carbon nanotubes. *J. Am. Chem. Soc.* **2002,** *124* (5), 760-761.

274. Wang, Y. Z.; Li, Y. X.; Yang, S. T.; Zhang, G. L.; An, D. M.; Wang, C.; Yang, Q. B.; Chen, X. S.; Jing, X. B.; Wei, Y. A convenient route to polyvinyl pyrrolidone/silver nanocomposite by electrospinning. *Nanotechnol.* **2006,** *17* (13), 3304-3307.

275. Dezfoli, A. R. A.; Mehrabian, M. A.; Rafsanjani, H. H. Structural properties of water around uncharged and charged carbon nanotubes. *Korean J. Chem. Eng.* **2013,** *30* (3), 693-699.

276. Foroutan, M.; Moshari, M. Molecular dynamics simulations of functionalized carbon nanotubes in water: Effects of type and position of functional groups. *Physica E* **2010,** *43* (1), 359-365.

277. Cerpa, A.; Kober, M.; Calle, D.; Negri, V.; Gavira, J. M.; Hernanz, A.; Briones, F.; Cerdan, S.; Ballesteros, P. Single-walled carbon nanotubes as anisotropic relaxation probes for magnetic resonance imaging. *Med. Chem. Commun.* **2013,** *4* (4), 669-672.

278. Negri, V.; Cerpa, A.; López-Larrubia, P.; Nieto-Charques, L.; Cerdán, S.; Ballesteros, P. Nanotubular paramagnetic probes as contrast agents for magnetic resonance imaging based on the diffusion tensor. *Angew. Chem. Int. Ed.* **2010,** *49* (10), 1813-1815.

279. Turco, G.; Donati, I.; Grassi, M.; Marchioli, G.; Lapasin, R.; Paoletti, S. Mechanical Spectroscopy and Relaxometry on Alginate Hydrogels: A Comparative analysis for structural characterization and network mesh size determination. *Biomacromolecules* **2011,** *12* (4), 1272-1282.

280. Cheng, X.; Zhong, J.; Meng, J.; Yang, M.; Jia, F.; Zu, X.; Kong, H.; Xu, H. Characterization of multiwalled carbon nanotubes dispersing in water and association with biological effects. *J. Nanomater.* **2011,** *2011*.

281. Bertulli, C.; Beeson, H. J.; Hasan, T.; Huang, Y. Y. Spectroscopic characterization of protein-wrapped single-wall carbon nanotubes and quantification of their cellular uptake in multiple cell generations. *Nanotechnol.* **2013,** *24* (26), 265102.

282. O'Connell, M. J.; Bachilo, S. M.; Huffman, C. B.; Moore, V. C.; Strano, M. S.; Haroz, E. H.; Rialon, K. L.; Boul, P. J.; Noon, W. H.; Kittrell, C.; Ma, J.; Hauge, R. H.; Weisman, R. B.; Smalley, R. E. Band gap fluorescence from individual single-walled carbon nanotubes. *Science* **2002,** *297* (5581), 593-596.

283. Elias, H. G. Association and aggregation as studied via light scattering. In *Scattering from polymer soutions*, Academic Press, Ed.; Huglin, M. B.: London, **1972**; pp 397-457.

284. García-Gutiérrez, M. C.; Nogales, A.; Hernández, J. J.; Rueda, D. R.; Ezquerra, T. A. X-ray scattering applied to the analysis of carbon nanotubes, polymers and nanocomposites. *Opt. Pura Apl.* **2007,** *40* (2), 195-205.

285. Winter, H. H. Three views of viscoelasticity for Cox-Merz materials. *Rheol. Acta* **2009,** *48* (3), 241-243.

286. Chatterjee, T.; Krishnamoorti, R. Rheology of polymer carbon nanotubes composites. *Soft Matter* **2013,** *9* (40), 9515-9529.

287. Gupta, A.; Main, B. J.; Taylor, B. L.; Gupta, M.; Whitworth, C. A.; Cady, C.; Freeman, J. W.; El-Amin, S. F. In vitro evaluation of three-dimensional single-walled carbon nanotube composites for bone tissue engineering. *J. Biomed. Mater. Res.* **2014,** *102* (11), 4118-4126.

288. de Celis Alonso, B.; Rayment, P.; Ciampi, E.; Ablett, S.; Marciani, L.; Spiller, R. C.; Norton, I. T.; Gowland, P. A. NMR relaxometry and rheology of ionic and acid alginate gels. *Carbohydr. Polym.* **2010,** *82* (3), 663-669.

289. Travan, A.; Donati, I.; Marsich, E.; Bellomo, F.; Achanta, S.; Toppazzini, M.; Semeraro, S.; Scarpa, T.; Spreafico, V.; Paoletti, S. Surface modification and polysaccharide deposition on BisGMA/TEGDMA thermoset. *Biomacromolecules* **2010,** *11* (3), 583-592.

290. Garçia, A. J. Interfaces to control cell-biomaterial adhesive interactions. In *Polymers for Regenerative Medicine*, 203 ed.; Werner, C., Ed.; Springer Berlin Heidelberg: **2006**; pp 171-190.

291. Van Oss, C. J.; Chaudhury, M. K.; Good, R. J. Interfacial Lifshitz-van der Waals and polar interactions in macroscopic systems. *Chem. Rev.* **1988,** *88* (6), 927-941.

292. Lamour, G.; Eftekhari-Bafrooei, A.; Borguet, E.; Soues, S.; Hamraoui, A. Neuronal adhesion and differentiation driven by nanoscale surface free-energy gradients. *Biomaterials* **2010,** *31* (14), 3762-3771.

293. Assero, G.; Satriano, C.; Lupo, G.; Anfuso, C. D.; Marletta, G.; Alberghina, M. Pericyte adhesion and growth onto polyhydroxymethylsiloxane surfaces nanostructured by plasma treatment and ion irradiation. *Microvas. Res.* **2004,** *68* (3), 209-220.

294. Hallab, N. J.; Bundy KJ, F. A. U.; O'Connor, K. F.; Moses RL, F. A. U.; Jacobs, J. J. Evaluation of metallic and polymeric biomaterial surface energy and surface roughness characteristics for directed cell adhesion. *Tissue Eng.* **2001,** *7* (1), 55-71.

295. Siebler, M.; Koller, H.; Stichel, C. C.; Muller, H. W.; Freund, H. J. Spontaneous activity and recurrent inhibition in cultured hippocampal networks. *Synapse* **1993,** *14* (3), 206-213.

296. Camby, I.; Le Mercier, M.; Lefranc, F.; Kiss, R. Galectin-1: a small protein with major functions. *Glycobiology* **2006,** *16* (11), 137R-157R.

297. McGraw, J.; Gaudet, A. D.; Oschipok, L. W.; Kadoya, T.; Horie, H.; Steeves, J. D.; Tetzlaff, W.; Ramer, M. S. Regulation of neuronal and glial galectin-1 expression by peripheral and central axotomy of rat primary afferent neurons. *Exp. Neurol.* **2005,** *195* (1), 103-114.

298. Horie, H.; Kadoya, T.; Hikawa, N.; Sango, K.; Inoue, H.; Takeshita, K.; Asawa, R.; Hiroi, T.; Sato, M.; Yoshioka, T.; Ishikawa, Y. Oxidized galectin-1 stimulates macrophages to promote axonal regeneration in peripheral nerves after axotomy. *J. Neurosci.* **2004,** *24*, 1873-1880.

299. Kobow, K.; Auvin, S.; Jensen, F.; Löscher, W.; Mody, I.; Potschka, H.; Prince, D.; Sierra, A.; Simonato, M.; Pitkänen, A.; Nehlig, A.; Rho, J. M. Finding a better drug for epilepsy: Antiepileptogenesis targets. *Epilepsia* **2012,** *53* (11), 1868-1876.

300. Levine, E. S.; Dreyfus, C. F.; Black, I. B.; Plummer, M. R. Brain-derived neurotrophic factor rapidly enhances synaptic transmission in hippocampal neurons via postsynaptic tyrosine kinase receptors. *Proc. Natl. Acad. Sci* **1995,** *92* (17), 8074-8077.

301. Knipper, M.; Leung, L. S.; Zhao, D.; Rylett, R. J. Short-term modulation of glutamatergic synapses in adult rat hippocampus by NGF. *Neuroreport* **1994,** *5* (18), 2433-2436.

302. Vogel, V.; Sheetz, M. Local force and geometry sensing regulate cell functions. *Nat. Rev. Mol. Cell. Biol.* **2006,** *7* (4), 265-275.

303. Hildebrand, T.; Laib, A.; Müller, R.; Dequeker, J.; Rüegsegger, P. Direct three-dimensional morphometric analysis of human cancellous bone: microstructural data from spine, femur, iliac crest and calcaneous. *J. Bone Miner. Res.* **1999,** *14* (7), 1167-1174.

304. Odgaard, A.; Gundersen, H. J. G. Quantification of connectivity in cancellous bone, with special emphasis on 3-D reconstructions. *Bone* **1993,** *14* (2), 173-182.

305. Shanmugasundaram, N.; Ravichandran, P.; Neelakanta Reddy, P.; Ramamurty, N.; Pal, S.; Panduranga Rao, K. Collagen-chitosan polymeric scaffolds for the in vitro culture of human epidermoid carcinoma cells. *Biomaterials* **2001,** *22* (14), 1943-1951.

306. Ghadiri, M.; Chrzanowski, W.; Lee, W. H.; Fathi, A.; Dehghani, F.; Rohanizadeh, R. Physico-chemical, mechanical and cytotoxicity characterizations of Laponite®/alginate nanocomposite. *Appl. Clay Sci.* **2013,** *85*, 64-73.

307. Sudheesh Kumar, P. T.; Srinivasan, S.; Lakshmanan, V. K.; Tamura, H.; Nair, S. V.; Jayakumar, R. β-Chitin hydrogel/nano hydroxyapatite composite scaffolds for tissue engineering applications. *Carbohydr. Polym.* **2011,** *85* (3), 584-591.

308. Srinivasan, S.; Jayasree, R.; Chennazhi, K. P.; Nair, S. V.; Jayakumar, R. Biocompatible alginate/nano bioactive glass ceramic composite scaffolds for periodontal tissue regeneration. *Carbohydr. Polym.* **2012,** *87* (1), 274-283.

309. Frohbergh, M. E.; Katsman, A.; Botta, G. P.; Lazarovici, P.; Schauer, C. L.; Wegst, U. G.; Lelkes, P. I. Electrospun hydroxyapatite-containing chitosan nanofibers crosslinked with genipin for bone tissue engineering. *Biomaterials* **2012,** *33* (36), 9167-9178.

310. Zande, M. v. d.; Walboomers, X. F.; Olalde, B.; Jurado, M. J.; Boerman, O. C.; Jansen, J. A. Effect of nanotubes and apatite on growth factor release from PLLA scaffolds. *J. Tissue. Eng. Regen. Med.* **2011,** *5* (6), 476-482.

311. Intranuovo, F.; Gristina, R.; Brun, F.; Mohammadi, S.; Ceccone, G.; Sardella, E.; Rossi, F.; Tromba, G.; Favia, P. Plasma modification of PCL porous scaffolds fabricated by solvent-casting/particulate-leaching for tissue engineering. *Plasma Process. Polym.* **2014,** *11* (2), 184-195.

312. Ylä-Soininmäki, A.; Moritz, N.; Turco, G.; Paoletti, S.; Aro, H. T. Quantitative characterization of porous commercial and experimental bone graft substitutes with microcomputed tomography. *J. Biomed. Mater. Res., B* **2013,** *101* (8), 1538-1548.

313. Thitiset, T.; Damrongsakkul, S.; Bunaprasert, T.; Leeanansaksiri, W.; Honsawek, S. Development of collagen/demineralized bone powder scaffolds and periosteum-derived cells for bone tissue engineering application. *Int. J. Mol. Sci.* **2013,** *14*, 2056-2071.

314. Correia, C. O.; Leite, Á. J.; Mano, J. F. Chitosan/bioactive glass nanoparticles scaffolds with shape memory properties. *Carbohydr. Polym.* **2015,** *123*, 39-45.

315. Liu, X.; Zhao, K.; Gong, T.; Song, J.; Bao, C.; Luo, E.; Weng, J.; Zhou, S. Delivery of growth factors using a smart porous nanocomposite scaffold to repair a mandibular bone defect. *Biomacromolecules* **2014,** *15* (3), 1019-1030.

316. Liu, Y.; Lim, J.; Teoh, S. H. Review: Development of clinically relevant scaffolds for vascularised bone tissue engineering. *Biotechnol. Adv.* **2013,** *31* (5), 688-705.

317. Thornton, A. J.; Alsberg, E.; Albertelli, M.; Mooney, D. J. Shape-defining scaffolds for minimally invasive tissue engineering. *Transplantation* **2004,** *77* (12), 1798-1803.

318. Jin, H. H.; Kim, D. H.; Kim, T. W.; Shin, K. K.; Jung, J. S.; Park, H. C.; Yoon, S. Y. In vivo evaluation of porous hydroxyapatite/chitosan-alginate composite scaffolds for bone tissue engineering. *Int. J. Biol. Macromol.* **2012,** *51* (5), 1079-1085.

319. Ali-Boucetta, H.; Al-Jamal, K. T.; Kostarelos, K. Cytotoxic assessment of carbon nanotube interaction with cell cultures. *Methods Mol. Biol.* **2011,** *726*, 299-312.

320. Casey, A.; Herzog, E.; Davoren, M.; Lyng, F. M.; Byrne, H. J.; Chambers, G. Spectroscopic analysis confirms the interactions between single walled carbon nanotubes and various dyes commonly used to assess cytotoxicity. *Carbon* **2007,** *45* (7), 1425-1432.

321. Wang, X.; Guo, J.; Chen, T.; Nie, H.; Wang, H.; Zang, J.; Cui, X.; Jia, G. Multi-walled carbon nanotubes induce apoptosis via mitochondrial pathway and scavenger receptor. *Toxicol. In Vitro* **2012,** *26* (6), 799-806.

322. Wörle-Knirsch, J. M.; Pulskamp, K.; Krug, H. F. Oops they did it again! Carbon nanotubes hoax scientists in viability assays. *Nano Lett.* **2006,** *6* (6), 1261-1268.

323. Li, H.; Wijekoon, A.; Leipzig, N. D. 3D differentiation of neural stem cells in macroporous photopolymerizable hydrogel scaffolds. *PLoS ONE* **2012,** *7* (11), e48824.

324. Tadier, S.; Galea, L.; Charbonnier, B.; Baroud, G.; Bohner, M. Phase and size separations occurring during the injection of model pastes composed of b-tricalcium phosphate powder, glass beads and aqueous solutions. *Acta Biomater.* **2014,** *10* (5), 2259-2268.

325. Ghanaati, S.; Barbeck, M.; Hilbig, U.; Hoffmann, C.; Unger, R. E.; Sader, R. A.; Peters, F.; Kirkpatrick, C. J. An injectable bone substitute composed of beta-tricalcium phosphate granules, methylcellulose and hyaluronic acid inhibits connective tissue influx into its implantation bed in vivo. *Acta Biomater.* **2011,** *7* (11), 4018-4028.

326. von Doernberg, M. C.; von Rechenberg, B.; Bohner, M.; Grünenfelder, S.; van Lenthe, G. H.; Müller, R.; Gasser, B.; Mathys, R.; Baroud, G.; Auer, J. In vivo behavior of calcium phosphate scaffolds with four different pore sizes. *Biomaterials* **2006,** *27* (30), 5186-5198.

327. Grynpas, M. D.; Pilliar, R. M.; Kandel, R. A.; Renlund, R.; Filiaggi, M.; Dumitriu, M. Porous calcium polyphosphate scaffolds for bone substitute applications in vivo studies. *Biomaterials* **2002,** *23* (9), 2063-2070.

328. Urist, M. R. Bone: Formation by Autoinduction. *Science* **1965,** *150* (3698), 893-899.

329. Moran, E.; Byren, I.; Atkins, B. L. The diagnosis and management of prosthetic joint infections. *J. Antimicr. Chemother.* **2010,** *65* (suppl 3), iii45-iii54.

330. Parvizi, J.; Azzam, K.; Ghanem, E.; Austin, M. S.; Rothman, R. H. Periprosthetic infection due to resistant staphylococci: serious problems on the horizon. *Clin. Orthop. Relat. Res.* **2009,** *467* (7), 1732-1739.

331. Toms, A. D.; Davidson, D.; Masri, B. A.; Duncan, C. P. The management of peri-prosthetic infection in total joint arthroplasty. *J. Bone Joint Surg., Br. Vol.* **2006,** *88-B* (2), 149-155.

332. Kilgus, D. J.; Howe, D.J.; Strang, A. Results of periprosthetic hip and knee infections caused by resistant bacteria. *Clin. Orthop. Relat. Res.* **2002,** *404*, 116-124.

333. Gottenbos, B.; van der Mei, H. C.; Busscher, H. J. Initial adhesion and surface growth of Staphylococcus epidermidis and Pseudomonas aeruginosa on biomedical polymers. *J. Biomed. Mater. Res.* **2000,** *50* (2), 208-214.

334. Leid, J. G.; Willson, C. J.; Shirtliff, M. E.; Hassett, D. J.; Parsek, M. R.; Jeffers, A. K. The exopolysaccharide alginate protects Pseudomonas aeruginosa biofilm bacreria from IFN-gamma-mediated macrophage killing. *J. Immunol.* **2005,** *175* (11), 7512-7518.

335. Biological evaluation of medical devices - Part 5: Tests for in vitro cytotoxicity, ISO 10993-5. [3rd]. 1-6-**2009**. International Organization for Standardization: Geneva, Switzerland.

336. Sohrabi, M.; Hesaraki, S.; Kazemzadeh, A.; Alizadeh, M. Development of injectable biocomposites from hyaluronic acid and bioactive glass nano-particles obtained from different sol-gel routes. *Mater. Sci. Eng., C* **2013,** *33* (7), 3730-3744.

337. Dicker, K. T.; Gurski, L. A.; Pradhan-Bhatt, S.; Witt, R. L.; Farach-Carson, M. C.; Jia, X. Hyaluronan: a simple polysaccharide with diverse biological functions. *Acta Biomater.* **2014,** *10* (4), 1558-1570.

338. Vold, I. M. N.; Kristiansen, K. A.; Christensen, B. E. A study of the chain stiffness and extension of alginates, in vitro epimerized alginates, and periodate-oxidized alginates using size-exclusion chromatography combined with light scattering and viscosity detectors. *Biomacromolecules* **2006,** *7* (7), 2136-2146.

339. Grasdalen, H. High-field, ^{1}H-NMR spectroscopy of alginate: sequential structure and linkage conformations. *Carbohydr. Res.* **1983,** *118*, 255-260.

340. Grasdalen, H.; Larsen, B.; Smidsröd, O. A p.m.r. study of the composition and sequence of uronate residues in alginates. *Carbohydr. Res.* **1979,** *68* (1), 23-31.

341. Ström, A.; Williams, M. A. K. Controlled calcium release in the absence and presence of an ion-binding polymer. *J. Phys. Chem. B* **2003,** *107* (40), 10995-10999.

342. https://www.elettra.trieste.it/it/lightsources/labs-and-services/tomolab/tomolab.html

343. Otsu, N. A threshold selection method from gray-level histograms. *IEE Trans. Syst. Man Cybern.* **1979,** *9* (1), 62-66.

344. Parfitt, A. M.; Mathews, C. H. E.; Villanueva, A. R.; Kleerekoper, M. Relationship between surface, volume, and thickness of iliac trabecular bone in aging and in osteoporosis. *J. Clin. Invest.* **1983,** *72*, 1396-1409.

345. Kwok, D. Y.; Neumann, A. W. Contact angle measurement and contact angle interpretation. *Adv. Colloid Interface Sci.* **1999,** *81* (3), 167-249.

346. Kokubo, T.; Kushitani, H.; Sakka, S.; Kitsugi, T.; Yamamuro, T. Solutions able to reproduce in vivo surface-structure changes in bioactive glass-ceramic A-W. *J. Biomed. Mater. Res.* **1990,** *24*, 721-734.

347. Lovat, V.; Pantarotto, D.; Lagostena, L.; Cacciari, B.; Grandolfo, M.; Righi, M.; Spalluto, G.; Prato, M.; Ballerini, L. Carbon nanotube substrates boost neuronal electrical signaling. *Nano Lett.* **2005,** *5* (6), 1107-1110.

348. Cellot, G.; Cilia, E.; Cipollone, S.; Rancic, V.; Sucapane, A.; Giordani, S.; Gambazzi, L.; Markram, H.; Grandolfo, M.; Scaini, D.; Gelain, F.; Casalis, L.; Prato, M.; Giugliano, M.; Ballerini, L. Carbon nanotubes might improve neuronal performance by favouring electrical shortcuts. *Nat. Nanotech.* **2009,** *4* (2), 126-133.

349. Galvez, B. G.; Sampaolesi, M.; Brunelli, S.; Covarello, D.; Gavina, M.; Rossi, B.; Constantin, G.; Torrente, Y.; Cossu, G. Complete repair of dystrophic skeletal muscle by mesoangioblasts with enhanced migration ability. *J. Cell. Biol.* **2006,** *147* (2), 231-243.

Ringrazio di cuore il Prof. Sergio Paoletti per avermi dato l'opportunità di lavorare nel Suo gruppo di ricerca, per tutti i Suoi insegnamenti e per tutte le occasioni di confronto, per la passione e la serietà che mostra ogni giorno e in ogni aspetto della ricerca e della didattica, per l'attenzione e la cura con cui mi ha seguito durante il mio percorso, per essere un esempio e un modello fondamentale dentro e fuori l'ambito lavorativo.
E per gli stessi motivi ringrazio Ivan, Ele, Massi, Andrea e Gianluca; grazie per l'aiuto e i consigli, per avermi trasmesso la vostra conoscenza e la vostra passione, per avermi aiutato a formare e affinare il mio approccio alla ricerca e il mio senso critico, per avermi dato modo di crescere moltissimo come ricercatore, ma anche come persona.
E Francesca, Lorena e Pasquale, per quello ho imparato e che abbiamo condiviso lavorando fianco a fianco.

Un sentito ringraziamento a tutti i colleghi con i quali ho collaborato durante questo dottorato: il Prof. Mario Grassi, la Prof. Laura Ballerini, Michela C., Manuela, Susanna, Raffaella, Matteo, Francesco, Niko, Julia, Petteri, Mervi, Marco B., Luca, Andrea C., Gabriele B., Michela A. e Denis; per tutte le occasioni di confronto che ci sono state e che mi hanno aiutato nella mia formazione.
Un ringraziamento speciale a Niko e Julia, per la vostra accoglienza, la vostra professionalità, i vostri insegnamenti e, soprattutto, il vostro affetto e aiuto in uno dei momenti più critici della mia vita. E un sincero grazie anche a Tarek e Marina per il loro affetto e la loro vicinanza, mentre ero così in difficoltà e lontano da casa.

Un GRAZIE (tutto in maiuscolo) a Mattia N., Fabio T., Mattia P. e Fede, l'entusiasmo, la passione e la dedizione che avete mostrato "sotto le armi" sono stati un nutrimento essenziale per me; aver avuto la possibilità di seguirvi e affiancarvi nella vostra formazione e di confrontarmi con voi è stata un'esperienza fondamentale e un onore durante questo dottorato. Ed è stato un piacere immenso conoscervi dentro e fuori il laboratorio. Vi voglio bene.

A Claudio (bella zì!!!), grazie infinite per il tuo entusiasmo incrollabile e il tuo sostegno pieno di passione, e per quest'amicizia lunga una vita che regala sempre stimoli. Martina P. grazie per l'amicizia che ci lega; grazie per il tuo affetto, per la fiducia e le speranze che hai per il mio futuro, per il tuo supporto, per le tue strigliate e tirate d'orecchio, e soprattutto perché la forza e la determinazione che mostri ogni giorno e con cui persegui i tuoi sogni e obiettivi sono un esempio che non dimentico mai, sei unica. E grazie agli amici di Roma: Marti, Giova, Michi, Silvia, Chicco, Simo, Maria, per l'affetto che ci unisce, per tutto il sostegno che mi avete sempre dato e per essere delle persone meravigliose.
Voglio un bene infinito anche a tutti voi.

E agli amici, ai colleghi e a tutti i compagni d'avventura: Bea, Giulia G., Greta G., Ilaria, Marco, Tomasz, Andrea M., Gabriele L., Greta G., di nuovo Michi C. e Andrea C., Grazia, Alessio, Ilenia, Mario, Giulia R., Cinzia, Marghe, Claudia, Maria, Davide, Xhika, Tex, Mix, Pic, Valentina, Fabio. P, Stefano, Monica, Milena... a chi per una risata, a chi per un aiuto o un consiglio, a chi per avermi ascoltato anche in momenti in cui era difficile sopportarmi… grazie a tutti voi per le mille sfumature di questi tre anni di dottorato.

E infine alla mia famiglia il ringraziamento più grande di tutti; per tutto il costante, immenso, necessario e vitale amore e sostegno, e per la pazienza infinita che dovete avere con me. Vi amo.